SPARSE PHASED ARRAY ANTENNAS ON PLANAR AND CONFORMAL PLATFORMS BASED ON LOW-DISCREPANCY SEQUENCES

by

Travis Torres

A thesis submitted to the Faculty and the Board of Trustees of the Colorado School of Mines in partial fulfillment of the requirements for the degree of Doctor of Philosophy (Electrical Engineering).

Golden, Colorado

Date _____

Signed: _____

Travis Torres

Signed: _____

Dr. Payam Nayeri
Thesis Advisor

Golden, Colorado

Date _____

Signed: _____

Dr. Peter Aaen
Department Head
Department of Electrical Engineering

ABSTRACT

Numerous applications in sensing, radar, and long-distance communication require antenna arrays with very directive beams. In order to achieve the high directivity, the array aperture size has to be very large, which significantly drives the cost due to the large number of elements needed on the aperture with traditional Nyquist sampling. The cost-effective solution to this problem is by using sparse arrays, i.e. a reduced number of elements that undersample the aperture. These sparse arrays have an average element spacing larger than 1 wavelength, and significantly reduce the cost of the antenna array. The biggest issue with sparse arrays however is that due to undersampling, grating lobes appear in the visible region which degrade the array performance. To mitigate this issue, synthesis approaches for sparse arrays work to spread the energy of the grating lobes in space in order to reduce the sidelobe levels of the antenna. In addition to the grating lobe issue, many applications in defense and first responder operations also require real-time techniques for sparse array synthesis.

Despite decades of work on sparse antenna arrays, a cost-effective and time-efficient solution for synthesis of large sparse arrays was not available. Random element spacing removes the grating lobes but produces large variations in element density across the aperture. In fact, some areas are so dense that the elements will overlap. This work presents the first solution to this problem by using low discrepancy sequence (LDS) sampling. Analytical methods, numerical methods, statistical and probabilistic approaches, have been studied over the years, and it is shown that none of these methods can yield a solution even close to the true optimum. The difficulty is due to the fact that side lobe level depends on the element spacing in a highly nonlinear manner, and in general there is no analytical method to determine the highest side lobe level or the angular direction where the highest side lobe may occur, unless an entire three dimensional pattern is computed. As such, the only adopted solution thus far is based on optimization approaches which are: 1) computationally slow,

2) not hierarchical, and 3) typically require amplitude and phase control over the elements which significantly increase the cost. A cost effective sparse array uses elements with unity amplitude and zero phase. This significantly simplifies the feed network and amplification circuits, which reduce the cost. The only existing work that is comparable are thinned arrays. However, we show that thinned arrays cannot achieve a low side lobe performance once average element spacing exceeds one wavelength. Moreover, our proposed approach is directly applicable to non-planar surfaces without the need for any modifications. In this dissertation, a complete analysis of LDS methods for synthesis of large planar and cylindrical sparse arrays is presented. In summary the primary intellectual merits of this work are: 1) The first cost-effective and time-efficient solution to synthesis of large sparse arrays, with the elements having a unity amplitude and zero phase, 2) The synthesis algorithm is based on mathematical sequences that are hierarchical, enabling real-time synthesis of sparse arrays over planar and non-planar apertures, 3) The approach is transformative as it promises revolutionary improvements over existing sparse analog techniques, and it applies to a broad range of applications in electromagnetics including measurements, sensing, and communications.

TABLE OF CONTENTS

LIST OF FIGURES

LIST OF TABLES

ACKNOWLEDGMENTS

I would like to thank Salman Mohagheghi, Michael Wakin, and Dorit Hammerling for serving on my thesis committee and for their contributions to this work. Thank you for having me in your classes throughout the years and for the time and effort that you put into the students and your work here at Mines.

I would also like to thank Jamal Rostami and NIOSH for their support with the Smart Bit project and the guidance they have given me while pursuing this degree. Also thanks to Austin Oltmanns and Syndey Slouka for being partners on this project and for the fun that we've had traveling for SME and working together.

Thanks to Payam Nayeri for taking me under his wing for the last five years and helping me grow as a researcher and for aiding me in my job search. Thank you for pushing me to move out of my comfort zone and encouraging me to never stop learning.

Thanks to my family for their constant love and support through everything, especially for my time at Mines. Thanks for always pushing me to give my best. Thank you for everything. I'd finally like to thank God for bringing all of these people into my life. Each person He has brought in has helped me grow and learn. I would not be in the position I am today if it weren't for Him guiding my steps all these years.

Dedicated to: Dad, Mom, and Trent

CHAPTER 1

INTRODUCTION

In this chapter, we present the central theme, concepts, and background of this dissertation. We then provide the reader with a list of the main contributions of this work. This chapter then ends with an outline and overview of the material in each chapter.

1.1 Background

Many modern day sensing applications require large antenna arrays, such as: communications, defense, and weather radar. Large antenna arrays with many antenna elements offer high resolution, high directivity (dependent on element spacing), and robustness against noise. With the development of the internet of things (IoT) and ongoing evolution of wireless technology, the frequency spectrum has become more congested and busier than ever, due to the many added users to it in recent years, particularly the WiFi (2.45 GHz) and Bluetooth (5.8 GHz) frequencies of operation. This has led to a further utilization of antenna arrays for wireless applications, particularly because of their high gain/directivity. Antenna arrays are able to transmit or receive signals with a much higher signal to noise (SNR) compared to that of a single antenna element. Antenna arrays are also desirable because of the capability to change the phase at any element, in order to change the beam pattern of the antenna array which can enhance signals received in particular directions and completely reject unwanted signals from other directions, where the degrees of freedom increase with the number of elements in the aperture.

When it comes to design of antenna arrays, a few major considerations are:

- Array configuration
- Spatial and temporal characteristics of the signal
- Spatial and temporal characteristics of the interfering signals

- Intended use of the array

For the work in this dissertation, we focus on the first and the last issue, which consists of designing a sparse array configuration for the intended use of transmitting data with the highest SNR/Gain for a communication system in a noisy environment. When it comes to the array configuration, there are two parts which must be considered, the first being the antenna pattern of the individual elements. For a transmitting RF array, the overall array pattern will be a function of the physical configuration of the sensors (array geometry) and the current distribution on each of the elements [1]. In most of the preliminary cases, the elements are assumed to be isotropic antennas, meaning that their antenna radiation pattern's are uniform in all directions, which is that of a spherical radiation pattern. It will be shown later, that this simplifies calculations and reduces the computation time for calculating the radiation pattern of the antenna array. This is useful when the array consists of many elements. It isn't until later in the array analysis, that the pattern of each of the elements is accounted for, which will result in a more ideal and accurate radiation pattern.

The second part, as briefly mentioned in the above paragraph, is the geometry of the array configuration (physical location of the array elements). Array geometries are divided into three categories, which consist of:

- Linear
- Planar
- Volumetric (3-D)

When describing the array geometry, it's best to use the Cartesian Coordinate system, which consists uses the (x, y, z) - axis as reference. For readers that aren't familiar with antenna array theory, note that linear arrays are arrays that reside on an axis, most literature and work completed in this field places the elements on the z-axis, due to that it simplifies many of the calculations. Planar arrays are elements positioned in a plane, usually in the

xy-plane. Volumetric arrays are a unique case because they consist of elements that are located using all three axes of the Cartesian Coordinate system. These volumetric arrays then branch off into a different classification known as conformal antenna arrays. Most of these volumetric arrays consist of the elements being placed on a cylindrical or spherical geometry, meaning that the antennas will need to be designed so that they can conform to the designated geometry. This often leads to, changes in the radiation pattern of the antenna, shift in the resonating frequency, and potentially feed network design issues. Conformal antenna arrays will be discussed more in depth in Chapter 2.

Following the array geometry, antenna arrays are then classified even further by the sampling method/spacing used to place the elements within the aperture of the array, where the cases of interest are:

- Uniform spacing
- Non-uniform spacing
- Random spacing

It will be shown in later chapters that the dimensions of the array aperture, element spacing, and the aperture geometry affects the design of sparse antenna arrays. Take for example, a planar array where the boundary of the array aperture and the element geometry (square or triangular) will have an impact on the radiation pattern of the array. A planar array can have an aperture that consists of a circular geometry but the element geometry is either square or triangular. These core-fundamental array parameters are a central theme used throughout this dissertation for designing sparse antenna arrays and antenna array theory in general.

1.1.1 Motivation of Array Sparsity

There are many advantages and benefits to using an antenna array. However, there are some major drawbacks to using an array for any application and for some instances, there

can be strict design restraints that restrict the use of the amount of elements and aperture size. Needless to say, the main issue on every antenna design engineer's mind is the financial cost to design the array. Antenna arrays are financially costly to design, where the costs stem from fabrication, testing, and gathering the required components for the RF chain. An RF chain is a cascade of many electronic components, with the sensor (antenna) at the beginning or end of the chain, which depends on if the system is meant to receive or transmit a signal, as seen in Figure 1.1.

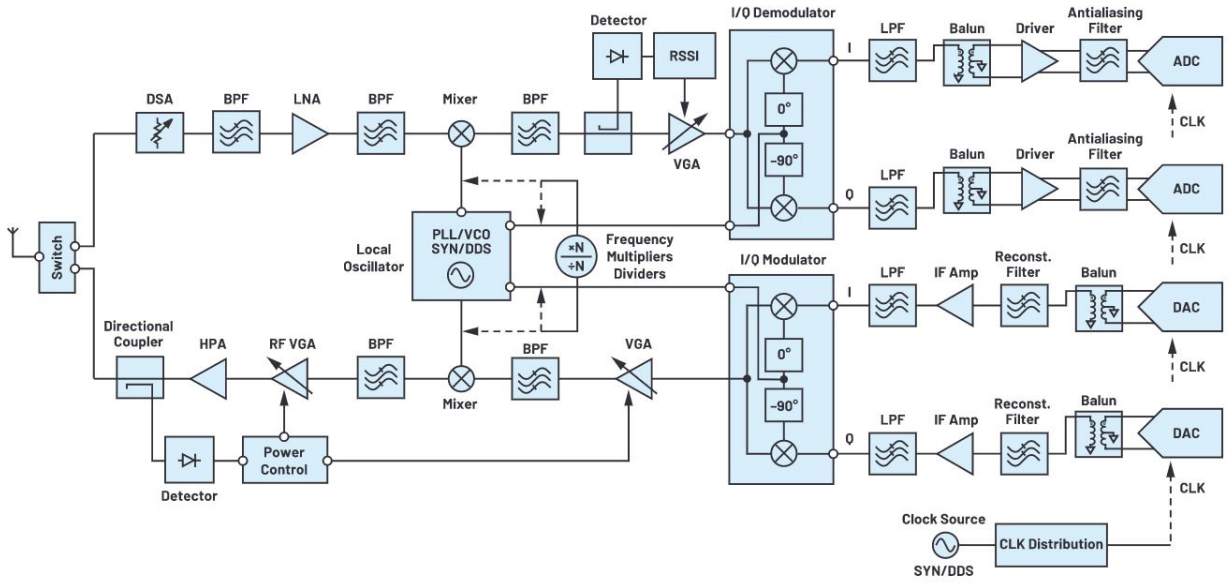

Figure 1.1 A generic RF chain and architecture for a transceiver system [2]

Granted, that the RF chain in Figure 1.1 is for a transceiver architecture and may be used for a more complex application, lets examine a much simpler case, where the RF system is designed to solely be a receiver. For the receiving architecture, the RF chain would still consist of the antenna, digital step attenuator, multiple bandpass filters, RF mixer, IQ demodulator, base band channel selector, analog to digital converter (ADC), low pass filter, anti aliasing filter, and if the system utilizes beamforming capabilities, then a phase shifter at every element and a central processing unit (CPU). The majority of the electronic components cost hundreds of dollars a piece, so an antenna array consisting of

< 100 antenna elements will be costly, let alone arrays used for defense applications that use > 100 elements. For most commercial phased arrays, which consist of few antenna elements, one would be looking at a price upwards of $\$20,000$ or more.

Due to the cost detriments of antenna arrays, the research area of sparse antenna arrays has garnered the attention of many, because it is without a doubt, that large antenna arrays are beneficial for many radar and communication type applications. The only draw back is their financial cost. Asides from cost, the intended application may also require a low-profile and low weight design structure, which is just another case when a sparse array would be desired. Note that sparse arrays fill an aperture with elements that are widely separated from each other in order to reduce the fabrication cost but maintain a narrow beamwidth. The definition of sparsity is often very broad and is thrown around loosely in many different fields and applications. The IEEE standard defines a sparse antenna array as: "An array antenna that contains substantially fewer driven radiating elements than a conventional uniformly spaced array with the same beamwidth having identical elements. Interelement spacings in the sparse array can be chosen such that no large grating lobes are formed and sidelobes are reduced" [3]. This will be the same definition that we will use to define sparse arrays in this dissertation.

1.1.2 Current Sparse Array Design Methods

In the research field of sparse array design, the current design methods that exist and that are frequently used consist of:

- Array thinning
- Convex optimization
- Random sampling
- Utilize special array structures

In the realm of array thinning, a set of elements N, are designated to a grid within a given aperture where the elements are uniformly spaced by some distance d and then a genetic algorithm (GA) is used to turn "off" some elements within the array and keep "on" a selected sub-sampled set of elements M, where $M < N$. The motivation behind array thinning was from the fact that it's difficult to implement sparsity on larger antenna arrays while also achieving a low sidelobe level (SLL) [4]. When the number of elements increase, traditional optimization methods start to become ill-equipped for solving for an ideally thinned array [5].

Array thinning can easily be summed up as solving for a binary weight taper which is represented by the vector $\boldsymbol{x}$, where x_n represents the weight for the element n and $x_n \in \{0, 1\}$, where a 0 indicates that the element is "off" and a 1 symbolizes an element that is "on". Thinned arrays share this same attribute that the element density is greatest in the center of the array and will gradually decrease towards the edges of the aperture. What this means is that the side lobes closest to the main beam will decrease while the side lobes far from the main lobe will increase. Since the elements of the array are fixed on a grid, it's simpler to thin an array because the thinned array has 2^N possible combinations, where N represents the number of array elements. Note that if the array is symmetric, then the number of possibilities becomes much smaller. However, when the elements can be non-uniformly placed within the aperture, the problem becomes more difficult to solve because there are now an infinite number of possibilites for where the elements can be placed.

The idea of array thinning is easy to grasp but the methods for solving for the desired thinned array are more complicated. Since thinning a large array for low sidelobes involves checking a large amount of different outcomes for the optimal thinned aperture, exhaustive searches will only be practical for small arrays. Optimization methods such as: down-hill simplex, Powell's method, and conjugate gradient descent, are unsuitable for thinning the array [4]. They can only optimize a few amount of continuous variables and are known to get stuck in local minima. This can easily be fixed by the use of a genetic algorithms (GA),

where GA has no limit to the amount of variables that can be optimized and isn't impacted by large arrays [6]. However, they are known to be quite slow. GA significantly differ than most optimization methods because they work with coding of the parameters and not the parameters themselves, search for many points instead of a single point (as seen with particle swarm), don't use derivatives, and use random transition rules instead of deterministic rules [7].

In [8], GA is used on both a linear and planar array, where each array consists of 200 elements. The results support the claim that the element density is greatest in the center of the array and decreases towards the edges of the aperture. The goal of achieving a maximum SLL of -20 dB was achieved, as depicted in the given plots. However, all array configurations given use anywhere between 75% and 85% of the original elements, which in some design cases, can be considered to not represent a high level of sparsity.

One of the most accepted and popular methods used for sparse array design is the use of convex optimization. For more information on this approach, the interested reader is encouraged to read the following sources [9, 10]. The research in this area approaches the sparse antenna array design by the formulation of a convex optimization problem which is typically an l_1-minimization problem. This approach solves for the sparsest weighting vector that satisfies the given constraints in the convex problem formulation. The l_1-minimization can be described by the following. Take for example, we are trying to design a sparse linear array that is centered on the z-axis. The $M \times N$ array manifold matrix is given as $\mathbf{A} = [\boldsymbol{a}_1, \boldsymbol{a}_2, \cdots, \boldsymbol{a}_N]$ for N elements. Here, the array manifold vectors are a function of the element position on the z-axis and can be written as

$$\boldsymbol{a}(z_n) = [e^{j\frac{2\pi}{\lambda} z_n \cos\theta_1}, e^{j\frac{2\pi}{\lambda} z_n \cos\theta_2}, \cdots, e^{j\frac{2\pi}{\lambda} z_n \cos\theta_M}]^\top$$

for M samples in the theta-space. The radiation pattern of the array can be expressed as a weighted linear combination of the columns of the array manifold matrix by the following weighting vector $\boldsymbol{x} = [x_1, x_2, \cdots, x_N]^\top$. A convex optimization can then be formed to solve

for the sparsest $\boldsymbol{x}$, so that the array can reproduce a known radiation pattern $\boldsymbol{y}$ so that it satisfies some error criterion ϵ. The convex optimization is defined as

$$\begin{aligned} &\min_{\boldsymbol{x}} \|\boldsymbol{x}\|_1 \\ &\text{subject to } \|\boldsymbol{y} - \mathbf{A}\boldsymbol{x}\|_2 \leq \epsilon \end{aligned}$$

which is the typical formulation for the majority of most sparse recovery problems in the field of compressive sensing. Note that the sparse solution will be a vector of a few large values and many small values that are close to but not exactly zero. A threshold can be used to set these values to zero, which indicates that the antenna element can be switched "off" or discarded from the array. Meanwhile, the non-zero values correspond to the kept antennas.

Although this method is common and is proven to work for designing a sparse array with a performance that doesn't deviate too much from the fully populated array, there are some undesirable drawbacks. The first, is that the element locations are fixed, meaning that locations of each of the sensors are located on a grid, and the optimized array will only consist of elements on this grid, which doesn't utilize the entire area of the aperture for positioning elements. This means that there's a possibility that a more optimal solution exists by placing an element or elements somewhere off the generated grid. Another drawback, is that if an element from the original array were to be added or removed, the problem will have to be reformulated and resolved. Since the array manifold vectors are a function of the position of the elements, they would need to be changed so that they can account for the new or removed elements. This can be rather inconvenient, especially with such a small adjustment. The final reason is that for most of these convex formulations, they optimize the weights (x_n) of the elements, which results in values that are above unity in order to perfectly recreate the desired radiation pattern. The reason why this can be problematic is that the current distribution will then need to be amplified so that the array weight can reach a value above unity. This is typically achieved by adding a power amplifier into the RF chain, which will

then need an external power source so that the power amplification can be supplied to the element. This would then increase the chain complexity, physical profile of the array, and cost of the array, which defeats one of the main purposes of designing sparse arrays, making it a novel approach with the use of convex optimization but not one used often to design and fabricate an array.

The third method used for designing sparse antenna arrays is known as random sampling, which randomly places elements within the aperture. The way that this method works is that the aperture size is fixed, and the element spacing d, is increased, so that less elements can fit within the aperture, as seen in the following figure.

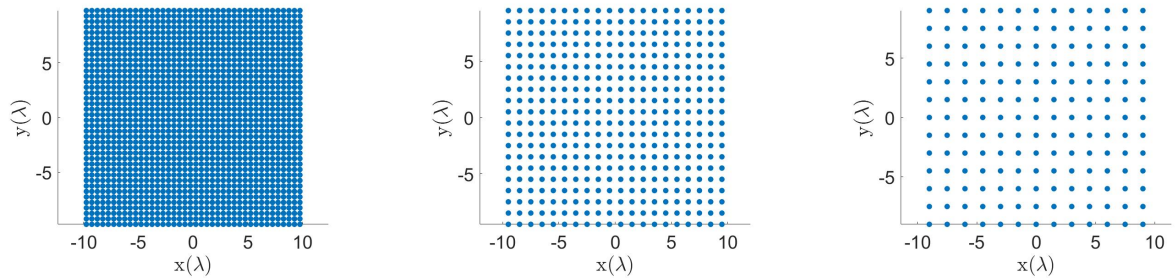

Figure 1.2 Element positions with various uniform element spacings d for a $10\lambda \times 10\lambda$ aperture: (a) $d = \lambda/2$, (b) $d = \lambda$, (c) $d = 3\lambda/2$.

It's easy to see that as the element spacing d for a fixed aperture increases, the array becomes more sparse. However, since the array is uniformly sampled across the aperture, the phenomena known as grating lobes is encountered, which is the equivalent of spectral aliasing, except that it occurs in the spatial domain. More on this in the next section. The way that the grating lobes are removed from the radiation pattern and the sparsity of the array is preserved is by generating M random samples on the aperture, where $M << N$ and N is the number of elements for the fully populated array case which occurs when $d = \lambda/2$. Next to array thinning, this is one of the most commonly used methods for designing analog antenna arrays and is the contemporary method in the field of sparse antenna array design.

Unlike array thinning and convex optimization, random sampling avoids the use of selecting pre-located elements on a grid and generates the elements on off grid locations. Random sampling methods will be discussed more in depth in Chapter 3 of this dissertation.

The last type of sparse arrays that exist are known as co-arrays. However, the use of co-arrays are used in the realm of digital arrays, which is outside of the scope and focus of this dissertation, which focuses on the design of analog antenna arrays. However, the interested read is encouraged to examine the following resources, if they are interested in the digital aspect of antenna arrays [11–14].

1.1.3 The Aliasing Problem

All of the methods mentioned above share one thing in common, which is that there are elements within the array that are spaced by distances greater than the traditional wavelength. As shown at the beginning of the random sampling method, when a uniformly spaced array is started with, the average minimum element spacing can be greater than one wavelength. The array becomes more sparse as the element spacing increases, however, aliasing then occurs in the spatial domain where this type of aliasing is known as grating lobes. Similar to the Nyquist sampling rate in traditional signal processing that states that certain rules must be followed to prevent aliasing in the spectral domain, antenna arrays must also follow certain rules to prevent aliasing in the spatial domain. Nyquist sampling theory tells us that in order to convert an analog signal into a digital signal, the signal must be sampled at a rate F_s, that is at least twice the rate of the highest frequency F_0 present within the signal $2F_0 < F_s$. If F_s falls beneath the Nyquist rate, the phenomena of aliasing occurs, which means that discrete time sinusoids whose frequencies are ω are separated by multiples of 2π are now indistinguishable in the frequency domain. This is troublesome because sinusoids at higher frequencies now appear as sinusoids at lower frequencies because we are sampling too slowly. However, if $|\frac{F_0}{F_s}| < \frac{1}{2}$, then we can expect to avoid this issue.

Like Nyquist sampling, antenna arrays are also a sampling mechanism, where in receiving mode, they take samples of amplitudes and phases at a point in space at the location of

each element. When the array is transmitting, the elements, assumed to be isotropic, are represented by complex sinusoids that add up constructively or destructively in the far-field of the array, this is commonly known as the array factor. When the spacing of the array elements is large, aliasing occurs in the spatial domain, resulting in the grating lobes because copies of the main lobe appear in the radiation pattern. This is detrimental because grating lobes are larger than the typical side lobe and take power away from the main beam and transmit the signal at a high gain in these directions. From a communications stand point, this can generate significant multi path fading and interference at the receiving end. To be exact, grating lobes appear within the radiation pattern when the element spacing is greater than or equal to one wavelength $d \geq \lambda$. In Figure 1.3, a planar array centered in the xy-plane with an aperture size of $5\lambda \times 5\lambda$ is given, where the elements are spaced by $\lambda/2$. The normalized power pattern is also shown, where the main beam is presented in the uv-space and the main beam is steered to $u = 0$ and $v = 0$.

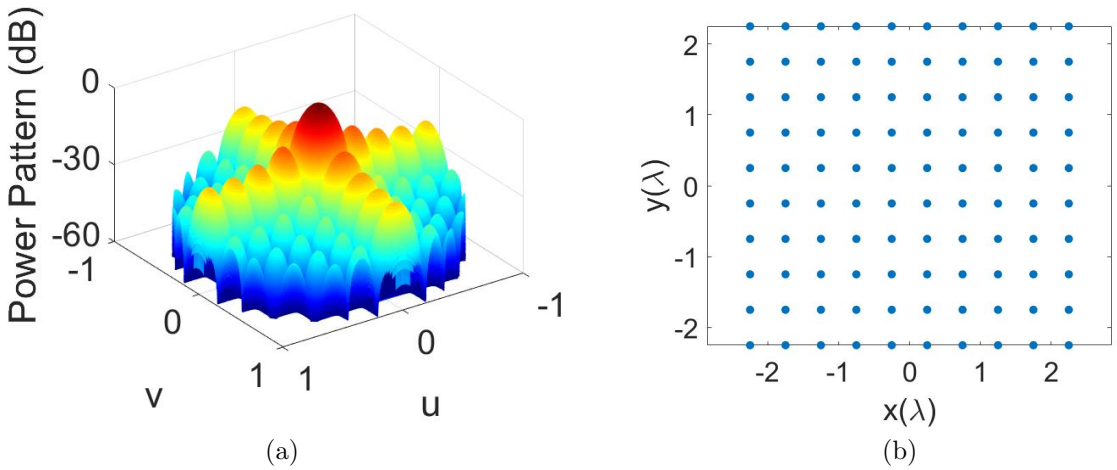

(a) (b)

Figure 1.3 Planar array centered around the xy-plane with an aperture size of $5\lambda \times 5\lambda$. The array consists of 100 elements spaced when $d = \lambda/2$: (a) Normalized power pattern of the antenna array, (b) Element distribution in the xy-plane.

When the aperture size is held constant and the wavelength is increased to $d = \lambda$, this results in a sparse array that utilizes a quarter of the original elements. However, as mentioned before, since $d \geq \lambda$ the grating lobes are heavily present within the normalized

power pattern, as shown in Figure 1.4. By taking this approach, it's observed that when comparing Figures 1.3 and 1.4, that there is a trade off when using uniform sampling. The trade off is that a dense array will use many elements but have a highly directive power pattern and a sparse array will use fewer elements but sacrifice a highly directive power pattern for one with grating lobes. However, in recent years the field of compressive sensing has proven that if our signal is sparse with respect to some basis (Fourier, Wavelet, etc.) then we can actually violate the Nyquist sampling theorem by sampling sub-Nyquist. In most articles on compressive sensing, research has proven that when we sampled sub-Nyquist, the probability of recovery is higher when we use non-uniform sampling methods and spectral aliasing can be avoided [15]. Similar to the Nyquist limit, grating lobes can be removed from the power pattern when we utilize non-uniform sampling methods for element placement within the aperture, which was already mentioned for the random sampling case for sparse array design. The purpose of this thesis is to go beyond the typical method of random sampling and employ newer methods that can remove grating lobes from the power pattern and that can still maintain an average minimum element spacing of λ.

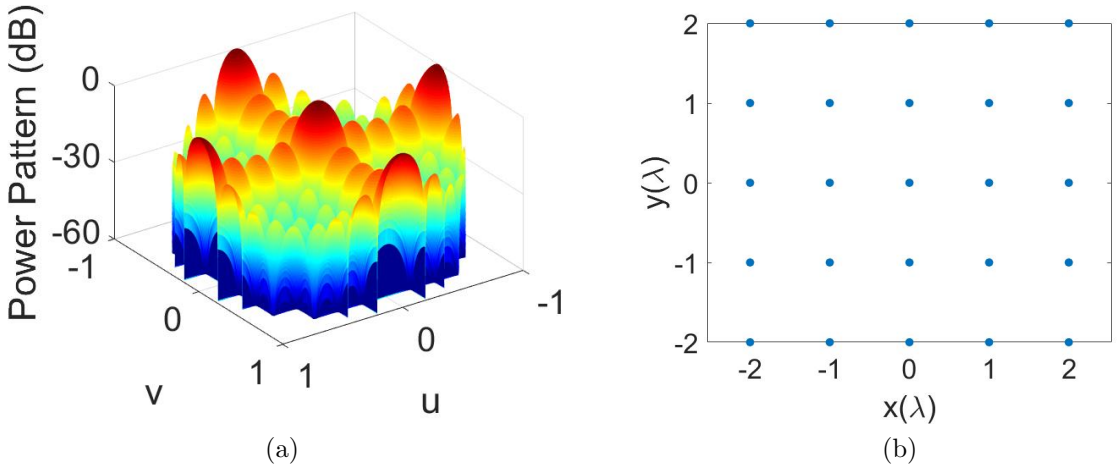

Figure 1.4 Planar array centered around the xy-plane with an aperture size of $5\lambda \times 5\lambda$. The array consists of 25 elements each spaced by $d = \lambda$. The new array uses a quarter of the original elements but the grating lobes are visibly present within the power pattern: (a) Normalized power pattern of the antenna array, (b) Element distribution across the xy-plane.

1.2 Overview and Contributions

In this dissertation, a new time-efficient approach to designing sparse antenna arrays is presented. The sparse arrays that are designed do not need to have amplitude or phase taper which significantly reduces the complexity and cost of the sparse array feed network. In the previous section, we gave a brief overview of the current methods that exist and the ones that are frequently used for designing sparse arrays. Based on the the current methods that exist, we develop a series of different techniques that use non-uniform sampling sequences to design sparse arrays that take into account the previous disadvantages and try to solve them, such as: element clustering, elements being stuck to a pre-allocated grid, and weight excitations that require power amplifiers to achieve the desired excitation. These sequences are used to overcome these issues and design a sparse array that can ultimately satisfy a set of design constraints. Since the area of antenna array theory is very broad and many different parameters are involved in an antenna array, we focus on using these design techniques for planar arrays and conformal cylindrical arrays, where element number, aperture size, beam steering, and aperture shape are all examples of various parameters that we consider. We first start off with applying these new techniques to planar arrays and then we close by extending these techniques to conformal cylindrical arrays. An electromagnetic model is also provided for the sparse conformal arrays on a cylindrical surface using Ansys High Frequency Structure Simulator (HFSS).

Our contributions to the antenna society include a new:

- *method* for designing sparse antenna arrays by using non-uniform sampling sequences that were used in image processing and computer science, to strategically place the antenna elements in a sparse configuration that can eliminate grating lobes from the power pattern and place the elements far enough away from each other so that the array can be fabricable.

- *analysis* for the anti-aliasing problem in the spatial domain for 2D and 3D antenna arrays

- *grid-less based approach* for designing sparse antenna arrays, in cases where the sparse set makes up $< 80\%$ of the original set of elements

- *analysis* for the EM model of a designed sparse antenna array to demonstrate that these methods aren't significantly impacted by mutual coupling

- *more efficient* array architecture that has a higher directivity and lower side lobe level than the uniformly sampled array

- *analysis* for when to use the newly proposed methods and when to resort to an already existing technique

- *perspective* to the antenna array design problem that could lead to a better understanding and the development of future techniques

In Chapter 2, we give a brief overview to the reader of the basics of antenna and antenna design theory. The way that this dissertation is different than a lot of the current resources and articles on the area of sparse array design is that the majority of these sources focus solely on the mathematical aspect of antenna array synthesis and neglect the electromagnetic (EM) portion of antenna array design but this thesis considers the EM model. We highlight the main antenna parameters, such as: impedance bandwidth, gain, directivity, and antenna efficiency. After the basic antenna radiation principles and parameters are defined, we then provide some basic patch antenna design theory and then discuss the inset fed patch antenna, which is used to increase matching between the antenna and the feed to minimize reflection loss and is the antenna used for one of the designed arrays for the work in Appendix C. Our designed inset fed patch antenna is presented, along with the impedance bandwidth, pattern cuts for $\phi = 0^\circ, 90^\circ$, and the 3D radiation pattern. We then conclude the chapter by the

presentation of the conformal patch model and how we plan on using it to model our sparse conformal arrays.

In Chapter 3, we provide an in depth mathematical overview of the previous work accomplished in this area and then discuss the mathematical sequences that previously existed and will be used for our newly proposed methods. These sequences are known as low discrepancy sequences because they appear random but actually have structure to them, where they are designed to fill an interval or an aperture more uniformly than a set of random points. These sampling techniques are proven to be beneficial because they can place elements off the original grid, which array thinning and convex optimization can't do. The basis for using these sampling methods, is that the element spacing of the fully populated array (array spaced by $\lambda/2$) is increased, which results in a sparse representation of the array, because some of the elements can't fall within the aperture with this increased element spacing. The remaining elements are then re-placed within the aperture by mapping the coordinates of the elements to the proposed sequences.

In Chapter 4, these LDS methods are used to design low discrepancy sparse phased arrays for arrays with a square aperture, specifically in the xy-plane. The performance of the LDS arrays are compared not only with each other, but also with the uniform and random array designs, where the random case randomly places the elements in the aperture, by mapping the x and y coordinates to uniform random variables. The metrics used to analyze of the performance of the arrays consist of: average minimum element spacing (λ), peak side lobe level, directivity, and aperture efficiency. The results of the LDS arrays, demonstrate that by using LDS sequences to map the elements to the aperture, the grating lobes can be removed from the power pattern, the elements are placed far enough from each other so that the array can be fabricated and avoid the effects of mutual coupling, have a higher directivity and lower side lobe level than the uniform and random sampled arrays. The sampling sequences are also proven to holdup for different aperture shapes: circular, elliptical, and rectangular, and can still avoid grating lobes when scanning in θ and in ϕ.

In Chapter 5, we provide the first ever in depth analysis of sparse array design between many of the existing methods and the proposed LDS techniques. The previous methods we examine are convex optimization, array thinning with and without GA, and GA for element geometry optimization. The chapter starts off by demonstrating the effects of aperture size on the LDS techniques and the effectiveness of uniform sampling before the element spacing approaches λ. The pre-existing methods are then presented and modified so that they fit along the lines of element selection and are compared to the performance of the LDS methods, where we see that the LDS methods are efficient at quickly designing an array for any sparsity level and reducing the SLL and removing grating lobes.

In Chapter 6, we see a similar structure to Chapter 4, where we extend the LDS methods from the planar array to cylindrical arrays. We once again, compare the cylindrical array produced with uniform sampling but only with the two methods that we found to be the most successful in Chapter 4, which is Halton sampling and Poisson disk sampling. We discuss and explain that as we saw in Chapter 4, the directivity of the array will decrease with high sparsity levels, so our primary focus in this chapter is to remove the grating lobes and lower the SLL of the cylindrical arrays with the two LDS sampling methods. The 3D power pattern is given, along with pattern cuts in the main principal planes (xy, xz, yz), element distribution on the cylinder, and the distribution of the minimum element spacing between elements. We show with the results that the grating lobes are once again removed from the power pattern and that the elements avoid clustering together. The chapter then concludes by explaining the concept of an active sector for a sparse cylindrical array and providing an EM-model designed in Ansys HFSS for uniform and Halton LDS.

In Chapter 7, we conclude this dissertation and review the achievements in this thesis and possible areas of future work.

CHAPTER 2

PLANAR AND CONFORMAL PRINTED ANTENNAS

In this chapter, detailed descriptions of the functionality of planar and conformal antennas is presented. This chapter begins with an overview of the definition of an antenna, the fundamental principles of antenna radiation, and the main antenna parameters that are taken into consideration for antenna design. An example of a radiation half wavelength dipole is also presented. We then go over the design of a microstrip patch antenna and then one of the many modified versions of the microstrip antenna, known as the inset fed microstrip antenna. Since the work in this dissertation focuses on both the planar and the conformal case, we then conclude this chapter with the presentation of the conformal patch antenna model on cylindrical surfaces. Due to the curvature of the cylindrical surfaces, the radiation pattern of the microstrip antenna is affected, so the planar model can not be used for the conformal case, resulting in the need for a more appropriate model. Simulated results in Ansys HFSS [16] and S-Parameter measurements are also presented for both the planar and conformal models.

2.1 Antenna Functionality Overview

In the area of communications, two devices can be used which consist of a transmission line or an antenna. Wired communications (transmission lines) consist of a source a point that are connected by a transmission line where the data is sent in the form of modulated electromagnetic (EM) waves. Wireless communication systems exclude the use of connecting the two sources by a transmission line and use an antenna to transmit modulated EM-waves through free space or in a medium. Both devices have their benefits and should be used depending on if the device is appropriately suited for the intended application. Typically, antennas are more desirable than transmission lines when the transmission distance is large, as shown in Figure 2.1. This is specifically when the decay of a transmission line can be

modeled by $e^{-\alpha z}$, where α is the decay constant and z is the distance from the source. For larger distances, it's shown that the power loss of the antenna is less than that of a transmission line, where the power loss for transmission lines decays rapidly at great distances. However, with the development with fiber optic lines, which are lossless, they can also be used for transmission at large distances. For some communications, antennas are necessary, such as for airplanes, ships, and personal communication devices.

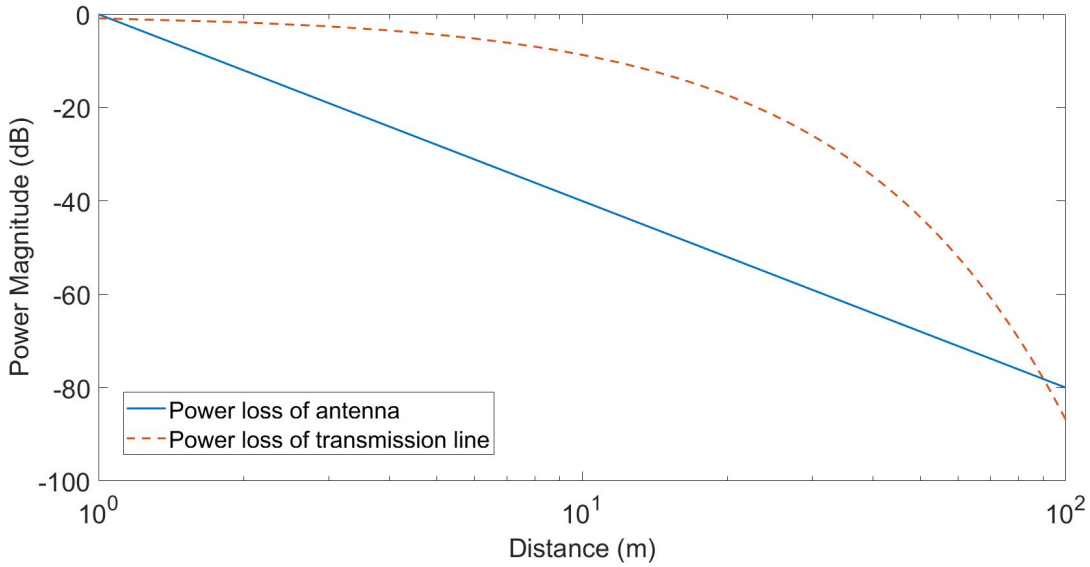

Figure 2.1 Power loss of an antenna and a transmission line with a decay constant of $\alpha = 0.1$

Antennas are devices used to transmit or receive electromagnetic (EM) waves from a point in space. In the transmit mode, an antenna converts a guided wave propagating on a transmission line into an EM wave that propagates in an unbounded medium by creating disturbances in the nearby electric field (E-field), as seen in Figure 2.2. Antennas are also reciprocal devices, which means that they exhibit the same radiation characteristics for transmission and reception (note that the only time this statement isn't true is when the RF chain contains active elements). Antennas can ultimately be thought of as frequency and spatial filters, because they will reject EM signals within some portion of the frequency spectrum and receives EM signals in other parts of the frequency spectrum, and can also

receive signals coming from a particular direction and can also reject signals coming from other directions, thus acting as a filter in frequency and in space.

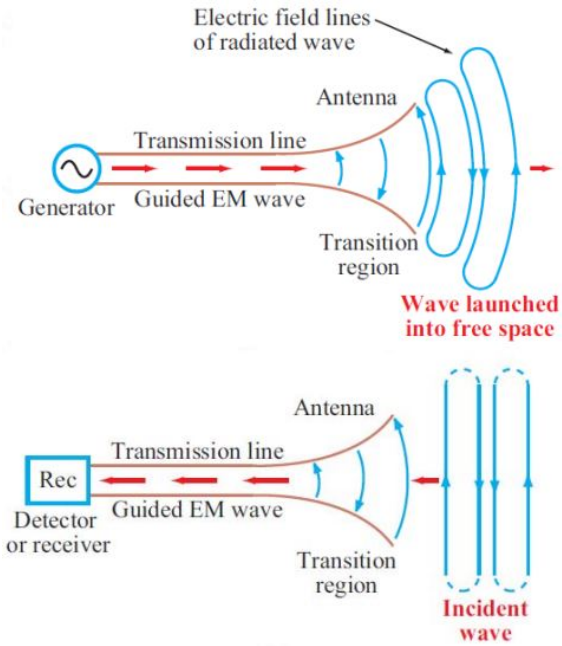

Figure 2.2 Basic antenna functionality as a transducer between a guided electromagnetic wave and a free space wave [2]

Antenna EM-radiation is based off of the fundamental physics of the acceleration of an electric charge, where radiation is the emission or transmission of energy in the form of waves or particles through free space or through a material medium. The IEEE definition of antenna radiation is, "the emission of electromagnetic energy from a finite region in the form of unguided waves" [3]. This radiation is triggered by a disturbance in the EM-fields that propagates away from the source of the disturbance. This disturbance is created by a time varying current that has an an associated accelerated charge distribution. For a steady (constant) flow of charge through a surface, the current is given by the following

$$I = \frac{Q}{t} \tag{2.1}$$

where Q represents charge and t is the length of time. More generally, the equation for a time varying current can be expressed as

$$I = \frac{dQ}{dt} \tag{2.2}$$

This principle can easily be explained by Figure 2.3. Prior to arrival at point A, the charge is moving with a constant velocity and the static electric field lines extend radially away from the charge to infinity and move with the charge. The charge then accelerates from point A to point B, where it continues on at the acquired velocity. The distance between the circles Δr is the distance light would travel in time $\Delta r = r_B - r_A = \Delta t/c$. Since the charge moves relatively slow compared to the speed of light, the circles are nearly concentric. The electric field lines in the Δr region are still joined together, because of the required continuity of electric field lines in the absence of charges. It can be seen in this region that the structure of the electric field is disturbed, from the acceleration of the charge, where the disturbance then propagates outward at the speed of light. The main purpose/takeaway from this example is for the reader to understand that accelerated charges radiate. The acceleration of the charge is caused by the change of speed or change of direction of the charge. For an antenna, this acceleration is caused by charges moving back and forth on a wire, or due to some source generator that incites an oscillation of charges. The charge's direction is reversed at the ends of the wire, which in return, results in radiation from the wire. The analogy that can be used to explain how an antenna emits EM radiation is the disturbance made when an object is thrown in still waters, where the surface of the water begins to radiate out radially from the point of where the object was thrown into the water. The other analogy that can be used to describe antenna functionality is credited to Leonardo da Vinci, who compared antenna radiation to the way that waves move across a field of wheat, where the field first starts out at a stand still, and then a blowing wind creates a propagating wave across the tops of the stalks of the wheat [17].

The simplest antenna design that brings together the concepts of accelerated charge, alternating current on a wire, and EM-radiation would be the half-wavelength dipole antenna,

as shown in Figure 2.4. The dipole antenna originates from an open-circuited transmission line, where the ends of the line are bent so that the length is approximately $\frac{\lambda}{2}$, where λ is the wavelength at the operating frequency of the antenna. Note that the key to making the antenna radiate, is the alternating current (AC) on the line, where the bends at the end of the transmission line, cause for the electrons of the induced AC source to accelerate, thus creating the disturbance needed, to create a propagating EM wave.

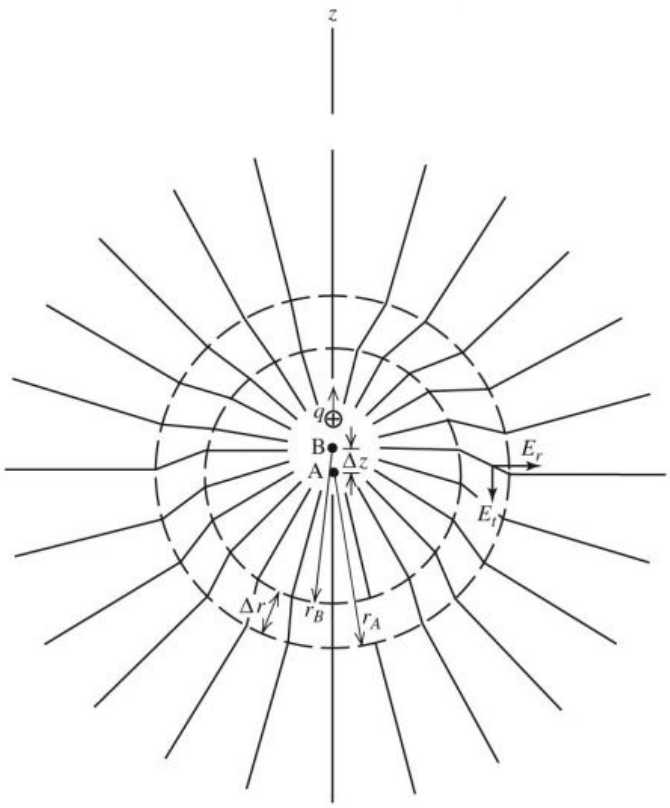

Figure 2.3 Radiation induced by an accelerating electric charge that causes a disturbance in the nearby E-field lines [17]

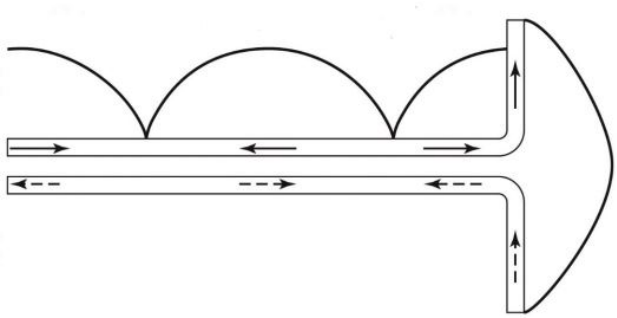

Figure 2.4 Basic functionality of a dipole antenna, where the radiation emitted from the ends of the wire due to an oscillating charge [17]

2.2 Antenna Parameters

Antennas are devices that have a great deal of parameters that are used to describe their characteristics and their performance. The list of antenna parameters include: frequency & wavelength, radiation pattern, polarization, impedance, bandwidth, directivity, gain and scanning. For the purpose of this dissertation, we will omit discussion on antenna polarization because it's outside the scope of this work. There are many papers and articles that are available that discuss the topic of antenna polarization and the interested reader is referred to the following sources [18–21].

2.2.1 Frequency & Wavelength

The simplest of all the antenna parameters is the frequency and the wavelength of the antenna. The frequency of the antenna is often referred to as the operation frequency of the antenna, which is the center frequency of the bandwidth (bandwidth describe in later section) of the antenna, often referred to as f_0. The wavelength can can easily be found by the following equation

$$\lambda = \frac{c}{f_0} \tag{2.3}$$

where c represents the speed of light in free space. Wavelength is often an important parameter because it relates directly to the design dimensions of the antenna, as shown with the half-wavelength dipole example in the previous section.

2.2.2 Radiation Pattern

One of the most important performance parameters used to determine the antenna performance and characterize the antenna is the radiation pattern. The radiation pattern or antenna pattern is defined as, "a mathematical function or a graphical representation of the radiation properties of the antenna as a function of spatial coordinates (spatial distribution)" [3]. Note that any of the following are also a suitable definition of antenna pattern:

- A mathematical function or a graphical representation
- Quantities that are equal or proportional to the power flux density, radiation intensity, directivity, phase, and field strength
- Spatial distribution over any surface or path

The radiation pattern of the antenna shows the variation of the radiation with respect to the angle around the antenna, where Cartesian Coordinates are used to depict the geometry of the antenna and the pattern is given in polar coordinates which uses the elevation and azimuthal planes as references, governed by θ and ϕ respectively.

When the antenna is receiving, the radiation pattern will indicate which directions and how strongly the antenna can receive EM-waves from. In transmission mode, the antenna pattern will indicate the directions and the intensity that the antenna will transmit EM-waves in. As mentioned before, antennas are reciprocal devices so their radiation pattern will tell be the same for transmitting and receiving.

Antenna radiation patterns are given in dB and are given in one of three forms: a 3D pattern depicted in Cartesian Coordinates, slices from the 3D pattern for some slice in ϕ over a range of theta, or some slice in θ over a range of ϕ. Two slices of interest are the slices

that give us the x-y plane and the x-z or y-z planes (depending on the antenna orientation). These slices are important because from basic EM-theory, we know that a transverse EM-wave consists of an E-field and magnetic field (H-field) that are perpendicular to each other and continuously oscillate in a plane. So by collecting these slices, we can exclusively examine the E and H planes of the antenna radiation pattern. By using these three ways to view the pattern, we can also classify different portions of the antenna pattern. The first being the main beam or main lobe of the antenna, which is the direction of maximum radiation, given by (θ_0, ϕ_0). Antennas will also have a side lobe region, which are known as the lobes or the region that doesn't include the main lobe. The last lobe, being the back lobe, which is directly opposite of the peak direction of the main lobe. Whether in transmit or receive mode, an antenna will transmit or receive a signal in the directions of these lobes, so it's important to minimize the level/radiation intensity of the antenna in these directions.

Antennas can be categorized based on their type of radiation sources, such as: current fields and aperture fields. For current fields, a time-varying current is flowing in the conducting wires, which gives rise to radiated EM fields, as shown in Figure 2.4. For aperture fields, the EM fields across the aperture serve as the sources of radiation, however, note that the aperture fields are induced by time-varying currents on the surfaces of the antennas. A particular type of aperture antenna is the microstrip patch antenna, which will be described in the next section.

2.2.3 Impedance & Bandwidth

The next couple antenna parameters used to evaluate antenna performance are the impedance and the bandwidth of the antenna. The bandwidth of an antenna can be defined as the range of frequencies over which the antenna parameters are acceptable. From the half-wavelength dipole example, we saw that the dimensions of the antenna are chosen by some operating frequency f_0. So by changing the dimensions of the antenna, we can shift our operating frequency to higher or lower frequencies by changing the dimensions of our antenna. By using Equation 2.3, we see that smaller antenna dimensions will result

in a higher operating frequency and bigger antenna dimensions result in a lower operating frequency. Note, that Equation 2.4 is usually a rough estimate for calculating the length of the antenna, but other factors such as: antenna material, material of the medium the wave is travelling in, thickness of the antenna, all play a factor in the resulting operating frequency of the antenna.

Antenna bandwidth can't be talked about without also discussing the antenna impedance. The impedance of the antenna refers to the input impedance at the antenna terminals, which is the point where the feed or transmission line meets the antenna (load). For the majority of transmission lines, whether it be a microstrip line or a coax cable, the standard impedance used is 50Ω. This then leads to the topic of impedance matching. The antenna must be designed so that it has an input impedance of 50Ω for some operating frequency f_0, since the impedance of the antenna is a function of frequency. If the antenna impedance isn't that of the 50Ω line, then there will be a impedance mismatch and the traveling wave on the transmission line will be reflected back to the source. In order to ensure that the antenna will receive/transmit at a f_0, the antenna should be designed and optimized so that its impedance Z_a will match the impedance of the line so that reflections will be minimized. The reflections of the wave for the antenna as a function of frequency is characterized by the reflection coefficient $\Gamma(f)$. Equation 2.4 is used to calculate the reflection coefficient for some frequency f, where Z_c refers to the impedance of the transmission line. In proper RF terminology, the performance of the antenna relating to reflected power within the system is referred to as the scattering parameters. Note that for an RF system, the parameter S_{11}, indicates the amount of power that makes it to the load, which directly corresponds to the reflection coefficient, so $S_{11} = \Gamma$.

$$\Gamma(f) = \frac{Z_a(f) - Z_c}{Z_a(f) + Z_c} \tag{2.4}$$

The reflection coefficient is plotted as a function of frequency on the decibel (dB) scale, which explains the functionality of the antenna more efficiently. It's from this plot that we

can determine the bandwidth of the antenna. In dB scale, we see that at -3 dB, half of the power makes it to the antenna and half is reflected back to the source and at -10 dB, roughly 90% of the power makes it to the antenna and 10% is reflected back. We use this -10 dB point to indicate the range of frequencies that the antenna parameters are acceptable, where f_l and f_h are the lowest and highest frequencies of this range respectively.

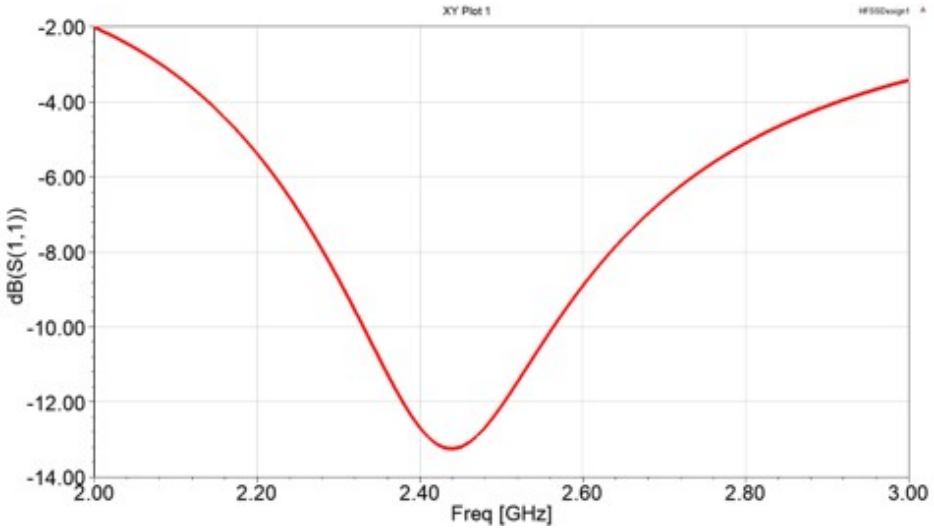

Figure 2.5 S_{11} for 2-3 GHz

As seen in Figure 2.5, we can easily determine the values of f_l and f_h, where the bandwidth $\Delta f = f_h - f_l$ results in a bandwidth of about 240 MHz, roughly with an f_0 of 2.45 GHz.

2.2.4 Directivity and Gain

The last two parameters to be discussed are directivity and gain. The directivity of an antenna is defined as the ratio of power density in the direction of the pattern peak to the average power density. Directivity is an important parameter because it tells us how much radiated power is concentrated in a particular direction. The expression for directivity is shown below in Equation 2.5

$$D(\theta, \phi) = \frac{P(\theta_0, \phi_0)}{\int_0^{2\pi} \int_0^{\pi} P(\theta, \phi) \sin\theta d\theta d\phi} \tag{2.5}$$

where $P(\theta, \phi)$ is the normalized power pattern of the antenna at a given frequency, in terms of elevation and azimuth angles and (θ_0, ϕ_0) corresponds to the direction of the pattern peak. Note that directivity is dimensionless. Directivity is often used to characterize antennas, where antennas with lower directivity are often known as omni-directional antennas and highly directive antennas are referred to as pencil beam antennas. It will be shown in a later chapter that by placing multiple antennas in an array configuration, their antenna patterns can add up constructively or destructively. When the elements add up constructively, the directivity of the the array will increase. This is a fundamental idea in antenna array design.

Gain and directivity are mentioned together because the gain of an antenna is found from the directivity. Of the total power supplied to the antenna (P_t), a portion of it is radiated into space (P_{rad}) and the rest if dissipated as heat in the antenna, which defines the radiation efficiency of the antenna as

$$\xi = \frac{P_{rad}}{P_t} \tag{2.6}$$

and then can be used to calculate the gain of the antenna

$$G = \xi D \tag{2.7}$$

which is defined as the directivity reduced by the losses on the antenna. It's important to note that gain does not include losses arising from impedance mismatch and if an antenna is without dissipative loss, then for any direction, the gain is equal to the directivity of the antenna.

2.3 Microstrip Patch Antennas

2.3.1 Patch Antenna Overview

Microstrip antennas are a special case of printed antennas, which are created by using similar techniques to that of designing printed circuit boards. Microstrip antennas are highly desirable because they are low-profile devices, simple and inexpensive, can be shaped in

various ways to satisfy certain radiation characteristics (polarization, directivity, bandwidth, etc.), and are conformal to planar and non-planar surfaces. However, microstrip antennas are low-power devices, have narrow bandwidth, small gain, and extra radiation occurs from the feeds and junctions.

More specifically, microstrip antennas are antennas that consist of thin metallic conductors that are attached/boned to a grounded dielectric substrate or an insulator. The radiation and functionality principles of the microstrip patch antenna are shown in Figure 2.6. We see that since the E-field is vertically oriented, the magnetic current will then be horizontally oriented, based off of a the properties of a transverse EM-wave. Since the image magnetic current is in the same direction as the source current, the radiations from the two currents will reinforce each other. It's this concept of equivalent currents for the responsibility of EM-radiation from the microstrip antenna. In Figure 2.6, we see another important principle of the functionality of microstrip antennas, which is that the top conductor (patch) has a length L, is long enough to sustain the E-field such that the E-field in the dielectric substrate is equal in magnitude but opposite in polarity at opposite ends of the antenna. This is desirable because the E-field lines fringe around the patch and meet in-phase in the far-field, constructively creating the radiation pattern. However, there is a consequence to this, which is briefly discussed in the figure caption and will be elaborated in the microstrip design section. Typically, the rule of thumb that will achieve the E-field being equal in magnitude but opposite in polarity at opposite ends of the patch is for $L = \lambda/2$.

For analysis of microstrip patch antennas, the microstrip patch antenna is oriented so that the patch resides in the xy-plane, where the top metallic conductor is at $z = 0$, where the width of the patch W, goes along the y-axis and the length of the patch L, goes along the z-axis. This means that the E-plane resides in the xz-plane and the H plane is found in the yz-plane. The mathematical analysis of the E and H planes over θ, of a rectangular patch antenna can be expressed by the following equations:

$$F_E(\theta) = \cos\left(\frac{\beta L}{2}\sin\theta\right) \tag{2.8}$$

$$F_H(\theta) = \cos\theta \frac{\sin\left[\frac{\beta W}{2}\sin\theta\right]}{\frac{\beta W}{2}\sin\theta} \tag{2.9}$$

where $\beta = 2\pi/\lambda$. Plots for the E and H planes of a rectangular patch antenna with $L = W = .49\lambda$ is shown in Figure 2.7.

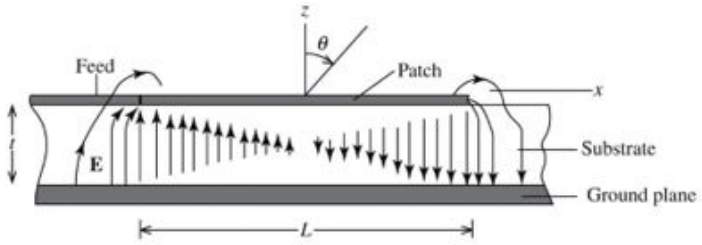

Figure 2.6 Side view of the E-field induced within the dielectric of the patch antenna, with varying polarities at opposite ends of the patch. The E-field fringes around the edges of the patch, makes the length of the patch seem longer than it actually is [17]

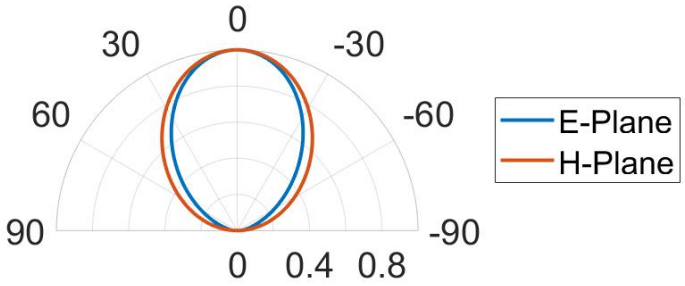

Figure 2.7 Polar plot of equations 2.8 and 2.9 over θ for a rectangular microstrip patch antenna with the dimensions $L = W = .49\lambda$

Note that there are several methods of analysis used for microstrip patch antennas. The first being the transmission line method, which is the simplest to set up, but is also the least accurate of the two methods. The other, is known as the cavity method, which is more complex to set up but is more accurate. This method will be used later in the chapter for the analysis of conformal microstrip antennas on a cylindrical surface. Despite their accuracy's, both methods provide ample physical insight into the performance of the patch antenna.

There are four popular feeding techniques used to excite the microstrip patch antenna which consist of: microstrip line, coaxial probe, proximity coupling and aperture coupling. For transmission line feeds, these are the easiest of the four to fabricate and it's fairly simple to match the antenna to the feed by controlling the inset feed position (discussed in next section of this chapter). However, they result in a narrow bandwidth (less than 10%) and as the substrate height increases, the surface waves and spurious feed radiation increases as well. Coaxial feed lines are easy to fabricate and match, since they can be placed at any position on the patch. They also have low spurious radiation, unlike the transmission line feed but they also are narrow bandwidth (less than 10%). Coax feeds also become more difficult to model with thicker substrates. Proximity couple feeds are easy to model and have low spurious radiation. Proximity coupled feeds have the largest bandwidth of all the methods (as high as 15%) but are more difficult to fabricate. Lastly, aperture couple feeds consist of a ground plane between substrates which isolates the feed from the radiating element which minimizes interference. They are relatively easy to model and are low bandwidth (less than 10%) and are the most difficult of the four techniques to fabricate. The geometry and layout of each technique is displayed in Figure 2.8.

2.3.2 Microstrip Patch Antenna Design

Empirical formulas have been derived in order to determine the dimensions of the patch antenna for a given design frequency [17]. When the patch is approximately half wavelength long, the patch will become resonant, where the input reactance is zero. The top view of the E-field lines for a half wavelength patch antenna are shown in Figure 2.9, along with its

corresponding 3D radiation pattern in HFSS. The E-field lines in Figure 2.6 and 2.9 shows fringing fields that extend beyond the patch antenna, making the patch effectively longer than its actual physical length. This results in the resonant length being slightly smaller than half wavelength. When accounting for the dielectric constant ϵ_r, a simple approximation to find the length and width of the patch for some frequency f_0 can be found by

$$L = .49\frac{\lambda}{\sqrt{\epsilon_r}} \tag{2.10}$$

$$W = \frac{c}{2f_0}\sqrt{\frac{2}{\epsilon_r + 1}} \tag{2.11}$$

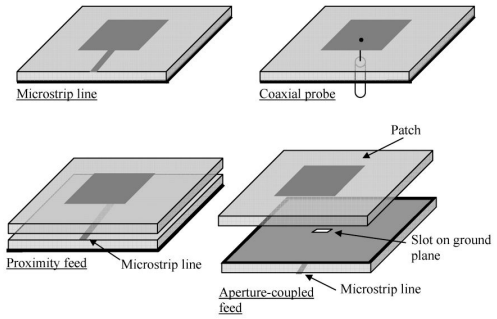

Figure 2.8 Popular feeding techniques for microstrip patch antennas: microstrip line, coaxial probe, proximity feed, aperture coupling. Image is used from [22]

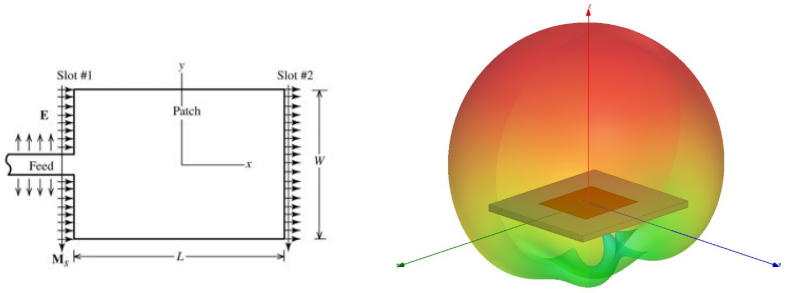

(a) (b)

Figure 2.9 (a) Top view of the E-field of the patch antenna, excited by a microstrip feed, where the fringing effects make the length of the patch seem longer [17], (b) Radiation pattern of a patch antenna, where red indicates high intensity of the E-field and green indicates a less intense E-field. The sidelobes and back lobe are also visible

When we don't include fringing within the calculations, the resonant frequency of the patch antenna can be approximated as

$$f_r = \frac{c}{2L\sqrt{\epsilon_r}} \tag{2.12}$$

However, it's more realistic and accurate to take the fringing fields into account. Shown in Figure 2.10 is a rectangular patch antenna with the fringing regions identified by ΔL.

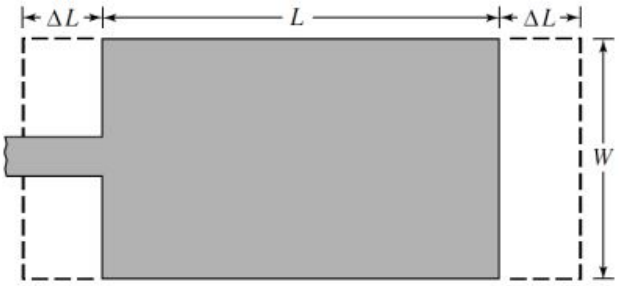

Figure 2.10 Image of fringing fields of a rectangular patch antenna. The fringing field regions are shown by ΔL. Image is used from [23]

From the new rectangular patch antenna model, we see that the effective length of the patch antenna is actually $L + 2\Delta L$, so the actual resonant frequency can be solved for. Note that the increased length of the patch causes the actual resonant frequency to be slightly less than f_0 by a factor q, so the resonant frequency can be expressed as

$$f_{rc} = \frac{c}{2(L + 2\Delta L)\sqrt{\epsilon_{\text{reff}}}} = q\frac{c}{2L\sqrt{\epsilon_r}} \tag{2.13}$$

where

$$q = \frac{f_{rc}}{f_0} \tag{2.14}$$

and

$$\epsilon_{\text{reff}} = \frac{\epsilon_r + 1}{2} + \frac{\epsilon_r - 1}{2}\left[1 + 12\frac{h}{W}\right]^{-\frac{1}{2}} \tag{2.15}$$

Note that h is the height of the dielectric substrate. ΔL can then be found from h, W, and ϵ_{reff} by the following equation

$$\Delta L = 0.412h\frac{(\epsilon_{\text{reff}} + .3)(\frac{W}{h} + 0.264)}{(\epsilon_{\text{reff}} - 0.258)(\frac{W}{h} + 0.8)} \tag{2.16}$$

2.3.3 Inset Fed Microstrip Patch Antenna

A modification made to the geometry of a rectangular microstrip patch antenna is a recessed feed line, which is used to improve the impedance matching between the antenna and the feed line. This type of antenna is known as an inset fed patch antenna. The geometry of the inset fed patch antenna is show in Figure 2.11.

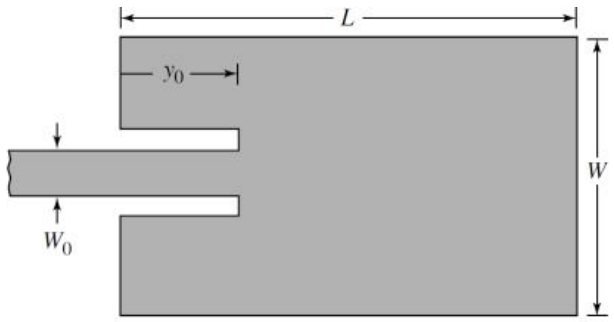

Figure 2.11 Geometry of the inset fed patch antenna where W_0 corresponds to the width of the feed line and y_0 is the amount of recession of the feed line into the patch antenna. Image is used from [23]

It was mentioned in a previous section that the disadvantage of a transmission line feed compared to a coaxial feed is that the coax feed can be placed anywhere on the patch, which is convenient when trying to match the 50Ω line to the antenna. The way that this is achieved with a transmission line is by recessing the feed into the patch, as shown in Figure 2.11. The impedance of the patch antenna is higher at the edges of the patch and decreases towards the center, and then starts to slowly increase past the midpoint of the patch. Figure 2.12 depicts how the normalized resistance varies for different positions of the feed line y_0, where the input resistance R_{in} in terms of y_0 can be expressed as

$$R_{in}(y = y_0) = R_{in}(y = 0)\cos^2\left(\frac{\pi}{L}y_0\right) \tag{2.17}$$

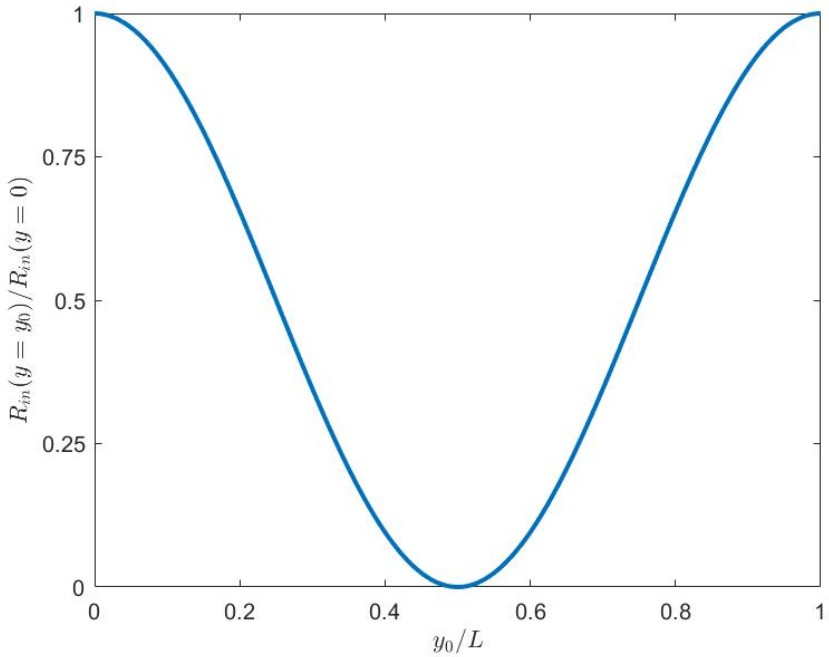

Figure 2.12 The normalized input resistance of the patch antenna for variations of the feed line position y_0

We can use the plot shown in Figure 2.12 to help give a rough estimate on where the position of the feed should be when designing an inset fed patch antenna. Note that the width of the slots w_s on each side of the feed line impact the resonating frequency, where thicker slot widths shift the resonating frequency to higher frequencies and smaller slots to lower frequencies but are not included in the model. An different method that can be used to improve impedance matching is to use a quarter wave impedance transformer. A quarter wave impedance transformer is effectively a separate transmission line with a particular W_q and L_q that is placed between the feed line and the antenna so that it can match the feed line to the antenna. However, this requires adding in an additional amount of line L_q, which increases the physical profile of the antenna, which an inset feed preserves, since it doesn't

increase or decrease the physical dimensions of the antenna or feed line. A designed inset fed patch antenna and its corresponding radiation pattern are shown in Figure 2.13. Because of the many advantages of an inset fed patch antenna, the inset fed patch antenna will be the basis for the majority of our work and will be used for the simulation of the designed sparse arrays. The designed inset fed patch antenna and results will be in the final section of this chapter.

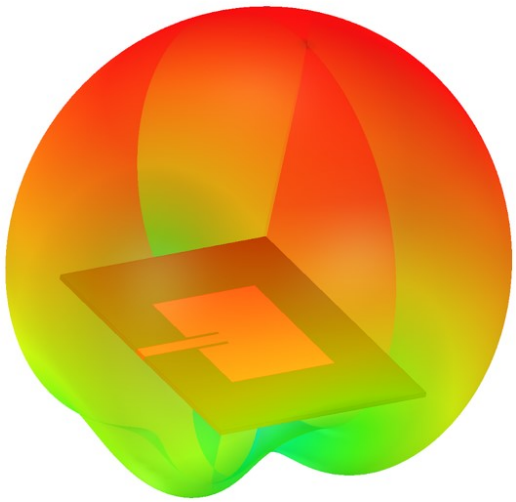

Figure 2.13 Radiation pattern of inset fed patch antenna at $f_0 = 2.45$ GHz

2.4 Microstrip Antennas on a Cylindrical Surface

The focus of this work is not only on planar antennas, but also on conformal antennas, particularly on a cylindrical surface. The IEEE Standard Definition for a conformal antenna is, "An antenna that conforms to a surface whose shape is determined by considerations other than electromagnetic; for example, aerodynamic or hydrodynamic" [3]. Conformal microstrip antennas are used in many applications, such as: missiles, aircraft, and satellites to name a few. It's been said in that there can be up to 20 different antennas or more on the

standard military aircraft [24] and due to the amount of drag introduced by the antennas, it's highly desired to integrate the antennas into the aircraft [25]. These examples are just a few to demonstrate the desire and motivation for work in the field of conformal antenna design.

The purpose of this section is to provide a model for the E and H planes for a rectangular patch on a cylindrical surface. We will show through conformal antenna theory that when a patch antenna is on a curved surface, the radiation pattern will vary, compared to the planar case, depending on the amount of curvature which is controlled by the radius of the cylinder R. When the radius is large, the amount of curvature will be small, so the planar model can be used. However, when the radius is small, the amount of curvature will be large, so a new model will be necessary, so simulating the E and H planes. Note that for the analysis in the following paragraphs, the cavity model is used for a single rectangular microstrip patch antenna on an infinitely long cylinder.

Microstrip antennas ultimately can be considered as dielectric-loaded cavities, where the resemble higher order resonances [23]. Despite that the cavity model is more complicated than the transmission line mode, the fields within the substrate (dielectric between the top and bottom metallic conductors) are computed with higher precision by treating the dielectric as a cavity bounded by the top conductors and surrounded by four magnetic walls. This can ultimately be thought of as an open circuit. By using the internal and external fields, we can find not only find the input impedance but also the radiation pattern of the rectangular patch on the cylindrical surface. Note that despite that this section focuses on the cavity model, there is another method to approximate the input impedance and radiation pattern which uses the surface currents. The interested reader is referred to [26].

It's already been shown in current literature that the curvature also impacts the resonant frequency and the input impedance of the rectangular patch and that the resistance and susceptance vary with the radius R [27]. Depending on the polarization of the antenna, just the resistance may vary. Since we acknowledge that the patch is ultimately a cavity, we

notice that there are several modes excited from the fields. The first set of modes are the modes being excited by the feed, where the field distribution on the four magnetic walls are deduced, which results in these fields being the sources for the radiation from the patch. The rectangular patch can also be modeled by two axial and two circumferential slots, where the field distribution can be found by solving the boundary value problem, where the solution is made up of the number of modes that give rise to a set of field distributions in the side walls of the cavity. From the planar case, the E and H-fields can be derived from the following set of equations

$$\begin{aligned} E_\rho(\phi,z) &= jI_0Z_0k\sum_{p=0}^{\infty}\sum_{q=0}^{\infty}\frac{\psi_{pq}(\phi,z)\psi_{pq}(\phi_f,z_f)}{k^2-k_{pq}^2}G_{pq} \\ H_\phi &= -I_0\sum_{p=0}^{\infty}\sum_{q=0}^{\infty}\frac{\psi_{pq}(\phi,z)\psi_{pq}(\phi_f,z_f)}{k^2-k_{pq}^2}\tan\Big(\frac{q\pi z}{z_m}\Big)\frac{q\pi}{z_m}G_{pq} \\ H_z(\phi,z) &= -I_0\sum_{p=0}^{\infty}\sum_{q=0}^{\infty}\frac{\psi_{pq}(\phi,z)\psi_{pq}(\phi_f,z_f)}{k^2-k_{pq}^2}\tan\Big(\frac{p\pi\phi}{2\phi_0}\Big)\frac{p\pi}{2R\phi_0}G_{pq} \end{aligned} \tag{2.18}$$

where

$$k_{pq}^2 = \Big(\frac{p\pi}{2R\phi_0}\Big)^2+\Big(\frac{q\pi}{z_m}\Big)^2 \tag{2.19}$$

$$k^2 = \epsilon_r(1-\delta_{eff})k_0^2 \tag{2.20}$$

$$\psi_{pq}(\phi,z) = \sqrt{\frac{\epsilon_{0p}\epsilon_{0q}}{z_m d}}\cos\Big(\frac{p\pi\phi}{2\phi_0}\Big)\cos\Big(\frac{q\pi z}{z_m}\Big) \tag{2.21}$$

$$\epsilon_{0k} = \begin{cases} 1, & k=0 \\ 2, & k\neq 0 \end{cases} \tag{2.22}$$

and

$$G_{pq} = \mathrm{sinc}\Big(\frac{p\pi\Delta_\phi}{2d}\Big)\mathrm{sinc}\Big(\frac{q\pi\Delta_z}{2z_m}\Big) \tag{2.23}$$

p and q are the modal numbers, $k_0 = 2\pi/\lambda$; ϵ_r is the dielectric constant of the substrate; ϕ_f and z_f is the feed location; and Δ_ϕ, Δ_z are the probe extensions in ϕ and z for a rectangular probe for the planar approximation, which is when the top and bottom metallic conductors

of the patch reside in a single plane, compared to the cylindrical case, where the metallic conductors wrap around the z-axis and are in multiple planes. $\phi_0 = d/2R$, z_m, d, and R are given in Figure 2.14. Note that the effective loss tangent δ_{eff} is used to account for the losses in the model.

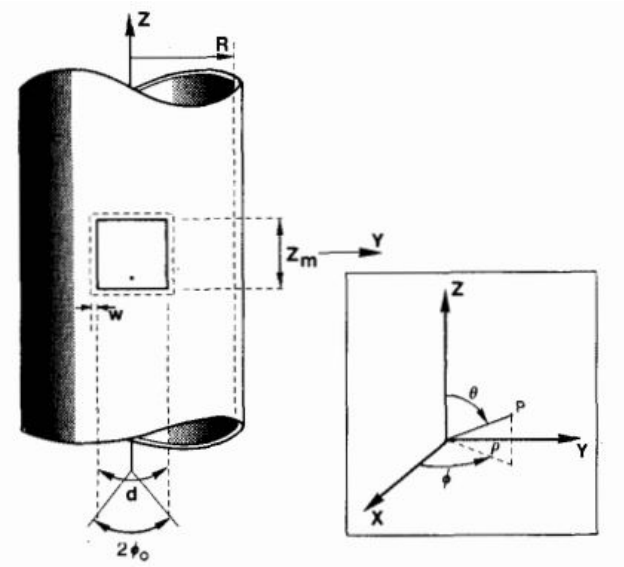

Figure 2.14 Geometry and coordinate system for the patch on a cylindrical surface model [27]

The calculations and model are based off of a cylinder that extends to infinity in both axial directions. By using a two dimensional Fourier transform, the boundary problem can be properly solved, which means that the fields outside the cylinder will need to be expanded, in order to match the known aperture distribution of a slot in the cylinder. This can be done by obtaining two orthogonal components of the vector potentials, such as A_z and F_z, where A denotes the magnetic field and F is the electric vector potential. The axial components of the vector potentials are found by expanding the field in the slot and radiated fields outside the cylinder in cylindrical modes. The radiation condition at infinity indicates that Hankel functions of the second kind are used to replace $e^{j\omega t}$, which can be seen is time dependent. The following two equations are used to obtain A_θ and F_θ in the far field, when using an asymptotic formula for the near field to far field transformation

$$A_\theta = \frac{e^{-jk_0 r}}{k_0 \pi r \eta} \sum_{-\infty}^{\infty} e^{jn\phi} j^n \frac{\tilde{E}_z^s(n, k_0 \cos\theta)}{H_n^{(2)}(k_0 R \sin\theta) \sin\theta} \tag{2.24}$$

$$F_\theta = \frac{-jk_0 r}{k_0 \pi r} \sum_{n=-\infty}^{\infty} e^{jn\phi} j^{n+1} \left[\frac{\cos\theta n \tilde{E}_z^s(n, k_0 \cos\theta)}{k_0 R \sin^2\theta H_n^{(2)'}(k_0 R \sin\theta)} - \frac{\tilde{E}_\phi^s(n, k_0 \cos\theta)}{H_n^{(2)'}(k_0 R \sin\theta)} \right] \tag{2.25}$$

where $\tilde{E}_z^s(n, k_z)$ and $\tilde{E}_\phi^s(n, k_z)$ are the Fourier transforms of the slot fields $E_z^s(\phi)$ and $E_\phi^s(z)$, $H_n^{(2)}(z)$ is the Hankel function of the second kind and nth order, and $H_n^{(n)'}(z)$ is the derivative with respect to the argument of the Hankel function. The far field approximations can then be used to find the radiated electric and magnetic fields

$$E_\theta = \eta H_\phi = -j\omega\mu A_\theta \tag{2.26}$$

$$E_\phi = -\eta H_\theta = jk_0 F_\theta \tag{2.27}$$

where η is the impedance of free space. The Fourier transformed aperture fields are then inserted into Equations 2.26 and 2.27, where the radiated far field from each mode in the axial slots are given by

$$\begin{aligned} E_{\phi,q}(r, \phi, \theta) = V_{pq} \frac{e^{-jk_0 r}}{2\pi^2 r R} & \frac{k_0 \cos\theta [e^{jk_0 z_m \cos\theta} \cos(q\pi) - 1]}{(q\pi/z_m)^2 - k_0^2 \cos^2\theta} \\ \times\ e^{-jk_0 \cos\theta z_m/2} & \sum_{n=0}^{\infty} \frac{\epsilon_n j^{n+1} \cos[n(\phi \pm \phi_0)]}{H_n^{(2)'}(kR \sin\theta)} \\ & \times \operatorname{sinc}\left(\frac{nw}{2R}\right) \begin{bmatrix} 1 \\ -\cos(p\pi) \end{bmatrix} \end{aligned} \tag{2.28}$$

where the upper and lower terms within the bracket are used for slots positioned at $\phi = -\phi_0$ and $\phi = +\phi_0$ respectively, and $-z_m/2 \leq z \leq z_m/2$ [26]

$$\epsilon_n = \begin{cases} 1, & n = 0 \\ 2, & n > 1 \end{cases} \tag{2.29}$$

From the derived E and H field patterns, we can then use the HFSS software to verify how the curvature of a cylindrical surface would effect an inset fed patch antenna. The geometry of the patch antenna and the cylinder are shown in Figure 2.15, where the radius of the

cylinder is given as r and the total angle of curvature is 2α. The E and H field equations indicate that as the radius of the cylinder decreases, the pattern slices for the principle planes will broaden, ultimately lowering the gain of the antenna.

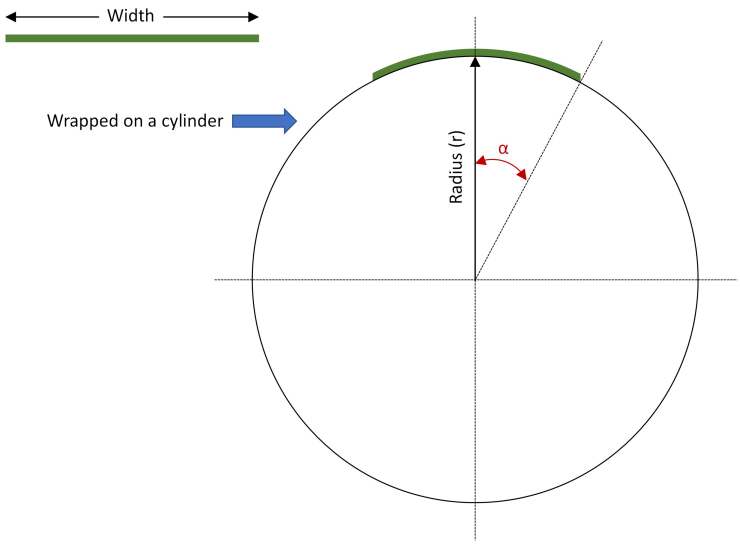

Figure 2.15 Conformal patch antenna geometry for an inset fed patch antenna wrapped around the surface of a cylinder with radius r. The full angle of curvature applied to the patch can be found by 2α

To study the effects of the curvature, we will vary the radius for 5 different cases to verify the E and H fields distribution. We will start off with a radius of 50 mm and double it each time, so the different values we will examine are $r = 50, 100, 200, 400, 800$ mm. The HFSS model for each patch and it's corresponding 3D radiation patterns are shown below in Figures 2.16-2.20.

As shown in the 3D radiation patterns, the gain of the antenna dropped as the radius of the cylinder increased. In Figure 2.21, we see that the E and H planes broaden as predicted, when the radius of the cylinder is small. Meanwhile, the E and H planes for the $r = 800$ mm case are relatively unchanged, when compared to the planar case. Note that the resonant frequency is not changed when the radius of the cylinder is varied, which will be shown in the following section. When an angle of curvature is added, the resonant frequency will stay close to that of the planar case, as demonstrated by the HFSS results in the next section.

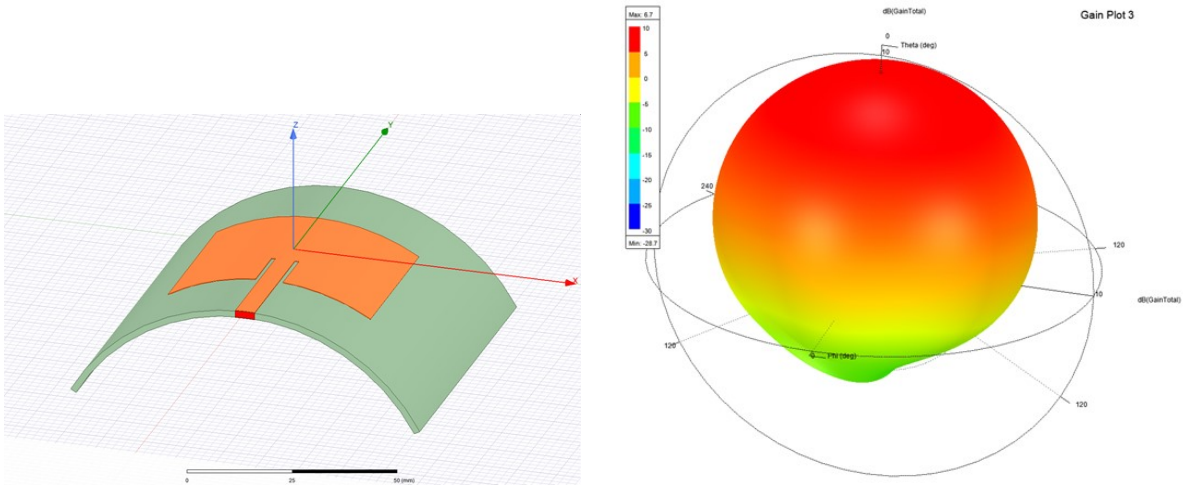

(a) (b)

Figure 2.16 Conformal inset fed patch antenna designed for $f_0 = 2.45$ GHz (a) Conformal patch geometry for $r = 50$ mm, (b) Corresponding 3D radiation pattern of the patch antenna for $r = 50$ mm

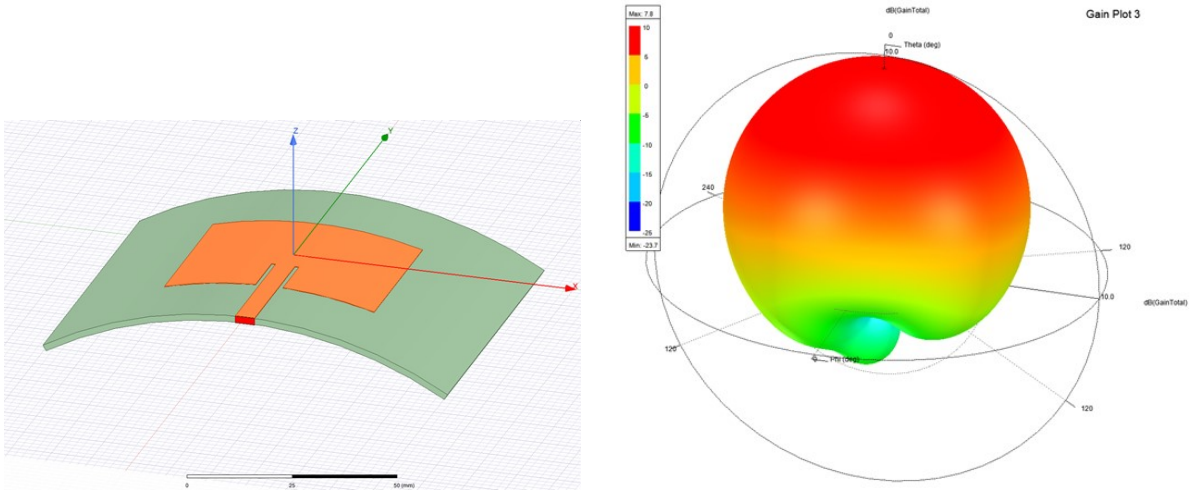

(a) (b)

Figure 2.17 Conformal inset fed patch antenna designed for $f_0 = 2.45$ GHz (a) Conformal patch geometry for $r = 100$ mm, (b) Corresponding 3D radiation pattern of the patch antenna for $r = 100$ mm

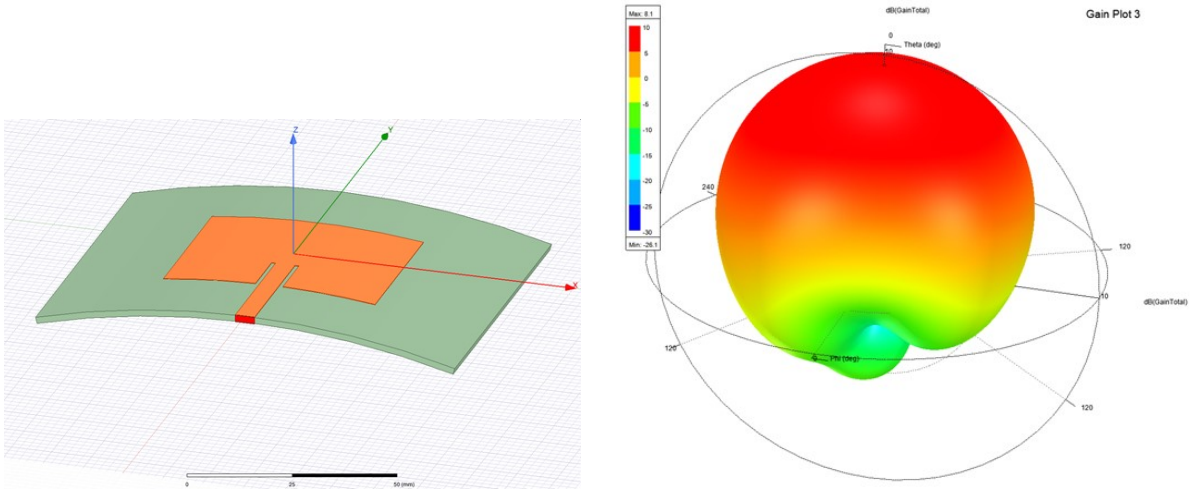

(a) (b)

Figure 2.18 Conformal inset fed patch antenna designed for $f_0 = 2.45$ GHz (a) Conformal patch geometry for $r = 200$ mm, (b) Corresponding 3D radiation pattern of the patch antenna for $r = 200$ mm

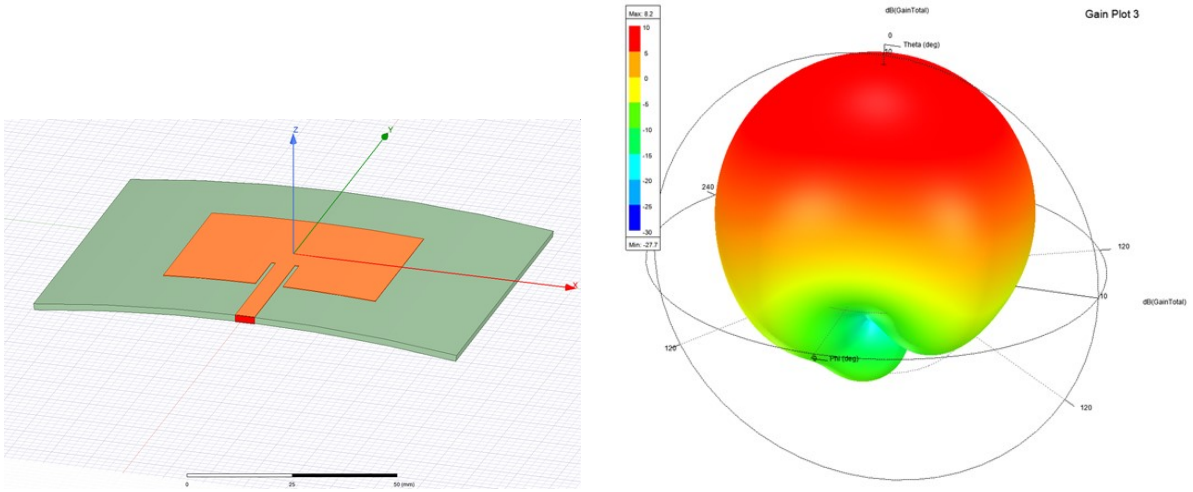

(a) (b)

Figure 2.19 Conformal inset fed patch antenna designed for $f_0 = 2.45$ GHz (a) Conformal patch geometry for $r = 400$ mm, (b) Corresponding 3D radiation pattern of the patch antenna for $r = 400$ mm

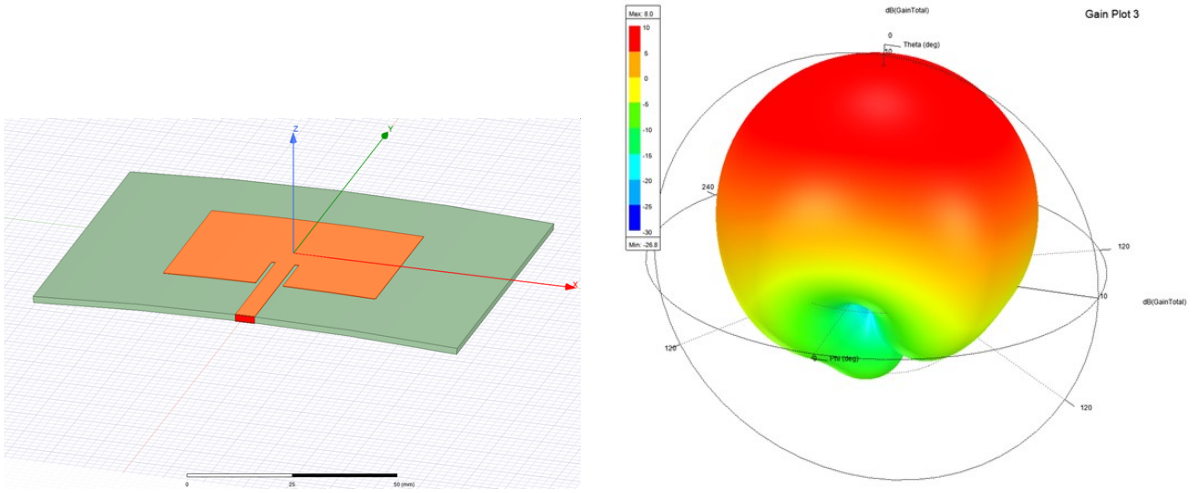

(a) (b)

Figure 2.20 Conformal inset fed patch antenna designed for $f_0 = 2.45$ GHz (a) Conformal patch geometry for $r = 800$ mm, (b) Corresponding 3D radiation pattern of the patch antenna for $r = 800$ mm

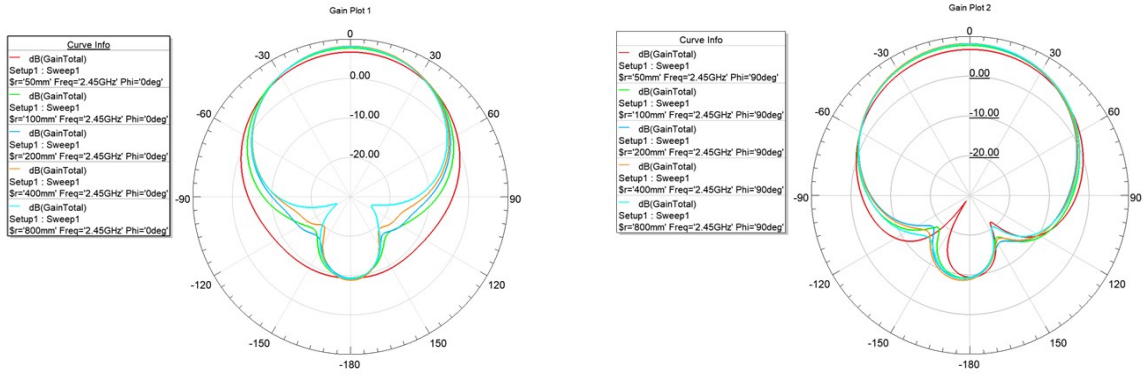

(a) (b)

Figure 2.21 Conformal inset fed patch antenna designed for $f_0 = 2.45$ GHz. We see that as the radius is decreased, the E and H planes begin to broaden, which ultimately decreases the overall gain of the antenna (a) E-planes for all five simulated cases, (b) H-planes for all five simulated cases

2.5 Antenna Fabrication

This section details the design, fabrications, and measured results for the planar and conformal inset fed patch antennas. As the name suggests, both patch antennas will be fed via transmission line and the intended operating frequency of both antennas is $f_0 =$ 2.45 GHz. The planar antenna design is straight forward, however, the conformal case is more complicated. The conformal case will be for a cylindrical surface, with radius R and height h, where the corresponding dimensions are 2 ft and 2 ft respectively, which translates to about .6096 meters. Both the planar and conformal case designs are for transmitting communications systems. The coordinate system and setup of the cylinder are displayed in Figure 2.22. Since we know our intended operating frequency, we can compute the wavelength by using the speed of light in free space which gives us a wavelength of about 12.25 cm. This will then allow us to write our radius and height in terms of wavelength, which translate to $R = h = 4.97\lambda$.

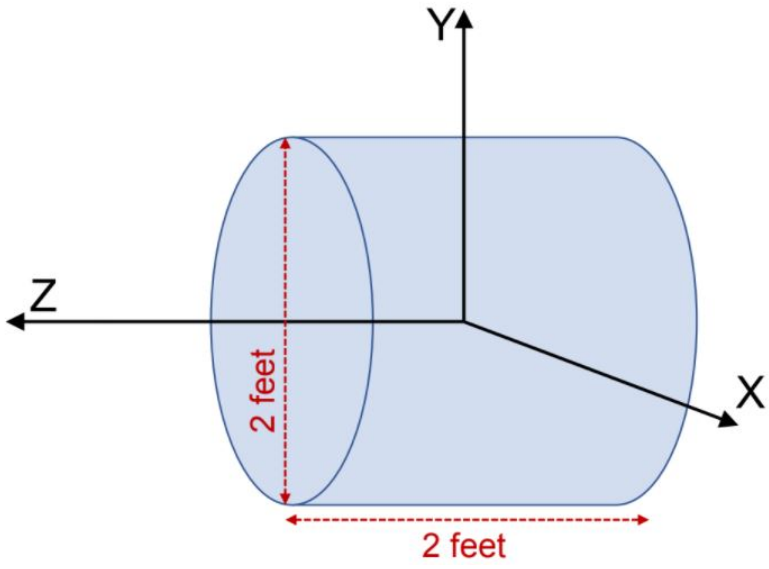

Figure 2.22 Dimensions of the cylindrical surface and coordinate setup

2.5.1 Planar Inset Fed Patch Antenna Design

The planar patch antenna was designed and modeled in the HFSS software. The board used was the Rogers Duroid 5880 which has a dielectric constant of $\epsilon_r = 2.2$. As mentioned previously, the patch was fed via transmission line and was designed using the design equations and methods mentioned previously in this chapter. The geometric orientation and designed patch is displayed in Figure 2.23. Note that since the design equations were based off of a ground plane with infinite length, slight adjustments were made to the length, width, and dimensions of the slots, so that the patch could properly resonate at 2.45 GHz. These slight modifications were made because HFSS uses the Finite Element Method (FEM), which yields slightly different results.

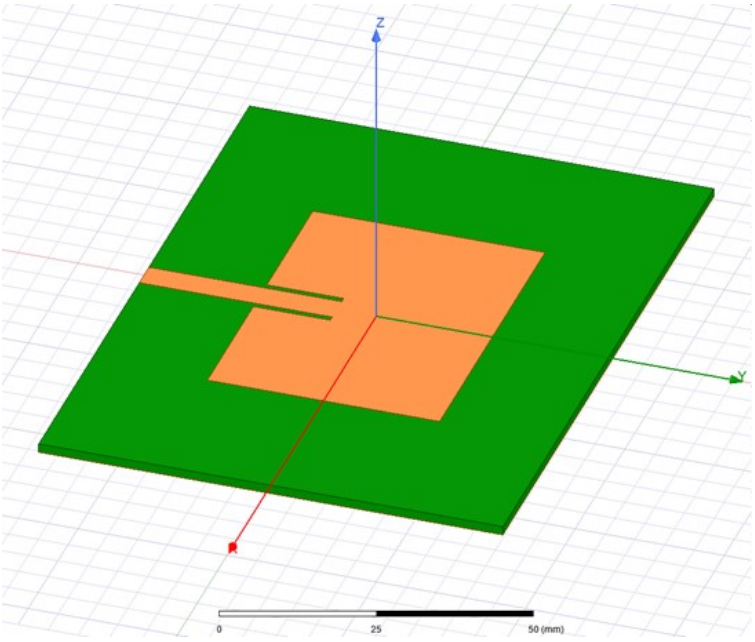

Figure 2.23 Inset fed patch antenna designed in HFSS

After tuning the dimensions of the patch, the simulated results indicate that the patch was correctly designed for 2.45 GHz, as shown in the S_{11} plot in Figure 2.24. The overall bandwidth of the antenna can be found by taking $f_h - f_l = 2.4673$ GHz $- 2.4320$ GHz. In Figure 2.25 (a) the radiation pattern for the antenna is displayed in the polar coordinate

system, where θ is with respect to the elevation plane and ϕ is the angle in the azimuth plane. Figure 2.25 (b) displays the radiation pattern in the two principle planes, for a sweep over θ where $\phi = 0°$ and $\phi = 90°$, which are the E-field and H-field planes respectively. The resulting gain at the pattern peak ($\theta = 0°, \phi = 0°$) is 7.99 dB, as expected for microstrip patch antennas, since they are known to be relatively low gain antennas.

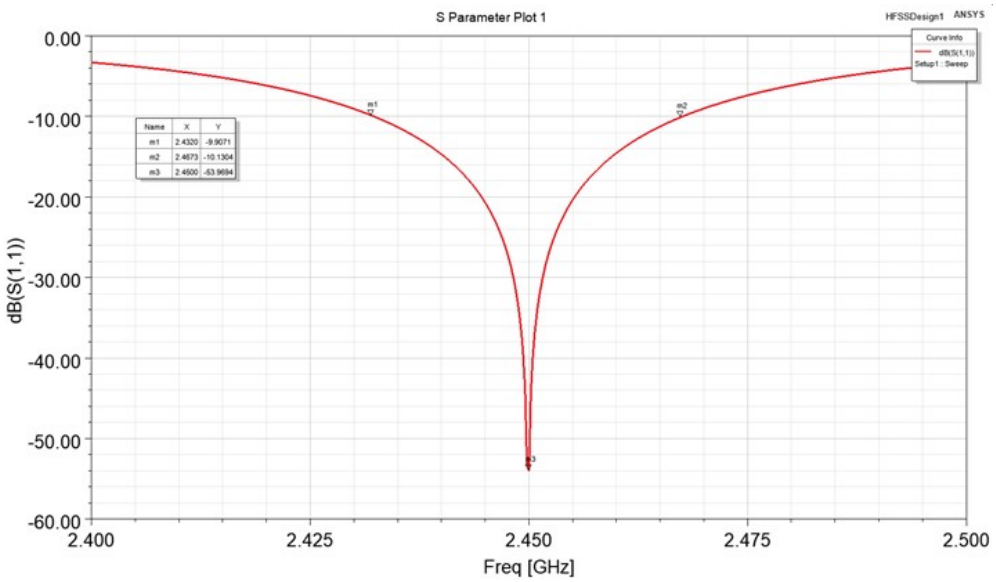

Figure 2.24 S_{11} for designed inset fed patch antenna. The high and low frequencies for the bandwidth are $f_h = 2.4573$ GHz and $f_l = 2.4320$ GHz

2.5.2 Fabricated Planar and Conformal Antennas

The inset fed patch antenna designed in the previous section was fabricated with the use of a milling machine and the Roger's 5880 fabrication board. Four sets of antennas were fabricated: two for the planar case and two for the conformal case. The fabricated antennas are shown in Figure 2.26. The two for the conformal case were then bent to satisfy the design constraint for the cylinder with $r = h = 2$ ft. Since the width of the patches and radius of the cylinder are known, the arc length formula can be used to determine the angle of curvature (θ_c) of the patches, where the equation for arc length is given in Equation 2.30.

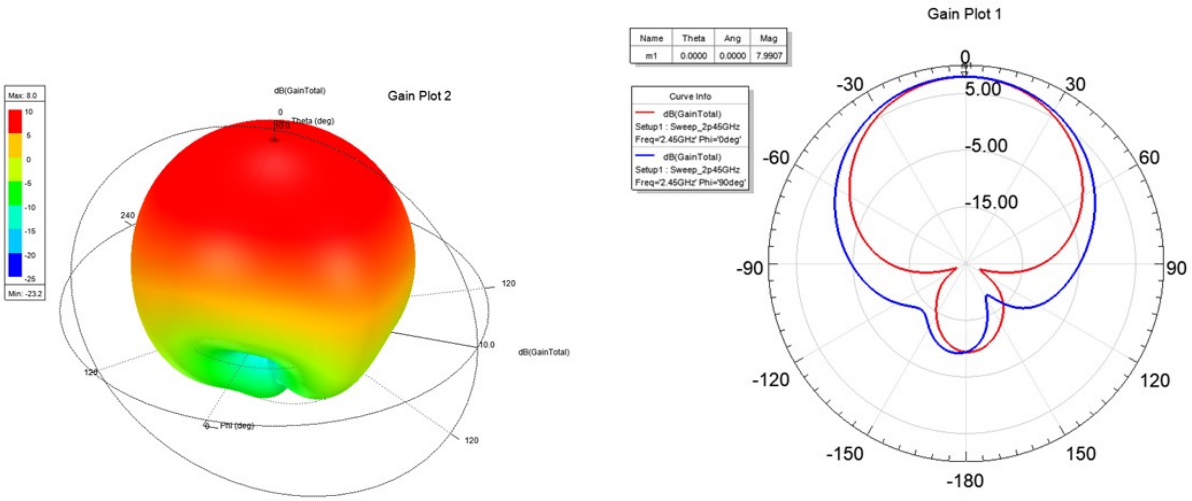

(a) (b)

Figure 2.25 Full radiation pattern and slices of the radiation pattern for the designed inset fed patch antenna (a) 3D radiation pattern of the designed patch antenna at 2.45 GHz, (b) E-plane (red) and H-plane (blue) slices of the radiation pattern at 2.45 GHz

$$\theta_c = \frac{W}{R} \tag{2.30}$$

The two planar patches were tested using a vector network analyzer, where the results are displayed in Figure 2.27. The results depict that there was a slight shift in the frequency response for the S_{11} parameter, where the operating frequency moved up to about 2.52 GHz, which is approximately 70 MHz off the intended design frequency. The issue with using an in house milling machine is that sometimes the tolerance and error of the machine is unknown and is typically higher than that of getting it professionally fabricated, which would yield more accurate results. By using the design equations, we know that larger dimensions of the patch antenna will shift the resonant frequency to lower frequencies, so the HFSS model was changed, so that the resonating frequency would be at 2.38 GHz, which when fabricated, would shift the resonate frequency to 2.45 GHz. Fortunately, there was no change in the bandwidth of the antenna, where the bandwidth of the simulated antenna was approximately the same size as that of the fabricated antenna.

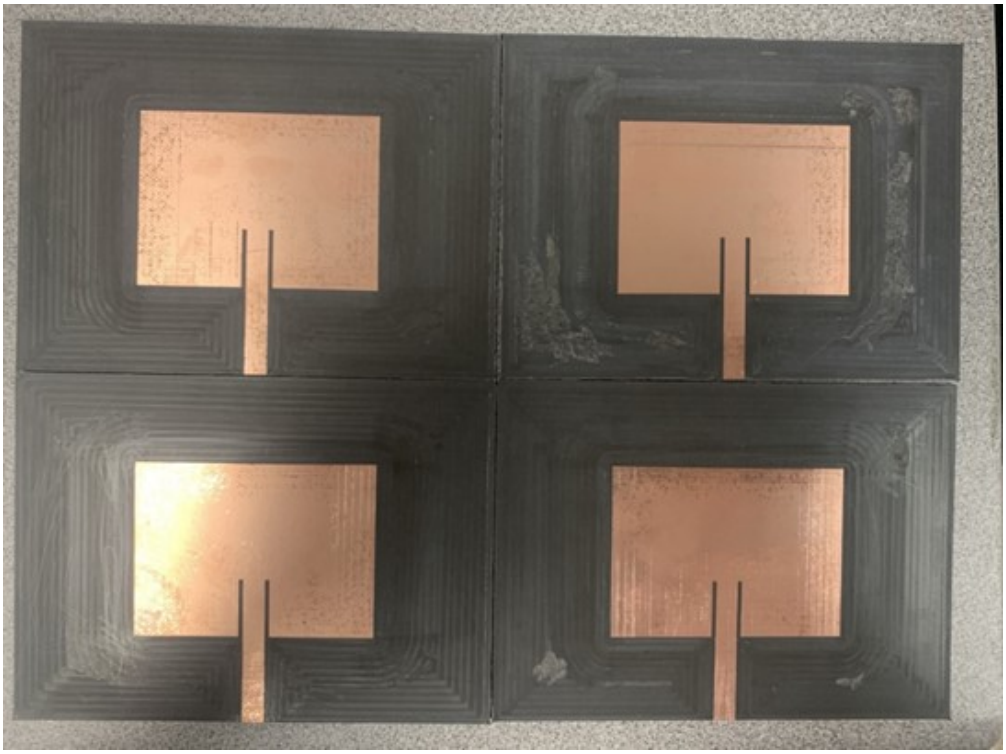

Figure 2.26 Fabricated inset fed patch antennas

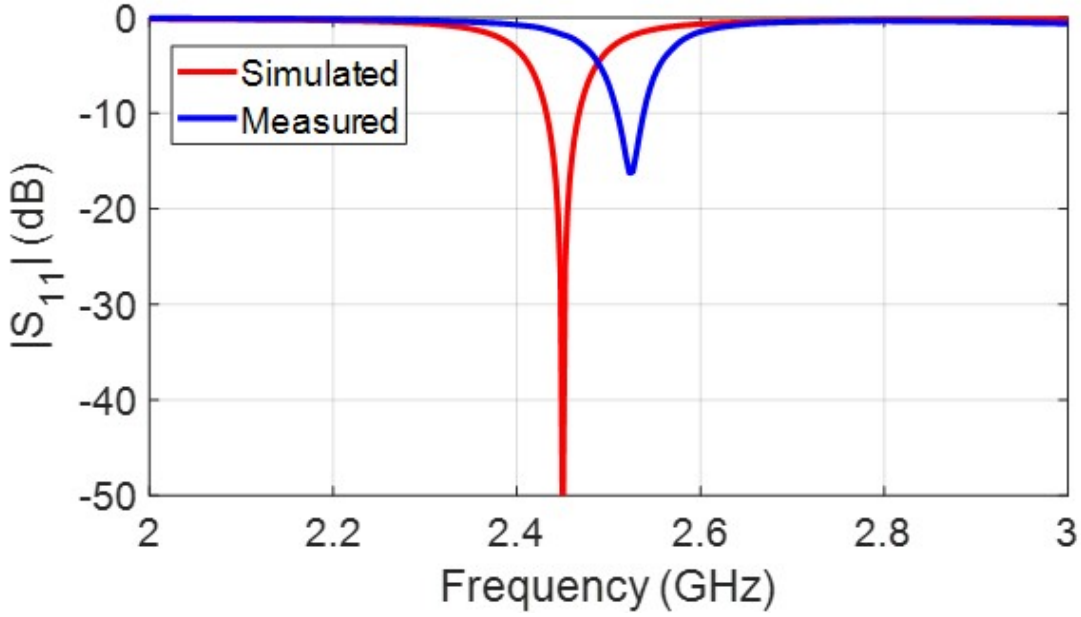

Figure 2.27 S_{11} for simulated and fabricated antennas

Moving from the planar to the conformal case, the last two fabricated antennas were bent to satisfy the angle of curvature so that they would conform to the surface of the cylinder. Images for the conformal antennas are displayed in Figure 2.28.

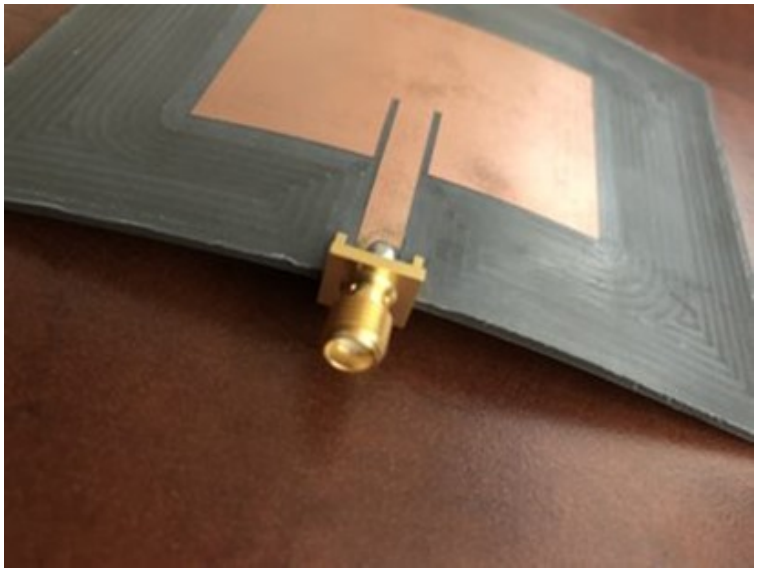

Figure 2.28 Fabricated conformal antennas

The planar patches demonstrated similar results for S_{11}, where the resonant frequencies for both patches was approximately the same, with $f_0 = 2.52$ GHz, as displayed in Figure 2.29.

The measured bandwidth for both patches is equal to 40 MHz and the second patch is more properly matched to the feed line, which is likely due to the precision of the in house milling machine. These fabrication errors are not only introduced by the fabricated dimensions being slightly off, but because of the width of the slots on the patch. Since the width of the slots are less than three millimeters, a fine drill is needed to fabricate the slots with high precision. A thicker drill will lead to the edges of the slots being distorted and a higher fabrication error.

Figure 2.30 shows that for the conformal case, there is little to no change in the frequency response for the conformal patch when compared to the planar prototype. The conformal antenna had a measured resonant frequency of 2.53 GHz and a bandwidth of 50 MHz, which

is a 10 MHz increase compared to the planar patches.

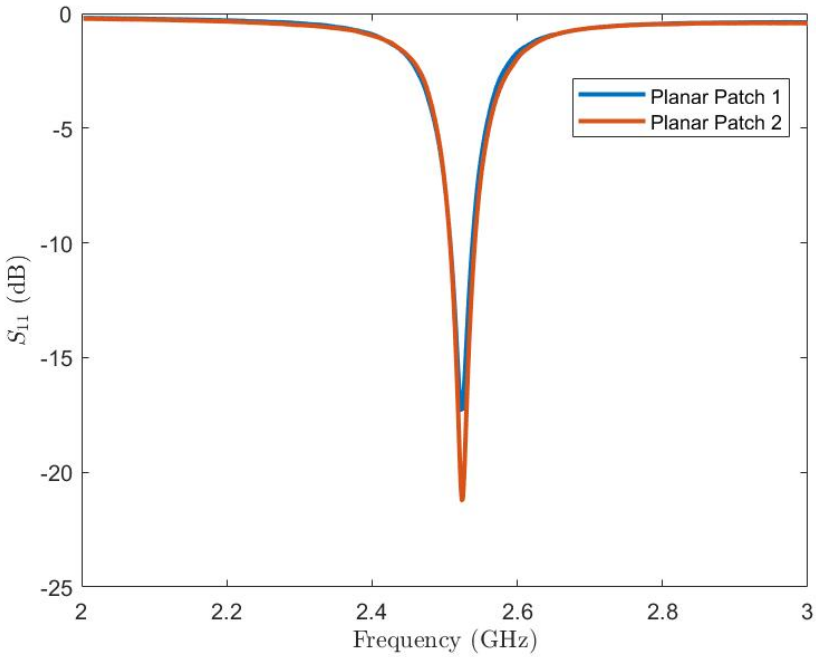

Figure 2.29 Frequency response (S_{11}) for both fabricated planar patch antennas from 2 to 3 GHz in dB. The measured results suggest that despite that the resonant frequencies were shifted up from the desired frequency, the frequency responses for both antennas is relatively the same

Measured results in Figure 2.31 also suggest that the patch antennas are highly sensitive to the bending process. In Figure 2.31, we see that the frequency response of the first conformal patch is shifted down to 2.38 GHz, which is down 70 MHz, compared to being shifted up by 70 MHz to 2.52 GHz like the other patch antennas. The measured results for conformal patch 1 show that the antenna has a bandwidth of 111 MHz, which is almost three times the bandwidth of the two planar patch antennas. Results indicate that resonant frequency can be shifted by a significant amount, which is problematic if the patches were designed perfectly for 2.45 GHz. However, the results for both conformal patches are consistent to conclude that the introduced curvature increases the the bandwidth of the antenna, where the bandwidth for one conformal patch increased by 25% and the other nearly tripled.

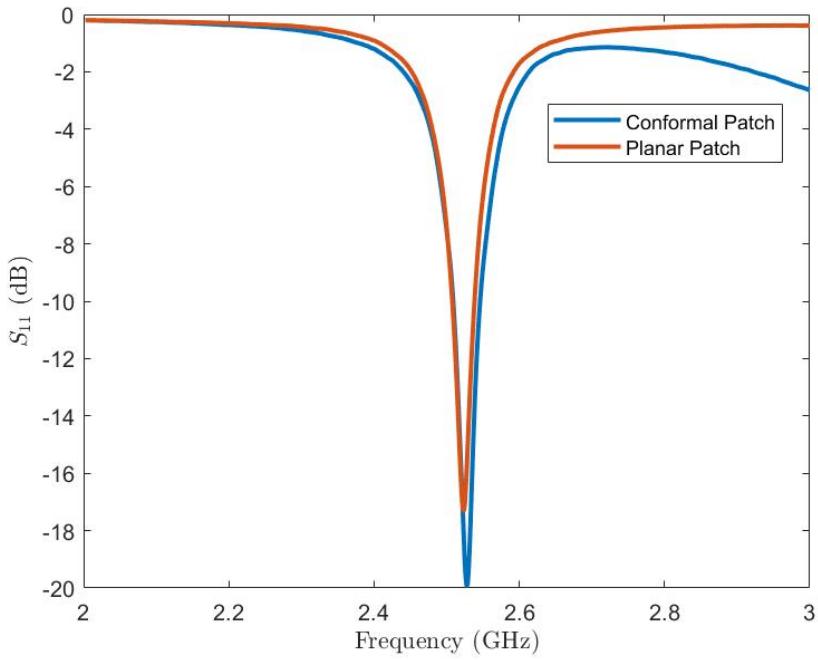

Figure 2.30 Frequency response S_{11} for planar patch 1 and one of the conformal patch antennas. The conformal patch was designed to conform to a cylindrical surface with a diameter of 2 ft and the results suggest that there was not much change in the frequency response of the conformal patch. The only difference is that there was a slight increase in bandwidth for the conformal patch

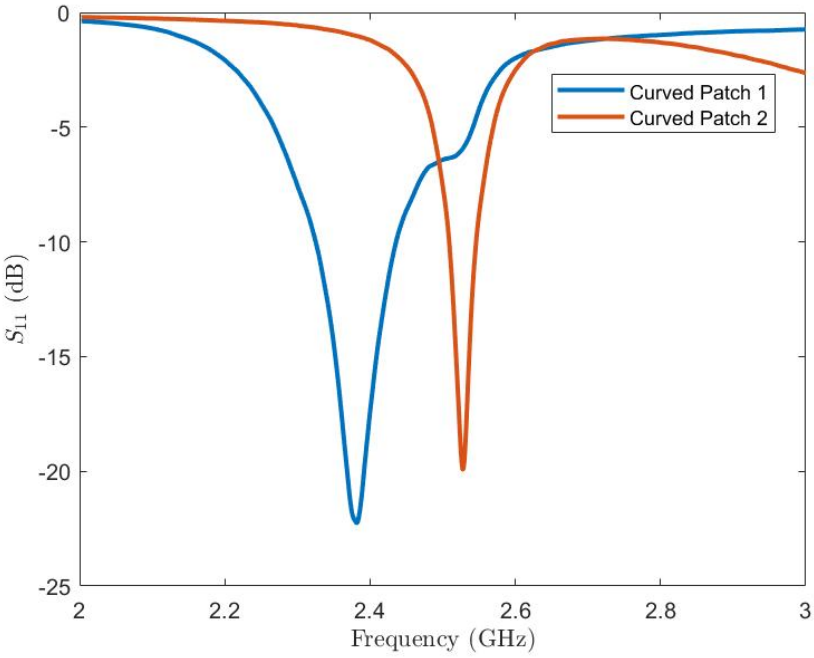

Figure 2.31 Frequency response (S_{11}) for both conformal patch antennas. The results depict that the patches are sensitive to the conforming process, where conformal patch 1 had its resonant frequency shifted below 2.4 GHz while conformal patch 2 had only a slight change in bandwidth, compared to both planar patches

CHAPTER 3
SPARSITY IN ANTENNA ARRAYS AND LOW DISCREPANCY SEQUENCES

In this chapter, we revisit the grating lobe problem along with the necessary array theory for the planar case, give an overview of sparse antenna arrays and discuss sparse sampling techniques based off of low discrepancy sequences (LDS). The purpose of this chapter is to give a formal definition of a sparse antenna array and discuss some of the points of interest for sparse array design, such as: element spacing, non-uniform sampling, eradicating grating lobes, and when/how the LDS work can be used to design sparse arrays. The mathematical formulation for implementing LDS generated element lattice for sparse planar arrays is presented. The majority of these methods are based off of the van der Corput sequence, which will be discussed in detail to provide the reader with a sufficient background to understand how to generate points in an LDS for different bases and dimensions. Randomly sampling methods are also discussed, along with two sequences that aren't based off the van der Corput sequence which include Sobol and Poisson disk sampling.

3.1 An Overview of Sparsity in Antenna Arrays

Sensing applications, such as radio telescopes, satellite communications, sonars, and defense radars, require large antenna arrays. Physically large arrays offer high resolution as well as high directivity (as long as the element spacing, or sampling remains small). Since the array cost is proportional to the number of elements in the array, designers try to minimize the number of elements in the aperture. However, if the array has a uniform grid of elements that undersamples the aperture (large element spacing), then grating lobes (extra main beams) result due to aliasing and are predictable from theory [28]. Most arrays are designed with an element spacing of $\lambda/(1+\sin\theta_{\max})$ or less, where λ is the wavelength and $\theta_{\max}$ is the maximum scan angle from broadside.

Thinned and aperiodic arrays have fewer elements than dense periodic arrays [29]. For a dense array, thinning (removing elements from a regular grid [8]) and aperiodic spacing

(spacing between elements are not constant [30]) mimic low sidelobe amplitude distributions through an amplitude density across the aperture. These arrays have far field patterns with low sidelobes near the main beam and increased sidelobe levels farther from the main beam.

Thinned and aperiodic arrays have fewer elements than dense periodic arrays [29]. For a dense array, thinning (removing elements from a regular grid [8]) and aperiodic spacing (spacing between elements are not constant [30]) mimic low sidelobe amplitude distributions through an amplitude density across the aperture. These arrays have far field patterns with low sidelobes near the main beam and increased sidelobe levels farther from the main beam. Sparse arrays fill an antenna aperture with elements that are widely separated from each other in order to reduce the cost but maintain a narrow beamwidth. The definition of a sparse array in both the antenna and signal processing literature is vague. For instance, the IEEE standard defines a sparse antenna array as [31]: "An array antenna that contains substantially fewer driven radiating elements than a conventional uniformly spaced array with the same beamwidth having identical elements. Inter element spacings in the sparse array can be chosen such that no large grating lobes are formed and sidelobes are reduced." On the other hand, mathematics has a different definition: a sparse matrix has most elements equal to zero [32]. Sparsity of a matrix equals the number of zero valued elements divided by the total number of elements. The words "fewer" and "most" do not specify a sharp dividing line between dense and sparsity. It is important to note here that while these two definitions of sparsity are different, both have been used in designing sparse arrays. For the latter, compressive sensing (CS) approaches aim at solving a system of linear equations, forcing the solution to be maximally sparse, namely, to have the minimum number of nonzero coefficients, with respect to an expansion basis [33]. Accordingly, CS-based methods have been applied to the synthesis of sparse arrays by properly reformulating the design problem as a pattern matching one [34]. The problem unknowns are the set of complex (amplitude and phase) excitation coefficients of the "candidate" array elements, the positions of these latter obtained through a dense sampling of the array aperture. The CS solution is the sparse

complex-valued vector of the excitations and the positions of the array elements are obtained as a byproduct and correspond to the candidate locations having non-null coefficient [34]. CS has been applied to the design of both linear [35], [36] and planar [10], [37] sparse arrays, considering symmetric [35], [10] as well as asymmetric [36], [37] pattern shapes. The obtained results have shown achieving up to 40% elements reduction with respect to regular/uniform array arrangements. It is important to note that CS approaches don't change the definition of sparse arrays; but deal with minimizing the number of nonzero coefficients in the system of equations in designing the array.

With the following definition of sparsity, based on the IEEE definition [31], it's added to the definition that: a sparse array has an average element spacing greater than λ. If the array has a uniform square grid of isotropic elements, then grating lobes exist when the main beam points at broadside. Periodic sparse arrays have grating lobes with the same gain as the main beam. A random distribution of elements in the sparse array lowers the grating lobes to a level of the surrounding sidelobes. Low sidelobes are not an option for sparse arrays.

Figure 3.1 distinguishes between dense and sparse arrays. Given this definition, previous research on sparse arrays emphasizes papers that present arrays with an average element spacing of at least one wavelength. Sparse arrays (by the definition above) in the literature generally have random element spacing [38–40].

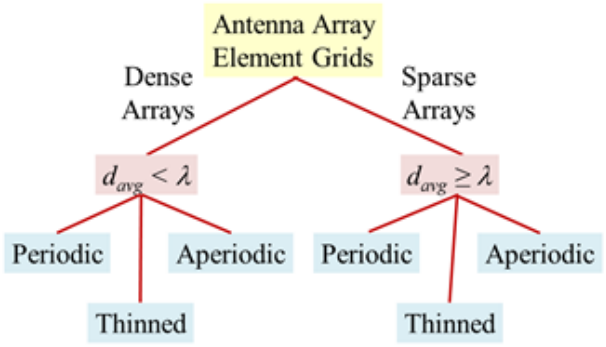

Figure 3.1 Categories of antenna array grids.

Sparse arrays are widely used in radio telescopes and MIMO systems, as well as other sensing systems. The Long Wavelength Array Station 1 (LWA1) is an aperture synthesis imaging array (20 to 80 MHz) for radio astronomy [41]. It contains 512 antenna elements inside an ellipse that has a 100m major axis and a 100m minor axis. To reduce grating lobes in this sparse array at 80 MHz, the elements are pseudorandomly distributed with a 5m minimum spacing constraint that results in an average element spacing of about 5.4m or 1.44λ at 80 MHz. The Low Frequency Array (LOFAR) Low Band Antenna (LBA) in the Square Kilometer Array (SKA) consists of 96 dual polarized crossed dipole active antennas operating from 30 to 80 MHz [42]. An inner array of 46 randomly spaced dual-polarized elements have average element spacings between 0.4λ and 0.8λ within a 30m radius, while the outer array of 48 randomly spaced dual-polarized elements have average element spacings between 0.8λ and 1.7λ within an annulus having an inner diameter of 30m and outer diameter of 85m [43].

Some examples of very sparse radio telescopes include the Very Long Baseline Array (VLBA) that has 10 parabolic reflectors that are 25m in diameter forming a total collecting area of $19,635\text{m}^2$ [44], The Atacama Large Millimeter/submillimeter Array (ALMA) that has 10 parabolic reflectors that are 12m in diameter forming a total collecting area of 6600 m^2 [45], and the Very Large Array (VLA) that has 27 parabolic reflectors that are 25m that extend in a "Y" shape with each arm over 15km long [46].

Microwave imaging experiments were performed using an array aperture of 320×320 mm operating over 17 to 20 GHz [47]. The first model was a fully-populated planar array of 64×64 elements on a square grid. The second model was a sparse array of randomly placed elements. An x-y positioner moved a single antenna to the designated element positions in the aperture to form the dense and sparse arrays. A compressive sensing algorithm (average sampling rate that is less than the Nyquist rate) outperformed other reconstruction algorithms for sparse arrays having 1024, 400, and 160 antennas which correspond to 25%, 10%, and 4% of the elements in the fully populated array.

Sparse antenna arrays with random element spacing significantly improve the sum rate capacity (maximum aggregation of all the users' data rates) of a MIMO base station antenna system [48]. The sparse array aperiodicity spreads the grating lobe (GL) energy over all the lower sidelobes [49].

3.2 Planar Array Theory

Before we move on to discussing the grating lobe issue encountered with large element spacing and the sampling techniques that will be used throughout this dissertation, we must first provide a brief overview of planar array theory.

The array element positions are expressed in the Cartesian coordinate system, where the (x_n, y_n, z_n) positioning of the n^{th} element as a function of angular coordinates with reference to the elevation and azimuthal plane is represented as $(x_n \sin\theta\cos\phi, y_n \sin\theta \sin\phi, z_n \cos\theta)$. In order to simplify many of our calculations for planar arrays, we place the elements in the xy-plane, meaning that the third coordinate $z_n \cos\theta$ will be equal to zero for each of our samples/generated elements within the aperture. For any arbitrary array geometry with N elements in the xy-plane, the array factor can be represented as

$$AF(\theta, \phi) = \sum_{n=1}^{N} w_n^* e^{jk[x_n \sin\theta\cos\phi + y_n \sin\theta\sin\phi]} \tag{3.1}$$

where w_n is the weight excitation of the n^{th} element, k is the wavenumber ($k = 2\pi/\lambda$), and (x_n, y_n) represent the coordinates of the n^{th} element in the xy-plane. For our work, we will only be considering weight elements that are equal to 1 or 0, meaning that we only consider element selection or element placement within the aperture. The interested reader is referred to the following sources for array synthesis techniques that optimize or taper the weights for an array [50–53]. The meaning behind the array factor is that it is the far-field radiation pattern of the antenna array when the elements within the array are replaced with isotropic point sources (antennas with equal radiation in all directions). The array factor is useful when we are designing arrays with large amounts of elements because it allows us to closely

approximate the pattern of the array without modeling it in an EM-solver such as HFSS, CST, or FEKO. It's not only difficult and time consuming to design large arrays in any of the mentioned software but large EM-models take up a lot of memory and time for the solver to run, which is why the array factor is convenient to use. However, some array structures require for the antenna pattern to be considered in the calculation or modeling process, such as the cylindrical case which we will see in Chapter 6.

When we plot the radiation pattern of a planar antenna array, we often do so in the uv-space. The uv-space is used to represent a 3D model/object as a flat representation of the surface. This is the equivalent of us unwrapping the $3D$ radiation pattern and representing it as a flat surface. We are able to map to the uv-spacing by substituting in for the directional cosines as $u = \sin\theta\cos\phi$ and $v = \sin\theta\sin\phi$. Note that $u, v \in [0, 1]$ and the visible region u_r for the radiation pattern is defined as

$$u_r \triangleq \sqrt{u^2 + v^2} \leq 1 \tag{3.2}$$

3.3 Solution to the Grating Lobe Problem

It's been mentioned previously that the Nyquist Sampling theorem states that the sampling rate F_s must be greater than twice the highest frequency of the signal of interest, or else we will encounter aliasing within the spectral domain. The concept of grating lobes with antenna arrays is very similar to Nyquist sampling theory where the rule of thumb is that uniformly spaced antenna elements must be spaced $< \lambda$ or else grating lobes will appear in the radiation pattern. The question that arises is can we translate these non-uniform sampling methods over to antenna array theory to have element spacing $> \lambda$ and not encounter the grating lobe issue? In the field of signal processing and sparse sampling, we see we can fully recover signals without aliasing in the frequency domain by using non-uniform sampling methods. Non-uniform sampling is proven to remove the aliased signals that appear reflected about the limits of the effective bandwidth in the frequency domain [54–57]. Since Nyquist sampling and antenna array spacing share many similarities, we hypothesize that

non-uniform element spacing can be used to break down the grating lobes and preserve the main beam. We can make a fair assumption about this by comparing the Discrete Fourier Transform (DFT) for a 1D signal and the array factor equation for a linear array on the z-axis, where the equation for the DFT is given below

$$c_k = \sum_{n=0}^{N-1} f_n e^{-j\frac{2\pi kn}{N}} \tag{3.3}$$

where $\{f_n\}_{n\in\mathbb{Z}}$ is a periodic-time signal with N samples in time and c_k is the k^{th} Fourier coefficient for all discrete frequencies $k \in \{0, 1, \cdots, N-1\}$. For the linear array case, we know that in spherical coordinates, the z-component is represented by $r\cos\theta$ so the array factor (radiation pattern of an antenna array where the radiation patterns of are elements are isotropic point sources) for an array on the z-axis is given by

$$AF(\theta) = \sum_{n=0}^{N-1} w_n e^{jnkd\cos\theta} \tag{3.4}$$

where w_n corresponds to the complex gain (weight) of the antenna element, k represents the wavenumber $\frac{2\pi}{\lambda}$, d is the element spacing, N is the total number of array elements, and θ is the angular position in the spherical coordinate system and $\theta \in [0, \pi]$.

By closely inspecting Equations 3.3 and 3.4, we see that they are ultimately the same equation, where Equation 3.3 is a sum of complex sinusoids that are a function of a frequency component k, and Equation 3.4 is also a sum of complex sinusoids but as a function of a spatial coordinate θ. The other thing to notice is that both equations are dependent on samples taken from an evenly spaced grid, where the grid for the DFT is based off of the n/N term and the grid for the array factor is found by the nd term. Since both equations are the same but represent different functions (frequency or spatial domain), we can easily imply that non-uniform methods can remove the aliasing problem for antenna arrays and the results in Chapter 4 support this argument. The new question that arises is why do these methods successfully remove aliased peaks/grating lobes?

The answer to this question can easily be answered by closely examining the properties and functionality of the DFT equation. When we obey the Nyquist theorem, we achieve the largest sampling interval to avoid aliasing, where the sampling interval also happens to be the reciprocal of the spectral bandwidth. We can picture the sampling frequency as a tunable knob, where when we uniformly sample exactly at the Nyquist rate for a bandlimited signal, we will have the bandwidth centered at frequency $\omega = 0$ and the bandwidth will be in the interval $\omega \in [-\pi, \pi]$, where we will see spectral copies every $\pm 2\pi$. When we increase F_s, we can expect for the spectral copies to still appear every $\pm 2\pi$, with the main copy centered at $\omega = 0$, but the effective bandwidth to appear thinner, in proportion to the spectral interval. So it's by sampling slower that the bandwidth of the signal will be larger in the interval $[-\pi, \pi]$. It's when we sample below the Nyquist rate that the bandwidth of the the spectral copies will leak into the interval $[-\pi, \pi]$ which gives rise to aliases in the spectral domain.

However, when we sample non-uniformly, the Nyquist theorem no longer holds. By using non-uniform sampling, this allows us to sample at frequency points that are off grid (points not generated by a set of uniformly sampled points) which breaks the periodicity of the DFT. The DFT is ultimately comprised of a set of basis vectors of complex sinusoids with frequencies dependent on the sampling frequency. By sampling off-grid, our Fourier basis will consist of vectors that may not be within the original set of Fourier vectors, which allows us in the analysis process, to preserve the spectral features of the original signal and disperse the energy of the aliased peaks in the spectrum. So by using non-uniform sampling, we can expect to keep the desired peak but see high side lobe levels within the frequency spectrum.

We see that by sampling off the frequency grid in terms of the DFT translates over to placing antenna elements in off-grid positions for antenna arrays. A simple illustration of this idea is shown in Figure 3.2, where the example used in Chapter 1 for a uniformly spaced planar array in the xy-plane with element spacing $d = \lambda$. We then apply the random sampling technique to randomly place the 100 elements within the aperture, where the off-grid sampling is shown to successfully remove the grating lobes that were introduced with

uniform sampling.

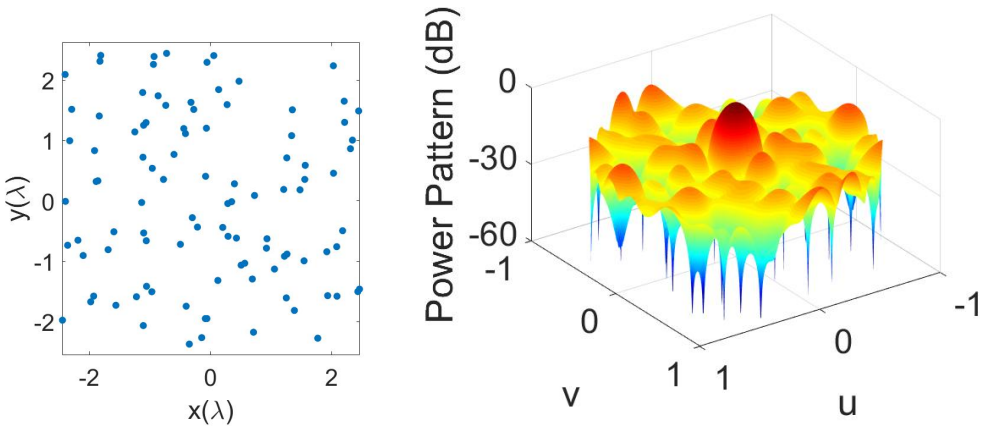

(a) (b)

Figure 3.2 Re-sampled planar array from Chapter 1 using random sampling to remove the grating lobes from the radiation patter: (a) Element locations of the planar array in the xy-plane, (b) Radiation pattern of the resulting array in the uv-space. We are able to see that off-grid/random sampling is successfully able to remove the grating lobes from the radiation pattern.

We can see that the random element positions shifts some of the power from the grating lobes into the rest of the pattern. Note that random element placing is one of the most current methods that are used for sparsely sampling an aperture but is also very inefficient when compared to the methods that we propose later in this section and in later chapters of this dissertation. Since random element placement is used in sparse array design applications, we will discuss it more in depth for the next section and will compare the results for the random methods to our newly proposed methods in Chapters 4 and 5. From this section, we see that in order to break down the grating lobes in the radiation pattern, we need to use sampling methods that are either random or appear random, so that we can strategically place elements in off-grid locations so that we can not only remove the grating lobes but also preserve the main beam. The rest of this chapter details methods that can achieve these desired features and will be the methods used in Chapters 5 and 6 for designing planar and conformal sparse arrays.

3.4 Sparse Antenna Arrays Based on Random Techniques

Random methods for sparse array design can be defined as any method that is dependent on or uses random variables to place elements within the aperture without any placement criterion. The last part of the definition is what distinguishes methods that we consider to be random compared to Poisson Disk Sampling, which randomly places elements within the aperture but restrains the elements from being some distance r from each other. For all methods in this dissertation, uniform random variables are used to map the elements to a location within the aperture. Note that by using random sampling or any modification of random sampling as mentioned in this section, the average element spacing will increase which not only removes grating lobes from the pattern but also results in an average minimum element spacing close to λ. Even though the random methods succeed in removing the grating lobes, there are some significant draw backs to using them, which is that the elements tend to cluster together when there are many sampling points or when the aperture size is small. Even when the aperture size is large and a few sampling points are generated, there is still a small probability that points can be generated together that are $< \lambda/2$ from each other. This is problematic because we elements that are too close to each other will result in mutual coupling (energy absorbed by one antenna's receiver when another antenna is close by) or an unfabricatable array, because the elements may lie on top of each other.

3.4.1 Random Sampling

Random sampling is the most basic random method, which consists of distributing the elements on a random lattice, which is defined by

$$(x_n, y_n) = (\alpha_n x_{\max}, \beta_n y_{\max}) \tag{3.5}$$

where α_n and β_n are uniformly distributed random variables between 0 and 1, and $x_{\max}$ and $y_{\max}$ are the maximum lattice size of the aperture in x and y. Random element sampling is known as a hierarchical sampling method because adding an additional element, does not

require recalculating the previous element locations, meaning that we can easily generate a new point in the sequence. From probability theory, we know that the probability distribution function of a a continuous uniform random variable X has an amplitude of $\frac{1}{b-a}$, as shown in Figure 3.3.

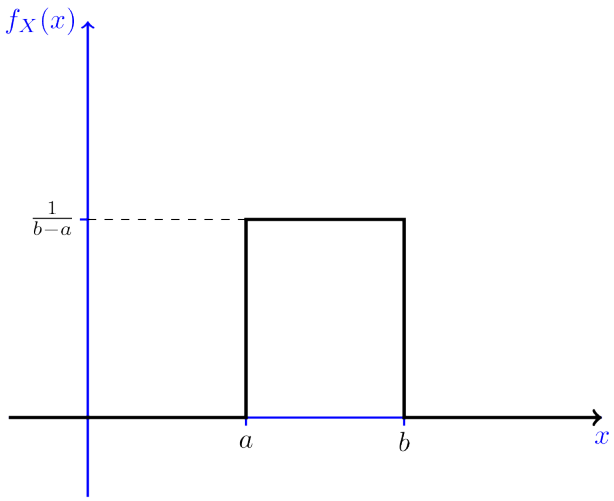

Figure 3.3 PDF $f_X(x)$ of a uniform random variable. Image from [58]

As mentioned before, we do not want for antenna elements to be placed $< \lambda/2$ of each other because this gives way to mutual coupling and the possibility of an unfabricatable antenna array. With random techniques, there is no way to ensure this, however, we can easily determine the probability that an element will fall within a distance r from another element.

We see, as the example of the with the unit square, that when the number of points starts to increase, element clustering is encountered more frequently. Will lower sample numbers, random sampling tends to not utilize the entire area of the aperture and even when there are a large number of sample points, the aperture still isn't fully utilized, which is depicted in Figure 3.4, for an original sample set of 50 samples, and then an increase of $50 samples$, and then 50 more samples added, for a total of 150 samples. In Chapter 4, it will be shown that random sampling has a high variance for the element distribution, where some average element spacing can be $> \lambda$ and $< \lambda/2$ on the lower end.

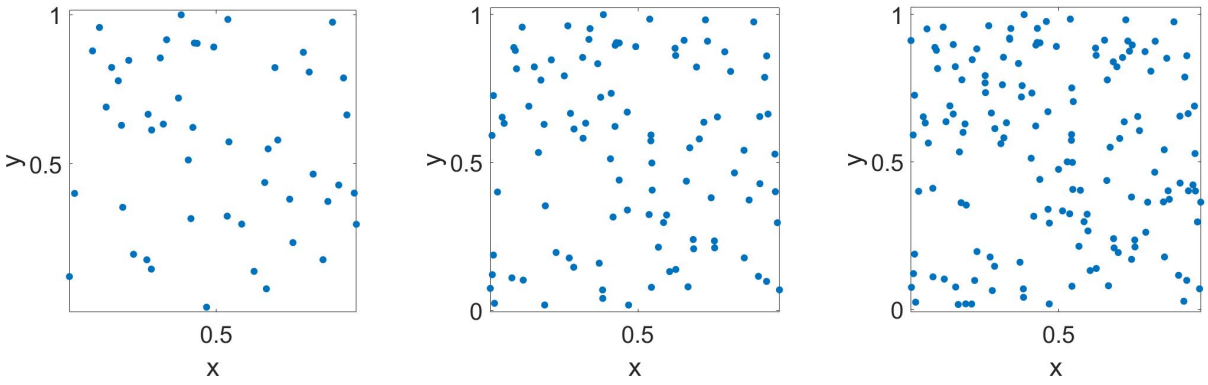

Figure 3.4 Distribution of random samples within the unit square for: (a) 50 random samples, (b) 100 random samples, (c) 150 random samples. The random samples are either too close together or too far apart from each other, which results in a wasted portion of the aperture, mutual coupling, and fabrication complications.

3.4.2 Random Sampling with Jitter

A modification made to random sampling which is commonly used in image processing is known as jitter [59]. Jitter adds a small random variation to the element location given by

$$(x_n, y_n) = (x'_n + \alpha_n r_{\max} \cos(2\pi\beta_n) + \alpha_n r_{\max} \sin(2\pi\beta_n)) \tag{3.6}$$

where (x'_n, y'_n) are the rectangular lattice, $r_{\max}$ is the maximum distance that the new sample point moves from the regular lattice, and α_n and β_n are uniform random variables that are distributed on the interval $[0, 1]$. Jitter is great at adding a small variation to the position of an element on a uniform grid, where the distance that the element can move from its original position is governed by $r_{\max}$ and and the angular variation is determined by $\cos(2\pi\beta_n)$ and $\sin(2\pi\beta_n)$. When $r_{\max}$ is sufficiently large, jitter is approximately equal to random sampling, since it allows for the elements to deviate greatly from their original positions. Figure 3.5 demonstrates the effects of jitter with a varying $r_{\max}$ for 100 uniform samples on a square grid within the unit square.

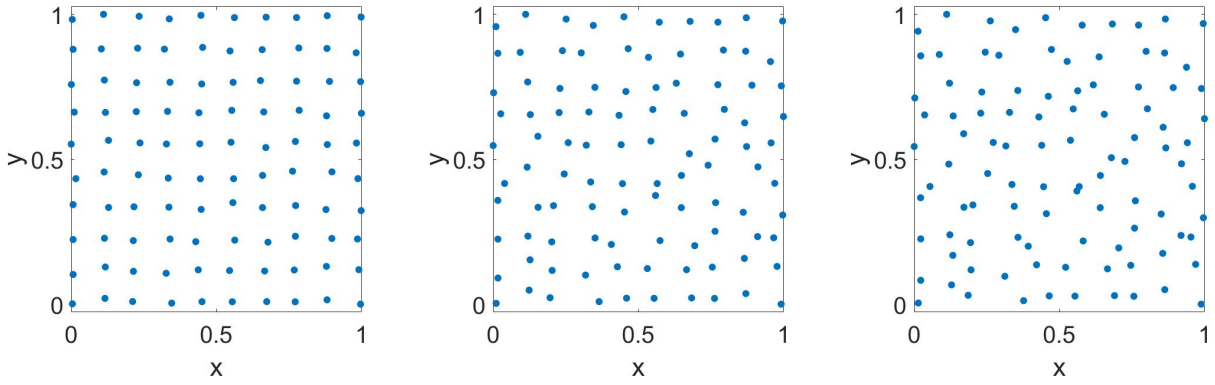

(a) (b) (c)

Figure 3.5 Distribution of samples within the unit square with jitter for a varying $r_{\max}$: (a) $r_{\max} = .02$, (b) $r_{\max} = .05$, (c) $r_{\max} = .07$. We see that as $r_{\max}$ begins to increase, the amount variation of element results in the distribution appearing like random sampling.

3.4.3 Random Hyperuniform Spatial Arrangements

Another important category of random distributions are random hyperuniform spatial arrangements which have been observed in different physical systems ranging from disordered ground state to jammed particle packing [60–62]. Hyperuniform systems are exotic states of matter which exploit designed disorder laying between a crystal and a liquid. A statistically homogeneous hyperuniform points configuration in d-dimensions is one in which the number variance of N points within a spherical observation window of radius R grows more slowly than R^d, i.e.,

$$\sigma_N^2(R) \sim R^{d-1} \tag{3.7}$$

This is equivalent to having a structure factor that tends to zero as the wavenumber tends to zero, implying that single scattering of incident radiation at infinite wavelengths is completely suppressed, i.e., they don't have Bragg peaks. From an array sampling point perspective, these types of distributions can eliminate grating lobes. Due to the random nature of these distributions, the discussions on these hyperuniform arrangements will be limited and focus on LDS techniques, and refer the interested reader to [60–64].

3.5 Low Discrepancy for Sparse Array Antenna Arrays

The difference between the uniform element grid and the randomized element grid is mathematically known as the discrepancy. Using a low discrepancy sequence (LDS) to place elements in an array aperture ensures that elements do not overlap while keeping a uniform sampling of the aperture. An LDS produces a random-like equidistribution of elements using a deterministic generating formula. Equidistributed means that if the aperture is divided into equal subareas, then the number of elements in all subareas is the same. The aperture discrepancy approaches zero as the number of elements approaches infinity. Random element spacing has the highest discrepancy, because large areas of empty space as well as high densities of elements exist within the aperture. In contrast, elements on a regular grid have the lowest possible discrepancy. A low discrepancy element distribution appears random, but the elements also appear to be evenly distributed across the aperture.

Discrepancy theory has its origin in a paper by H. Weyl on the uniform distribution of sequences [65]. Different LDSs have been introduced from the early 1960s, including the Hammersley point set [66], the Sobol sequence [67], the Faure sequence [68], and the Niederreiter sequence [69]. LDSs find their first applications in the 1990s for numerical analysis and integration for numerical simulation, in the fields of computer graphics [48], computational physics [70], and finance engineering [71]. The application of LDS to the generation of sample points for Monte Carlo sampling (i.e., the quasi-Monte Carlo approach) is theoretically superior to a standard Monte Carlo technique.

The first paper to apply an LDS (Hammersley sequence) to element spacing explored sparse aperiodic spacing on a spherical array [72].The advantages of LDS for sparse phased array design demonstrated that the Hammersley sequence maintains the large separation between the elements, while reducing the grating lobes compared to element spacings derived from random, pseudo-random, and uniform plus jitter sequences [73].

In this dissertation we use low discrepancy sequences to distribute elements in a sparse planar array aperture while maintaining the following properties:

- Sufficient elements to achieve a desired gain
- Aperture size is large enough to achieve the desired beamwidth
- Elements have a minimum separation distance, so they can physically fit into the aperture and mutual coupling is not a problem
- No GLs present at maximum scan angles
- The average element spacing is greater than λ

3.5.1 Low Discrepancy Sampling Approaches

A Low discrepancy sequence (LDS) is a set of points positioned on a surface that fills the aperture/area more uniformly than an equal set of uncorrelated random points [74]. This is done by reducing gaps between sample points but also increasing the distance between points enough so that they don't cluster. The difference between LDS and uniform random numbers and quasi random sequences is that for uniform random numbers on $[0, 1)$, each trial has the same probability of generating points on equal sub-intervals. For this example, take $[0, 1/2)$ and $[1/2, 1)$, where it is possible for N trials to all lie on the first half of the interval and for the point $(N + 1)$ to fall within the other two halves with equal probability of $1/2$. For quasi-random sequences, points are generated in a correlated manner, where the next point in the sequence has previous knowledge of all previous points before it. This is useful because it allows for certain constraints to be applied to the point sequence, such as a a low-discrepancy requirement. LDS like quasi-random sequences, partitions an interval into a grid and the sequence dances around the mid-point of the grid to ensure that the interval is populated as uniformly as possible, and by keeping the points well enough away from each other, which uniform random sampling fails to do. Figure 3.6 shows the points on the xy-plane of a unit square for the case of uniform, random, and LDS Poisson disk distributions. From this figure, we can see how random sampling leaves large gaps between elements and

also has some areas where points are too close to each other, compared to the LDS method that separates the points well enough to avoid clustering and fill in unpopulated gaps.

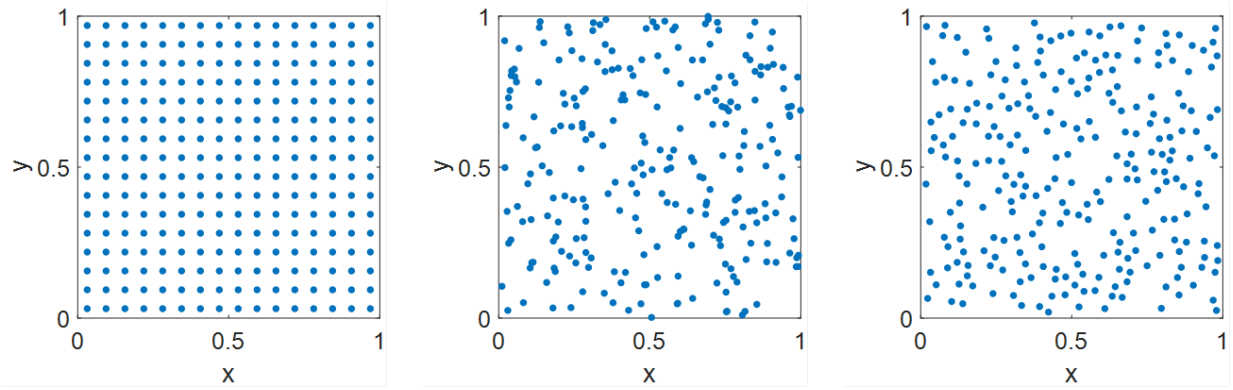

(a) (b) (c)

Figure 3.6 A generic representation of the position of points on a unit-square with different distributions: (a) Uniform, (b) random, (c) LDS Poisson disk. The total number of elements is equal in all three cases but note that the LDS method fills the space more uniformly while avoiding too close spacings.

3.5.2 Hammersley Sampling

Before discussing Hammersley sampling, the representation of an integer in a prime base must be revisited. Any positive integer can be represented by a prime base as

$$n = \sum_{k=0}^{L(n)} a_k(n) b^k \tag{3.8}$$

where b is the prime base in which number n is represented, $a_k(n)$ is an integer in $[0, b-1]$, and $L(n)$ is the lowest integer value that allows expressing the integer n in base b as the summation of $L(n)+1$ terms.

It's important when discussing LDSs, to explain the van der Corput sequence, which is what these LDSs, which is what several of these LDSs are based on. The van der Corput sequence was first published by Dutch mathematician, van der Corput in 1935. This sequence is only defined for the unit interval $\mathcal{I} = [0, 1]$, however, the interval can be scaled for applica-

tions where the length of the interval is greater than one, and even to different dimensions, such as the unit square and the unit cube. This is achieved by using a uniform sequence for one coordinate and the van der Corput sequence for another, or by using multiple van der Corput sequences with different prime bases for each coordinate. These methods are known as Hammersley and Halton sampling and will be discussed later in this section. The van der Corput sequence is expressed as

$$\Phi_b(n) = \sum_{k=0}^{L(n)} a_k(n) b^{-k-1} \tag{3.9}$$

In order to explain the nature of the van der Corput sequence, the uniform set of samples must be given as an example. For a set of uniform samples with $N = 16$, the sample set can be written as $S = \{i/16 \mid 0 \leq i < 16\}$, which evenly spaces the 16 points on $\mathcal{I}$ at intervals of length 1/16. The van der Corput sequence populates the unit interval, like the uniform example, except it does it by reversing the bits in the binary decimal representation of the uniform sequence, as demonstrated in Table 3.1.

Table 3.1 van der Corput Sequence Derivation

i	Uniform Sequence	Reverse Binary	Binary Reverse	van der Corput
1	0	.0000	.0000	0
2	1/16	.0001	.1000	1/2
3	1/8	.0010	.0100	1/4
4	3/16	.0011	.1100	3/4
5	1/4	.0100	.0010	1/8
6	5/16	.0101	.1010	5/8
7	3/8	.0110	.0110	3/8
8	7/16	.0111	.1110	7/8
9	1/2	.1000	.0001	1/16
10	9/16	.1001	.1001	9/16
11	5/8	.1010	.0101	5/16
12	11/16	.1011	.1101	13/16
13	3/4	.1100	.0011	3/16
14	13/16	.1101	.1011	11/16
15	7/8	.1110	.0111	7/16
16	15/16	.1111	.1111	15/16

Equation 3.6 and 3.7 when written out, show the calculation for each point in the sequence in the example above with a base of 2:

$$
\begin{aligned}
&n = 1: \ 1 * 2^0 = 1, \ x_1 = \Phi_2(1) = \frac{1}{2} \\
&n = 2: \ 1 * 2^1 + 0 * 2^0 = 2, \ x_2 = \Phi_2(2) = \frac{0}{2} + \frac{1}{4} = \frac{1}{4} \\
&n = 3: \ 1 * 2^1 + 1 * 2^0 = 11, \ x_3 = \Phi_2(3) = \frac{1}{2} + \frac{1}{4} = \frac{3}{4} \\
&n = 4: \ 1 * 2^2 + 0 * 2^1 + 0 * 2^0 = 100, \ x_4 = \Phi_2(4) = \frac{0}{2} + \frac{0}{4} + \frac{1}{8} = \frac{1}{8}
\end{aligned} \tag{3.10}
$$

Hammersley sampling is accomplished for a 2D space by mapping the x-coordinate to a uniform sequence (n/N), where N is the total number of points and n is the n^{th} point in the sequence, and then mapping the y-coordinate to the van der Corput sequence for some prime base b. The n^{th} Hammersley sample can be found by the following

$$
(x_n, y_n) = \left(\frac{n}{N}, \Phi_b(n)\right), \ n = 0, 1, 2, \cdots, N-1 \tag{3.11}
$$

Hammersley sampling is not hierarchical due to the n/N term in Equation 3.9, because adding an additional element, does require recalculating the previous element locations. In Figure 3.7, we see a sample set of 500 Hammersley samples for 3 different prime bases.

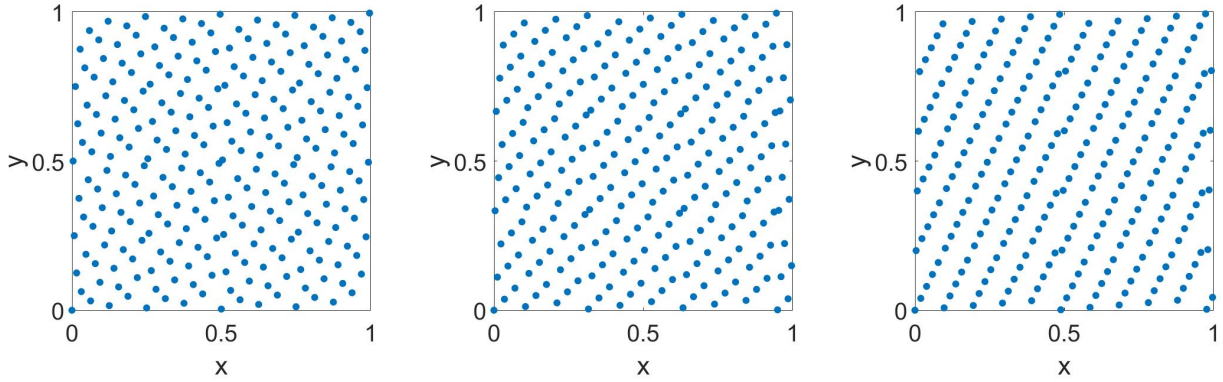

Figure 3.7 A geometric representation of the position of Hammersley points on a unit-square with different bases: (a) $b = 2$, (b) $b = 3$, (c) $b = 5$

What's noticed is that as we increase the prime base b, the points begin to form in a correlated/linear manner, which is due to the hierarchical term. We see that from the nature of Hammersley sampling, this undesired feature is inevitable but it can be postponed for higher bases. In Figure 3.8, we see the sample distribution of Hammersley points, for various sample set sizes. This is an important observation to make because in a later chapter, we see that the less Hammersley samples we take, the worse the performance for sparse array applications. This can be conclude from the hierarchical term combined with a sparse ruler that is too sparse. The van der Corput sequence for a given base is a sequence that is fixed, where the n^{th} point for a sample set of $N_1 = 200$ will be the same as that of $N_2 = 300$, where $n < N_1$. This can almost be viewed as another form of aliasing, where when the sample set is small, the van der Corput samples will be sufficiently far from one another so the Hammersley points will start to wrap around the unit square in a linear fashion. Take for example the first three samples of the van der Corput sequence for bases $b = 2$ and $b = 3$, where $b_2 = \{1/2, 1/4, 3/4\}$ and $b_3 = \{0, 1/3, 2/3\}$. The first three samples are spaced by $1/4$ from the nearest sample point while the b_3 point sets are spaced $1/3$ from the nearest point, which is greater than the b_2 point set.

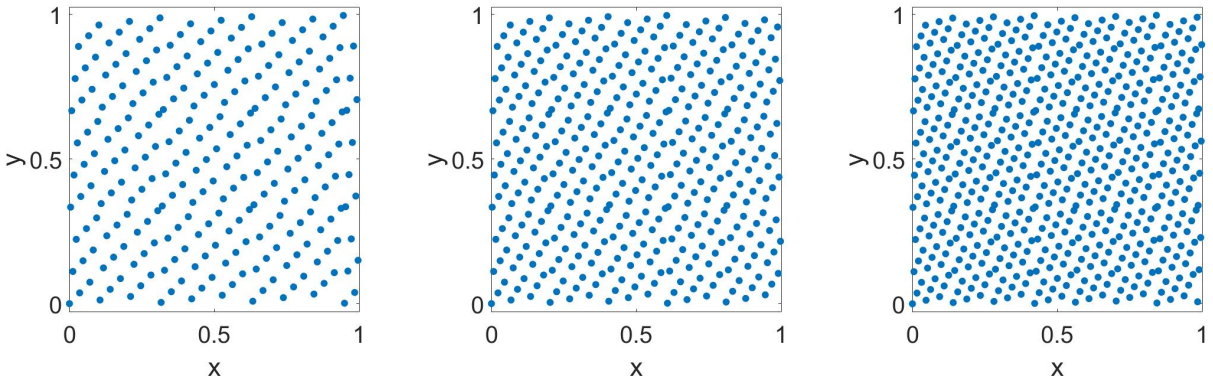

Figure 3.8 A geometric representation of the position of Hammersley points on a unit-square for $b = 3$ and varying sample set sizes N: (a) $N = 256$, (b) $N = 400$, (c) $N = 576$

3.5.3 Halton Sampling

Halton sampling replaces the n/N term in the Hammersley sampling by another van der Corput sequence with a different base. By doing this, we are available to avoid the aliasing feature that is encountered with Hammersley sampling. This allows us to go up to higher base values and not have the points align in a highly correlated manner. However, we do notice that for higher base values, we see wider gaps in the sample placements and point clustering, like in random sampling. The n^{th} point in a Halton sequence can be represented as

$$(x_n, y_n) = \Big(\Phi_{b_1}(n), \Phi_{b_2}(n)\Big),\ n = 0, 1, 2, \cdots, N-1 \tag{3.12}$$

where b_1 and b_2 are the two different prime basis. Note that Halton sampling is hierarchical, meaning that a new point in the sequence can easily be calculated without having to recalculate all of the previous points in the sequence, since the n/N term is replaced with another van der Corput sequence. In order for Halton sampling to work properly, the two van der Corput sequences used must be two different prime bases. Like Hammersley sampling, Halton sampling is also defined for the unit interval and can be extended to any dimension s, where the s-dimensional sequence is defined for any unit hypercube as $[0, 1]^s$. For the 2D case, the first dimension typically is represented by a van der Corput sequence with $b_1 = 2$ and the second dimension by a second van der Corput sequence with $b_2 = 3$. Any s-dimensional case following the 2D case would just use the s^{th} prime number as the base.

Even though Halton sampling fixes the correlated point problem, as shown with Hammersley sampling, similar problems are encountered when the prime base is large. Such as when the 25^{th} and 26^{th} prime bases are used (which correspond to 97 and 101 respectively), the points once again form in a correlated manner and it takes a longer amount of time to populate the unit square. It will be shown in a later chapter, which bases and above result in a point set of correlated samples and for how many points as well.

In Figure 3.9, we are able to see how a second van der Corput sequence fixes the correlated point issue. The image displays the geometric distributions for two separate cases, the first is when the x-component is mapped to a van der Corput sequence with a base value of 2 and the base value for the y-component is slowly increased. The second case is when the x-component has a base value of 3 and the y-component is once again increased. We are able to see that Halton sequences with relatively small bases result in a point distribution where the samples aren't placed too far from one another but are also placed far enough to prevent clustering. However, when bigger base values are used, such as in Figures (e) and (f), the points starts to form clusters, where groups of samples are relatively far from one another and the samples within the group are all closely spaced together.

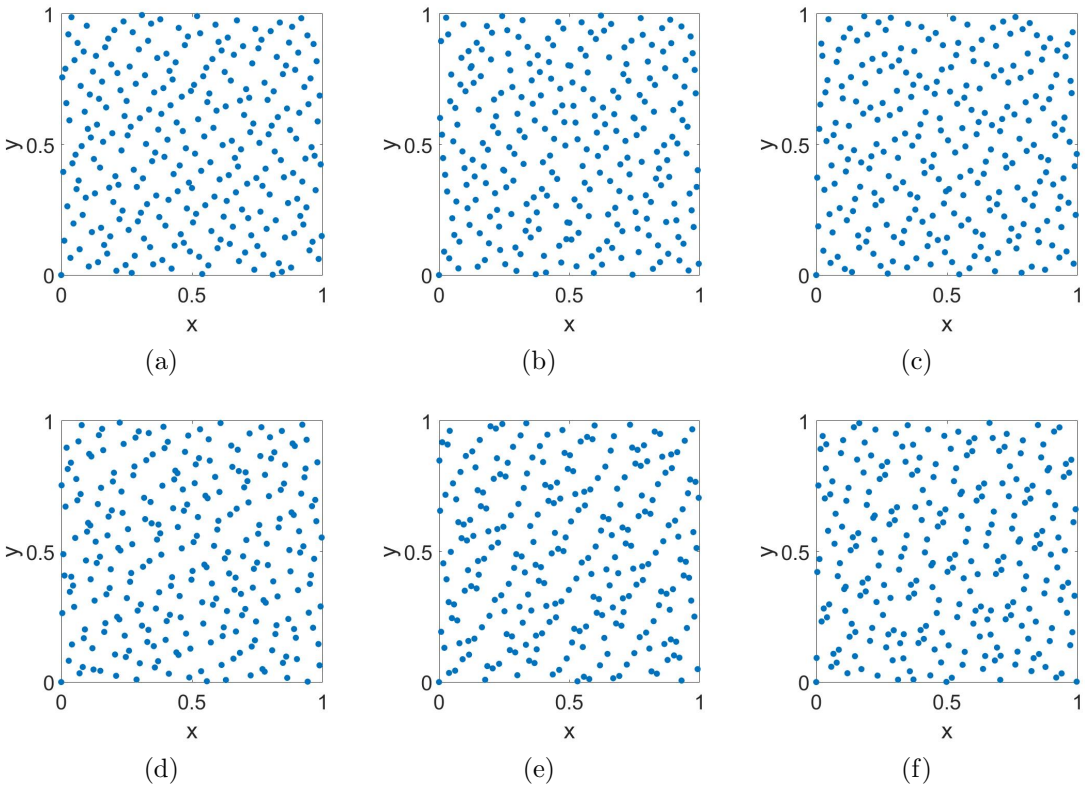

Figure 3.9 A geometric representation of the position of Halton points on a unit-square with different bases: (a) $b_1 = 2,\ b_2 = 3$, (b) $b_1 = 2,\ b_2 = 5$, (c) $b_1 = 2,\ b_2 = 7$ (d) $b_1 = 3,\ b_2 = 5$, (e) $b_1 = 3,\ b_2 = 7$, (f) $b_1 = 3,\ b_2 = 11$

3.5.4 Sobol Sampling Sampling

One of the most common low-discrepancy sequences is known as the Sobol sequence. The Sobol sequence is commonly used for Monte Carlo simulation methods in finance [75] and in the field of scientific computing [76]. Out of all the sampling sequences used in this research, the Sobol sequence is the most complex and loosely defined, since many of the variables that are used in a Sobol sequence are determined by the user. The motivation we find for the construction of the Sobol sequence is similar to Halton and Hammersley sampling, where we want to generate a set of points $\{n_1, n_2, \cdots, n_N\}$ that aren't spaced too close together, for some s-dimensional hypercube $\mathcal{I}^s = [0,1]^s$. The measure used to signify the spacing between the points is the discrepancy, which measures the deviation of a point set from a uniform distribution. So say we have a point set $\{n_1, n_2, \cdots, n_N\} \in \mathcal{I}^s$ and a subset $B \subset \mathcal{I}^s$, where we can then define a counting function $S_N(B)$ as the number of points in the sequence that fall into the subset $n_i \in B$. For every point in the sample set, $\{n_1, n_2, \cdots, n_N\} \in \mathcal{I}^s$ let B_n be an s-dimensional region where

$$B_x = [0, n_1) \times [0, n_2) \times \cdots \times [0, n_s) \tag{3.13}$$

which has volume $n_1, n_2, \cdots, n_s$. The discrepancy of the point set can then be defined as

$$D_N(\{n_1, n_2, \cdots, n_N\}) = \sup_{n \in \mathcal{I}^s} |S_N(B_n) - NV(n_1 n_2 \cdots n_s)| \tag{3.14}$$

where $V(\cdot)$ represents the volume of $\{n_1, n_2, \cdots, n_N\}$. Note that a point set that is well spaced will have a low discrepancy, since it slightly deviates from a uniform point set.

In order to construct a Sobol sequence in one dimension, the following process is used, where our intended goal is to achieve a sequence $\{n_1, n_2, \cdots, n_N\}$, $0 < n_i < 1$, and has low discrepancy over $\mathcal{I}$. We then define a set of direction numbers $v_1, v_2, \cdots$ where each v_i is a binary fraction and can be expressed as

$$v_i = 0.v_{i1}v_{i2}v_{i3}\cdots \tag{3.15}$$

and v_{ij} is the j^{th} bit following the decimal point of v_i. The directional numbers can also be represented as

$$v_i = \frac{m_i}{2^i} \tag{3.16}$$

where m_i is an odd integer $0 < m_i < 2^i$. The directional numbers are obtained from primitive polynomials with binary coefficients $\{0, 1\}$, where these primitive polynomials are found in the field $\mathbb{Z}_2$. These primitive polynomials have the following form

$$P \equiv x^d + a_1x^{d-1} + \cdots + a_{d-1}x + 1 \tag{3.17}$$

where $a_i = 0$ or 1 and P represents the primitive polynomial of degree d. Note that in order for P to be a primitive polynomial, the constant term a_d must be equal to 1 and the polynomial can be chosen by the user, thus explaining why the Sobol sequence is loosely defined. Shown below in Table 2 are the first 6 directional numbers.

Table 3.2 First 6 directional numbers

i	m_i	v_i
1	1	0.1
2	3	0.11
3	7	0.111
4	5	0.0101
5	7	0.111
6	43	0.101011

Once a primitive polynomial is chosen by the user, the coefficients from the polynomial can be used to continuously define the next v_i by

$$v_i = a_1v_{i-1} \oplus a_2v_{i-2} \oplus \cdots \oplus a_{d-1}v_{i-d+1} \oplus v_{i-d} \oplus [v_{i-d}/2^d],\ i > d \tag{3.18}$$

where $\oplus$ denotes the bitwise xor operation and the bits of the final term v_{i-d} are shifted to the right by d positions. This also allows us to further define the m_i as

$$m_i = 2a_1 m_{i-1} \oplus 2^2 a_2 m_{i-2} \oplus \cdots \oplus 2^{d-1} a_{d-1} m_{i-d+1} \oplus 2^d m_{i-d} \oplus m_{i-d} \tag{3.19}$$

For any primitive polynomial of degree d, the values of m_i are up to the user to decide upon as long as each m_i is odd and $m_i < 2^i$. For example, the values of m_i in Table 2 were chosen from the following primitive polynomial

$$x^3 + x + 1 \tag{3.20}$$

and this results in the following form for Equation 3.20

$$m_i = 4m_{i-2} \oplus 8m_{i-3} \oplus m_{i-3} \tag{3.21}$$

For the Sobol sequence, there are several fast algorithms that are used to construct a Sobol sequence. The resulting sequence is ultimately determined by the users starting value and values for the directional number. For a simple Sobol sequence algorithm, we randomly choose an integer and for this example, say we choose $i = 2$. This integer marks the starting point of our process and we will increase the value by 1 to find the next point in the sequence. What we then do next is compute the gray code representation $G(i)$ of the integer value, which is found by the following

$$G(i) = i \oplus \text{int}\left[\frac{i}{2}\right] \tag{3.22}$$

where int$[\cdot]$ is the largest integer inferior or equal to $i/2$. For our example of $i = 2$, the gray code representation is equal to

$$G(2) = 2 \oplus 1 \tag{3.23}$$

and in its binary form we get

$$G(2) = 10 \oplus 01 = 11 \tag{3.24}$$

where 11 in binary base 2 is 3.

The next step in the process is to determine our directional numbers. From the above list of candidate directional numbers, we will use the three following values

$$\begin{aligned} v_1 &= 0.1 \\ v_2 &= 0.11 \\ v_3 &= 0.111 \end{aligned} \tag{3.25}$$

In order to generate the first point n for the Sobol sequence $S(n)$, we then xor the directional numbers, scaled by the the associated bits of the gray code representation of the integer i, where the least significant bit is associated with the first directional number. Since we have three directional numbers, $G(i)$ for $i = 2$ represented by three bits is 011, so we see that we only xor the first and second directional numbers, resulting in the first value for our Sobol sequence

$$S(1) = 0.10 \oplus 0.11 = 0.01 \tag{3.26}$$

which has a decimal value of 0.25. We then increase i by one to get the next point in the sequence, such as for the fourth point in the sequence $i = 5$, we see that $S(4)$ can be expressed as

$$S(4) = 1 * 0.1 \oplus 0 * 0.11 \oplus 1 * 0.111 = 0.1 \oplus 0 \oplus 0.111 = 0.011 \tag{3.27}$$

The example presented is the one of the simplest cases for constructing a Sobol sequence, where the simplest case would be to start at $i = 1$ instead of choosing i randomly. There are more sophisticated and complex algorithms used to construct a Sobol sequence, where in [77], the user has the ability to generate their own directional numbers and choose the

starting value in the sequence (either randomly or saying that they want to skip the first 1000 values for i) and decide how many integer values that they want to increase i by to get the next point in the sequence.

Sobol sampling is a hierarchical sampling method, since the next point in the sequence is not dependent on any of the previous points, so we can easily generate a new point without having to recalculate all previous points before it. For Sobol sampling in higher dimensions, we map different Sobol sequences to each of the dimensional coordinates. So say for the 2D case, we would map a Sobol sequence $S_1(n)$ to the x-coordinate and then map a second Sobol sequence $S_2(n)$ with a different starting value and values of i to the y-coordinate. This is similar to Halton sampling. Another option is to turn Sobol sampling into a non-hierarchical sampling method and to map a uniform sequence to the x-coordinate and map a Sobol sequence $S_1(n)$ to the y-coordinate, which is similar to Hammersley sampling. Figure 3.10 displays a sample set of Sobol samples on the unit square, using two different Sobol sequences for the x and y coordinates.

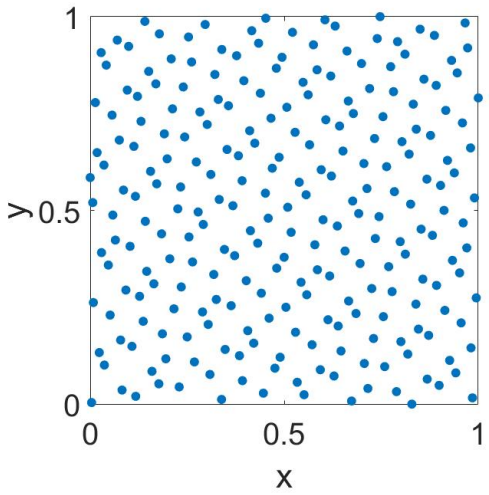

Figure 3.10 A geometric representation of Sobol points on a unit-square

3.5.5 Poisson Disk Sampling

The final LDS sampling method used for this work is Poisson disk sampling. Poisson disk sampling is similar to the random methods discussed in the earlier section, particularly sampling with uniform random variables. The concept of Poisson disk sampling is that a sample is mapped to some s-dimensional spaced, particularly $\mathcal{I}^s$ by using uniform random variables. Where Poisson disk sampling differs from random sampling is that a criterion is placed on each sample, where each sample must be a distance r from each of the previously generated samples. By placing this restraint on each of the generated points, it is inherently surrounding each of the points with a circular disk with radius r, where each disk must be disk free of all the other disks.

This constraint fixes the two problems voiced for the random sampling methods. The first being that random sampling places elements too close to each other, which in the terms of array design, can result in high levels of mutual coupling or even an unfabricatable antenna array, since elements may be placed on top of each other. This also helps out when the physical size of the antenna is large, where if we know that the elements must be some distance d apart, we can easily utilize the Poisson disk sampling algorithm to place the elements $d < r$ apart from one another.

The other issue concerning random methods that is fixed with Poisson disk sampling is that the samples are placed more uniformly around the aperture. With a large value for r, we are able to space out the samples more and fill in the gaps that random sampling fails to do. As seen in Figure 3.11, each of the samples has a disk associated with it and with a large disk, the samples look more uniform and reduce the amount of unused spaced in the area that we are sampling in. This ultimately lowers the discrepancy of the point set and explains why we refer to Poisson disk sampling as an LDS instead of a random method. However, what we notice is that when the radius of the disk is small (close to zero), we converge to random sampling using uniform random variables and when the radius is sufficiently large, we struggle with convergence of the Poisson disk algorithm. Reason being is that since the

points are randomly placed within the sampling domain, the probability of a new point falling within the disk of another point is much higher, since the probability can be found by the sum of the areas/volumes of the disks divided by the area/volume of the sampling domain. We see that this not only happens when we have a large value for r but also when we have a dense sampling set (large values of points N).

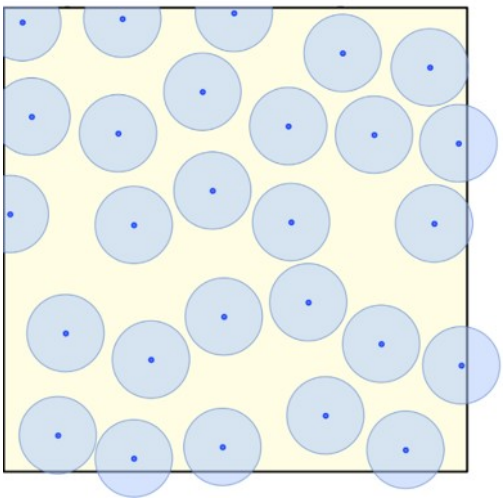

Figure 3.11 Poisson disk sampling within a square area. For a sample to be valid, it must be "disk free" of another sample. Image from [78]

An issue with Poisson disk sampling that isn't encountered with any of the previously mentioned sampling methods is that Poisson disk sampling is computationally heavy. For random sampling, points are generated in an instant by a uniform random variable. For Hammersley and Halton sampling, points are generated by a series of computations of the van der Corput sequence for a given base and points in Sobol sampling are generated by a series of xor operations. When it comes to Poisson disk sampling, we are randomly generating a point and having to check to make sure that the euclidean distance between the new point is greater than r for every previously generated point. When the first couple points are generated, the computations will be few. However, when we are dealing with large sample sets, say $500 < N$, then we will have to compute many euclidean distances each point iteration. And if the newly generated point violates the disk criterion, then the calculated

euclidean distances for that point are futile and a new point must be generated and the process must restart. This happens frequently when we have a large r and are approaching the desired amount of samples in the set, since the probability of a newly generated point being in a disk free space is much lower.

Note that the sampling is known as maximal if no more points can be added to the distribution. This method for generating points is inherently bias-free, since every point has a equal chance of being selected as the next point in the sequence. Ultimately, this says that the probability of the next generated point being inside any disk-free subdomain is proportional to the subdomain's area, as mentioned previously. It will be shown in the next chapter, that this method is one of the superior methods mentioned in this chapter despite being one of the more computationally heavy methods. One of the main benefits to using this method is that we are guaranteed to have a minimum spacing between two elements r, where with random, Hammersley, Halton, and Sobol sampling, we can elements $< r$ of each other. Large element spacing is necessary for sparse arrays because it not only allows us to sparsely populate an array aperture, but it also can be used to remove the grating lobe issue, as mentioned with the uniformly sampled case.

In more proper mathematical terms, we can derive three given properties regarding Poisson disk sampling. The first being that Poisson disk sampling produces a set of points, $X = \{n_i\}$, from a given domain, D, in an s-dimensional space, that are tightly-packed, but no closer than a specified minimum distance r. Here N is the number of elements in the array. The samples are at least a minimum distance apart, satisfying an empty disk criterion, i.e.

$$\forall n_i, n_j \in X,\ n_i \neq n_j : \|n_i - n_j\| \geq r \tag{3.28}$$

The second property is the maximal condition, which requires that the disks are simultaneously closely packed together, in the sense that the sample disks cover the whole domain. Mathematically this is given by

$$\forall n \in D,\ \exists n_i \in X : \|n - n_i\| < r \tag{3.29}$$

The Poisson distribution also possesses bias-free property which means that the expected number of sample points inside any sub-domain is proportional to the area of the sub-domain. This is achieved by ensuring that the probability of selecting a point for the next sample is equal to the probability of selecting any other point, provided these points are not already inside some prior sample's disk, i.e.

$$\forall n_i \in X,\ \forall \Omega \subset D : \mathbb{P}(n_i \in \Omega) = \frac{\text{Area}(\Omega)}{\text{Area}(D_i)} \tag{3.30}$$

Multiple algorithms have been developed to implement this technique, and the reader is referred to [79], [80] for detailed surveys of implementing Poisson sampling methods. Finally, note that since Poisson disk sampling requires the computation of euclidean distances between the new point and all the previous point, Poisson disk sampling is considered to be a non-hierarchical sampling method, since calculation of a new point is dependent on the points previously generated.

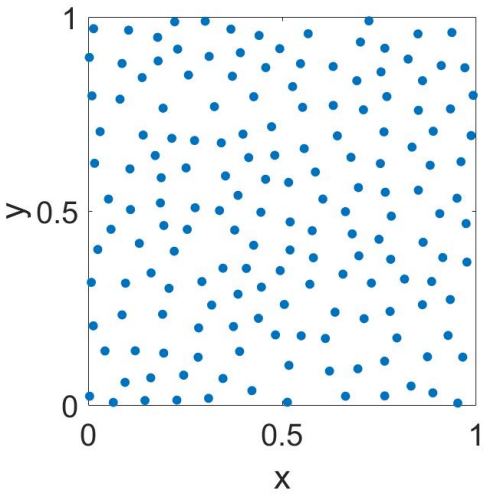

Figure 3.12 A geometric representation of the position of Poisson disk points on a unit-square

3.6 Application of LDS Sampling for Sparse Array Design

The mathematical formulation for LDS sampling was presented in this chapter. An LDS produces a random-like equidistribution of elements using a deterministic generating formula. This non-uniform sampling technique breaks the periodicity of the array and as a result it's expected that the grating lobe issues associated with sparse arrays can be removed by using any of the mentioned LDS sampling methods. The results in the next and remaining chapters will prove that the hypothesis in this chapter is true and grating lobes will be removed from the radiation pattern of the antenna array. Other metrics are also given to show that these methods can sustain an average minimum element spacing $> \lambda$ and maintain a relatively low sidelobe level. These methods will be used for and work on planar and conformal surface for various aperture shapes and steering angles as well.

CHAPTER 4

SPARSE PLANAR ARRAYS

Sparse arrays have grating lobes in the far field pattern due to the large spacing of elements residing in a rectangular or triangular grid. Random element spacing removes the grating lobes but produces large variations in element density across the aperture. In fact, some areas are so dense that the elements will overlap. This chapter[1] introduces a low discrepancy sequence (LDS) for generating the element spacing in sparse planar arrays. This nonrandom alternative finds an element layout that reduces the grating lobes while maintaining and keeping the elements far enough apart for practical construction. A mathematical formulation is presented for implementing LDS for sparse planar arrays, along with numerical results on their performance. It's shown that LDS sparse arrays with an average element spacing larger than one wavelength can significantly reduce the number of elements, maintain acceptable element spacing, and remove the grating lobes. Numerical results are presented for sparse LDS arrays with 86% less elements than a fully populated array on a square grid.

4.1 Sampling Points on a Planar Aperture

Assume a uniformly weighted N-element planar array lies in the $x-y$ plane bounded by $0 \leq x \leq x_{\max}$ and $0 \leq y \leq y_{\max}$. The array factor is given by

$$AF(u,v) = \sum_{n=1}^{N} e^{-jk[x_m u + y_n v]} \tag{4.1}$$

where $k = 2\pi/\lambda$, λ is the wavelength, (x_m, y_n) is the location of element n, θ and ϕ are the elevation and azimuth angle respectively, and $u = \sin\theta\cos\phi$, $v = \sin\theta\sin\phi$. Note that for a planar array, regular sampling takes the form of a rectangular lattice, triangular lattice,

[1]This work is in collaboration with Nicola Anselmi, Paolo Rocca, and Randy Haupt [81]

or concentric ring array [66]. In this chapter, the rectangular lattice serves as the reference, where the grating lobes for a rectangular lattice appear at

$$\begin{aligned} u_m &= u_s + m\lambda/d_x \quad \text{for } m = 0, \pm 1, \pm 2, \ldots \\ v_n &= v_s + n\lambda/d_y \quad \text{for } n = 0, \pm 1, \pm 2, \ldots \end{aligned} \tag{4.2}$$

where u_s and v_s are the main beam location in the sine space.

4.2 Sparse Planar Phased Array Antennas

In this section, the example used is a planar $32\lambda \times 32\lambda$ aperture with 576 elements. Note that a fully populated array with $\lambda/2$ element spacing with this aperture size would require 4096 elements, so this sparse array removes 86% of the elements. With a uniform grid, the average element spacing of this sparse array is $4\lambda/3$.

4.2.1 Element Distributions on the aperture

Examples of element distributions for uniform, random, and multiple LDS methods appear in Figure 4.1.

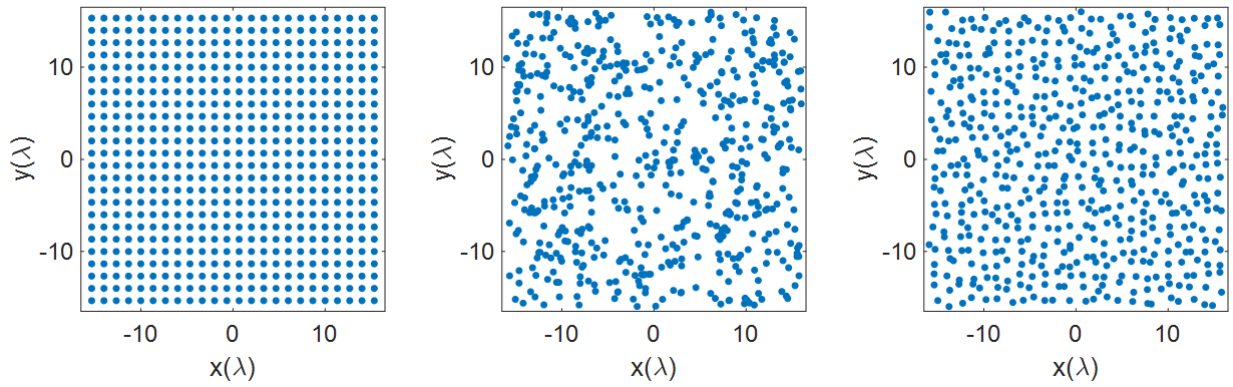

Figure 4.1 Position of elements on the aperture with different distributions: (a) uniform, (b) random, (c) random with jitter, (d) Hammersley (base 2), (e) Hammersley (base 3), (f) Hammersley (base 5), (g) Hammersley (base 7), (h) Halton (bases 2, 3), (i) Halton (bases 2, 5), (j) Halton (bases 2, 7), (k) Halton (bases 3, 5), (l) Halton (bases 3, 7), (m) Halton (bases 5, 7),(n) Sobol, (o) Poisson disk.

Figure 4.1 Continued

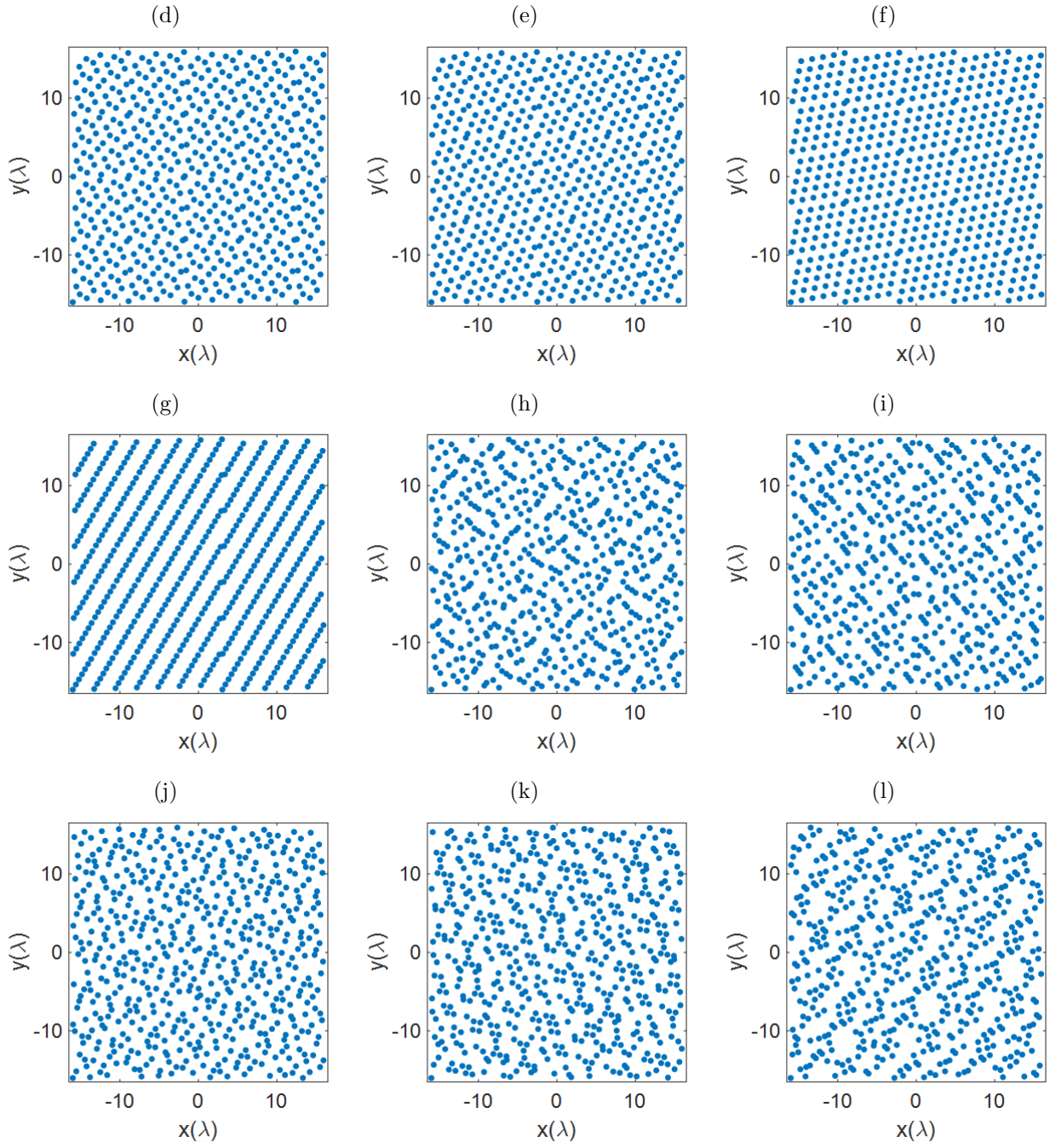

Figure 4.1 Continued

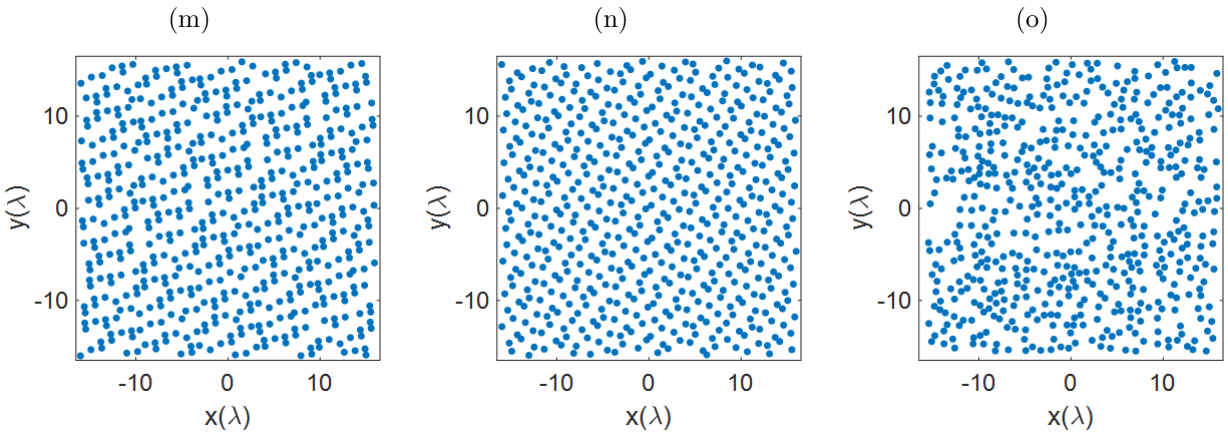

The LDS element placements in Figure 4.1 (d) to (o) do not correspond to a periodic grid. Neither are they random. In comparison of the techniques, higher order Hammersley methods, Figure 4.1 (f) and (g) with prime bases of 5 and 7 have shades of a periodic placement that potentially raise the peak sidelobe levels. This will be discussed further in the next section. Other LDS methods however appear more random and are suitable candidates for sparse arrays. Provided are some metrics on the element distributions.

As discussed earlier, from a practical fabrication perspective, it's needed that the elements are distributed on the aperture in a manner that the physical antenna elements do not touch. Bar plots in Figure 4.2 show the number of elements that fall within a minimum range of element spacing for the different distributions. As expected, for the uniform case, Figure 4.2 (a), all elements have the same minimum separation between them. The random distribution, Figure 4.2 (b), on the other hand almost produces a Gaussian-like distribution of elements but has several elements that are placed too close to each other. Random distribution with jitter, Figure 4.2 (c), has a similar Gaussian-like distribution, but provides a slightly larger minimum element spacing. The distribution however looks too regular. Hammersley distributions, Figure 4.2 (d) to (g), place many of the elements at a certain minimum spacing, which avoids the issue with minimum element spacing, but the distributions appear more periodic. This is primarily due to the hierarchical problem with this sampling method.

Halton samplings, Figure 4.2 (h) to (m), avoid both issues, i.e., too close placement of elements and a periodic distribution, although it appears that the performance improves as the base prime numbers are picked further away from each other, e.g., 2 and 7. Sobol and Poisson samplings also show a Gaussian distribution of elements and avoid small element spacings. Notably, the Poisson distribution here was set to half the element spacing of the uniform array, i.e., $4\lambda/6$, and it can be seen that the minimum element spacing is exactly $4\lambda/6$ as designed. Note that Halton, Sobol, and Poisson distributions provide a non-uniform and well distributed placement of the elements, while avoiding small element distances.

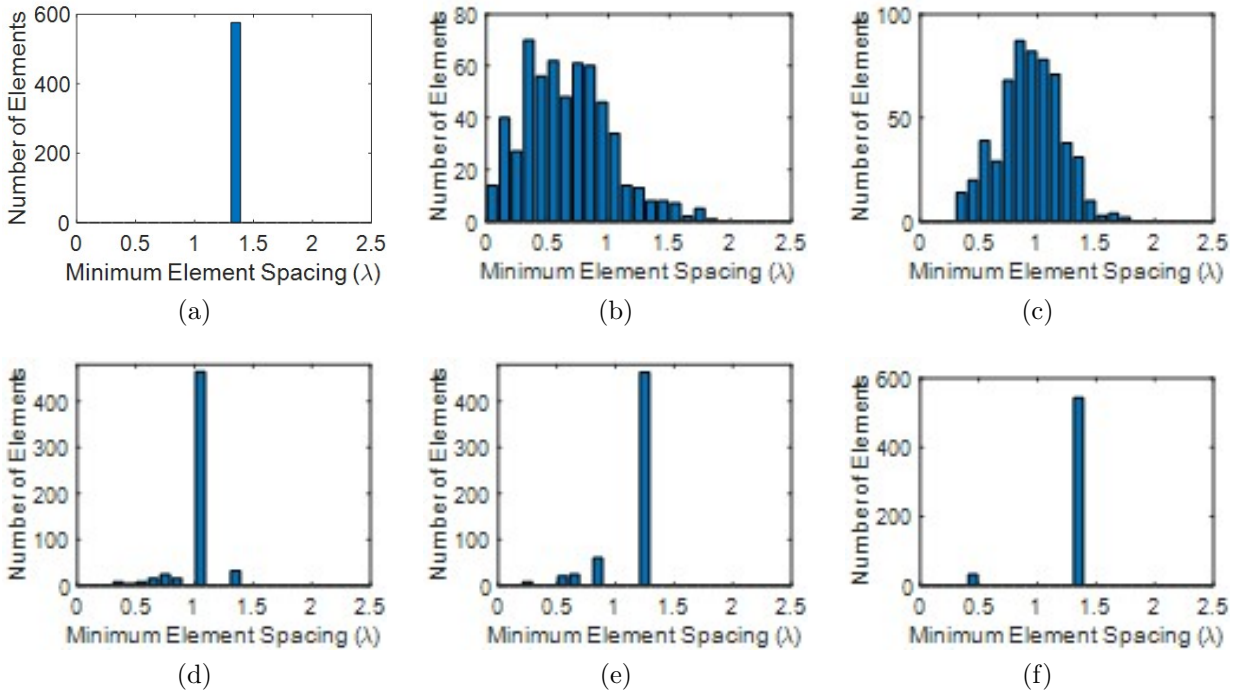

Figure 4.2 Bar plot of minimum element spacings with different distributions: (a) uniform, (b) random, (c) random with jitter, (d) Hammersley (base 2), (e) Hammersley (base 3), (f) Hammersley (base 5), (g) Hammersley (base 7), (h) Halton (bases 2, 3), (i) Halton (bases 2, 5), (j) Halton (bases 2, 7), (k) Halton (bases 3, 5), (l) Halton (bases 3, 7), (m) Halton (bases 5, 7), (n) Sobol, (o) Poisson disk.

Figure 4.2 Continued

(g)

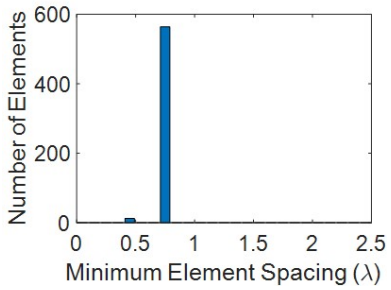

(h)

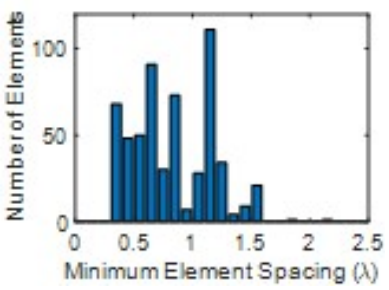

(i)

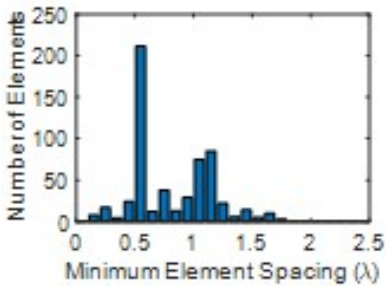

(j)

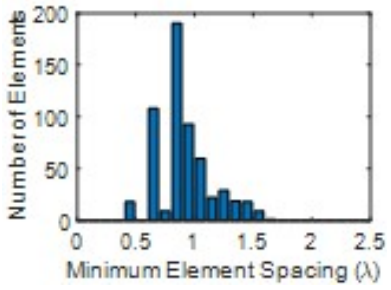

(k)

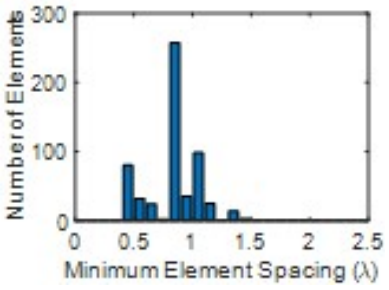

(l)

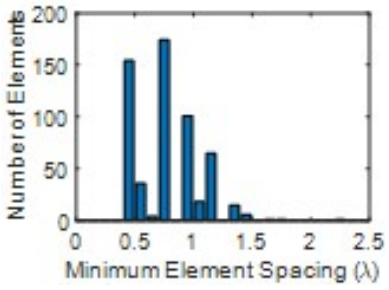

(m)

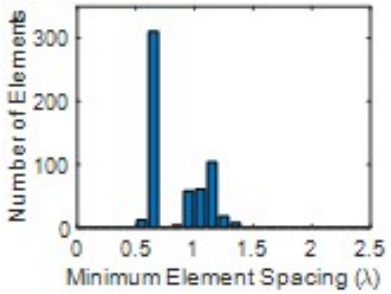

(n)

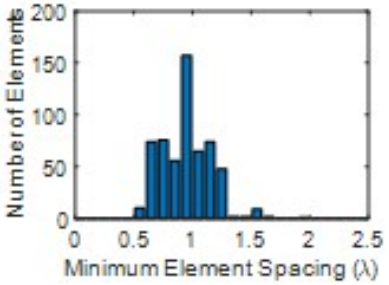

(o)

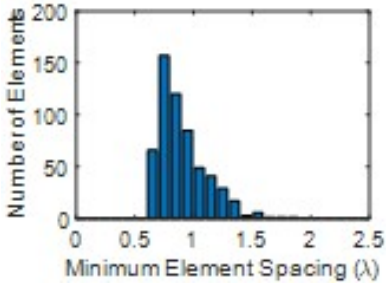

4.3 Radiation Patterns of the Sparse Phased Arrays

The complete far-field radiation pattern of an antenna array with identical elements is given by

$$F(u,v) = E(u,v)\sum_{n=1}^{N} a_n e^{-jk[x_n u + y_n v]} \tag{4.3}$$

where $E(u,v)$ is the element pattern in the u-v space, the summation represents the array factor, and $F(u,v)$ is the far-field radiation pattern of the antenna array. In this expression, a_n is the element weight, and the other terms are as defined in [29]. Note that the elements considered have unity amplitude and zero phase, so $a_n = 1$. The elements are also isotropic, so $E(u,v) = 1$.

The radiation patterns of the arrays in the uv-space are computed using Equation 4.3 and are given in Figure 4.3. In these graphs the visible region is a circle with $\sqrt{u^2+v^2} \leq 1$. It can be seen that the uniform case has the worst performance and four grating lobes with sidelobe level of 0 dB appear in the visible space. Random sampling completely removes the grating lobes, however as seen in the previous section, it places many elements too close together. Random sampling with jitter reduces the grating lobes but cannot break the grating lobes completely because its element spacing is too regular. On the other hand, all LDS methods are effective in reducing the SLLs while maintaining low discrepancy. In comparison between these methods, Hammersley sampling has the poorest performance due to its hierarchical problem. For Hammersley sampling, performance degrades as the prime base number is increased. Halton sampling on the other hand shows a much better performance, and all 6 cases studied here show that they can break the grating lobes. Due to its binary implementation, Sobol sampling shows a similar performance to Hammersley sampling with a prime base of 2. Poisson sampling appears to outperform all other LDS methods as well as the random distribution. The 2D uv-graphs in Figure 4.3, allow one to visually compare the radiation performance of all the sampling techniques, however, for better comparison, a

quantitative analysis is also provided in the next section.

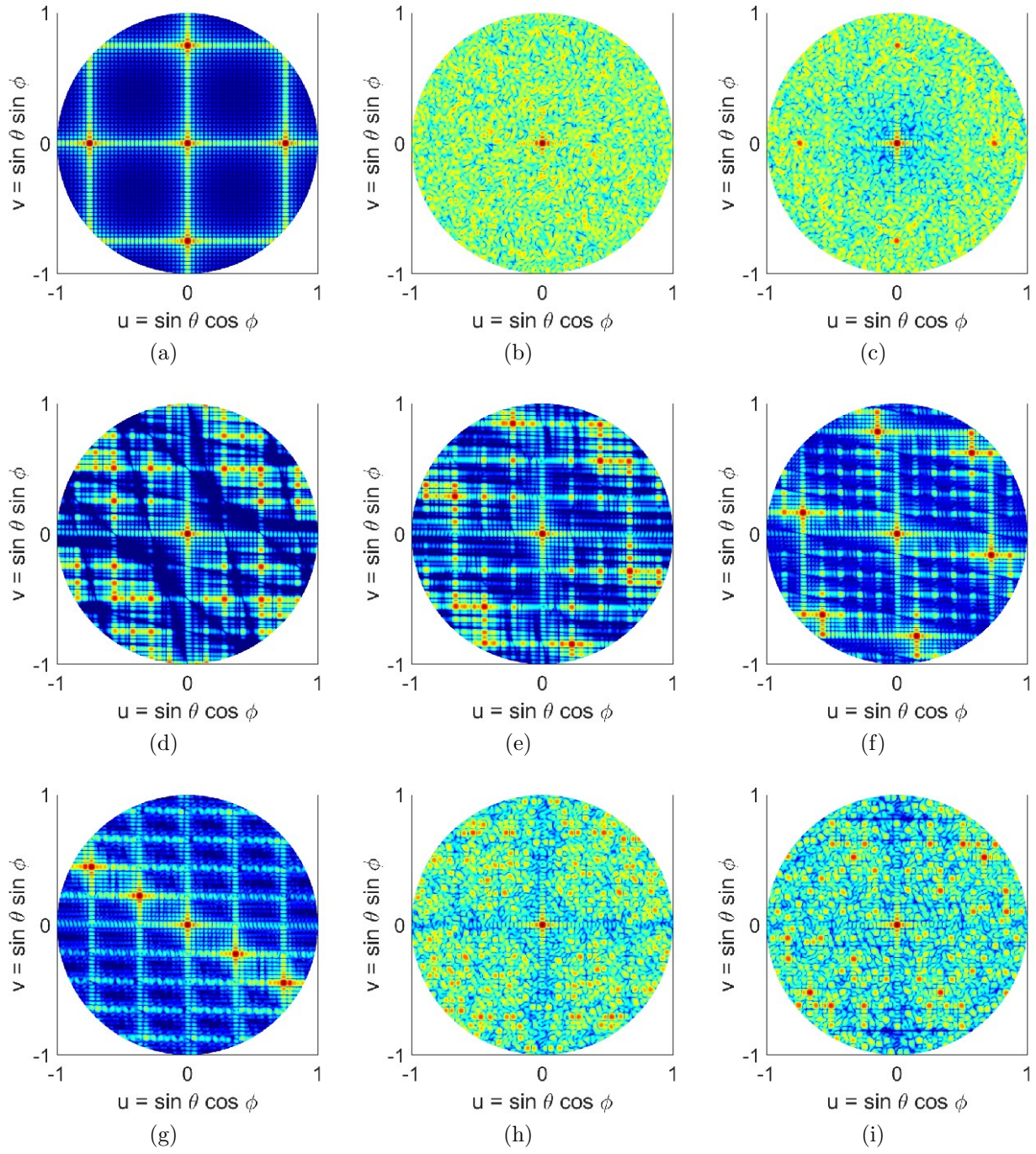

Figure 4.3 Normalized power patterns of the antenna arrays with different element distributions in the uv-space: (a) uniform, (b) random, (c) random with jitter, (d) Hammersley (base 2), (e) Hammersley (base 3), (f) Hammersley (base 5), (g) Hammersley (base 7), (h) Halton (bases 2, 3), (i) Halton (bases 2, 5), (j) Halton (bases 2, 7), (k) Halton (bases 3, 5), (l) Halton (bases 3, 7), (m) Halton (bases 5, 7), (n) Sobol, (o) Poisson disk.

Figure 4.3 Continued

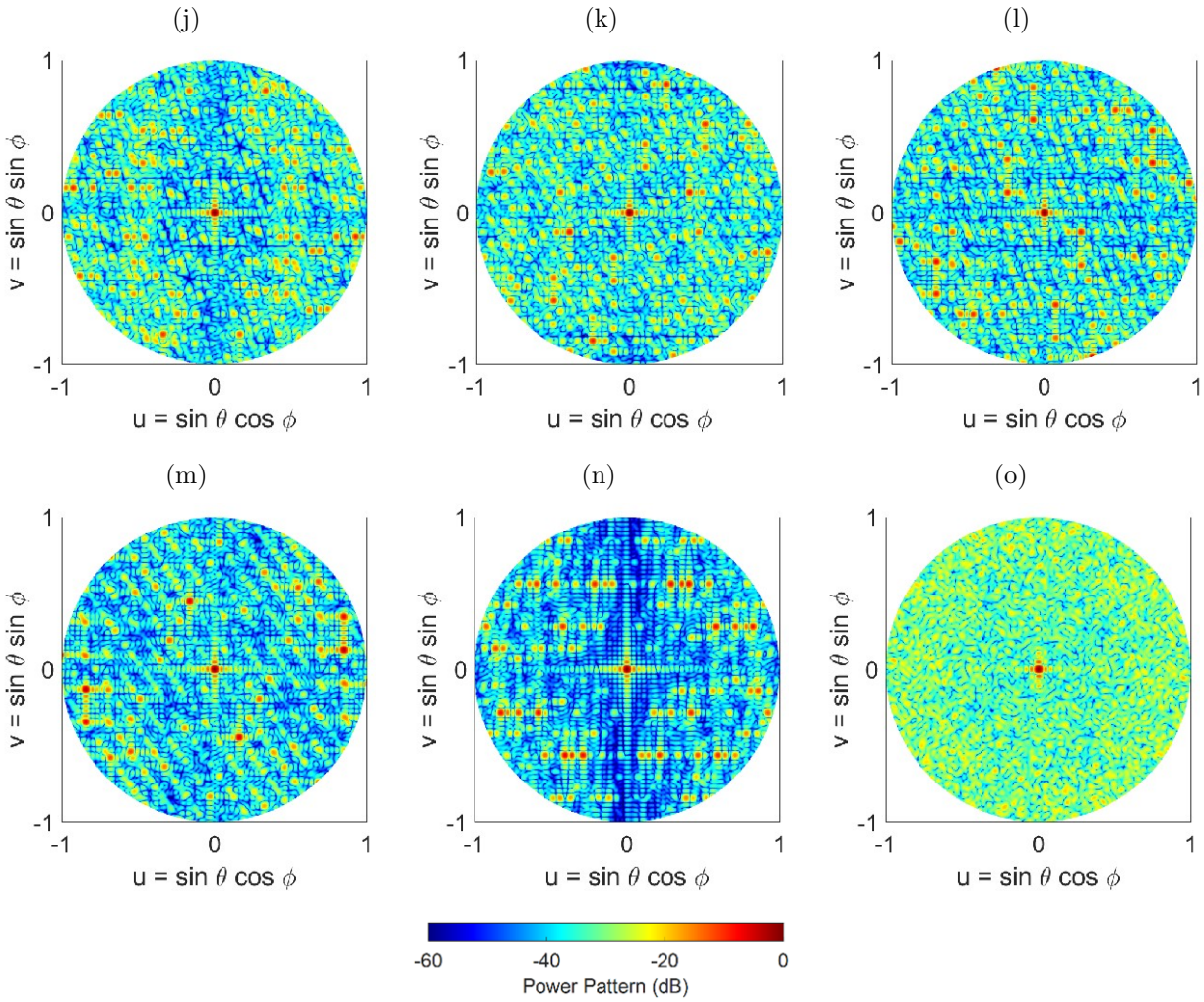

4.3.1 Quantitative Analysis of Sparse Array Performances

As discussed earlier in this work, for sparse arrays the interest is in removing the grating lobes, while at the same time having sampling that avoids too sparse or too dense element distributions. In order to quantitatively analyze these arrays, some metrics for element distributions and radiation pattern performances are examined.

For element distributions, an important statistical parameter, i.e., average minimum element spacing is used. This average value is obtained by computing the minimum element spacing for each element of the array, and then averaging the sum of those numbers over

the total number of elements. These results are given in Tables 4.1 and 4.2 for all 15 cases studied here. All LDS techniques provide a larger value of average minimum element spacing compared to the random technique, with Hammersley technique yielding the largest in comparison. From an element distribution perspective, it can be seen that LDS methods are very effective in providing a physically realizable distribution and outperform the random approach. For a quantitative study of radiation performance, peak sidelobe level (SLL) is used, as well as directivity and aperture efficiency. Peak SLL is the ratio of the pattern of the sidelobe peak F_{SLL}, to the pattern value of the main lobe ($F_{\max}$). Note that for a boresight beam $F_{\max}$ is the value of the far-field radiation pattern at $F(0,0)$. The directivity is defined as

$$D = \frac{4\pi F_{\max}}{\int_0^{\sqrt{u^2+v^2}\leq 1} \int_0^{\sqrt{u^2+v^2}\leq 1} F(u,v) du dv} \tag{4.4}$$

Aperture efficiency is defined as directivity divided by maximum aperture directivity, where the maximum aperture directivity is given by

$$D_{\mathrm{aperture}} = \frac{4\pi A}{\lambda^2} \tag{4.5}$$

Here, A is the size of the array aperture, which in the study conducted in this section is $32\lambda \times 32\lambda$, and λ is the wavelength.

These results are also given in Tables 4.1 and 4.2 for all 15 cases. It can be seen that the uniform case has the poorest performance in terms of SLL as well as directivity and efficiency. Random distribution can notably improve these, but as discussed earlier, the element distribution is undesirable. Random distribution with jitter improves directivity and efficiency but degrades SLL. In comparison between the LDS methods, Hammersley sampling has the poorest SLL performance, which degrades as the prime base number is increased. Halton sampling shows a better performance in comparison. The prime bases of 2 and 7 yield the best performance for this technique. Sobol sampling shows a similar performance

to Hammersley with a prime base of 2. Poisson disk sampling shows the best performance of all LDS techniques, with a SLL of -12.28 dB and close to 15% aperture efficiency. While all these LDS techniques outperform the uniform case, the best performances come from Halton and Poisson disk methods that outperform the random technique.

Table 4.1 Average minimum element spacing and peak SLL for sparse arrays with different element distributions

Method	Average Minimum Element Spacing (λ)	Peak SLL (dB)
Uniform	1.3333	0
Random	0.6667	-10.90
Random with Jitter	0.9325	-9.36
Hammersley (base 2)	1.0037	-7.0
Hammersley (base 3)	1.1688	-2.69
Hammersley (base 5)	1.2624	-0.55
Hammersley (base 7)	0.7538	-0.25
Halton (bases 2, 3)	0.8436	-10.10
Halton (bases 2, 5)	0.8115	-4.33
Halton (bases 2, 7)	0.9172	-12.35
Halton (bases 3, 5)	0.8430	-8.10
Halton (bases 3, 7)	0.7663	-5.90
Halton (bases 5, 7)	0.8633	-5.60
Sobol	0.9307	-6.58
Poisson Disk	0.9031	-12.28

4.4 Aperture Shape Effects on the Performance of Sparse Phased Array Antennas

To see the impact of aperture shape on the performance of these LDS arrays, in this section, three different types of arrays with rectangular, circular, and elliptical apertures are studied. All apertures are designed with the same surface area of $1024\lambda^2$ as the square aperture studied in the previous sections. The rectangular aperture has an aspect ratio of 9/4, i.e., the ratio of its longer side to its shorter side, corresponding to longer and shorter side lengths of 48λ and $64\lambda/3$, respectively. The circular aperture has a radius of 18λ. To maintain the same aspect ratio as the rectangle and the same aperture size as the other arrays, the elliptical array major and minor axis are 27λ and 12λ, respectively. Here, the

performance of two LDS sparse arrays that showed the best performance are compared, namely Halton (with bases of 2 and 7) and Poisson distributions, with uniform distribution. The element distributions for these arrays are given in Figure 4.4.

Table 4.2 Directivity and aperture efficiency for sparse arrays with different element distributions

Method	Directivity (dB)	Aperture Efficiency (%)
Uniform	31.5478	11.168
Random	31.9619	12.209
Random with Jitter	32.5775	14.068
Hammersley (base 2)	32.7075	14.166
Hammersley (base 3)	32.6226	14.215
Hammersley (base 5)	31.6892	11.466
Hammersley (base 7)	33.8949	19.054
Halton (bases 2, 3)	32.4609	13.696
Halton (bases 2, 5)	32.3534	13.361
Halton (bases 2, 7)	32.8188	14.872
Halton (bases 3, 5)	32.8611	15.018
Halton (bases 3, 7)	32.2561	13.065
Halton (bases 5, 7)	32.9511	15.332
Sobol	32.7127	14.513
Poisson Disk	32.8212	14.880

Bar plots in Figure 4.5 show the number of elements that fall within a minimum range of element spacing for the different distributions. Similar to Figure 4.2, for the uniform case, all elements have the same minimum separation between them. Halton sampling avoids too close placement of elements and distributes them in the range around $\lambda/2$ to 2λ, while Poisson sampling provides a Gaussian distribution of elements with and minimum element spacing of $4\lambda/6$. Note that these observations are similar to the square aperture studies given in Section 4.3. The radiation patterns of these arrays in the uv-space are given in Figure 4.6, where it can be seen that similar to the square aperture array, the uniform case has the worst performance and four grating lobes with sidelobe level of 0 dB appear in the visible space. Both LDS techniques remove the grating lobes; however, it's shown that the Poisson technique outperforms Halton sampling. Nonetheless, these studies show that

the performance of LDS sampling techniques are not impacted by the shape of the array aperture, and in general these sampling approaches can be used for arbitrary shaped arrays.

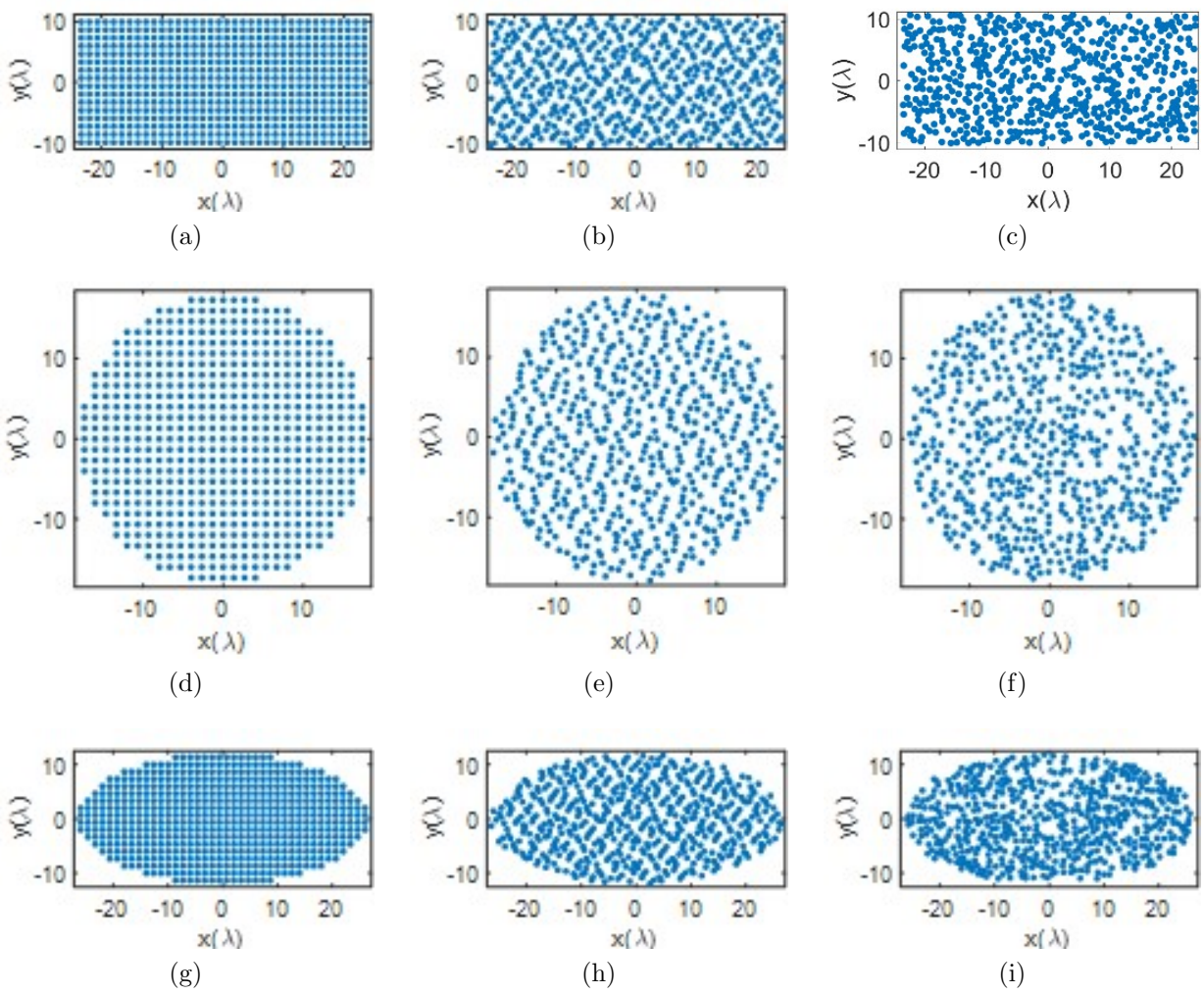

Figure 4.4 Position of elements on rectangular, circular, and elliptical apertures with different distributions: (a) uniform (rectangular), (b) Halton (rectangular), (c) Poisson disk (rectangular), (d) uniform (circular), (e) Halton (circular), (f) Poisson disk (circular), (g) uniform (elliptical), (h) Halton (elliptical), (i) Poisson disk (elliptical).

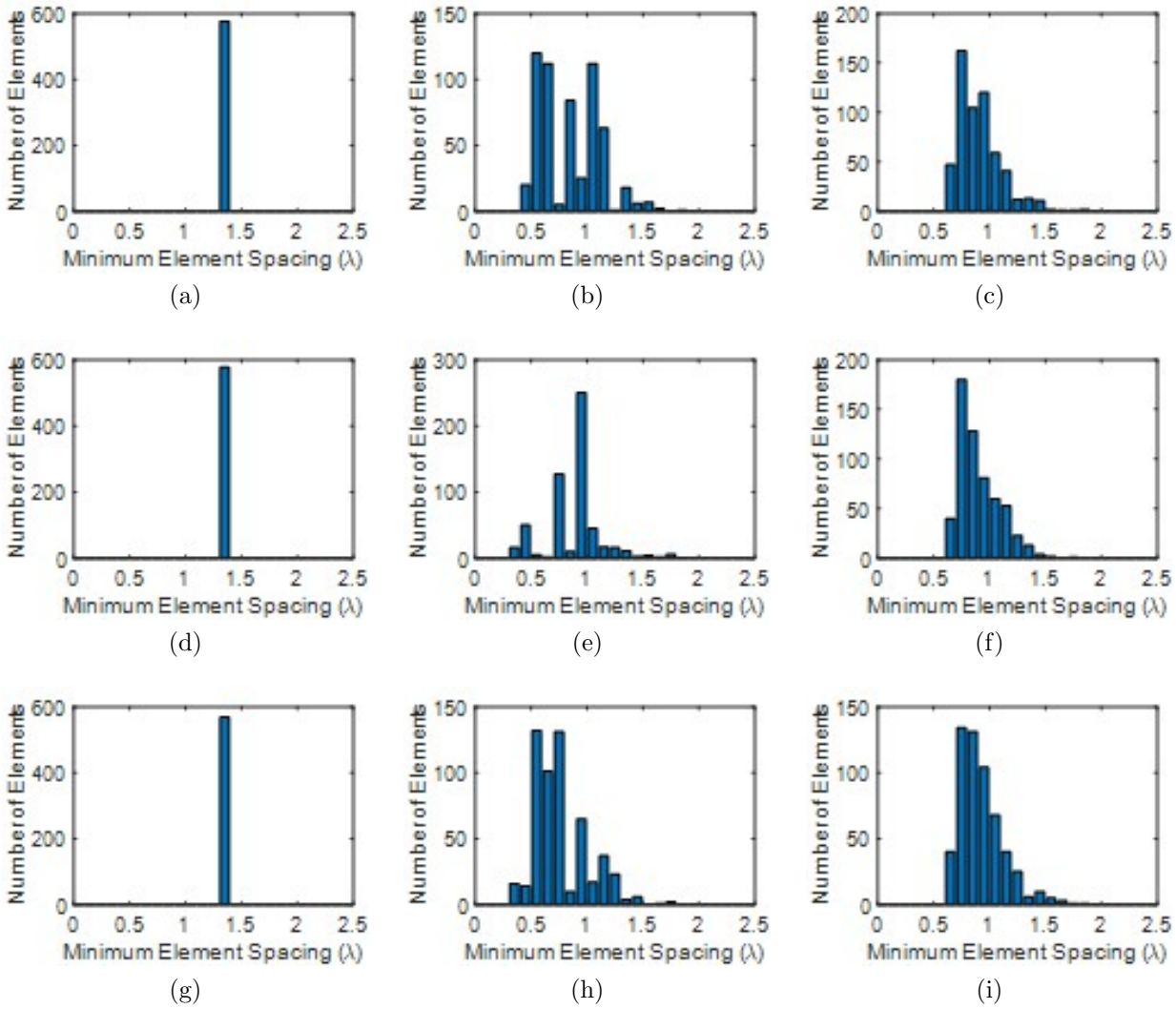

Figure 4.5 Bar plot of minimum element spacings on rectangular, circular, and elliptical apertures with different distributions: (a) uniform (rectangular), (b) Halton (rectangular), (c) Poisson disk (rectangular), (d) uniform (circular), (e) Halton (circular), (f) Poisson disk (circular), (g) uniform (elliptical), (h) Halton (elliptical), (i) Poisson disk (elliptical).

Tables 4.3 and 4.4 summarize the performance factors for these three types of arrays. As expected, the uniform case has the poorest performance in terms of SLL as well as directivity and efficiency. Both LDS techniques are effective in removing the grating lobes, but it can be seen that the Poisson technique provides the best results. It should be noted that in comparison between array aperture types, the circular aperture provides the best performance in terms of peak SLL, directivity, and efficiency.

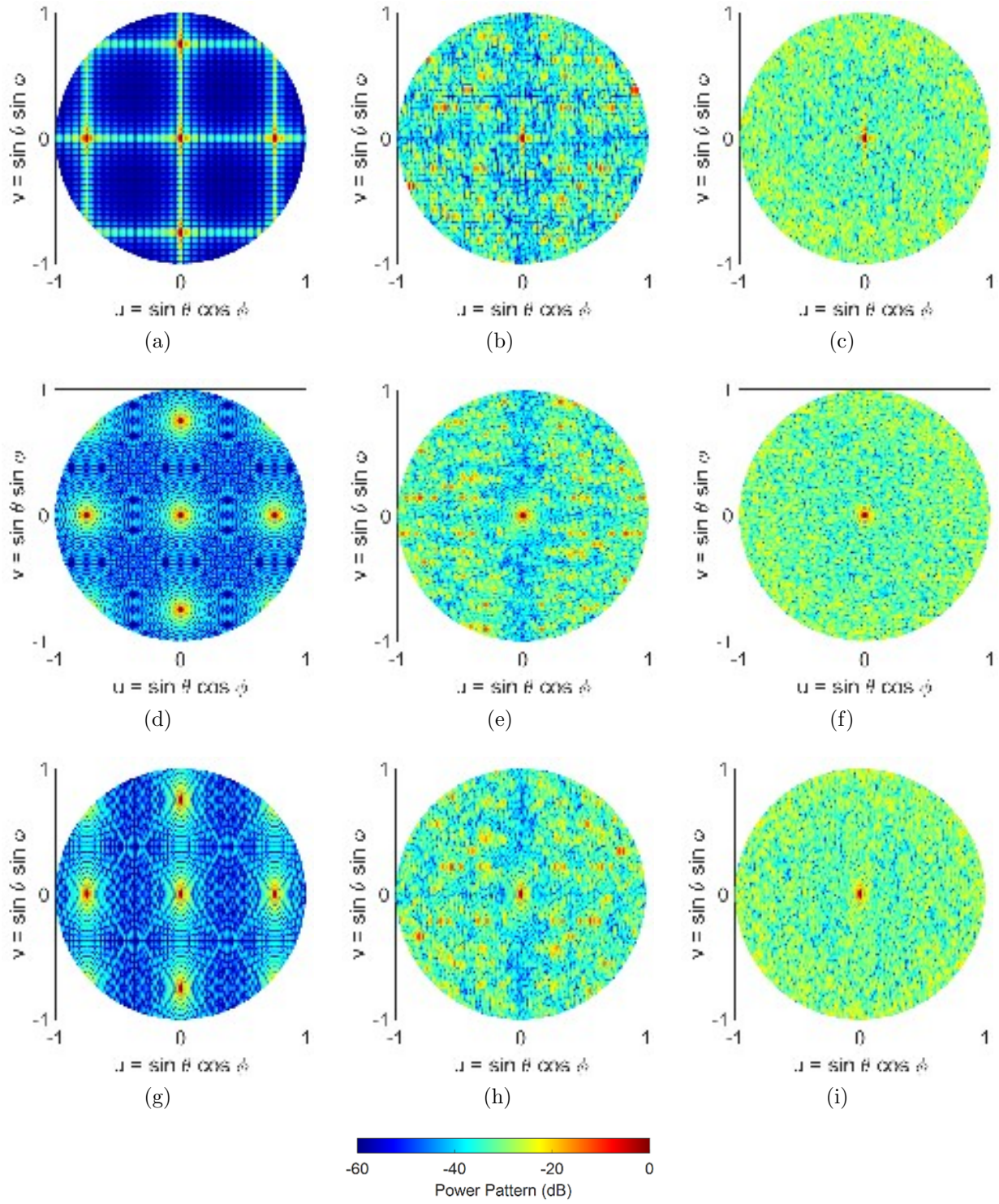

Figure 4.6 Resulting power patterns of sparse antenna arrays with various aperture shapes in the *uv*-space: (a) uniform (rectangular), (b) Halton (rectangular), (c) Poisson disk (rectangular), (d) uniform (circular), (e) Halton (circular), (f) Poisson disk (circular), (g) uniform (elliptical), (h) Halton (elliptical), (i) Poisson disk (elliptical).

Table 4.3 Average minimum element spacing and peak SLL for sparse arrays with different element distributions

Method	Average Minimum Element Spacing (λ)	Peak SLL (dB)
Uniform/Rectangular	1.3333	0
Uniform/Circular	1.3333	0
Uniform/Elliptical	1.3333	0
Halton/Rectangular	0.8481	-6.74
Halton/Circular	0.8967	-9.27
Halton/Elliptical	0.7724	-8.94
Poisson/Rectangular	0.9094	-12.18
Poisson/Circular	0.9016	-15.30
Poisson/Elliptical	0.9245	-14.34

Table 4.4 Directivity and aperture efficiency for sparse arrays with different element distributions

Method	Directivity (dB)	Aperture Efficiency (%)
Uniform/Rectangular	31.5778	11.175
Uniform/Circular	31.5848	11.261
Uniform/Elliptical	31.5181	11.228
Halton/Rectangular	32.4857	13.774
Halton/Circular	32.6474	14.383
Halton/Elliptical	32.5883	14.365
Poisson/Rectangular	32.8062	14.829
Poisson/Circular	32.8643	15.119
Poisson/Elliptical	32.6634	14.616

4.5 Beam-Scanning Performance of Sparse Phased Array Antennas

In this section, the beam-scanning performance of sparse phased array antennas is studied. The studies conducted in Sections 4.3 and 4.4 showed that the performance of LDS distributions are not impacted by the type/shape of the array aperture, so for brevity, only the square aperture configuration in Section 3 is considered. By adding a progressive phase shift to the elements on the aperture, the sparse arrays can provide 2D beam scanning. Mathematically, the phase shift needed to scan the beam is given by

$$\psi(x_n, y_n) = k(x_n \sin\theta_s \cos\phi_s + y_n \sin\theta_s \sin\phi_s) \tag{4.6}$$

where $k = 2\pi/\lambda$, λ is the wavelength, (x_n, y_n) is the location of element n, θ_s and ϕ_s are the elevation and azimuth angle of the desired scanned beam direction, respectively.

Here, the 1D and 2D scanning performance of the arrays is investigated by studying scanning in the elevation plane at $\phi = 0°$ and $\phi = 45°$ directions, but similar results are observed for other scan directions. Note that scanning is essentially shifting the observation window. With sparse arrays this means that if grating lobes are created, scanning may result in more grating lobes appearing in the visible space.

Here, the scan performance of two LDS sparse arrays that showed the best performance is compared, namely Halton (with bases of 2 and 7), and Poisson distributions, along with uniform and random distributions. Scanned patterns of each of these arrays are given in Figure 4.7 ($\phi = 0°$) direction and Figure 4.8 ($\phi = 45°$), for 20°, 40°, and 60° elevation scans. Note that the array elements are isotropic point sources. For the uniform array, four grating lobes are observed when the array beam is at boresight, Figure 4.3 (a). When the array is scanned in 1D, Figure 4.7 a–c, the number of grating lobes increases to five at 20° and to seven when pointing at 40° and 60°. When the array is scanned in 2D, Figure 4.8 a–c, the number of grating lobes first reduces to three at 20° and 40°, and then increases to five when pointing at 60°. This change in the number of grating lobes degrades directivity, and in general the uniform array is not suitable for beam-scanning. The other three arrays

however, i.e., random, Halton, and Poisson, show a good beam-scanning performance. These arrays do not have grating lobes, and scanning does not change that. In particular, note that Poisson distribution, Figures 4.7 and 4.8 j–l, shows a performance better than random distribution, i.e., Figures 4.7 and 4.8 d–f, with the added advantage of having a physically realizable element distribution. It is important to see that while Halton sampling does have a higher SLL in the visible space, it does not have grating lobe issues, and again provides a notably better element distribution compared to the random case. Nonetheless, these studies also confirm that the Poisson disk sampling provides the best performance.

4.6 Conclusions

Sparse arrays have a significantly smaller number of elements compared to traditional dense arrays (with $\lambda/2$ element spacing) which minimizes their cost and complexity. A comprehensive study of sparse phased arrays using low-discrepancy sequence (LDS) element distribution is presented. It's shown that these LDS element distributions remove the grating lobes associated with large element spacing in sparse arrays, while at the same time avoid undesirable and impractical element distributions in random arrays. The mathematical formulation for implementing LDS for sparse planar arrays is presented, along with numerical studies on their performance. The studies conducted considered sparse arrays with 86% less elements than a fully populated array. The performance factors compared equidistribution on the aperture of the array by looking at average minimum element spacing, as well as array pattern peak SLL, directivity, and aperture efficiency. Different array aperture configurations were also studied, and it's shown that the performance of LDS distributions is not impacted by the type/shape of the array. Finally, the studies concluded that in comparison between the LDS techniques, the Poisson disk sampling technique outperforms all other approaches and is the recommended LDS technique for sparse arrays.

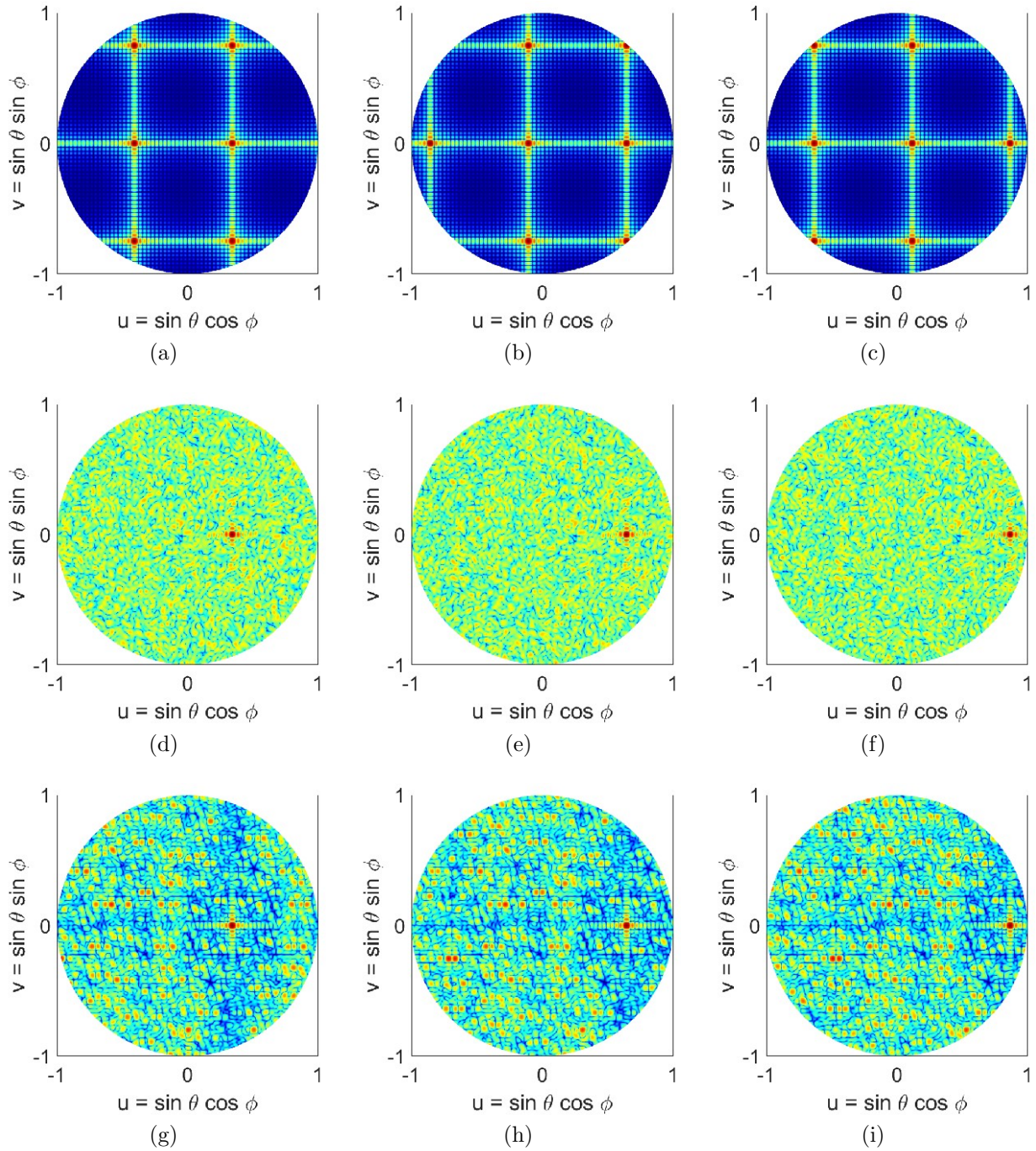

Figure 4.7 Normalized power patterns of the antenna arrays in the uv-space scanned along the elevation plane in $\phi = 0°$ direction with different element distributions: (a) uniform 20° scan, (b) uniform 40° scan, (c) uniform 60° scan, (d) random 20° scan, (e) random 40° scan, (f) random 60° scan, (g) Halton 20° scan, (h) Halton 40° scan, (i) Halton 60° scan, (j) Poisson disk 20° scan, (k) Poisson disk 40° scan, (l) Poisson disk 60° scan. The Halton sampling uses prime bases of 2 and 7.

Figure 4.7 Continued

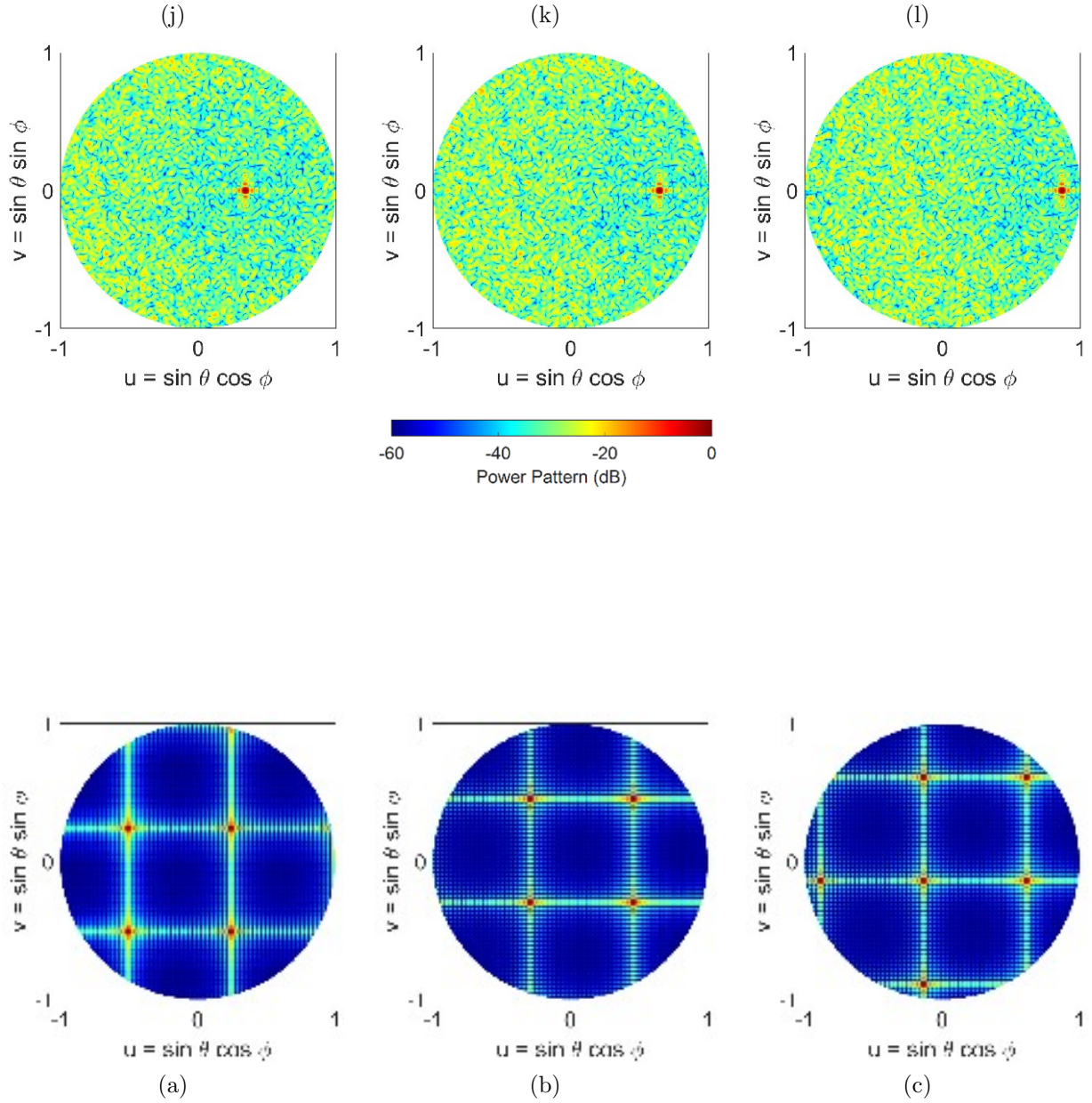

Figure 4.8 Normalized power patterns of the antenna arrays in the uv-space scanned along the elevation plane in $\phi = 45°$ direction with different element distributions: (a) uniform 20° scan, (b) uniform 40° scan, (c) uniform 60° scan, (d) random 20° scan, (e) random 40° scan, (f) random 60° scan, (g) Halton 20° scan, (h) Halton 40° scan, (i) Halton 60° scan, (j) Poisson disk 20° scan, (k) Poisson disk 40° scan, (l) Poisson disk 60° scan. The Halton sampling uses prime bases of 2 and 7.

Figure 4.8 Continued

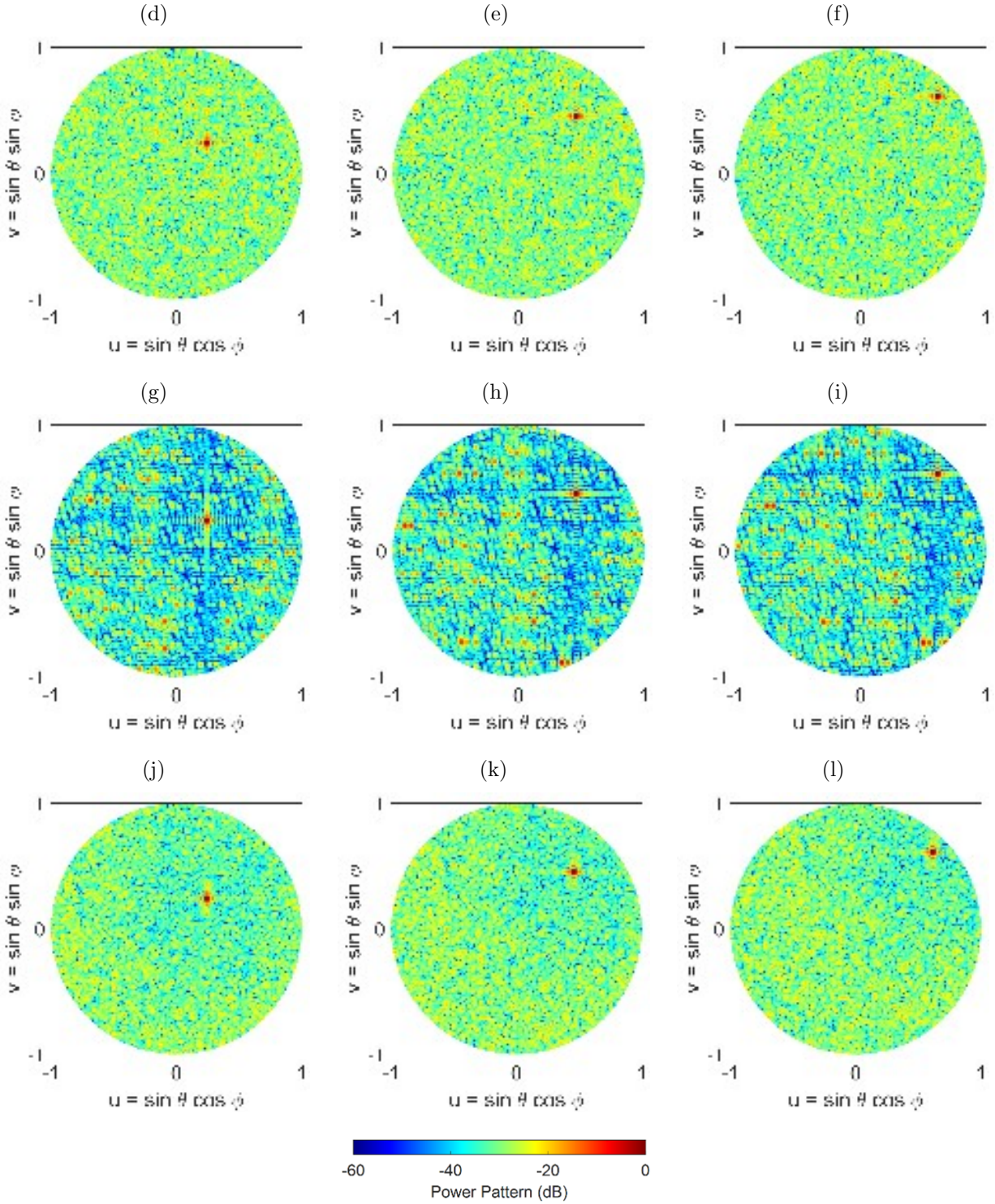

CHAPTER 5

ANALYSIS OF THE NATURE OF SPARSE PLANAR ARRAYS

In this chapter, we give a detailed overview and in depth analysis of the current methods that are used in sparse antenna array design, which include: the use of convex optimization, array thinning using genetic algorithms (GA), and array thinning using random element selection, which follows a similar approach to the random sampling methods used in the previous chapter. The purpose of this chapter is to examine the pre-existing methods and our proposed method of using LDS to design sparse antenna arrays, in order to study the nature and behavior of each technique and the resulting sparse array that it produces. The reason being is that in chapter four, we only studied one aperture size, which was a $32\lambda \times 32\lambda$ aperture with an element spacing of $4\lambda/3$, which resulted in a sparse array consisting of 576 elements. This chapter examines smaller aperture sizes and with various element spacings. The purpose of this analysis is to provide insight and knowledge about each of the existing approaches and show that the use of LDS are very valuable when the array uses element spacing $> \lambda$. By doing so, we will also be examining various sparsity levels of each array and see when a particular approach may be useful for a given application.

5.1 Sparse Array Analysis Models & Setup

In the field of sparse antenna array design, there are several methods that are used for designing sparse antenna arrays, where the pre-existing methods we will examine are convex optimization, array thinning using GA, and array thinning using random sampling. In the majority of existing literature on sparse array design, these methods are applied to a fully populated array ($d = \lambda/2$ case) or instances where the elements in the array have a spacing $< \lambda$. The elements are then removed by selecting them to be in an "on" or "off" state, where the elements that are turned off are discarded from the array. When it comes to using these element selection type methods, we run into a trade off of sacrificing directivity or side

lobe level (SLL), where sparse arrays can give rise to high SLL and significantly drop the directivity of the array. Some methods like convex optimization, optimize the weights so that the array can be sparse and also hold the SLL under a given level, however, this usually results in solving for a weighting vector that consists of complex weights or weights that are > 1. In order to remain consistent with the work presented in this dissertation, we will briefly cover these approaches but only use methods that result in a binary taper (element is either on or off). We will see that when we have element spacing with $d \geq \lambda$, grating lobes appear within the pattern and none of the prior existing methods work in general or as well as the LDS methods presented in Chapters 3 and 4. LDS still proves that they are sufficient for removing the grating lobes and maintaining a well balanced directivity and SLL trade off. This makes the LDS methods unique, because they are one of the only existing methods to function properly when $d > \lambda$.

When looking at $d < \lambda$, the questions that then arise are, are one of these methods superior to all of the others, are the performance of these methods based on the aperture size or number of elements in the array? We aim to answer these questions and give a definitive guide to the antenna array community to help further develop and innovate the area of sparse antenna array design. As mentioned previously, when the elements are allocated to a grid, the amount of possible array design selections is 2^N, where N represents the number of elements. But when we move the elements to off-grid locations, we now have an infinite selection of possible arrays to choose from. It was with the proposed LDS methods that we were able to move off-grid and actually improve the performance when compared to an array with a fixed uniform grid of elements. However, it may be with certain aperture sizes or number of elements that selecting elements from a uniform grid is the more optimal approach, which will be shown later in this chapter.

In order to answer these questions, we will need to conduct a sweep over various antenna aperture sizes and sample set sizes. For this work, we will examine arrays with an apertures ranging from $4\lambda \times 4\lambda$ up to $24\lambda \times 24\lambda$, in steps of 4λ, $(4\lambda \times 4\lambda, 8\lambda \times 8\lambda, 12\lambda \times 12\lambda, \cdots)$. The

optimal performance of each case will always be when the elements are uniformly spaced by $d = \lambda/2$, which is where we achieve maximum directivity and minimum max SLL. When we reduce the number of elements, it is guaranteed that directivity will drop but in return, we will save on the amount of elements used within the array. Our analysis will be the same as in Chapter 4, where we will increase the element spacing and the remaining elements will be the number of samples we will take within the aperture (note that for methods using convex optimization, it is difficult to specify the number of desired elements, but an error constraint can be used to sacrifice array performance for higher sparsity). For our analysis, we will examine the arrays with element spacings on the following interval, $d \in [\frac{\lambda}{2}, \frac{4\lambda}{3}]$. For this chapter, we will only consider the square aperture, since apertures with various geometries were already presented and studied in depth for Chapter 4.

In Chapter 4, we had used several metrics to examine the performance of each of the resulting arrays, which were: average minimum element spacing, directivity, and side lobe level. For this chapter, we will primarily focus on SLL, directivity, and SLL. Since methods such as array thinning and convex optimization are applied to arrays where $d_{\min} = \lambda/2$, the minimum spacing between any element will be $\lambda/2$, so we will not have to worry about elements clustering too close together. It has already been shown in Chapter 4 that LDS populate an aperture more uniformly than a set of random samples, so the element spacing for the LDS used in this chapter will also not be emphasized.

5.2 Applications of Convex Optimization for Sparse Arrays

Convex optimization has been applied to antenna array pattern synthesis problems for several decades, where one of the first papers to use convex optimization for antenna arrays was in [82]. The paper actually focuses on the antenna array synthesis problem, which is to adjust the excitation amplitudes, phases, and element positions of the antenna array, in order to obtain a radiation pattern with a required set of characteristics. We see that one of the first problem formulations, was to minimize the sidelobe level of a planar array with an arbitrary geometry (uniform or random), which consisted of the following optimization

problem

$$\min_{\boldsymbol{w}} \max \ |\mathbf{A_s}\boldsymbol{w}| \quad \text{subject to } \boldsymbol{a}_{\text{tar}}^{\top}\boldsymbol{w} = 1 \tag{5.1}$$

where $\boldsymbol{w}$ is the element weighting vector $\boldsymbol{w} = [w_1, w_2, \cdots, w_N]^{\top} \in \mathbb{C}^N$, N is the number of elements in the array, $\mathbf{A_s}$ is the array manifold matrix as a function of θ for a given sidelobe region that we wish to minimize $\theta_{SL} \in Sidelobe$, and $\boldsymbol{a}_{\text{tar}}$ is the vector from the array manifold matrix that corresponds to our desired peak location θ_0. The optimization solves for an optimal weighting vector that produces a peak at θ_0 and successfully minimizes the sidelobes < -20 dB for a desired region of θ, however, the magnitude of the resulting weights are typically very large, which is not a desired feature, because in practice, we need to limit the gain of the amplifiers since amplifiers with a high dynamic range have a much higher implementation cost associated with them [83]. It will be shown in the sparse design problem that the resulting weight sizes can be problematic by having large weight values. Array thinning using GA is also highly recommended for minimizing the maximum SLL, since it can achieve a target SLL and reduce the amount of elements within the array.

With the vast development in the area of compressive sensing and convex optimization, the problem of minimizing side lobe levels and the beamwidth of the antenna array expanded to designing sparse arrays using convex optimization based on Compressed Sensing (CS) theory as a sparse signal recovery problem. Sparse array design was no new problem at the time, since random techniques and array thinning were already in existence, where the first paper using genetic algorithms for array thinning was in 1994 [8]. It wasn't until around 2010, when we first see the sparse array design problem approached as an l_1 sparse recovery formulation [84, 85]. Since then, we have seen many variations and modifications made to the l_1-minimization problem for sparse array design. It has been shown that the sparse recovery problem was originally derived from an l_0 minimization, where

$$\begin{aligned} &\min \|\boldsymbol{w}\|_0 \\ &\text{subject to } \|\boldsymbol{F_d}(\theta) - \boldsymbol{F}(\theta)\|_2 \leq \epsilon \end{aligned} \tag{5.2}$$

where $\boldsymbol{F_d}$ is a vector that represents a desired radiation pattern and $\boldsymbol{F}(\theta)$ is the radiation pattern of the optimized array, and ϵ is an error constraint term. Here, $\|\cdot\|_0$, represents the l_0-norm, which is ultimately the cardinality (number of entries that are non-zero) of the vector $\boldsymbol{w}$. However, since the l_0-norm is non-convex, we can formulate Equation 5.2 as a convex one by using the l_1-norm as a convex relaxation

$$\begin{aligned} &\min \|\boldsymbol{w}\|_1 \\ &\text{subject to } \|\boldsymbol{F_d}(\theta) - \boldsymbol{F}(\theta)\|_2 \leq \epsilon \end{aligned} \tag{5.3}$$

The solution to Equation 5.3 will be a vector with very few large entries and many entries that are close to or are slightly larger than zero. Note that for this convex minimization problem, $\boldsymbol{w} \in \mathbb{R}^N$. Since the entries of $\boldsymbol{w}$ are real valued, we are essentially solving for an element taper that indicates if the array elements on an uniform grid are "on" or "off". The excitation values are compared to a threshold t, where the values that fall below the threshold are rounded to zero and the excitations that satisfy the threshold requirement are kept, indicating that the element is "on". Unfortunately, this approach has not been developed enough to where we can specify the amount of elements that we want to keep in the array, so the sparsity of the array depends on ϵ, where sparsity of the array increases when ϵ increases. However, there's been some modifications to the sparse recovery problem to increase array sparsity, such as by increasing the threshold, and by treating the threshold as a random variable, where a threshold is randomly generated for each excitation comparison case, as seen in [86].

This approach is extremely useful for when we're trying to cut down on design costs or if we have an application where we are limited with the number of antennas we can use because of factors such as antenna weight and physical space. An example would be [87],

which uses an phased antenna array for an unmanned aerial system (UAS). The drawback to using this approach all deal with the resulting element weights. For the problem formulated in Equation 2.1, it was mentioned that the excitations are rather large, which leads to a high dynamic range for the power amplifiers and increases design cost. Even if the total power of the sparse array is inferior to the original array, it's uncommon in practice to not limit the gain of the amplifiers. The other drawback is at the opposite end of the spectrum, where the sparse solution has maximum excitation values $< .1$, as shown in [83]. The issue with this is that with such low excitation amplitudes, we will significantly lower the directivity and signal to noise ratio (SNR) of our transmitted signal, which is an undesirable feature when the transmitting array is in environments with lots of generated noise and interference.

Since the previous optimization problem resulted in weights that were too large, this can often make things difficult for selecting a threshold to determine which elements are on or off. The range of the element weights can be significantly adjusted by adding in a convex constraint, as shown in the following. We consider a planar array which consists of N elements in the xy-plane with isotropic antenna, where the array factor in the uv-space can be found by

$$F(u,v) = \sum_{n=1}^{N} w_n e^{j\beta(x_n u + y_n v)} \tag{5.4}$$

Note that the uv-space is defined as $-1 \leq u, v \leq 1$ and $\sqrt{u^2+v^2} \leq 1$. Here, $\beta = 2\pi/\lambda$ and w_n is the weight excitation corresponding to the n^{th} element. In terms of θ and ϕ, the uv-coordinates are expressed as $u = \sin\theta\cos\phi$ and $v = \sin\theta\sin\phi$. Since this optimization is for a planar array, we need to extend the array manifold matrix from the 1D linear case to the 2D one, where the array manifold vector for a planar array with arbitrary element positions in the uv-space is given as

$$\boldsymbol{a}(u,v) = [e^{j\beta(x_1 u + y_1 v)}, \cdots, e^{j\beta(x_N u + y_N v)}] \tag{5.5}$$

where the array manifold matrix is then derived by taking P uniform samples in u and v, so the array manifold matrix $\mathbf{A} \in \mathbb{R}^{P \times N}$ has the following form

$$\mathbf{A} = \begin{bmatrix} e^{j\beta(x_1 u_1 + y_1 v_1)} & \dots & e^{j\beta(x_N u_1 + y_N v_1)} \\ \vdots & \ddots & \vdots \\ e^{j\beta(x_1 u_P + y_1 v_P)} & \dots & e^{j\beta(x_N u_P + y_N v_P)} \end{bmatrix} \tag{5.6}$$

The next step is to derive the desired pattern that we would like to match the sparse array to. The desired pattern is found from the uniform array case consisting of no removed elements and uniform excitation values. In order to find the desired pattern, we multiply the array manifold matrix by an excitation vector of ones $\mathbf{1} = [1, \cdots, 1]^\top \in \mathbb{R}^N$

$$\boldsymbol{F_d} = \mathbf{A}\mathbf{1} \tag{5.7}$$

which result in $\boldsymbol{F_d}$ having the following form

$$\boldsymbol{F_d} = [F_d(u_1, v_1), \cdots, F_d(u_P, v_P)]^\top \tag{5.8}$$

which is a diagonal slice of the 3D array factor for the uniform planar array case.

For the convex model, we would like to solve for a sparse weighting vector $\boldsymbol{w} \in \mathbb{R}^N$ to result in an array with fewer elements than the original uniform half wavelength spaced case. We also desire for the element excitations to be realistic and not enormously large, particularly less than or equal to unity i.e., $\|\boldsymbol{w}\|_\infty \leq 1$. We will also desire for the array to be highly sparse, so the resulting entries of the weighting vector will be compared to a threshold of $t = .95$, where weighting values below this threshold will be set to 0 and the element is to be removed from the array. Note that this problem formulation will be one of the models used later in this chapter, where the model will be applied to each of the varying aperture sizes.

$$\begin{aligned} &\min_{\boldsymbol{w}} \|\boldsymbol{w}\|_1 \\ &\text{subject to } \|\boldsymbol{F_d} - \mathbf{A}\boldsymbol{w}\|_2 \leq \epsilon,\ \|\boldsymbol{w}\|_\infty \leq 1 \end{aligned} \tag{5.9}$$

In the following figure, we see the effect of having the l_∞-norm constraint in the problem for a 10×10 planar array. When the constraint is not added, the weights can become very large values, where we have several weights close to a magnitude of 4. This is problematic because power amplifiers with higher dynamic range result in a higher implementation cost. Also, allowing for the amplifiers to operate at a high output level will result in a higher dissipation of heat, which would lead to undesired losses and damage to the array. The sacrifice for having the constraint is that we now have to keep more elements to come close to matching the desired radiation pattern, where Figure 5.1 (a) keeps 48 elements (less than half the elements) and Figure 5.1 (b) keeps 80 elements (four fifths of the elements).

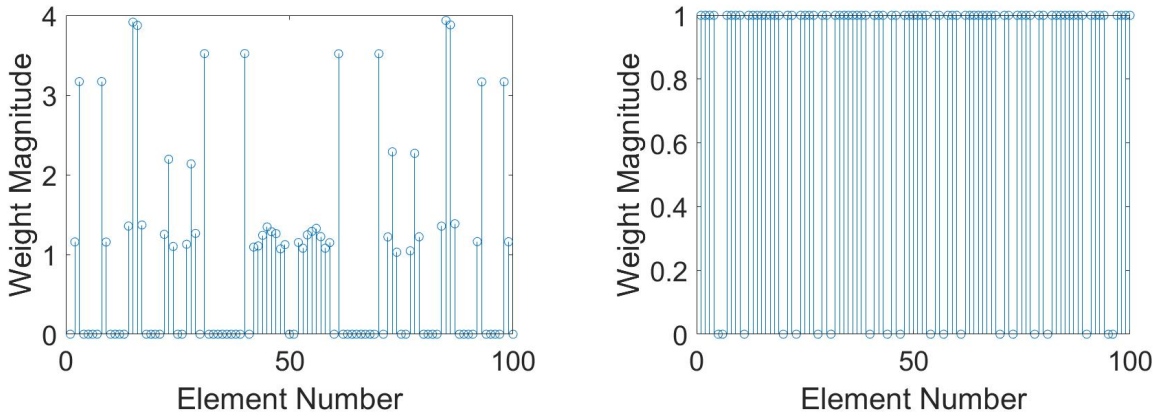

(a) (b)

Figure 5.1 Resulting element weights for a 10×10 planar array using an l_1 minimization (a) Weights when no l_∞-norm constraint is used. The weighting vector is sparser but this results in higher weighting values, (b) Weights when an l_∞-norm constraint is used. The weighting vector is not as sparse but the weighting values fall in a more desirable range

Note that when the l_∞ norm constraint is used, the array can be made sparser by increasing the value of ϵ. As we loosen the fitting error, we can expect for our weighting vector to become sparser. When we decrease the value of the fitting error, the problem will converge to the fully populated array case, so the solution to the convex optimization will be the weighting vector fully populated with ones.

5.2.1 Convex Models for Arbitrary Weighting Vectors

For the CS model that we presented, the weighting vector will ultimately result in a binary vector (vector of 0's and 1's) by the l_∞-norm constraint and the threshold t. Since this dissertation focuses on developing new methods and examining old methods for designing sparse antenna arrays, we believe it's necessary to mention two convex problem formulations that can be used to specify constraints relating to the side lobe level (SLL) and the directivity where the weighting vector is complex and non-binary and how they tie into this work.

The first convex model we will examine, is where the objective of the optimization is to implement sparsity with a constraint on the sidelobe level. The original problem to lower the SLL of an array was presented in Equation 5.1, where we're minimizing the maximum SLL with respect to a complex weighting vector $\boldsymbol{w} \in \mathbb{C}^N$. Note that the constraint in 5.1 is to ensure that the mainlobe is specified in a particular direction so that the solution doesn't result in $\boldsymbol{w} = 0$. It is noticed that originally in Equation 5.1, the problem is not formulated to implement a sparse constraint on the array. In order to enforce such a constraint, we need to first reformulate Equation 5.1 into the following linear programming problem

$$\begin{aligned} &\min_{\boldsymbol{w}} \ a \\ &\text{subject to } |\mathbf{A_s}\boldsymbol{w}| \leq a, \ \boldsymbol{a}_{\text{tar}}^{\top}\boldsymbol{w} = 1 \end{aligned} \tag{5.10}$$

where a is a positive scalar and is used to represent some maximum SLL constraint. We can then enforce sparsity by using an l_1-norm constraint in the objective function, where the resulting convex problem is

$$\begin{aligned} &\min_{\boldsymbol{w}} \ a + \alpha\|\boldsymbol{w}\|_1 \\ &\text{subject to } |\mathbf{A_s}\boldsymbol{w}| \leq a, \ \boldsymbol{a}_{\text{tar}}^{\top}\boldsymbol{w} = 1 \end{aligned} \tag{5.11}$$

where α is a positive scalar used to control the sparsity level of the array. This term can also be viewed as a knob which controls the trade-off between the sparsity of the array and the

SLL. This approach is useful when the targeted application calls for an array with low SLL and an array with few elements. Equation 5.11 can be improved upon when the application has a restricted power budget or if the dynamic range of the amplifiers is wanting to be kept to a minimum by implementing an l_∞-norm constraint to the weighting vector to ensure that the weights don't exceed a particular threshold value. Note that since this problem solves for a complex weighting vector instead of a real one, the array will need a feed network that has a phase shifter for each of the elements in the array, which will complicate the design process, where the proposed CS method in Equation 5.9 can use a commutator feed, which connects coax lines to each of the elements, ultimately being the least complicated feed network and inexpensive design as well.

The final convex formulation consists of Equation 5.9 with a directivity constraint. Directivity is a complex parameter to compute, where the original formulation of directivity in integral form for an antenna and antenna array for isotropic point sources is given in Chapters 2 and 4 respectively. The integral form not only takes a long time to compute but it also can't be formulated as a constraint for a convex optimization problem without first making some adjustments to the form that it's in, which consists of replacing the integral with vector matrix multiplications. There are many approximations that exist for directivity in matrix and vector form, however, many of them aren't as accurate as the integral computation, where the directivity approximations are relatively close to the integral form for uniform arrays but for arrays with non-uniform element spacing, the approximations can range from .5 to 2 dB off the actual value.

For an array with arbitrary geometry in the xy-plane, we can express the array factor in terms of θ and ϕ as

$$F(\theta,\phi) = \sum_{n=1}^{N} w_n^* e^{jk(x_n \sin\theta\cos\phi + y_n \sin\theta\sin\phi)} \tag{5.12}$$

We can then discretize the denominator of the directivity expression and write it as

$$Denominator \triangleq \frac{1}{4\pi}\int_0^{2\pi}\int_0^{\pi}|F(\theta,\phi)|^2\sin\theta d\theta d\phi \tag{5.13}$$
$$= \frac{1}{4\pi}\int_0^{2\pi}\int_0^{\pi}\sum_{n=1}^{N}\sum_{m=1}^{N}w_n^* w_m e^{jk\sin\theta[(x_n-x_m)\cos\phi+(y_n-y_m)\sin\phi]}\sin\theta d\theta d\phi$$

which can then simplify down to

$$Denominator = \sum_{n=1}^{N}\sum_{m=1}^{N}w_n^* w_m\int_0^{\pi}\frac{1}{2}\sin\theta d\theta\int_0^{2\pi}\frac{1}{2\pi}e^{jk\sin\theta(\Delta x_{nm}\cos\phi+\Delta y_{nm}\sin\phi)}d\phi \tag{5.14}$$

where Δx_{nm} is found by

$$\Delta x_{nm} \triangleq x_n - x_m \tag{5.15}$$

and Δy_{nm} is

$$\Delta y_{nm} \triangleq y_n - y_m \tag{5.16}$$

We then define two new variables ρ and ϕ_{nm}, which are expressed as

$$\rho_{nm} = \sqrt{(\Delta x_{nm})^2 + (\Delta y_{nm})^2} \tag{5.17}$$

and

$$\phi_{nm} = \arctan\left(\frac{\Delta y_{nm}}{\Delta x_{nm}}\right) \tag{5.18}$$

We can then write Δx_{nm} and Δy_{nm} as

$$\Delta x_{nm} = \rho_{nm}\cos\phi_{nm} \tag{5.19}$$

and

$$\Delta y_{nm} = \rho_{nm}\sin\phi_{nm} \tag{5.20}$$

Using the new expressions for Δx_{nm} and Δy_{nm}, we can plug them into the inner integral for Equation 5.14 which gives us

$$\begin{aligned}
&\int_0^{2\pi} \frac{1}{2\pi} e^{jk\rho_{nm}\sin\theta(\cos\phi\cos\phi_{nm}+\sin\phi\sin\phi_{nm})} d\phi \\
&= \int_0^{2\pi} \frac{1}{2\pi} e^{jk\rho_{nm}\sin\theta(\phi-\phi_{nm})} d\phi \\
&= J_0(k\rho_{nm}\sin\theta)
\end{aligned} \tag{5.21}$$

where $J_0(\cdot)$ is the Bessel function with an order of zero. When we insert the above equation into the rest of the integral for the denominator, we get

$$\begin{aligned}
Denominator &= \sum_{n=1}^{N}\sum_{m=1}^{N} w_n w_m^* \int_0^{\pi} \frac{1}{2}\sin\theta J_0(k\rho_{nm}\sin\theta) d\theta \\
&= \sum_{n=1}^{N}\sum_{m=1}^{N} w_n w_m^* \mathrm{sinc}(k\rho_{nm})
\end{aligned} \tag{5.22}$$

The above equation can be expressed as a matrix $\mathbf{B}$, where the nm^{th} entry of the matrix is given by

$$\mathbf{B}(n,m) = \mathrm{sinc}(k\rho_{nm}) \tag{5.23}$$

Since the numerator of the directivity equation is just $|F(\theta_0,\phi_0)|^2$, the numerator can be written as

$$Numerator = |\boldsymbol{w}^H \boldsymbol{v_0}|^2 \tag{5.24}$$

where $\boldsymbol{v_0}$ is the array manifold vector corresponding the the direction of the main beam $\boldsymbol{v}(\theta_0,\phi_0)$. We can finally express the approximation for directivity in matrix vector form as

$$D = \frac{|\boldsymbol{w}^H \boldsymbol{v_0}|^2}{\boldsymbol{w}^H \mathbf{B} \boldsymbol{w}} \tag{5.25}$$

Note that this approximation of directivity is from [1]. Since we can finally write directivity as a function of vectors and a matrix, we can formulate the following optimization problem

$$\begin{aligned} &\min_{\boldsymbol{w}} \|\boldsymbol{w}\|_1 \\ &\text{subject to } \|\boldsymbol{F_d} - \mathbf{A}\boldsymbol{w}\|_2 \leq \epsilon,\ \frac{|\boldsymbol{w}^H \boldsymbol{v_0}|^2}{\boldsymbol{w}^H \mathbf{B} \boldsymbol{w}} \geq \zeta \end{aligned} \tag{5.26}$$

which is the same as Equation 5.9 except that there is no bound on the weights and the directivity must be greater than some positive non-zero value ζ. The problem with this formulation is that the directivity constraint is non-convex so we would not be able to solve it with a convex optimization solver such as CVX. The way that we can transform Equation 5.26 into a convex problem is by minimizing the the denominator of Equation 5.25 since a smaller value of denominator would result in a higher value of directivity. By making this adjustment, Equation 5.26 can now be expressed as

$$\begin{aligned} &\min_{\boldsymbol{w}}\ \|\boldsymbol{w}\|_1 \\ &\text{subject to } \|\boldsymbol{F_d} - \mathbf{A}\boldsymbol{w}\|_2 \leq \epsilon,\ \boldsymbol{w}^H \mathbf{B} \boldsymbol{w} \leq \xi \end{aligned} \tag{5.27}$$

which is now a convex optimization problem and ξ is a positive non-zero scalar.

When it comes to using convex optimization to maximize the directivity of an antenna array under a sparse constraint, there are many difficulties encountered. The main problem is that the formulation for calculating directivity in matrix vector form is that the matrix vector form is not as accurate as the original integral form. Take for example, Figure 5.2. In this figure, we examined an array with an $8\lambda \times 8\lambda$ aperture that uses uniform sampling and another array that uses Hammersley sampling. The aperture size is fixed and the wavelength is slowly increased from $d = \lambda/2$ to $4\lambda/3$, where the array becomes sparser as the element spacing increases. For each element spacing instance, we calculate the directivity using the integral formulation and also the matrix formulation, as derived above. The importance of Figure 5.2 is that it shows the accuracy of the matrix formulation when $d \neq \lambda/2$ and

when non-uniform spacing is used. In the Figure, we see that the matrix formulation is very accurate when the array is uniformly spaced with a spacing of $d = \lambda/2$, but when the array using non-uniform spacing and spacing with $d \neq \lambda/2$, the matrix formulation is highly inaccurate.

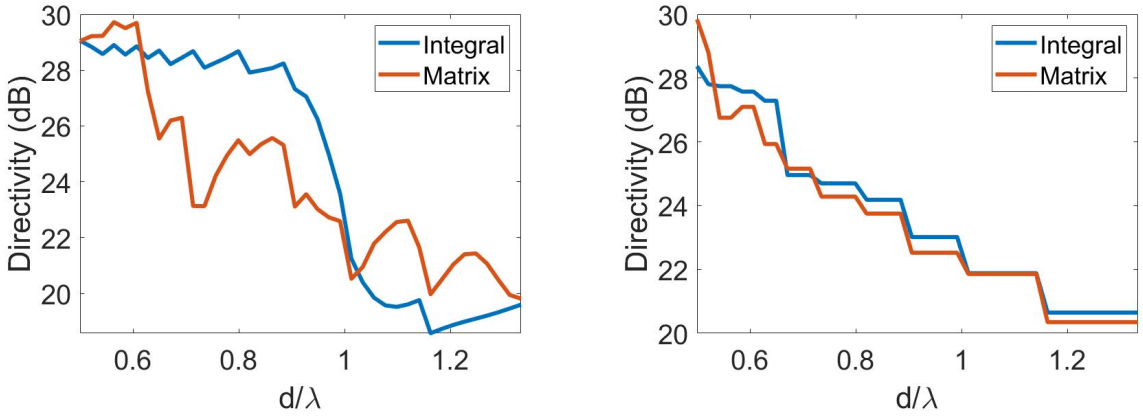

Figure 5.2 Comparison of the directivity calculation using integral and matrix form for an $8\lambda \times 8\lambda$ aperture. The integral form is the standard way to calculate directivity, but is computationally intense and slow to calculate. The matrix form can be used as a convex constraint and is quicker to compute, but it is not computationally accurate. However, the matrix formulation is equal to the integral instance when we use uniform spacing and $d = \lambda/2$ (a) Comparison of directivity calculations using the integral form and the matrix approximation when the array elements are uniform. We see a higher variance in the uniform case than when the elements are non-uniformly spaced, (b) Directivity comparison for the integral formulation and matrix formulation when Hammersley sampling is used. The matrix calculation is more accurate for the non-uniform case but it is still very inaccurate.

In order to show the inaccuracy of the matrix formulation for directivity, we examined another instance, where the aperture was larger, particularly for a $12\lambda \times 12\lambda$ aperture. The same process was followed, where the spacing of the array was slowly increased from $\lambda/2$ to $4\lambda/3$, ultimately decreasing the amount of elements within the aperture, where directivity was calculated at each instance. From Figure 5.3, we see some similar trends, where the calculations for a uniformly sampled aperture with $d = \lambda/2$ are the same for the integral and matrix formulations. However, the matrix form becomes highly inaccurate when d is

increased for the uniform spacing instance. For a Hammersley sampled array, the directivity calculation for the matrix formulation still deviates from the actual calculated value, but it not as inaccurate as the uniform sampled case.

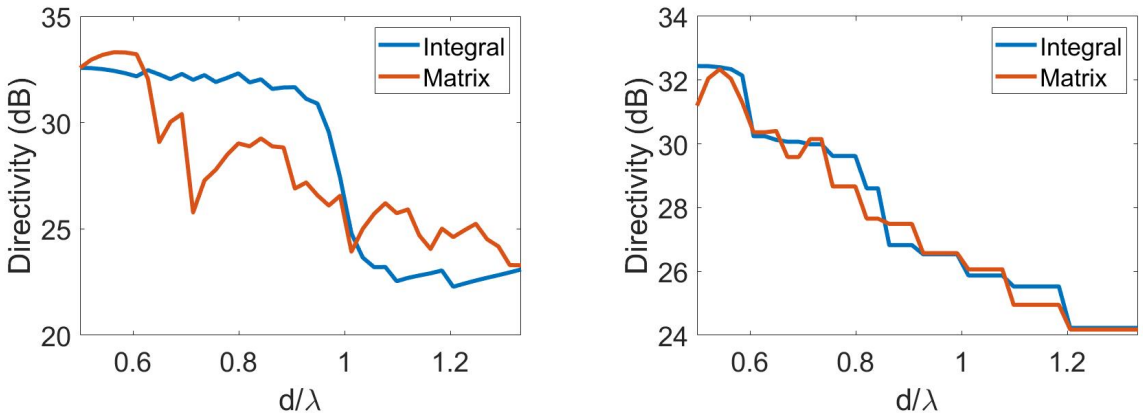

Figure 5.3 Comparison of the directivity calculation using integral and matrix form for a $12\lambda \times 12\lambda$. (a) Comparison of directivity calculations using the integral form and the matrix approximation when the array elements are uniformly spaced. Once again, we see a higher deviation from the actual value for the matrix case when uniform sampling is used, (b) Directivity comparison for the integral formulation and matrix formulation when Hammersley sampling is used. Calculations are still inaccurate but are more accurate than that of the uniform sampling case.

The other issue is that the formulation shown in Equation 5.26 is non-convex because of the formulation of directivity in the constraints. This means that we can't truly formulate directivity as a constraint, but can try to come close by either maximizing the numerator or minimizing the denominator. For our example we chose to minimize the denominator but in [88], the numerator is maximized. However, it's been shown in Figures 5.2 and 5.3, that the expression for directivity is not as accurate as the integral, so the problem formulation is inaccurate as well.

Asides from these two factors, the most important thing to point out is that with our CS formulation in Equation 5.9, the directivity is already accounted for since our weighting vector is being optimized to fit the resulting pattern to a desired pattern, which is the

fully populated array with $d = \lambda/2$ spacing. Since the aperture size is fixed, the maximum directivity for an array with $w_i \in [0, 1]$ will always be the fully populated array with half wavelength spacing, so the directivity constraint is actually a redundant term. However, when we remove the l_∞-norm constraint, the weight values will be become large so that they can satisfy the directivity criterion. Ultimately, directivity can be satisfied by using a reference pattern instead of using another constraint.

5.3 Thinning Methods for Sparse Arrays

Aside from convex optimization, one of the other methods that is commonly used for designing sparse antenna arrays are thinning methods. The concept of array thinning is quite simple, where a genetic algorithm (GA) or random generator is used to produce an amplitude taper of 0's and 1's, where a 0 corresponds to an element that is turned off and a 1 corresponds to an element that is kept in the array. The two methods we will discuss are random thinning and the algorithm used in [8], which is one of the most commonly cited and mentioned papers for array thinning.

5.3.1 Random Array Thinning for Sparse Arrays

For random array thinning, a uniform grid is generated for a fixed aperture, where the elements are spaced by $\lambda/2$. For the random thinning algorithm, we simply use a uniform random variable to select an element that we wish to discard from the grid. Unlike convex optimization, we are able to specify the amount of elements that we wish to discard, which makes it easier to design an array, just like the LDS methods mentioned in Chapters 3 and 4. Figure 5.4 shows the element distribution of random element array thinning and the corresponding radiation pattern of the array in the uv-space. The array thinning algorithm was applied to a $5\lambda \times 5\lambda$ aperture with $d = \lambda/2$ (100 elements). Out of the original 100 elements, 25% of them were discarded. As shown in Figure 5.4 (b), the trade off with random array thinning is SLL and number of elements. As we discard more elements from the array, we can expect for the SLL to rise. As we remove fewer elements from the array, the pattern

will converge to the original $d = \lambda/2$ uniformly sampled case.

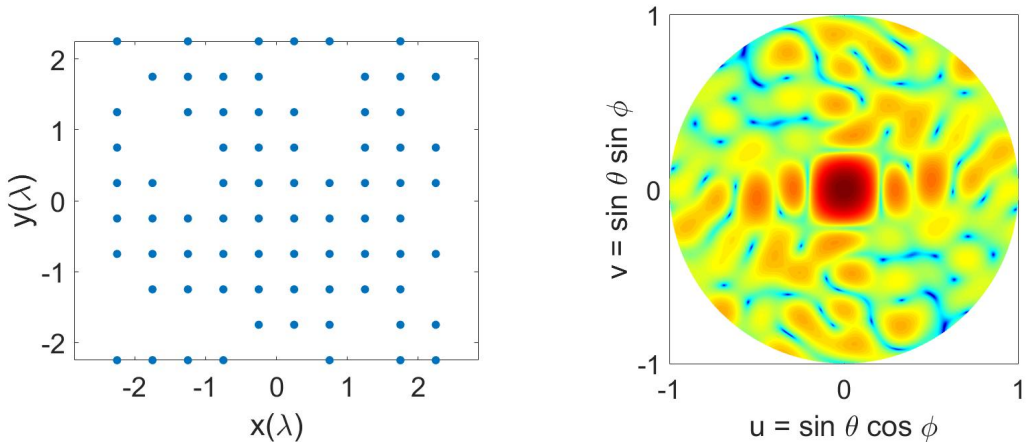

(a) (b)

Figure 5.4 Thinned antenna array using random element selection. The array thinning algorithm keeps .75% of the original elements (a) Element distribution across a $5\lambda \times 5\lambda$ aperture. The original array has the elements spaced by $d = \lambda/2$, (b) Corresponding radiation pattern in the uv-space.

5.3.2 Array Thinning Using GA for Sparse Arrays

For array thinning, the most common method used is the use of GA. Genetic algorithms differ from most existing optimization algorithms because GA works with a coding scheme for a set of parameters, instead of with the parameters themselves. GA also searches for a set of multiple points instead of just a single point and doesn't use any derivatives in the process. Random transition rules are also used instead of deterministic. Due to the nature and structure of GA, we will only examine two algorithms. The first algorithm applies to the concept of array thinning and takes a uniformly spaced array and removes elements from the array so that the SLL of the array can be minimized. The second algorithm we created emphasizes on optimizing the geometry of the elements within the array by maximizing the average minimum element spacing. The computational and run time of these GA are quite costly, where the run time of each of the scripts can range from a full day to three days until the algorithm converges. Since these methods can take days to run, we will not follow the

same procedure as we did for the rest of the methods in this chapter. The analysis procedure for each algorithm will be described in a later section in this chapter.

5.4 Sparse Planar Array Analysis (LDS)

For this section, we examine the pre-existing array thinning methods and the proposed CS formulation along with three of the LDS methods used in the previous chapter (Hammersley base 2, Halton (2,7), and Poisson disk sampling) for square apertures of various sizes. The array aperture sizes that we examine start at $4\lambda \times 4\lambda$ and increase by 4λ up to $24\lambda \times 24\lambda$ i.e. $\{4\lambda \times 4\lambda, 8\lambda \times 8\lambda, \cdots, 24\lambda \times 24\lambda\}$. For the first part of this analysis, we will examine the behavior of uniform sampling and the three LDS methods for all apertures, as we increase the element spacing from $\lambda/2$ to $4\lambda/3$. So as the element spacing increases, the sparsity level of the array increases as well. As we increase the element spacing, the two parameters that we will track are directivity and SLL, since these two parameters are highly used to characterize the performance of an antenna array. The purpose of this analysis is to examine for what sparsity levels, are the LDS methods superior to uniform sampling or when is uniform sampling more preferred than the LDS methods. This analysis will also help us to see when the pre-existing methods are/aren't better suited than the LDS methods and to see how they compare to uniform sampling.

Note that we can easily adjust the array thinning algorithm to compensate for the sparsity level of the array (program the algorithm so that it can remove the amount of elements for a given sparsity level) but we can not specify the amount of elements that we desire for the convex optimization models or for the array thinning methods that use GA. Since we aren't able to specify the amount of elements, we will run each algorithm for every aperture size and examine the statistics for the array that is produced, such as: sparsity level, directivity, and SLL. For the convex optimization methods, we will also examine three other cases, where we will solve the optimization problem in Equation 5.9 when we use different non-uniform grids. The original optimization problem implements sparsity on an array that uses uniform sampling and element spacing of $d = \lambda/2$, but for these other two models, we will use grids

that are produced by Hammersley ($b_1 = 2$), Halton ($b_1 = 2, b_2 = 7$), and Poisson disk samplings.

For the $4\lambda \times 4\lambda$ array case, a fully populated array with $d = \lambda/2$ results in an 8×8 array (64 elements). The maximum directivity of the array is when $d = \lambda/2$, where the directivity and SLL are 23.033 and -12.798 dB respectively. The directivity and SLL for when the element spacing is increased from $\lambda/2$ to $4\lambda/3$ is shown in Figure 5.5. From Figure 5.5, we make to observations. The first observation is that as the element spacing is increased from $.5\lambda$ to $.8\lambda$ (roughly about 40% of the original elements in the array remain), the directivity for the uniform sampling case barely deviates from the value for maximum directivity. The SLL also increases, but not by a large margin. In this range of element spacing, the directivity for the LDS methods start to drop more suddenly and the SLL begins to increase greatly as well, except for Poisson disk sampling. It's when $d = .9\lambda$ that we see a massive drop off in the directivity for uniform sampling and high increase in the SLL. When $d \geq \lambda$, the LDS methods out perform uniform sampling, which is due to the fact that grating lobes are produced in the pattern for uniform sampling, while the LDS methods tend to remove them. However, what we notice here compared to chapter 4, is that for a smaller aperture size, the SLL is much higher for the LDS methods than when the aperture size is large, where Poisson disk was the higher performing LDS methods for when $d \geq \lambda$.

For the $8\lambda \times 8\lambda$ case, the maximum directivity of the array is 29.054 dB and the maximum SLL is -13.149 dB. We see that compared to the smaller aperture ($4\lambda \times 4\lambda$), the directivity doesn't take a dive at $d = .8\lambda$ for the uniform sampling instance. Instead, it's around $d = .9\lambda$ when the directivity begins to significantly decrease and the SLL begins to steadily increase. Once again, at $d \geq \lambda$, the LDS methods outperform uniform sampling, primarily due to the grating lobe problem. So far from the two cases we've examined, LDS outperforms uniform sampling when we use $\leq 20\%$ of the remaining elements within the array. Another observation to point out is while all three LDS methods maintain about the same directivity for all variable d, Poisson disk sampling does the best at keep the SLL low, where Hammersley

and Halton allow for the SLL to rise when we have a high sparsity level.

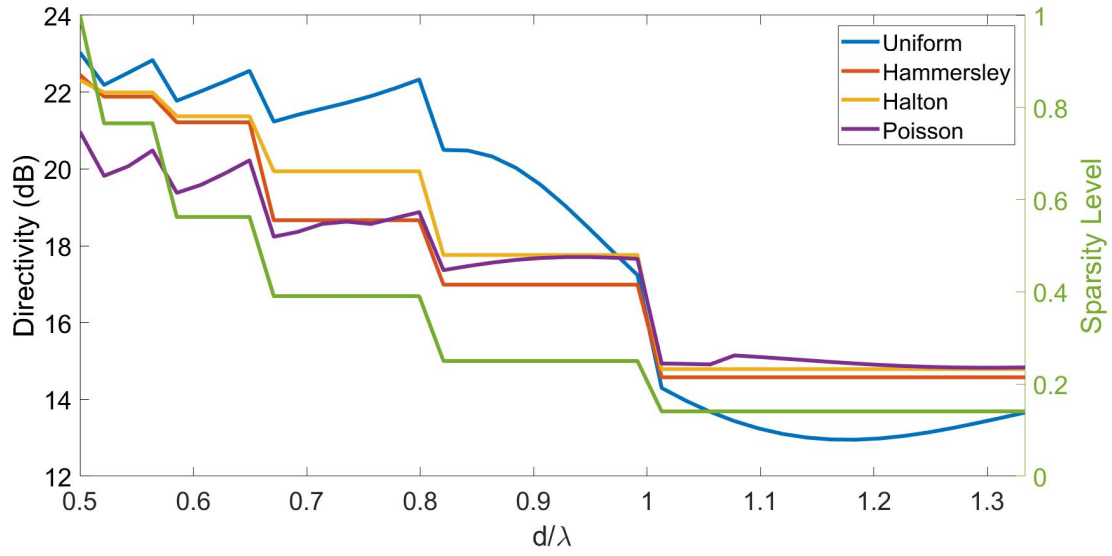

(a)

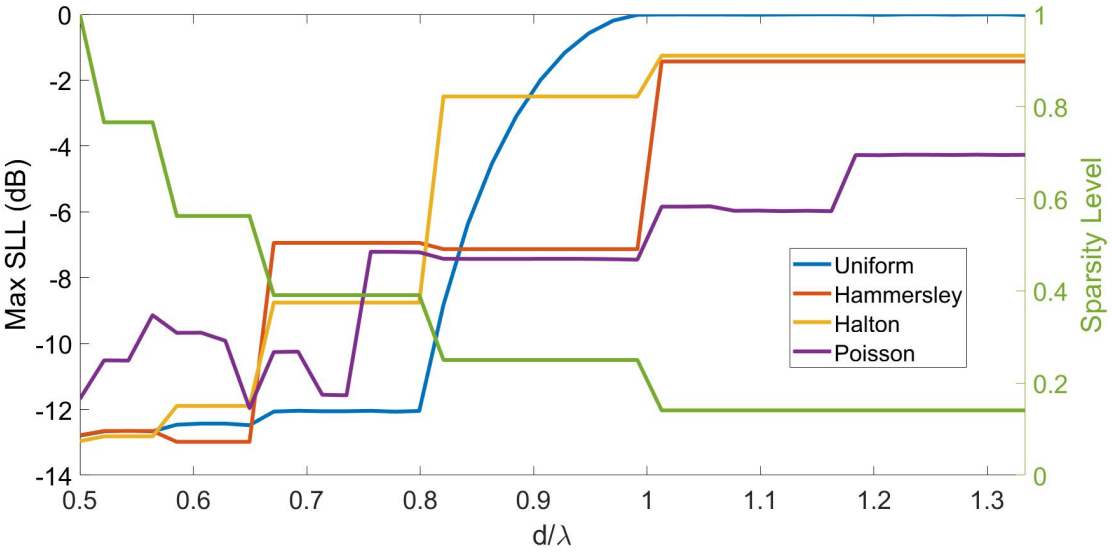

(b)

Figure 5.5 Resulting directivity and SLL for $4\lambda \times 4\lambda$ case when the element spacing is increased, which enhances the sparsity of the array. The sparsity level (green) shows the fraction of the original elements that remain in the array for each element spacing d (a) Directivity for the four array cases as the element spacing is increased (b) Tracked SLL for each array has sparsity within the array increases.

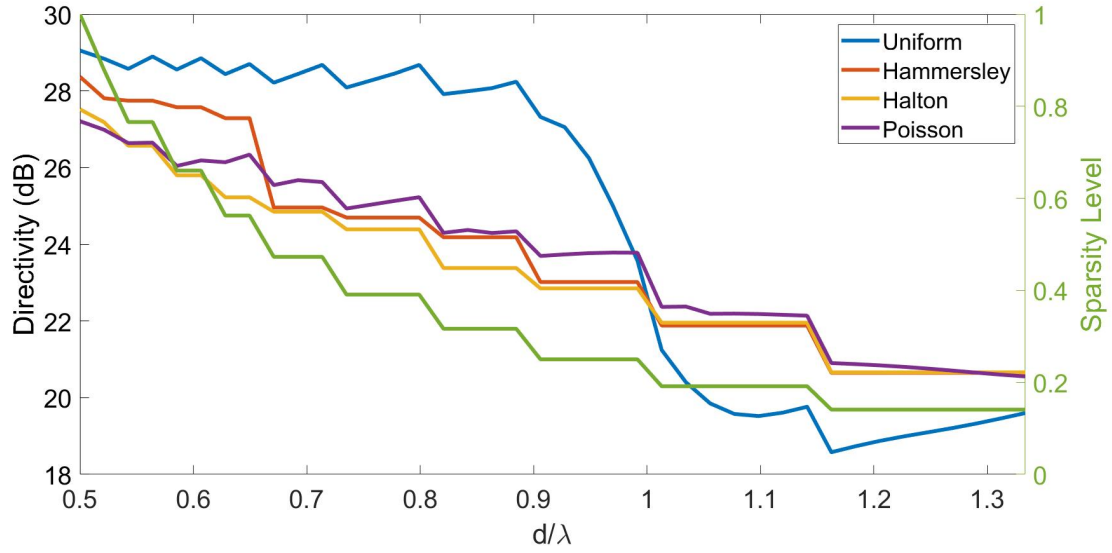

(a)

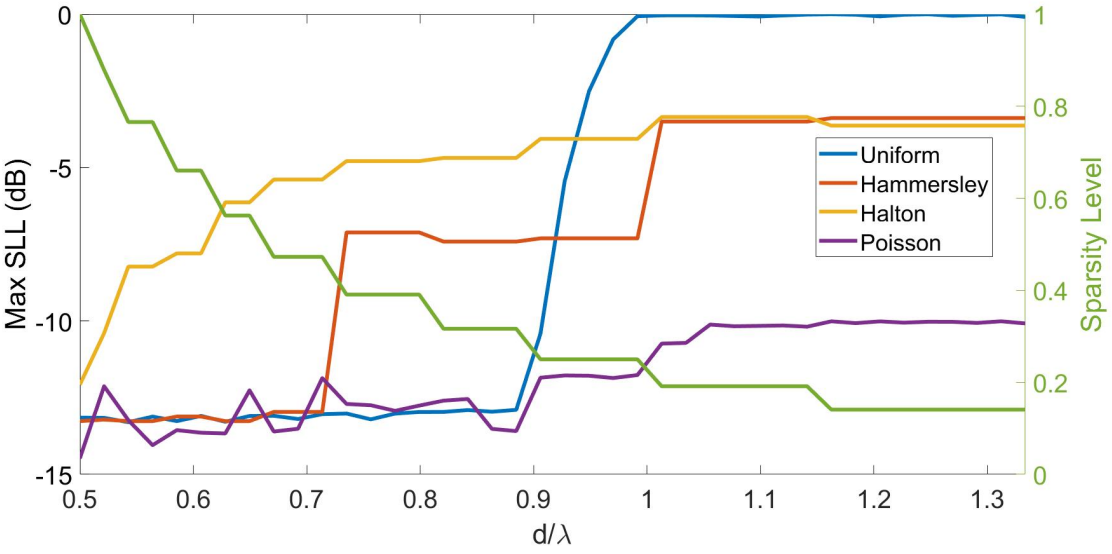

(b)

Figure 5.6 Resulting directivity and SLL for $8\lambda \times 8\lambda$ case when the element spacing is increased, which enhances the sparsity of the array. The sparsity level (green) shows the fraction of the original elements that remain in the array for each element spacing d (a) Directivity for the four array cases as the element spacing is increased (b) Tracked SLL for each array has sparsity within the array increases.

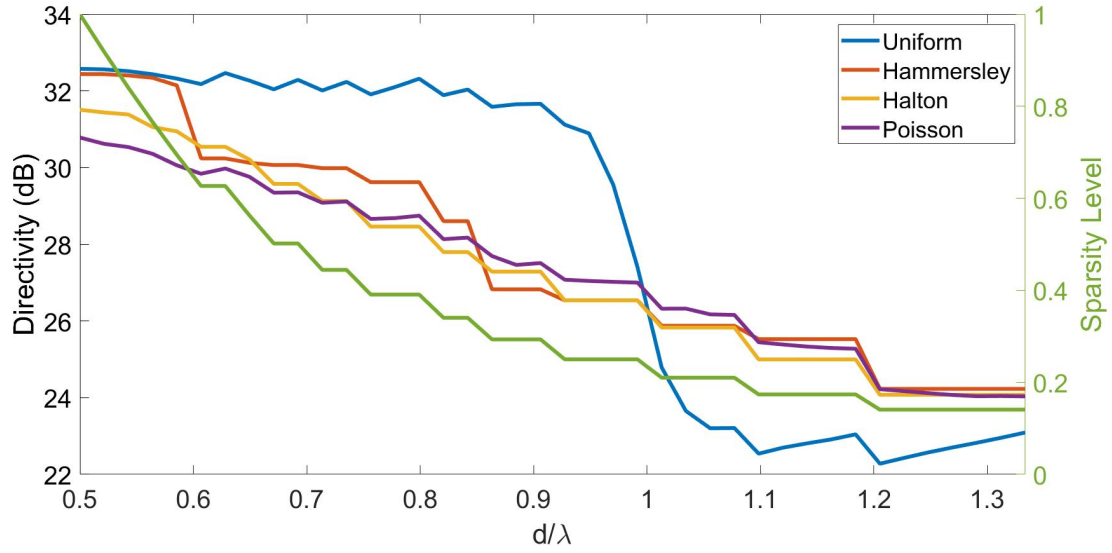

(a)

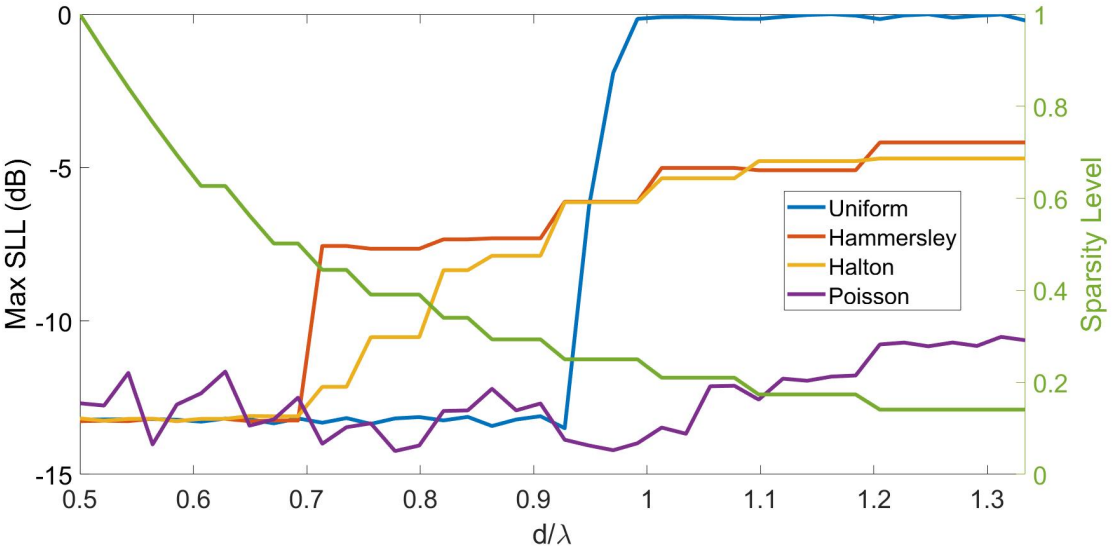

(b)

Figure 5.7 Resulting directivity and SLL for $12\lambda \times 12\lambda$ case when the element spacing is increased, which enhances the sparsity of the array. The sparsity level (green) shows the fraction of the original elements that remain in the array for each element spacing d (a) Directivity for the four array cases as the element spacing is increased (b) Tracked SLL for each array has sparsity within the array increases.

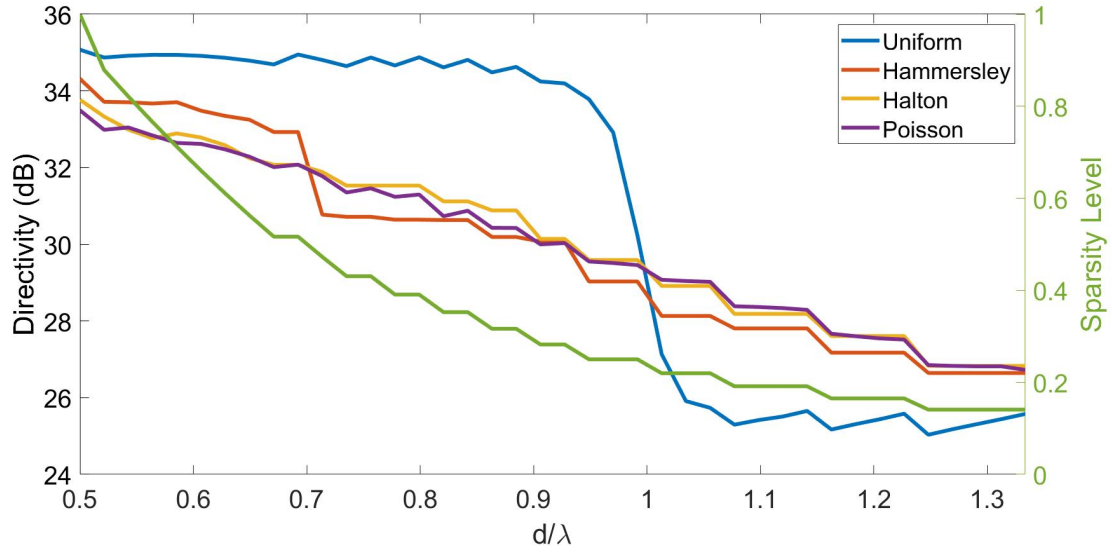

(a)

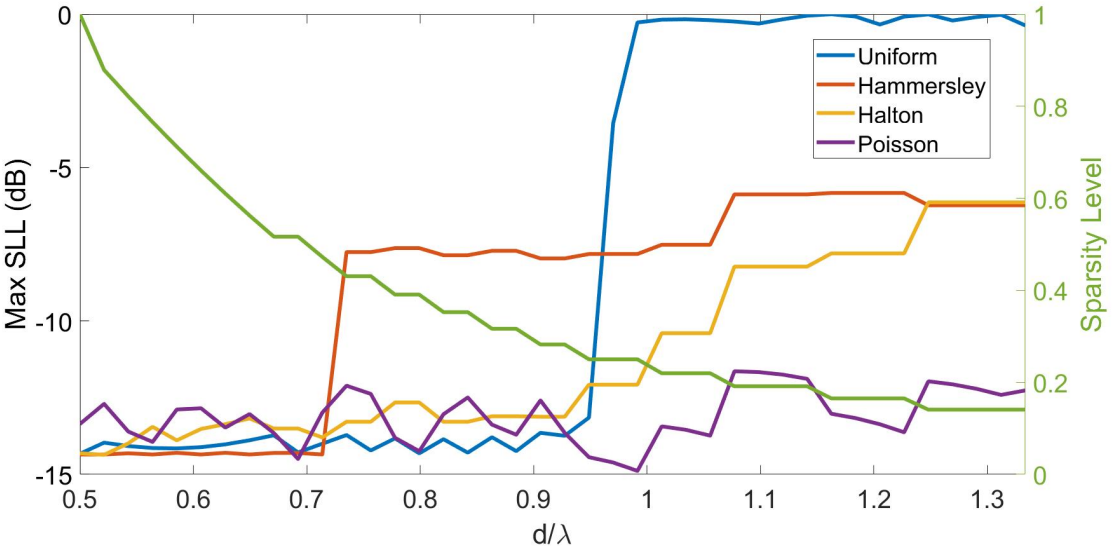

(b)

Figure 5.8 Resulting directivity and SLL for $16\lambda \times 16\lambda$ case when the element spacing is increased, which enhances the sparsity of the array. The sparsity level (green) shows the fraction of the original elements that remain in the array for each element spacing d (a) Directivity for the four array cases as the element spacing is increased (b) Tracked SLL for each array has sparsity within the array increases.

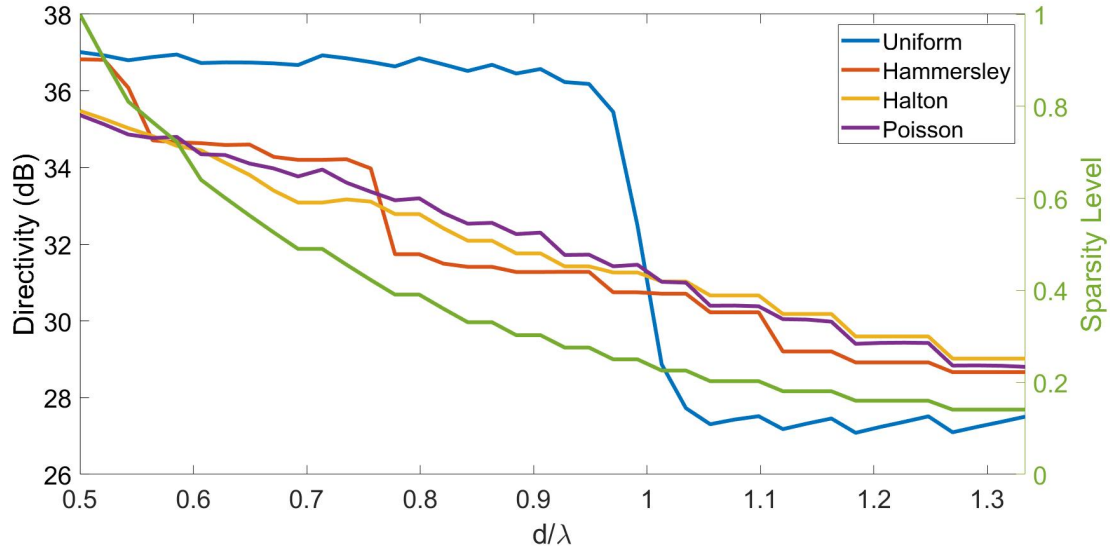

(a)

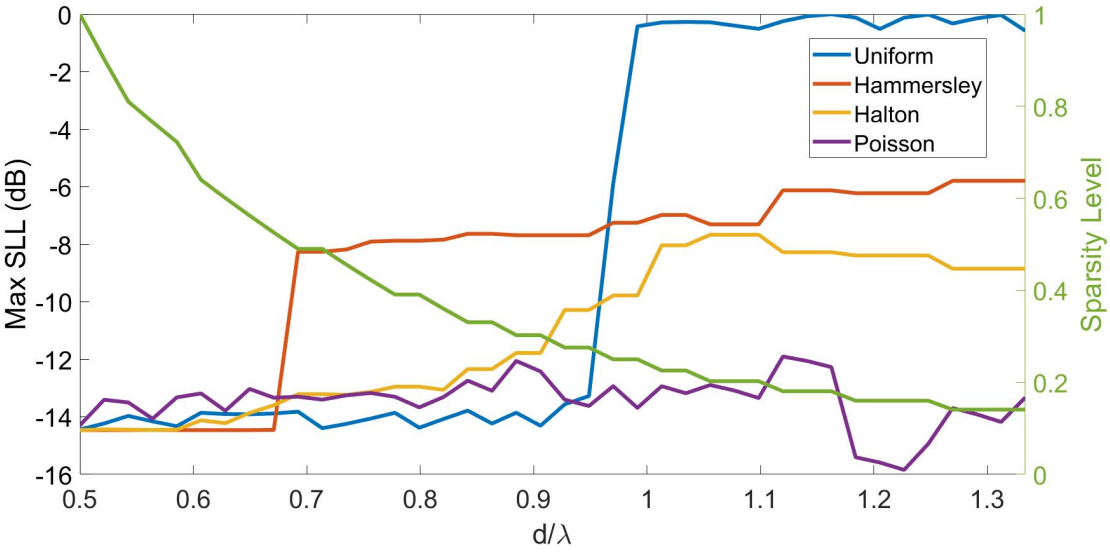

(b)

Figure 5.9 Resulting directivity and SLL for $20\lambda \times 20\lambda$ case when the element spacing is increased, which enhances the sparsity of the array. The sparsity level (green) shows the fraction of the original elements that remain in the array for each element spacing d (a) Directivity for the four array cases as the element spacing is increased (b) Tracked SLL for each array has sparsity within the array increases.

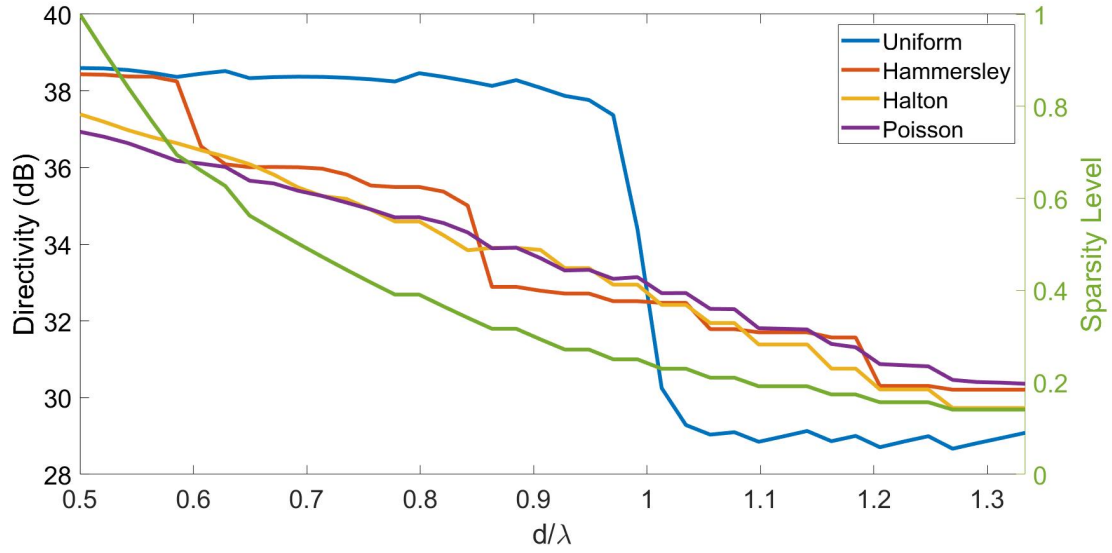

(a)

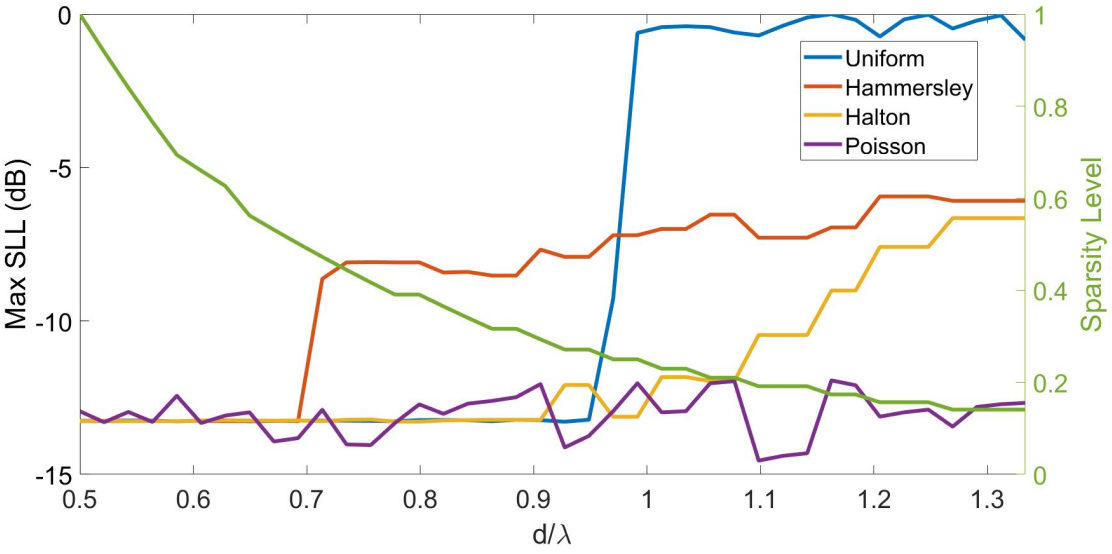

(b)

Figure 5.10 Resulting directivity and SLL for $24\lambda \times 24\lambda$ case when the element spacing is increased, which enhances the sparsity of the array. The sparsity level (green) shows the fraction of the original elements that remain in the array for each element spacing d (a) Directivity for the four array cases as the element spacing is increased (b) Tracked SLL for each array has sparsity within the array increases.

The next instance we examine is the $12\lambda \times 12\lambda$. The maximum directivity for this case is 32.576 dB with a corresponding SLL of -13.214 dB. What's important to point out with this larger aperture size is that Hammersley sampling almost has an identical performance to uniform sampling from $d = .5\lambda$ to $.6\lambda$, where the directivity and SLL are within close proximity to each other. This range of d accounts for when the array keeps between 60% and 100% of the original elements within the array. It's after $d \geq .6\lambda$ that the directivity for the Hammersley array begins to significantly decrease and the SLL begins to increase at a higher rate, particularly around $d = .7\lambda$. The trend of the directivity and SLL performance degrading for uniform sampling seems to be consistent for the $.9\lambda \leq d \leq \lambda$ range, however, as the aperture sizes increases, the interval sizes appears to decrease. Where the lower bound for the interval is now approximately $d = .92\lambda$. When $d \geq \lambda$, the LDS methods are far superior to uniform sampling, where the directivity values for each of the LDS methods are relatively the same, except that Poisson disk sampling is the only method to keep the SLL below -10 dB. Thus far, we can conclude that uniform sampling is the superior method for designing sparse arrays (uniform sampling with large element spacing) until we start to approach one wavelength. The directivity and SLL tend to remain around the original values of the $.5\lambda$ spacing instance, which accounts for when we remove approximately 80% of the elements in the array. It's when we remove more than 80% that we see the benefits of using the LDS techniques.

For the $16\lambda \times 16\lambda$ case, the maximum directivity is 35.075 dB and the corresponding SLL for this instance is -13.237 dB. With this larger aperture, we see that the trend of Hammersley sampling having similar performance to uniform sampling when the element spacing is relatively small is no longer true. Instead, the directivity for sampling is greater than that of Hammersley sampling by approximately .5 dB in this region. In the region of $.5\lambda \leq d \leq .7\lambda$, Hammersley sampling has a better performance than Halton and Poisson disk sampling, which has a maximum sparsity around .45. It's once we go past this limit that the performance of Hammersley sampling degrades significantly and Halton and Poisson

sampling begin to outperform it. Halton and Poisson disk sampling relatively perform about the same for the remaining values of d, except that Poisson disk sampling still keeps the SLL below -10 dB, which Halton sampling can not do. Once more, as the aperture size increases, the interval where the uniform sampling performance begins to degrade decreases. We see that it's around $d = .95\lambda$ when the directivity begins to drop off and the SLL begins to rise, which is still around when we keep 20% of the original elements in the array.

As we increase the aperture size to $20\lambda \times 20\lambda$, we see that the maximum directivity is 37.013 dB and the SLL is -13.247 dB. What we examine here is that the directivity performance of Hammersley sampling is approximately the same/better as Halton and Poisson disk sampling when $.5\lambda \leq d \leq .7\lambda$. As we increase past this point, the directivity for Hammersley sampling drops below that of Halton and Poisson disk sampling and the SLL shoots up from -14 dB to -8 dB. Halton sampling has a better directivity performance than Poisson disk sampling when $d \geq \lambda$ but the trade off is not by much, since the Halton directivity is only slightly better than the directivity for Poisson, and the SLL is much lower than that of Halton sampling. Halton sampling is able to reduce the SLL to about -10 dB for $d \geq \lambda$, but Poisson disk sampling keeps the SLL < -12 dB for the majority of that interval. When we look at uniform sampling, we see that the directivity and SLL are relatively constant up until we approach one wavelength. The only recognizable difference between this aperture size and the previous apertures, is that the LDS methods are starting to widen the gap between uniform sampling, where the directivity for LDS is much larger than that of uniform sampling when $d \geq \lambda$ and the SLL for the LDS techniques are starting to decrease as we increase the aperture size.

The final instance we will study is the $24\lambda \times 24\lambda$ aperture. The maximum directivity for this aperture size is 38.596 dB and a SLL of -13.253 dB. For this case, some notable differences from the previous array sizes is that the SLL for uniform sampling and Halton sampling are relatively the same until we start to approach one wavelength. The directivity and SLL performance for uniform sampling is unchanged until we reach close to λ, where

the shift in the performance degradation is much swifter than for the smaller aperture sizes. Hammersley also has the highest directivity out of the LDS techniques until we reach .85λ, where Halton and Poisson sampling then begin to takeover. Poisson disk sampling also keeps the SLL around the same initial value for the entire range of d, proving that it is one of the superior LDS methods for when $d \geq \lambda$.

After conducting the sparse array analysis for the LDS techniques, we can conclude that Halton and Poisson disk sampling are the two most successful LDS methods. When we are working with an element spacing from 0.5λ to about 0.7λ, we notice that Hammersley is preferable but once the element spacing increases beyond $d = 0.7\lambda$, the performance degrades rather quickly. This poor performance leaves us relying on the use of Halton and Poisson disk sampling for the higher sparsity levels but leaves us with the question, which sampling method is more preferable? In order to answer this question, we examine the directivity and SLL for Halton and Poisson disk sampling as we increase the aperture size from $5\lambda \times 5\lambda$ to $30\lambda \times 30\lambda$ for a fixed sparsity level, particularly when we have $d = \lambda$ and $d = 4/3\lambda$.

The results for the simulation are depicted in Figure 5.11. From these results, we can conclude that at the two sparsity levels both sampling methods have approximately the same directivity over all the simulated aperture sizes. For the lower sparsity level ($d = \lambda$), the directivity curves practically lie on top of one another, indicating that the difference in directivity is very minimal. The distinguishing factor between the two sampling techniques is the performance of the SLL. For this case, Halton sampling starts out with a SLL of -5 dB and the SLL decreases to -10 dB when the aperture area approaches $900\lambda^2$. When we examine Poisson disk sampling, the SLL starts out around -10 dB for the smallest aperture area and it decreases to -18 dB as we increase the aperture size. From the behavior of the curve, we can conclude that if we increase the aperture size beyond the region that we simulated, the SLL will eventually decrease to -20 dB or even lower since the curve is linearly decreasing at a fast rate.

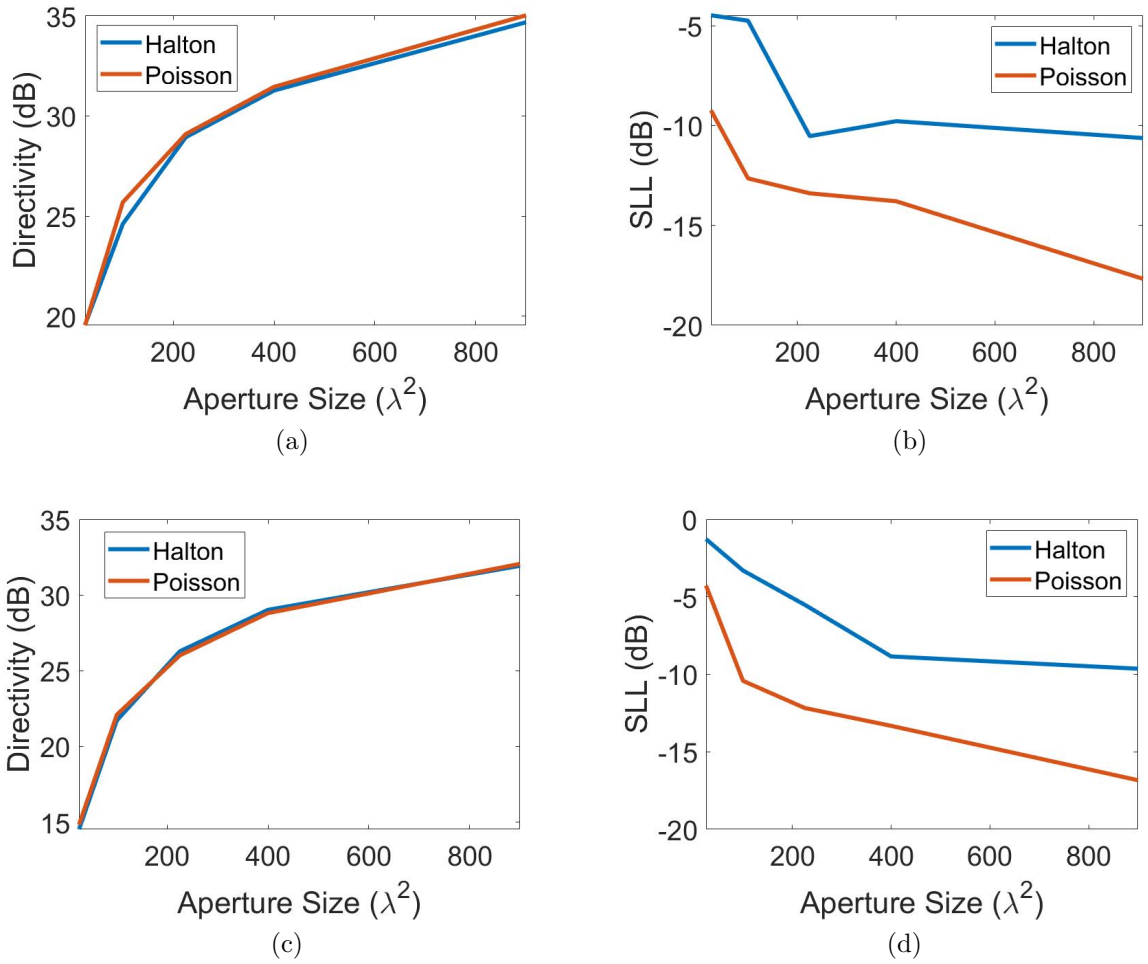

Figure 5.11 Resulting directivity and SLL for Halton and Poisson disk sampling at fixed sparsity levels when we increase the area of the square aperture (a) Directivity for Halton and Poisson disk sampling when we have an element spacing of $d = \lambda$ (b) SLL for the two sampling methods when the element spacing is $d = \lambda$ (c) Directivity for Halton and Poisson disk sampling when we have an element spacing of $d = 4/3\lambda$ (b) SLL for Halton and Poisson disk sampling when the element spacing is $d = 4/3\lambda$.

When the element spacing is increased to $d = 4/3\lambda$, the directivity curves have even less separation than the $d = \lambda$ case, indicating that there is no trade off between between the two sampling techniques in terms of directivity. However, the SLL continues to indicate that the Poisson disk method is the optimal method at lowering the SLL, when compared to Halton sampling. For the smallest aperture size, Halton sampling starts off close to 0 dB, and then rapidly declines until we reach an aperture size of $400\lambda^2$. After we reach $400\lambda^2$, we see that the SLL is not able to be lowered much more as we continue to increase the aperture size, where the SLL caps off at approximately -9.5 dB. For Poisson disk sampling, the SLL starts off at -5 dB when the aperture size is the smallest and quickly decreases to -10 dB at the $100\lambda^2$ point. From this mark forward, the rate at which the SLL decreases is much slower than before, but we still see that if we were to continue to increase the aperture size, we could possibly lower the SLL to -20 dB or less. The difference between the $d = \lambda$ and the $d = 4/3\lambda$ case is that we would require a larger aperture size to reach a SLL of -20 dB for when $d = 4/3\lambda$.

From these results, we can conclude that when we reach a sparsity level of $d \geq \lambda$, there is no trade off with the directivity because Halton and Poisson sampling approximately have the same values of directivity for various aperture sizes. However, when we examine the SLL, Poisson sampling results in a much lower SLL and indicates that we can continue to lower the SLL unlike Halton sampling, where the SLL converges to about -10 dB.

5.4.1 Sparse Planar Array Analysis (Random Array Thinning)

Since we can specify the amount of elements to remove for the random array thinning algorithm, we will follow the same procedure as above, where we will increase the element spacing and slowly remove elements from the aperture. The array to be thinned will be the uniform sampled aperture, where $d = \lambda/2$. Once again, we will track the directivity and SLL of the resulting array, where from the previous section, we can compare the performance of the algorithm to the LDS techniques and uniform sampling.

For the $4\lambda \times 4\lambda$ case, shown in Figure 5.12, we notice similar behavior when compared to the LDS methods for small aperture sizes. What we notice is that the SLL has an incredibly poor performance, especially as we increase the element spacing over a wavelength, where the SLL is < -5 dB. Since this algorithm randomly selects the elements to discard at random, we can expect for the SLL to constantly vary throughout the entire range of d. The directivity also follows a similar trend to that of the LDS for this aperture size as well, where the maximum directivity is equal to that of the fully populated array case (since no elements are removed when $d = \lambda/2$) and decreases to around 14 dB, when $d \geq \lambda$, which is around the same value that the directivity drops to for the LDS methods. From these results, we can conclude that the performance of the array thinning algorithm is no different than the LDS methods for this aperture size, where all methods struggled to reduce the SLL to a reasonable level for this small aperture size.

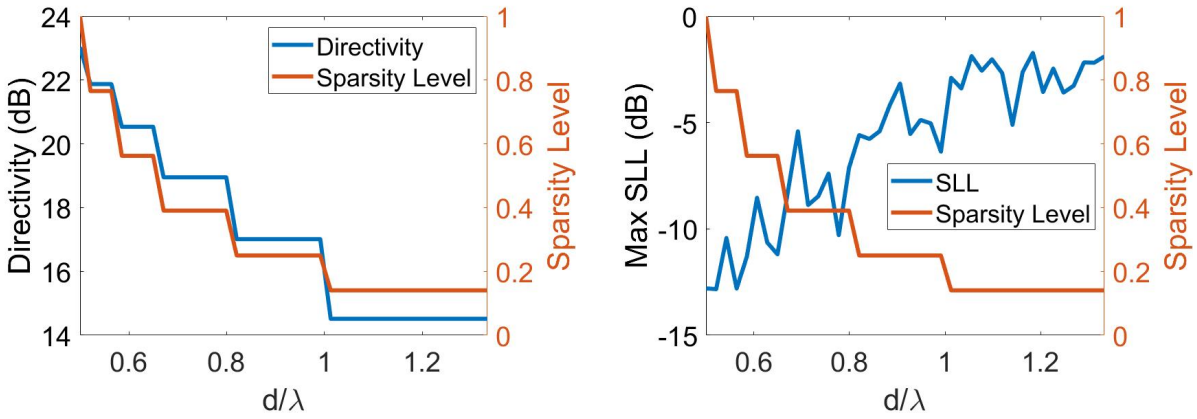

Figure 5.12 Resulting directivity and SLL for $4\lambda \times 4\lambda$ using the array thinning algorithm. The algorithm calculates the amount of elements to remove for an element spacing d. The sparsity level (orange) shows the fraction of the original elements that remain in the array for each element spacing instance (a) Directivity of the thinned array using the random thinning algorithm (b) Tracked SLL for the thinned array.

The results for the $8\lambda \times 8\lambda$ case shown in Figure 5.13. The main difference we see here between the LDS methods and the random array thinning algorithm is that Hammersley

and Halton sampling fail to get the SLL below -5 dB for $d \geq \lambda$. For the random thinning algorithm, the SLL is strictly kept below -6 dB for the entirety of this region. The random thinning algorithm is also able to keep the SLL below or around -10 dB for when $-.5\lambda \leq d \leq \lambda$, which neither Hammersley or Halton sampling can achieve. The only methods that succeeds at keeping the SLL below -10 dB for the entire range of d is Poisson disk sampling, which was very successful at keeping a constant SLL. Once more, the random array thinning algorithm had similar performance to the rest of the LDS methods, where there was nothing notable to distinguish its directivity performance from the other three methods.

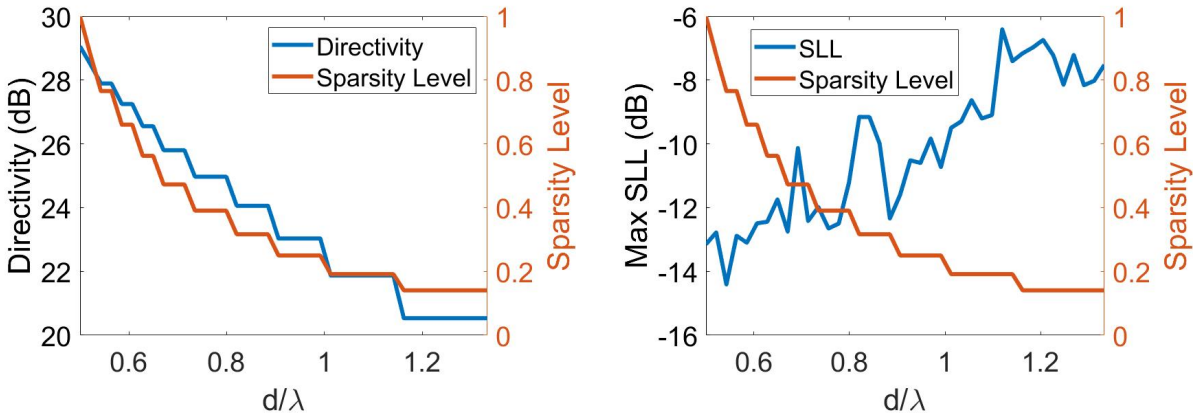

Figure 5.13 Resulting directivity and SLL for $8\lambda \times 8\lambda$ using the array thinning algorithm. The algorithm calculates the amount of elements to remove for an element spacing d. The sparsity level (orange) shows the fraction of the original elements that remain in the array for each element spacing instance (a) Directivity of the thinned array using the random thinning algorithm (b) Tracked SLL for the thinned array.

In the $12\lambda \times 12\lambda$ case, shown in Figure 5.14, we notice that the directivity for the random array thinning algorithm degrades a fast rate until it reaches $d = .6\lambda$. It was for this aperture size that Hammersley sampling performed nearly identical to the uniform sampling, until $d = .6\lambda$. What we can also point out is that the three LDS methods outperform the random array thinning algorithm up until the element spacing is increased to a wavelength. It's when we increase the element spacing beyond a wavelength that the thinning algorithm has

a similar directivity performance to the LDS methods. For the SLL, Halton and Hammersley finally bring the maximum SLL to -5 dB, while the random thinning algorithm reduces the maximum SLL to approximately -8 dB, which is about a 2 dB decrease from the previous aperture case. However, Poisson disk sampling is still proven to be the superior method at reducing the SLL, where the maximum SLL is kept below -10 dB.

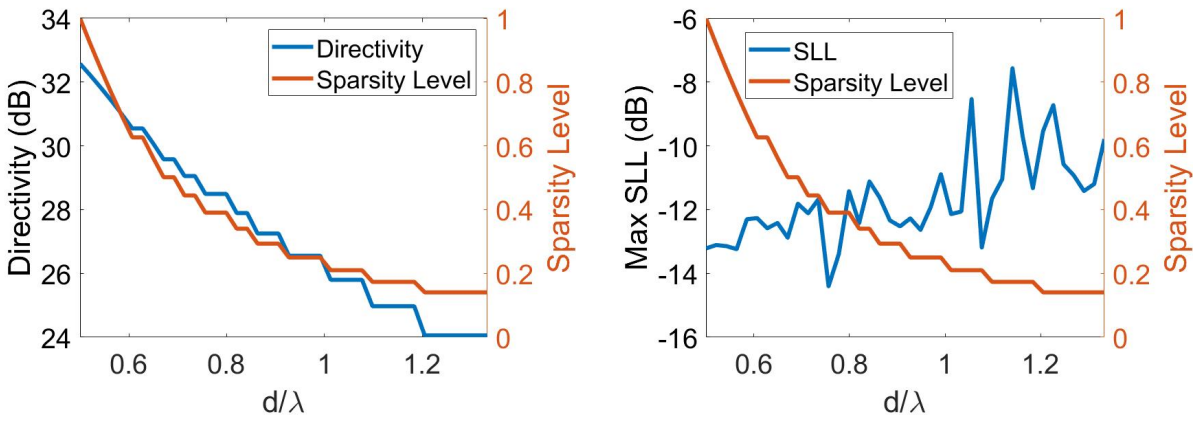

Figure 5.14 Resulting directivity and SLL for $12\lambda \times 12\lambda$ using the array thinning algorithm. The algorithm calculates the amount of elements to remove for an element spacing d. The sparsity level (orange) shows the fraction of the original elements that remain in the array for each element spacing instance (a) Directivity of the thinned array using the random thinning algorithm (b) Tracked SLL for the thinned array.

For the $16\lambda \times 16\lambda$ case, shown in Figure 5.15, the directivity performance of the random array thinning algorithm begins to decrease at higher rate until $d = .7\lambda$. After this benchmark, the directivity still decreases at a fast pace but not as rapidly as before. It isn't until $d \geq \lambda$ that the directivity for the random array thinning algorithm comes within close proximity of the LDS methods, however, the LDS methods have slowly started to widen the gap between the array thinning algorithm. In terms of the SLL performance, the array thinning algorithm keeps the SLL below -10 dB for over the entire interval. Up until one wavelength, the SLL is kept below -12 dB but its when we reach the 20% sparsity level that we see an increase in the SLL. Up until this point, we see that the random array thinning

algorithm may not be the best method for optimizing directivity but is fairly successful at keeping the SLL at a low value, which only Poisson disk sampling has been able to do until this point. It's also at higher element spacing values that the directivity performance for Poisson disk sampling begins to overtake Hammersley and Halton sampling, proven to be a much superior method for higher values of sparsity.

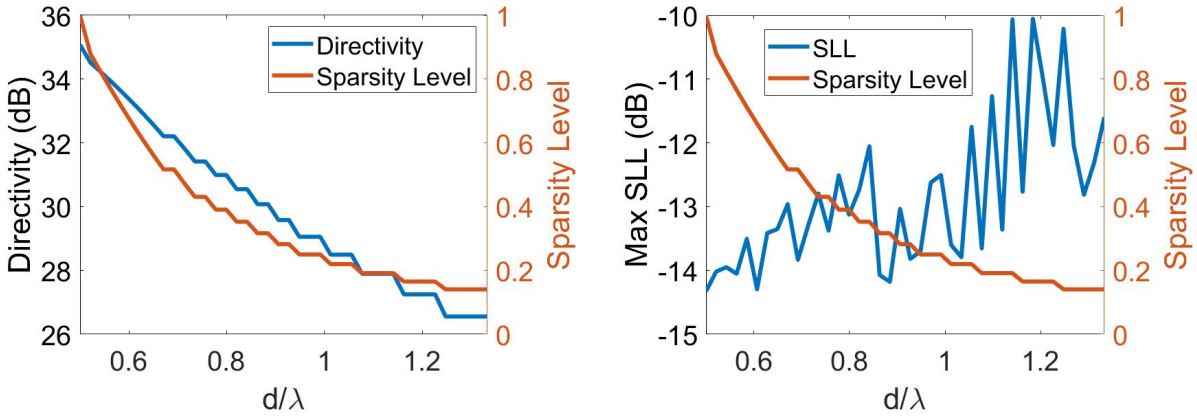

Figure 5.15 Resulting directivity and SLL for $16\lambda \times 16\lambda$ using the array thinning algorithm. The algorithm calculates the amount of elements to remove for an element spacing d. The sparsity level (orange) shows the fraction of the original elements that remain in the array for each element spacing instance (a) Directivity of the thinned array using the random thinning algorithm (b) Tracked SLL for the thinned array.

In Figure 5.16 for the $20\lambda \times 20\lambda$ case, we see that the trend of fast directivity decay remains consistent for the random array thinning algorithm, where this decay begins to slow down around $d = .7\lambda$. It's for this aperture size that we see that despite a large initial drop off, the directivity performance for the array thinning algorithm has caught up to the likes of the LDS methods. We notice this especially for when $d \geq \lambda$. The array thinning algorithm also is able to decrease the SLL even further, where the maximum SLL is approximately -12 dB and the average SLL is kept below -13 dB. Meanwhile, Hammersley and Halton sampling are only now able to maintain a SLL below -6 dB. Poisson disk sampling is still the superior method at maintaining a low SLL, where the average SLL for Poisson disk

sampling is approximately −14 dB. Once more, we can conclude that the random array thinning algorithm is a method that should be used when trying to suppress the SLL and the directivity is close to that of the LDS methods, particularly when the element spacing is large.

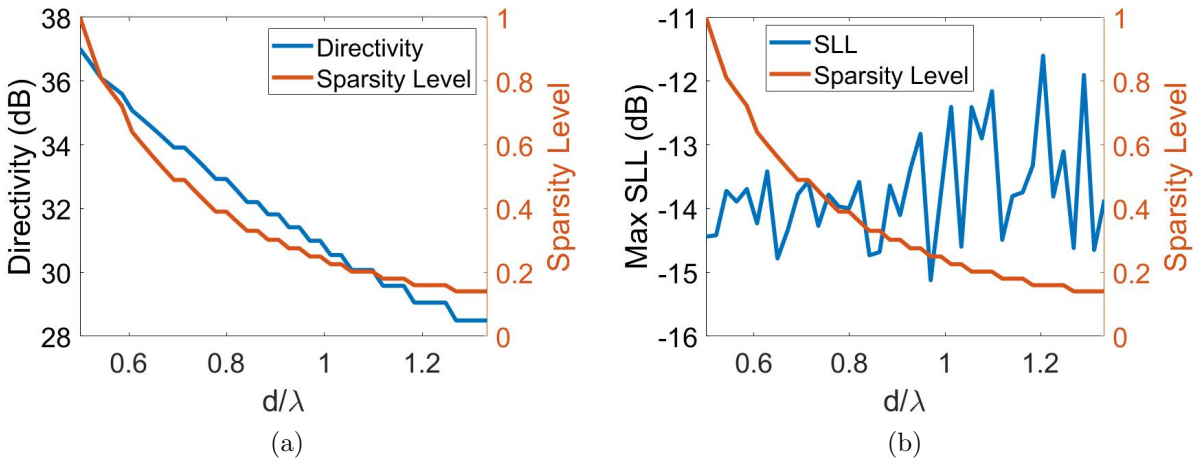

(a) (b)

Figure 5.16 Resulting directivity and SLL for $20\lambda \times 20\lambda$ using the array thinning algorithm. The algorithm calculates the amount of elements to remove for an element spacing d. The sparsity level (orange) shows the fraction of the original elements that remain in the array for each element spacing instance (a) Directivity of the thinned array using the random thinning algorithm (b) Tracked SLL for the thinned array.

Finally, for the $24\lambda \times 20\lambda$ case, shown in Figure 5.17, we notice a similar trend as in the $24\lambda \times 24\lambda$ case for the LDS techniques, where the SLL increases. The SLL for the LDS techniques slightly increased from the previous case, where the SLL for Hammersley went from −6 dB to −5 dB and the SLL for Halton sampling increased from −10 dB to −7 dB. Note that these values are the maximum SLL for when $d \geq \lambda$. When we examine Poisson disk sampling, we notice that the SLL is maintained around the same value as the $20\lambda \times 20\lambda$ case, with a slight more variation in the SLL measurements. The maximum SLL for the random array thinning algorithm increases from −12 dB to −11 dB and the average SLL in the range of $.5\lambda \leq d \leq .8\lambda$ increased to −12.5 dB. Lastly, the directivity for the random array thinning algorithm follows a similar trend to the directivity measurements in the previous

aperture cases, where the LDS methods have higher performance measurements for when $d \geq \lambda$.

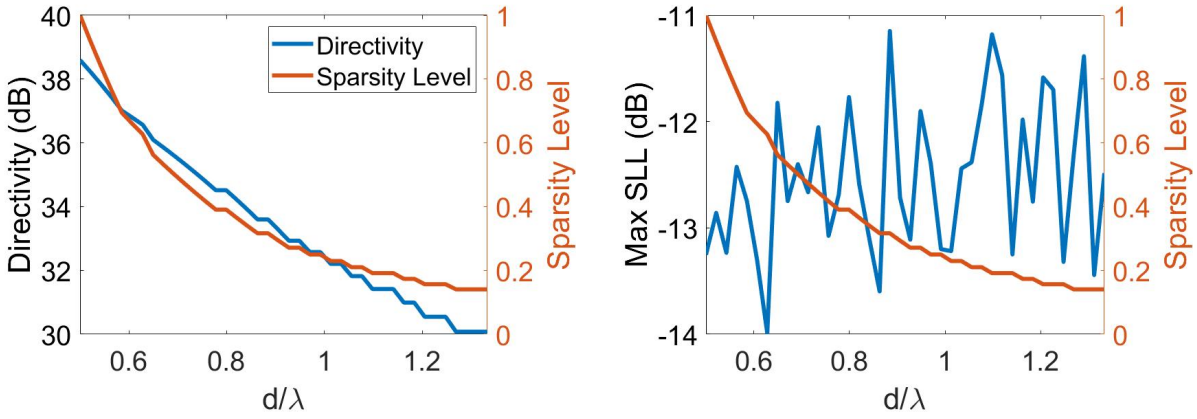

Figure 5.17 Resulting directivity and SLL for $24\lambda \times 24\lambda$ using the array thinning algorithm. The algorithm calculates the amount of elements to remove for an element spacing d. The sparsity level (orange) shows the fraction of the original elements that remain in the array for each element spacing instance (a) Directivity of the thinned array using the random thinning algorithm (b) Tracked SLL for the thinned array.

After conducting the analysis for the random array thinning algorithm, we can conclude that algorithm is successful at minimizing the SLL, similar to that of Poisson disk sampling. We see lots of fluctuations and occasionally large sporadic changes in the SLL measurements, which is primarily due to the fact that the algorithm is randomly selecting the elements to discard and isn't selecting them in an organized fashion (like how Hammersley and Halton sampling places the elements within the aperture). For the most part, we see that as the aperture size increases, the SLL lowers except when we reach the $24\lambda \times 24\lambda$ aperture, which results in a slight increase but this trend is also consistent with the LDS methods as well. When the array has a lower sparsity level, we see that the SLL is the lowest, but as we start to increase sparsity within the array, the SLL begins to slowly increase. Overall, Poisson disk sampling is the superior method that lowers the SLL, especially for higher sparsity levels. The random array thinning algorithm would then be the second best at lowering the SLL,

where Hammersley and Halton sampling then follow.

When we examine the directivity performance of the random array thinning algorithm, we see that the resulting directivity decays quite fast, when the element spacing is small, particularly when $.5\lambda \leq d \leq .7\lambda$. Hammersley sampling tends to result in a higher directivity than the random array thinning algorithm for this region, but then all methods approach similar values until we reach one full wavelength. It's when we increase the element spacing above a wavelength that we see the LDS methods outperforming the random array thinning algorithm. Particularly, Poisson disk sampling is far superior to this method in this region, since it has higher directivity and can sustain the SLL at lower values. We will also see in the next section, that the convex models outperform this method for the $4\lambda \times 4\lambda$ aperture at their given sparsity levels, but as we increase the area of the aperture, the directivity performance for the random array thinning method surpasses the convex models. The random method also is able to lower the SLL more than the convex models for larger apertures, even for the $24\lambda \times 24\lambda$ instance, which was the case when the SLL increased.

5.4.2 Sparse Planar Array Analysis (Convex Optimization)

For the convex optimization analysis, we solve Equation 5.9 for each of the aperture size cases. Since we can not specify the amount of elements to remove from the array, we compute the resulting sparsity level that is produced by solving the convex optimization problem. For the convex formulation, the l_1-minimization removes elements from a fully populated grid ($d = \lambda/2$), such as for the uniform grid on the $4\lambda \times 4\lambda$ case, we see that we will have an 8×8 square uniform aperture. Since the optimization removes the elements by optimizing the weighting vector, we will use a threshold of $t = .95$ to declare that any weight that falls $< t$ to "0", which turns off the element. For this, analysis, we will solve Equation 5.9 with four different grids, which consist of: uniform, Hammersley ($b_1 = 2$), Halton ($b_1 = 2, b_2 = 7$), and a grid generated by Poisson disk samples. For the convex analysis, we track the directivity, SLL, and sparsity level over the aperture area ($4\lambda \times 4\lambda = 16\lambda^2$), where we start the analysis from $16\lambda^2$ and end at $576\lambda^2$.

For the smallest aperture size case ($4\lambda \times 4\lambda$), the solution to the convex optimization results in a sparsity level of .563, which corresponds to a directivity less than that for Hammersley and Halton sampling for this particular sparsity level, as shown in Figure 5.18. However the convex optimization method did out perform Poisson disk sampling at this particular sparsity level. When we look at the SLL for this aperture size, we see that the convex method performed poorly compared to the LDS methods, where the resulting SLL for all the LDS methods were kept below -10 dB and the SLL for the convex method was -8.132 dB. What we notice as we increase the aperture size is that the solution to the optimization problem becomes less sparse, where the solution for the smallest aperture size has a sparsity of .563 and the sparsity of the final array size is .936. So the method starts out by removing around 50% of the original elements and keeps 93.6% of them in the final aperture case. What we tend to notice is that once we get to an aperture size above $150\lambda^2$, the SLL for the convex model with a uniform grid becomes relatively stable and stays around -13 dB. Also, as we compare the resulting directivity to the LDS methods, we see that Hammersley and the convex model with a uniform grid perform relatively the same at each sparsity level, where the only method to surpass each of them is uniform sampling.

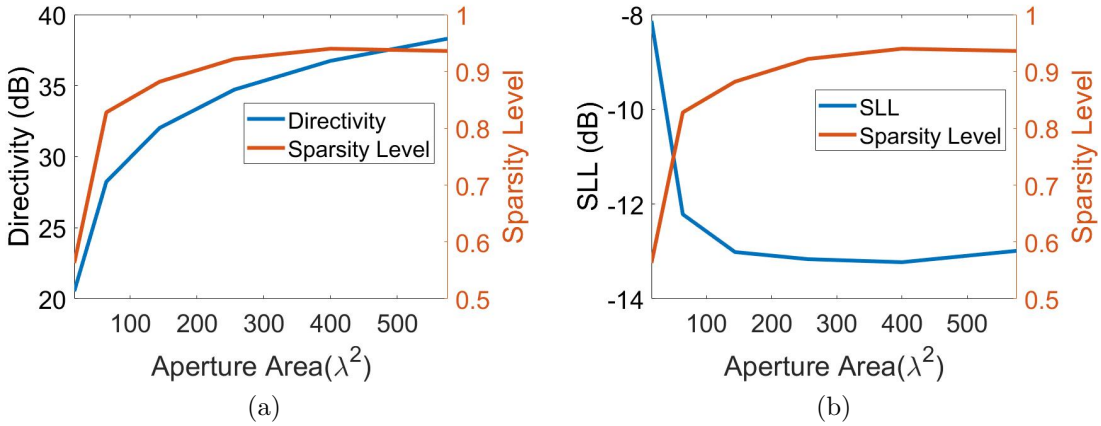

(a) (b)

Figure 5.18 Resulting directivity and SLL for the convex model using a uniform grid. The directivity, SLL, and sparsity level were tracked as we solve Equation 5.9 for different aperture sizes (a) Directivity and sparsity level for the convex model using a uniform grid (b) Tracked SLL and sparsity level for the convex model using a uniform grid.

For the second case, we solve Equation 5.9 when we use a grid that is generated by Hammersley ($b_1 = 2$) samples, where the results are depicted in Figure 5.19. We see once again, that as we increase the aperture area, the resulting weighting vector becomes less and less sparse, where the sparsity for the minimum area case is .5 and increases to .945 for the largest aperture case. Once more, as we increase the aperture size beyond $150\lambda^2$, the SLL is maintained around -13 dB, which is around the same values as the SLL produced by the LDS methods. In terms of sparsity, a Hammersley grid results in a solution that is sparser than the other three grids that are used, and when we look at the directivity for each aperture size and sparsity level, the Hammersley is the second best grid but falls short to the uniform grid. When we compare the directivity produced by the Hammersley grid to that of the LDS methods, we see that the Hammersley grid falls short and can't produce the same performance as the LDS methods. Since the directivity for the Hammersley grid falls short of expectation, it should be noted that the SLL surpasses that of the uniform grid, where the SLL for the $16\lambda^2$ instance is less than the SLL for the uniform grid and does so by using less elements that the uniform grid.

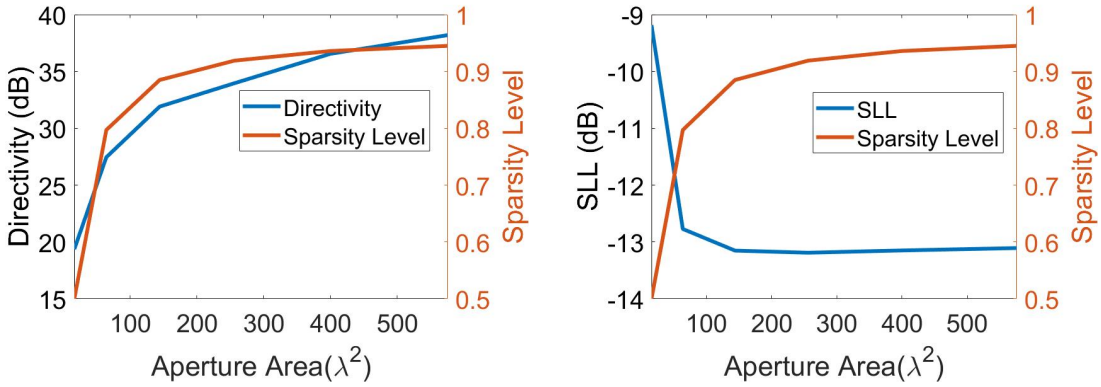

(a) (b)

Figure 5.19 Resulting directivity and SLL for the convex model using a grid generated by Hammersley samples. The directivity, SLL, and sparsity level were tracked as we solve Equation 5.9 for different aperture sizes (a) Directivity and sparsity level for the convex model using a uniform grid (b) Tracked SLL and sparsity level for the convex model using a uniform grid.

In the Halton ($b_1 = 2, b_2 = 7$) grid case, we see that it outperforms all the other three grids when the aperture size is at $16\lambda^2$. The results for the convex model using a Halton grid are shown in figure 5.20. The sparsity is the second lowest of all three grids for this aperture size, the SLL is is the lowest out of all four grids, and the directivity is the second highest, falling behind the directivity of the uniform grid. However, as we begin to move to larger aperture sizes, we see that the directivity for the Halton grid begins to fall behind the uniform and Hammersley grids, which means that the Halton grid falls far behind the LDS methods. The Halton grid is able to result in sparser solutions than that of the uniform grid and able to match it in terms of SLL performance, but is outmatched in terms of directivity. Meanwhile, the Hammersley grid outperforms the Halton grid in terms of sparsity and directivity, which allows us to conclude that the use of a Halton grid was the second worst performing model out of the four that we presented. Thus far, we can also conclude that the performance of the sampling metric has little correlation to the performance of the convex model. Such as the Hammersley sampling method has higher directivity than the directivity produced by Halton sampling when the array has a sparsity between 90-100% and the convex model using a Hammersley grid also has a higher resulting directivity than the convex model using a Halton grid.

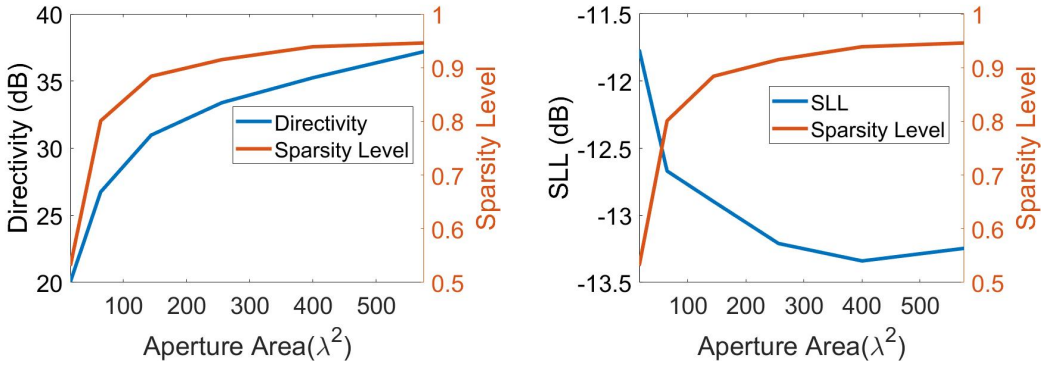

(a) (b)

Figure 5.20 Resulting directivity and SLL for the convex model using a grid generated by Halton samples (a) Directivity and sparsity level for the convex model using a uniform grid (b) Tracked SLL and sparsity level for the convex model using a uniform grid.

This claim becomes easier to verify with the grid generated by Poisson disk samples, where the results for the convex model using Poisson disk samples is shown in Figure 5.21. However, the main issue with the Poisson grid is that the resulting weighting vector is the least sparse out of the other three grids. We've seen with the analysis for the LDS methods that Poisson disk sampling outperforms the other LDS methods when the array becomes very sparse and surpasses the performance of uniform sampling when we remove around 80% of the elements within the array. However, since the optimization problem doesn't remove many of the elements, the array stays dense and the directivity is the lowest out of all four grids. The results for the LDS support these results, since we see that over all aperture sizes, the directivity for Poisson disk sampling is lower than Hammersley and Halton sampling when we have more than 80% of the original elements in the array. Despite that the directivity performance of the Poisson grid is not to the likes of the other three grids, it still is able to keep the SLL at a very low level over all aperture sizes, where the lowest SLL achieved with Poisson disk sampling is -15.463 dB for the $64\lambda^2$ case.

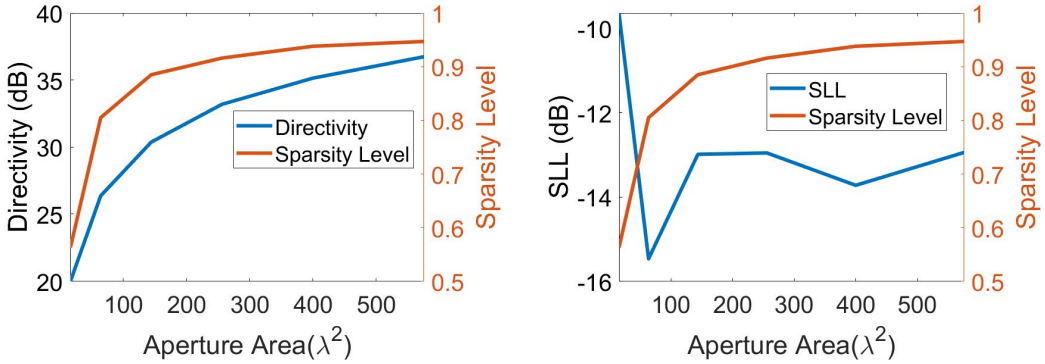

(a) (b)

Figure 5.21 Resulting directivity and SLL for the convex model using a grid generated by Poisson samples(a) Directivity and sparsity level for the convex model using a uniform grid (b) Tracked SLL and sparsity level for the convex model using a uniform grid.

From the convex model analysis, we can take away several observations and conclusions. The first conclusion is that as we increase the aperture area, the sparsity of the

array decreases. This is an unfortunate takeaway because out of all the methods that we have examined, the l_1-minimization is the worst at implementing sparsity within the array. However, the reason for the lack of sparsity is that the number of desired elements can't be implemented as a constraint and the l_1-minimization doesn't exactly choose whether an element is on or off, so this results in a solution that may not be very sparse. Sparsity can be improved by increasing the error term ϵ, but this in return, reduces the performance of the array, since we are allowing for the resulting array to deviate from our desired pattern.

Aside from these issues with the convex model, we can conclude that out of all the grids we examined, the Hammersley grid would be the more optimal grid. Since the uniform grid would be the grid with the second best performance, we see that the Hammersley grid results in a lower SLL and higher sparsity. Since directivity will drop as we remove more elements, we see that the Hammersley grid results in sparser solutions where the directivity is less than that of the uniform grid, but it close to that of the uniform case, which is why we can conclude that the Hammersley grid results in a more optimal performance for all four grids. Overall, we see that despite that the Hammersley and uniform grids performed fairly well, they were not able to achieve the performance values as that of the LDS methods, meaning that the LDS techniques are the more superior choice for designing sparse arrays.

5.4.3 Sparse Array Analysis (GA Array Thinning)

The final two methods that we will examine in this chapter involve the use of GA. The algorithm in this chapter is derived from [8] and uses GA to remove elements from a fully populated array so that the SLL of the array can be minimized. For this particular algorithm, we will focus on the linear array case since it will be more computationally efficient to compute than for the planar array case. Even though the focus of the work in this thesis is on planar and 3D arrays, we know that if a method doesn't work for the linear array case, it will not function for any of the others. Such as in Chapter 6, we see that the use of the LDS techniques work not only for planar apertures as seen in Chapter 4 but also for 3D arrays. So by showing the nature of the performance for this method on linear arrays, we

will be able to conclude that the results will be consistent for planar and 3D platforms.

A GA is a meta heuristic algorithm inspired by the process of natural selection and has been extensively used for antenna array synthesis problems [8]. The process of this particular GA is as follows:

- Generate initial population
- Score each individual
- Choose the best parents
- Breed (homogenize)
- Mutate children (diversify)
- Score each individual
- Check to see if a criterion is satisfied or if we have reached the final iteration

The purpose of the algorithm is to take an array consisting of elements distributed on a uniform grid and remove elements so that the SLL of the array can be minimized. In Figure 5.22, we give an example which properly explains how the above list of procedures is carried out so that the SLL is minimized for a 10 element linear array.

The first step in the process is to generate a set of parents, where for our simulation, we used a parent population of 40%. For the 10 element linear array example, this would consist of us generating four random vectors of length 10 that consist of 0's and 1's, where 0 corresponds to a removed element and 1 indicates an element that is kept. We then calculate the SLL for each of the parents and then score the parents by sorting them from lowest SLL to highest SLL. Half of the parents are removed, where the parents with the highest SLL's are kept and the ones with lowest SLL's are killed off through natural selection. We then replace them by having the remaining parents mate with each other and produce a set of offspring, as depicted in Figure 5.22. The offspring are produced by taking the genetic code

of one parent and mixing it with another. This is done by choosing a random crossover point, which in our example is 7. So we then take entries 7 through 10 of each parent and swap them with each other so that the offspring have genetic code of both parents. We then finally conclude the first iteration by mutating one of the genes by flipping a single bit at random. The process then repeats until we either reach a particular SLL or a given number of iterations. In our case, we terminate the algorithm after 1000 iterations.

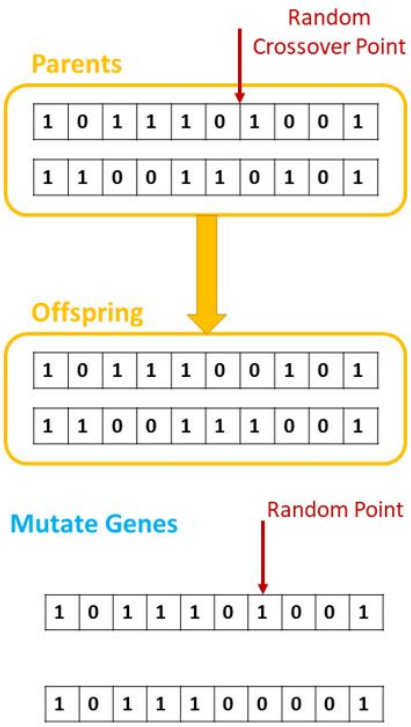

Figure 5.22 Given example of the functionality of the GA demonstrating the initialization of parents, production of offspring, and mutation

For our analysis setup, we start out with a uniform linear array residing on the z-axis with an aperture length of 40λ. We begin with the fully dense case where the element spacing is $d = \lambda/2$, which results in a total of 80 elements within the array. After running the algorithm, we converge after a total of 200 iterations for this particular instance. The algorithm removed 61 elements from the array, resulting in a sparsity level of 76.3%. The resulting SLL of the array is -20.165 dB, as seen in Figure 5.23. After running this first case, we see that this is the only method we have seen so far that can implement sparsity

and reduce the SLL below −20 dB. None of the other methods handle the SLL as well as the array thinning GA, where the next closest technique to manage the SLL performance at a low sparsity level is Poisson disk sampling. From these results, we can say that if the algorithm was used for a planar array, we can assume that the number of elements removed would approximately be 23.75% and the SLL would also be kept below −20 dB. As mentioned before, we can see that from the resulting element distribution, the majority of the elements kept are the elements within the center of the array and the elements that the algorithm removes are those that are close to the ends of the aperture.

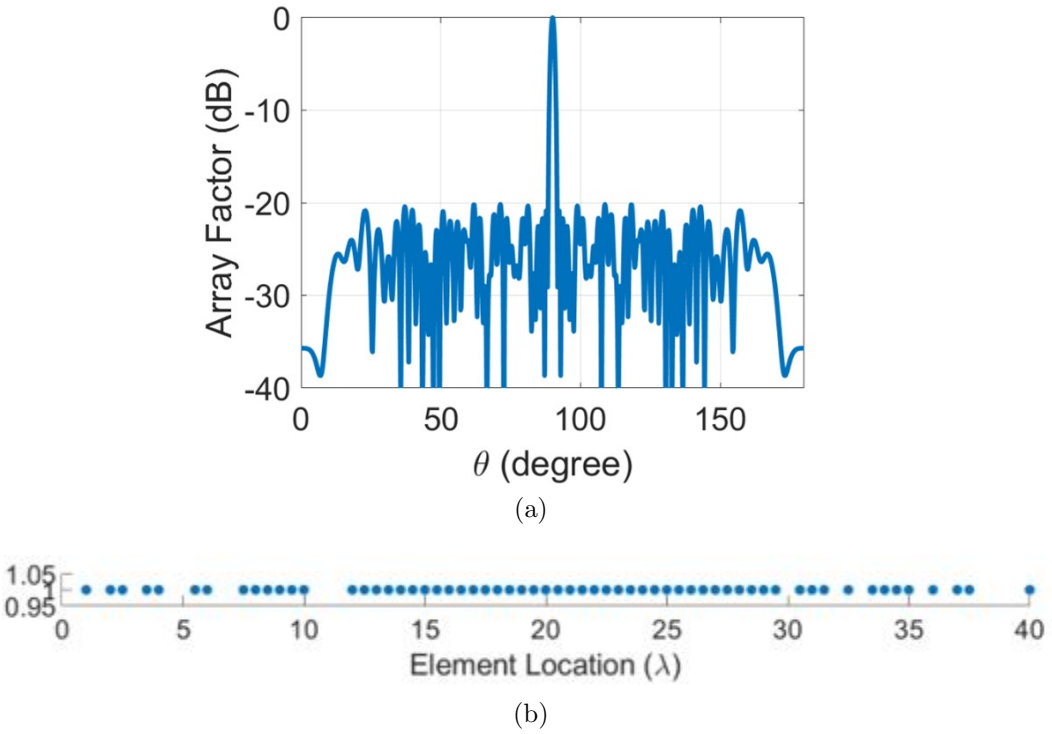

(a)

(b)

Figure 5.23 Resulting thinned array for when the element spacing is $d = \lambda/2$ (a) Resulting array factor for the thinned linear array (b) Element distribution of the thinned array along the z-axis.

For the next several instances, we will increase the element spacing so that fewer elements can fit within the aperture, effectively increasing the sparsity level. The next case consists of an element spacing of $d = 0.5714\lambda$, which results in an array of 70 elements. Before we even run the algorithm, the sparsity level is already at 87.5%. After we run the algorithm, the

number of elements within the array then reduces to 53, reducing the sparsity level further down to 66.3%. Despite that nearly 40% of the elements have been removed from the array, the SLL is still kept below -20 dB, where the measured SLL is -20.076 dB. Once more, we see that the resulting element distribution is highly concentrated within the center of the array aperture and the elements that are removed are those at the ends of the aperture.

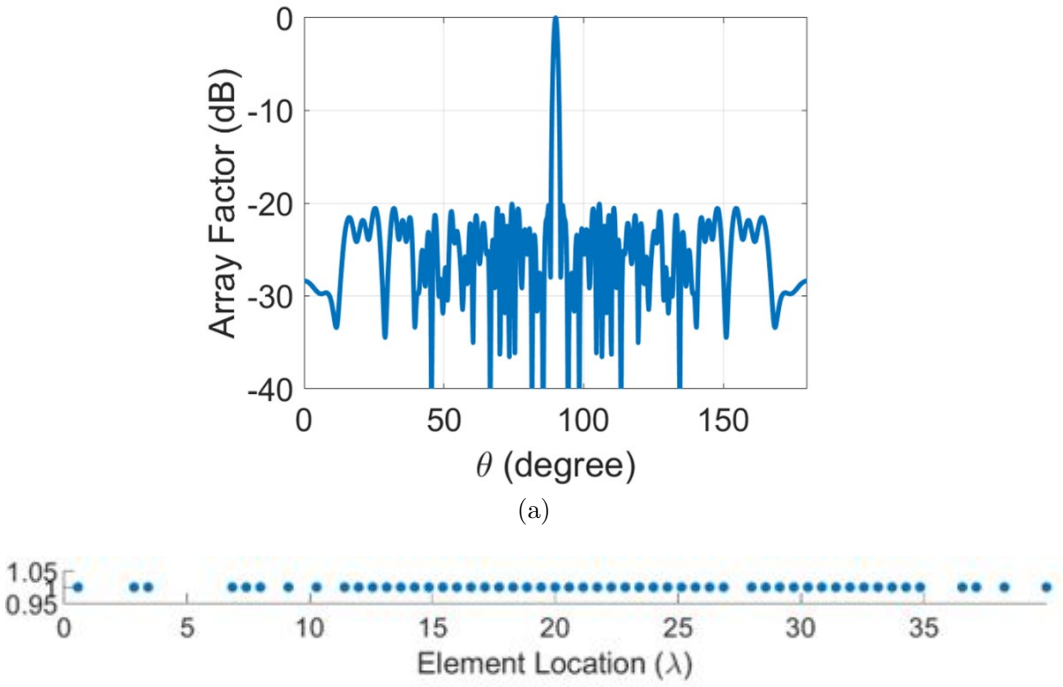

(a)

(b)

Figure 5.24 Resulting thinned array for when the element spacing is $d = 0.5714\lambda$ (a) Resulting array factor for the thinned linear array (b) Element distribution of the thinned array along the z-axis.

Over the next two cases, we increase the element spacing to $d = 0.6667\lambda$ and $d = 0.8\lambda$ which reduces the array size down from 80 elements to 60 and 50 elements respectively. Immediately for both arrays, we start out with a sparsity level of 75% for the $d = 0.667\lambda$ case and 62.5% for when $d = 0.8\lambda$. After running the algorithm for both arrays, the number of remaining elements in the array that utilizes $d = 0.6667\lambda$ spacing is 46 and the array with an element spacing of $d = 0.8\lambda$ is now left with 41 elements. The SLL of each array is -19.302 dB and -19.081 respectively.

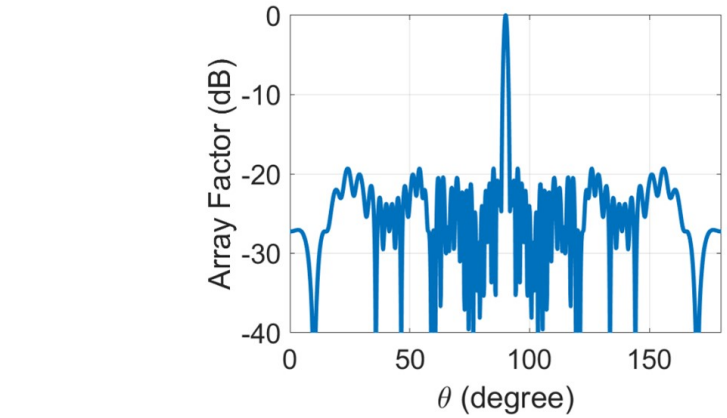

(a)

(b)

Figure 5.25 Resulting thinned array for when the element spacing is $d = 0.6667\lambda$ (a) Resulting array factor for the thinned linear array (b) Element distribution of the thinned array along the z-axis.

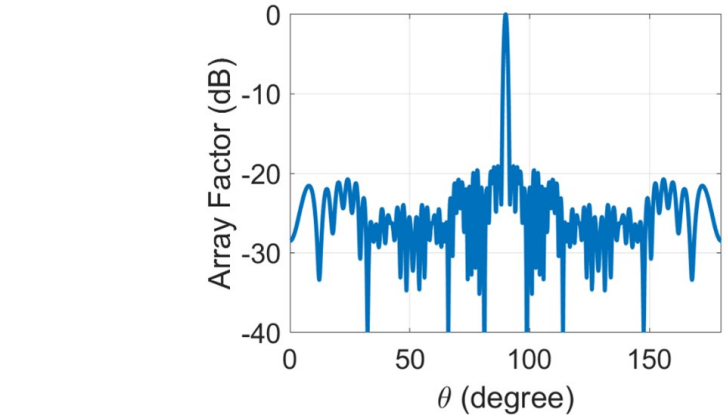

(a)

(b)

Figure 5.26 Resulting thinned array for when the element spacing is $d = 0.8\lambda$ (a) Resulting array factor for the thinned linear array (b) Element distribution of the thinned array along the z-axis.

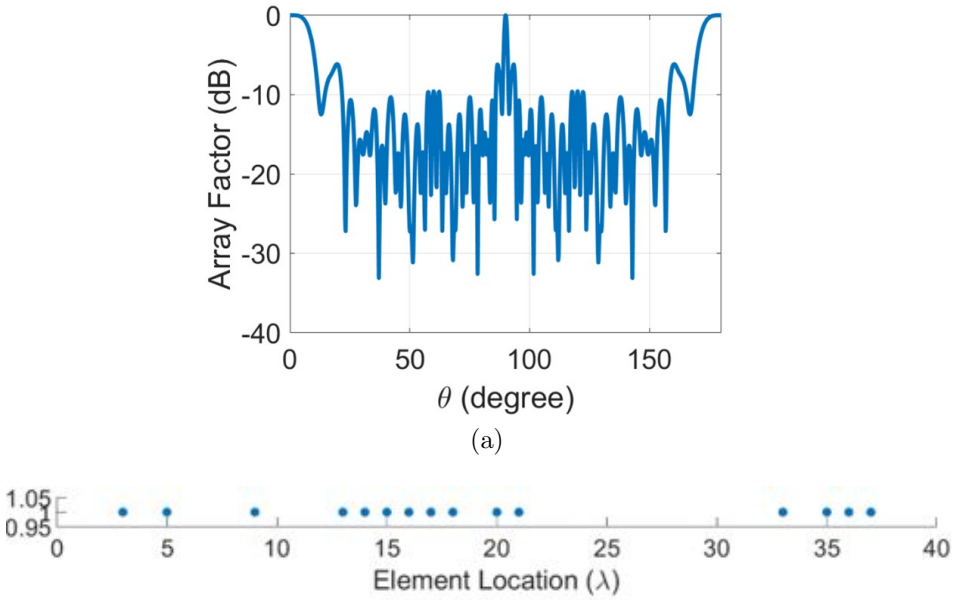

(a)

(b)

Figure 5.27 Resulting thinned array for when the element spacing is $d = \lambda$ (a) Resulting array factor for the thinned linear array (b) Element distribution of the thinned array along the z-axis.

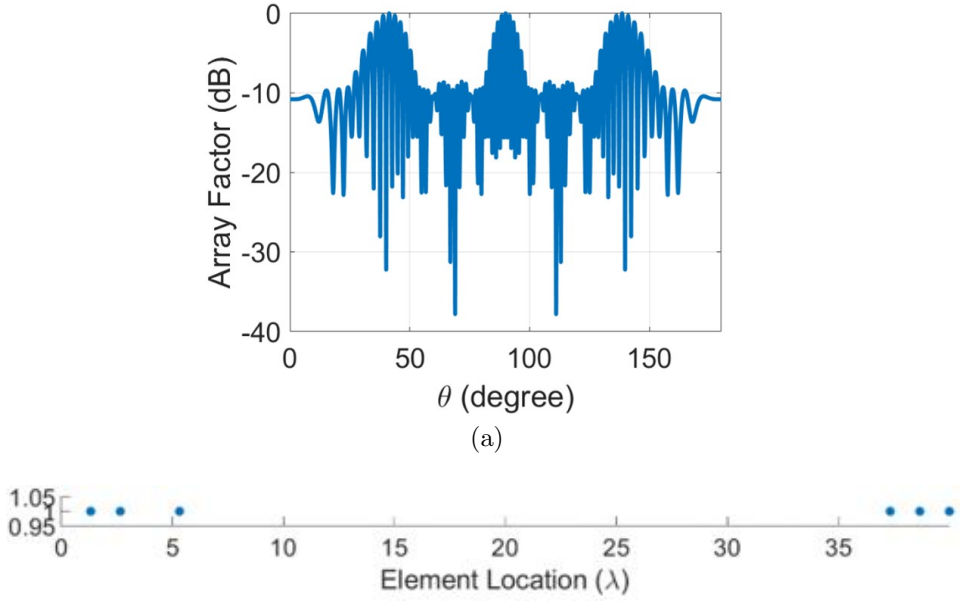

(a)

(b)

Figure 5.28 Resulting thinned array for when the element spacing is $d = 1.333\lambda$ (a) Resulting array factor for the thinned linear array (b) Element distribution of the thinned array along the z-axis.

The significance of the second array which has a sparsity level of 51.3% is that this algorithm proves that we can remove up to approximately 50% of the elements and still keep a SLL around -20 dB. Out of all the methods presented this chapter, none of them are able to produce an array that keeps the SLL close to -20 dB and remove half of the elements within the array, making the array thinning GA the most successful method that simultaneously implements sparsity and reduces the SLL.

In the final two cases, we increase the element spacing of the array to $d = \lambda$ and $d = 1.333\lambda$, which leaves us with 40 elements and 30 elements respectively before we run the algorithm. After we run the GA, we notice a similar trend that has occurred with every method except for the LDS techniques which is that once we increase the element spacing to be $d \geq \lambda$, the non-LDS methods can not prevent grating lobes and the SLL drastically rises. Despite that the GA array thinning method worked exceptionally well up until $d = \lambda$, the performance of the algorithm dropped tremendously, where the new measured SLL is 0 dB. When $d = \lambda$, the algorithm removes 15 more elements, thus resulting in a sparsity level of 31.25%. For the LDS techniques, we see that they are able to keep grating lobes out of the pattern and keep the SLL relatively low even when we have a sparsity level that falls $< 20\%$. In Figure 5.27, we see that the grating lobes are very visible within the pattern and that the SLL between the main lobe and grating lobe has risen above -10 dB. When $d = 1.333\lambda$, the algorithm fell apart altogether, where the resulting array now has 6 remaining elements and a sparsity level of 7.5%. We see that the algorithm leaves such large gaps between the remaining elements that the SLL is not only 0 dB but the pattern doesn't have any smoothness to it. The resulting array pattern now has lobes made of ripples that take away the majority of the power from the main beam.

After using this technique, we can conclude that the algorithm performs exceptionally at implementing sparsity and keeping the SLL low values, particularly around -20 dB. When we keep the element spacing on the interval $0.5 \leq d < \lambda$, the SLL is kept at least below -19 dB. However, as we saw with all the non-LDS techniques, the performance of the method

falls apart when $d \geq \lambda$, where the algorithm fails to keep grating lobes from entering the radiation pattern. When we reach higher sparsity levels, the algorithm falls apart completely and has the worst performance out of all of the previously mentioned methods, since it results in large spacing between elements which make the radiation pattern have no distinguished peaks. Instead, the radiation pattern is made up of ripples. Finally, we note here that when the element grid spacing is equal or larger to one wavelength, the array will naturally have grating lobes. As such, it's not possible to remove them by array thinning which further increases the average element spacing. As a result, array thinning is not effective when element spacing exceeds one wavelength.

In [8], it's mentioned that since the GA has many variables to control, the convergence of the algorithm and the computational time are directly impacted. By using GA, there is no guarantee that we will converge to the global minimum. However, in [89] we see that statistical aperiodic array theory predicts that over 900 elements are needed to obtain a -22 dB maximum SLL with 90% probability for a 40 lambda aperture. In [90], they perform an optimization study of their "glmulti" parameters to examine how each parameter directly impacts the performance of their GA. Such as they studied different values for: population size, mutation rate, sexual reproduction rate, immigration rate, and consecutive iterations. For this work, a similar analysis is performed, where we study different parent population sizes, mutation rates, and then take the best performing value for each case and examine it over the course of 5 trials to see how close we can get to -22 dB which is the optimal solution for this array size.

For the first simulation, we study how the parent population impacts the convergence speed and how close we can get to the global optimum by varying the parent population from 10% to 80% for a one gene mutation rate (flip one random bit on a single gene). We can see from Figure 5.29 that when we use a parent population that is $< 40\%$, we converge within the first 350 iterations but we converge to a values that are ≥ -20 dB, which is far off from the value that we desire to get to. When we use a parent population of 40% and 60% we

minimize the SLL to -20.5 dB which is just 1.5 dB away from reaching the global minimum. The difference between the two parent population sizes is that we converge at 800 iterations for the 40% case and 920 iterations for the 60% instance. Since a parent population of 40% consists of less computational complexity than that for the 60% case, we can conclude that a parent population of 40% is the more optimal choice for our selection for the algorithm. Note that for the other population sizes, we converged quite early on, specifically before we reach 300 iterations. However, each of these parent population sizes were only able to reach the -20 dB mark.

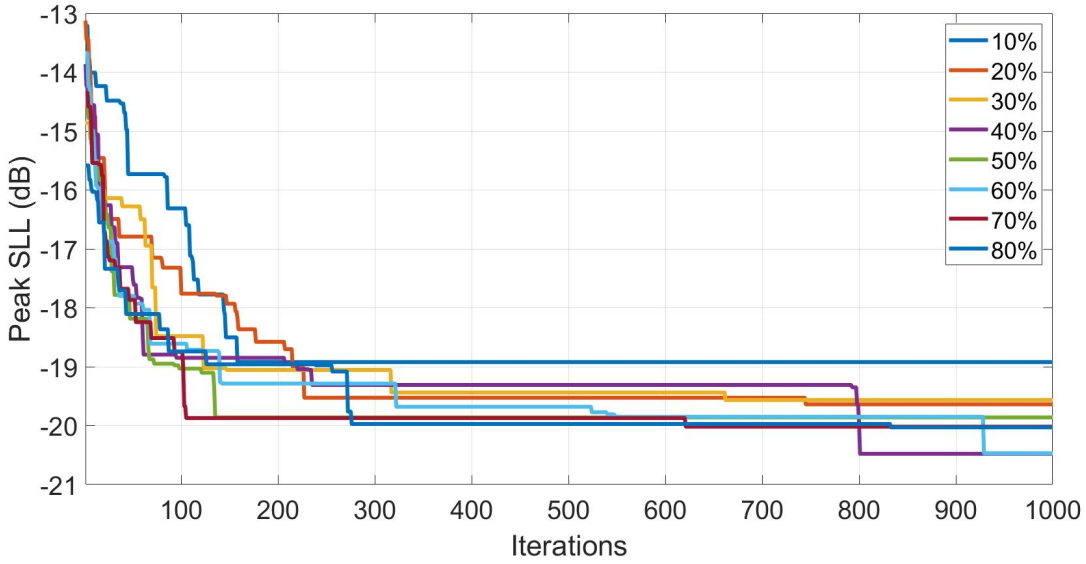

Figure 5.29 Convergence of the GA for various parent population sizes

The next parameter we studied is the mutation rate, where we considered the range of flipping one to five bits within the population with a fixed parent population of 40%. The results in Figure 5.30 demonstrate that choosing a single gene from the population and flipping one bit is the optimal choice. By only flipping a bit for a single gene, we are able to achieve a SLL < -20 dB after 800 iterations. We see that by changing more than one gene, the SLL increases, where the 5 gene mutations resulted in the worst SLL. The two, three, and four gene mutations all converged within 300 iterations, however, the SLL for

each mutation rate is ≥ -19 dB.

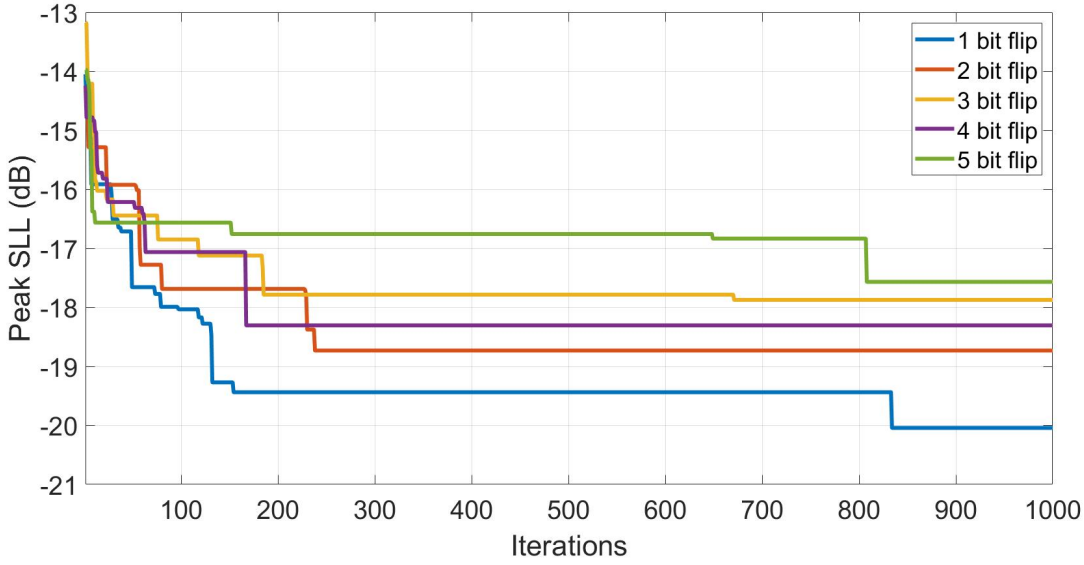

Figure 5.30 Convergence of the GA for various mutation rates

After examining the performance of the GA when we vary the parent population and mutation rate, we can conclude that a parent population of 40% and one gene mutation are the ideal values for the algorithm. We then examine the convergence of the algorithm over five different trials, as shown in Figure 5.31. From the results, we see that only trials two and three were able to achieve a SLL lower than -20 dB, where the rest of the trials came close to this mark but weren't able to breach it. However, the behavior of each of the curves indicate that given more trials, each curve would continue to decrease, showing room for improvement in the SLL. From the curves, we see that the SLL is still decreasing towards the 1000 iteration mark. The only trial that appears to be stuck in a local minima is trial three, since it converged after 200 iterations and showed no change in the SLL. From the analysis of the parent population and mutation rate, the lowest SLL we have achieved is -20.5 dB. We can conclude that the GA will produce a highly satisfactory performance by getting us within 1.5 dB of the optimal SLL for this particular aperture size.

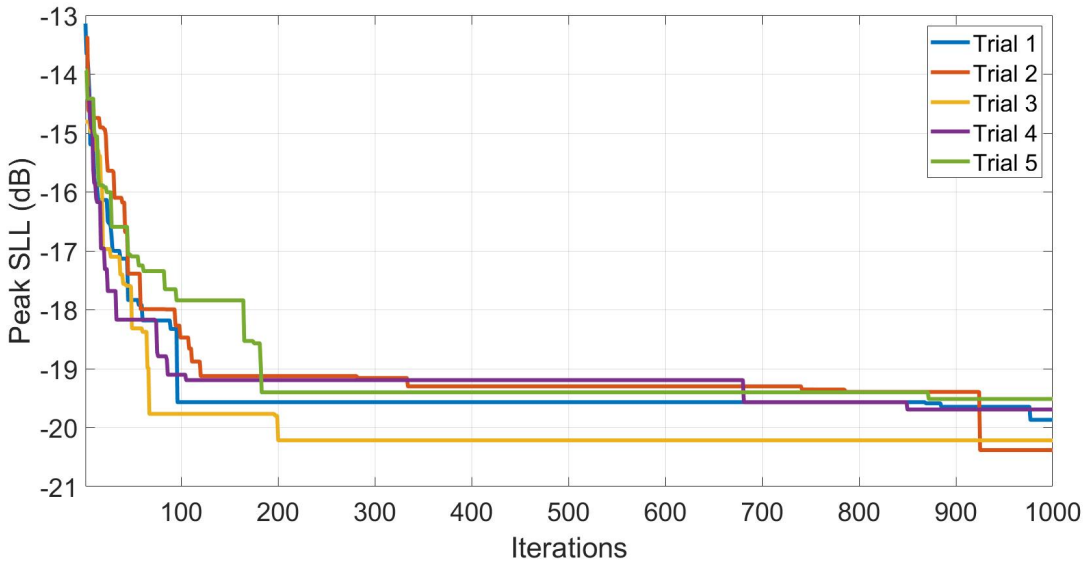

Figure 5.31 Convergence of the GA for the most successful parent population and mutation rate for five different trials

5.4.4 Sparse Array Analysis (GA Geometry Optimization)

The final method that we will examine in this sparse array analysis is also based off of a GA but instead of lowering SLL, we will optimize the element geometry. We created this GA from the motivation behind the design of the LDS, where we aim to optimize the element placement within the aperture by maximizing the average minimum element spacing, so that we can have a more optimal solution to equally distributing the elements within the aperture but yet doing so non-uniformly. For the GA planar case, we noted that the algorithm took several days to converge and the algorithm for the linear array took only a few minutes. For this GA, it takes a full day for the algorithm to converge, thus minimizing the amount of cases that we were able to examine.

For this analysis, we consider a planar array with 100 elements and $4\lambda/3$ element spacing. We then rearrange the elements within the aperture by using the proposed GA that focuses on maximizing the average minimum element spacing, Poisson disk sampling, and Halton $(b_1 = 2, b_2 = 7)$ sampling. The results for the GA are displayed in Figure 5.32, where we see

that the algorithm is able to prevent grating lobes from appearing in the pattern and keep the SLL relatively low. The algorithm has a resulting average minimum element spacing of 0.993λ, which is the largest when compared to the Poisson and Halton sparse arrays. The directivity and the SLL of the array are 25.105 dB and -11.889 respectively.

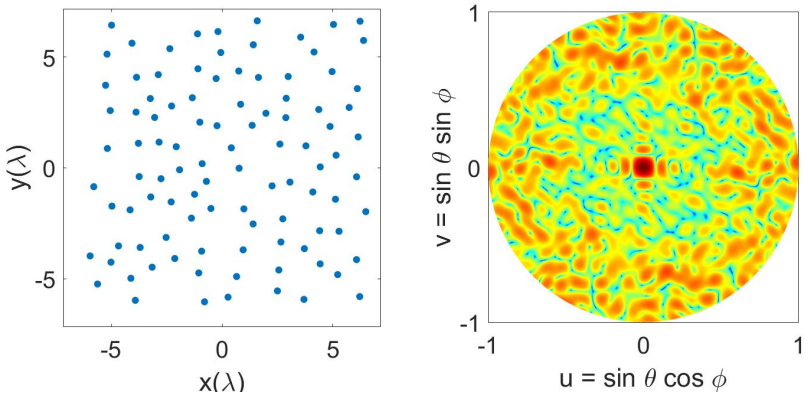

Figure 5.32 Resulting element distribution within the aperture and the corresponding radiation pattern for the sparse array using GA (a) Resulting element distribution from the convergence of the algorithm (b) Radiation pattern of the element distribution in the uv-space.

The results of the Poisson array indicate that it had the second best performance out of the other two arrays. The element distribution and pattern in the uv-space are shown in Figure 5.33. From the analysis between the LDS techniques in Chapter 4, we see that Poisson disk sampling has the largest average minimum element spacing since this sampling technique uses a constraint that prohibits elements from falling within a certain distance of each other. However, with an average minimum element spacing of 0.93406λ, we see that the GA has an average minimum element spacing far greater than that of the Poisson array. After calculating the performance of the array, we see that the Poisson has a more directive pattern, where the directivity was calculated at 25.295 dB but the SLL is much higher than the GA array, where the SLL for the Poisson array is -9.974 dB.

The final sampling technique we examined was the Halton ($b_1 = 2, b_2 = 7$) technique. The resulting element distribution and the corresponding pattern for the Halton array are

displayed in Figure 5.34. We see that for this instance, Halton sampling had the lowest average minimum element spacing which was calculated at 0.839λ. The Halton array not only had the worst performance for element optimization but the directivity and SLL of the array also had the worst performance amongst the three arrays, where the measured directivity and SLL for the Halton array were measured at 25.025 dB and -4.723 dB respectively.

From the results for this analysis with the use of the element optimization GA, the algorithm was able to successfully maximize the average minimum element spacing and have a higher average than Poisson disk and Halton sampling. By having a large non-uniform element spacing, the algorithm was able to avoid introducing grating lobes into the pattern and also keep the SLL the lowest out of the other two methods. The drawback to using such a method is that for a planar array consisting of 100 elements, the algorithm took more than a day to converge. But with with use of Poisson and Halton sampling, we are able to have an array designed within seconds. The Poisson disk sampling technique even produced an array that is more directive than the array produced by the GA, but failed to lower the SLL more than that of the GA array. In summary we note here that one advantage of this geometrical optimization of the arrays is the computational time. Traditionally, sparse array optimization requires calculation of the array factor as part of the fitness function calculation, which becomes extremely time consuming for heuristic search approaches that require thousands of iterations, since calculating mean element spacing by studying the geometry is significantly less computationally time-consuming than array pattern calculation. Nonetheless, while the approach studied here shows there is an advantage to optimizing the element locations, the LDS approaches provide almost similar performances, with the added advantage of significantly faster computational time, making them a practical solution for real-time sparse array reconfiguration.

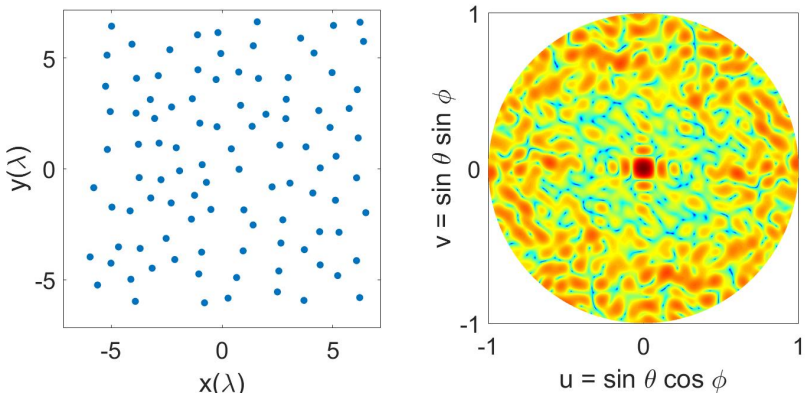

Figure 5.33 Resulting element distribution within the aperture and the corresponding radiation pattern for the sparse array using Poisson sampling (a) Resulting element distribution from the convergence of the algorithm (b) Radiation pattern of the element distribution in the *uv*-space.

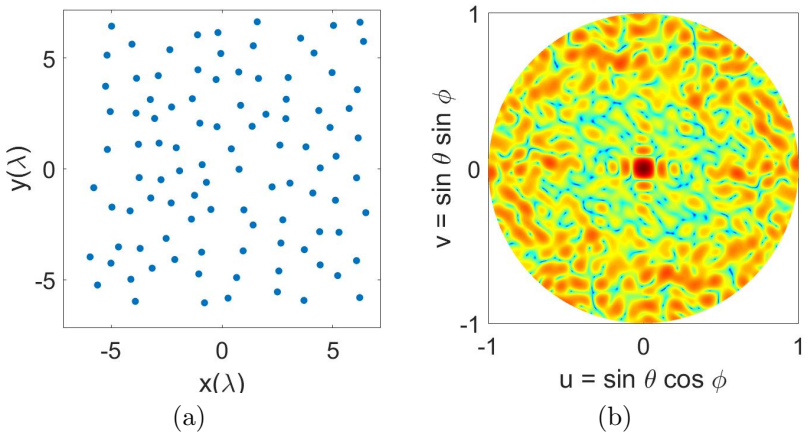

Figure 5.34 Resulting element distribution within the aperture and the corresponding radiation pattern for the sparse array using Halton sampling (a) Resulting element distribution from the convergence of the algorithm (b) Radiation pattern of the element distribution in the *uv*-space.

CHAPTER 6

SPARSE CYLINDRICAL ARRAYS

In this chapter, we explore the use of low discrepancy sequences (LDS) for the application of cylindrical apertures. The cylindrical aperture is a unique case because the antenna elements reside in a three dimensional space, instead of an axis or a plane, as we have seen and discussed in previous chapters in this dissertation. As in Chapter 4, we start out with a uniform array with $\lambda/2$ spacing in the cylindrical aperture and we increase the element spacing so that it's $> \lambda$, which results in an extremely high sidelobe level (SLL). From the directivity analysis results in Chapter 4, we can take away that when the array is reduced to $< 20\%$ of the original elements, the directivity can decrease up to 10 dB. So in this chapter, we highly emphasize the SLL and average minimum element spacing; which is our way of analyzing the performance of the resulting array configurations. We show that with the use of LDS, we are able to significantly reduce the grating lobes of an antenna array with a cylindrical aperture when the array consists of $< 20\%$ of the original elements.

6.1 Introduction

In chapter four, we discussed the use of LDS for sparse antenna array design for planar antenna arrays. We showed that when the element spacing is $\geq \lambda$, then grating lobes will appear in the radiation pattern, which takes away power from the main beam since grating lobes are replicas of the main beam. Cylindrical arrays are a unique case because a uniform cylindrical array consists of M ring arrays concentric around the z-axis with N elements in each of the arrays. Note that if the reader is unfamiliar with the theory and concept of ring antenna arrays, they are referred to Appendix C. Typically, the antenna elements will be conformed to the surface of an object/material which means that the main beam when steered to $\theta = 0^\circ$ and $\phi = 0^\circ$, would parallel with the object that the antennas are attached to. This is an inefficient use of a cylindrical array because this would result in

high losses, with the transmitted electromagnetic waves having to travel through another medium. Instead, the geometry of a cylindrical array is used to the advantage of being able to cover the entire azimuthal range, by steering the main beam to $\theta = 90°$.

Cylindrical antenna arrays are much more complex to design and compute when compared to linear and planar antenna arrays. Reason being is that the elements no longer reside in just an axis or a plane, but instead are in a 3D space. This intensifies the array factor calculations because we now need to use an x, y, and z term to specify element location. One of the biggest complexities that's now introduced is that the antennas used for a cylindrical array must now become conformal so that they can attach to the cylindrical surface. In Chapter 2, we demonstrated that when the radius r of the cylinder is small, the amount of curvature applied to the antenna is high and it affects the radiation pattern of the antenna by broadening the beamwidth of the radiation pattern. When the radius is large, the amount of curvature is decreased and the radiation pattern is still impacted by the curvature but not as much when the radius is small. Since, the element pattern is impacted, this can often lead to dissimilarities with an EM-model of the array and the array factor calculation. The purpose of the array factor is to serve as an approximation to the array radiation pattern when the array consists of many elements, since the EM-simulation would consist of many time consuming and intense calculations. With the array factor assuming that the array elements are isotropic (equal radiation in all directions), we know that from Chapter 2 that the radiation pattern of an isotropic element on a cylindrical surface will suffer some distortion, so we must consider the element pattern for the cylindrical case. In this chapter, we provide the results for the MATLAB simulation of the cylindrical array for a variety of cases, as in Chapter 4, and also present an EM-Model designed in HFSS to showcase the results of uniform sampling and one of the mentioned LDS techniques to provide a more realistic radiation pattern of the overall array.

The question that arises is why the interest in sparse cylindrical array design? Our primary interest in cylindrical antenna arrays is provided in Appendix C, along with detailed

results and fabrication for our intended application. Aside from our particular application, cylindrical arrays are highly used because of their possible 360° range of coverage in the azimuthal direction. This can be done with a single omnidirectional beam or with multiple beams that are steered in different directions [91, 92]. This makes cylindrical arrays a valuable asset to the telecommunication industry because they possess a 360° range of coverage but they also can be steered greater than $\theta = 90°$ to provide better line of sight communication for many of their users.

6.2 Cylindrical Array Theory

The array factor of the cylindrical array is built off of the array factor derivation for ring arrays. As mentioned before, the reader is referred to Appendix C for more information on ring antenna arrays. For our calculations for cylindrical antenna arrays, we assume that the ring arrays are concentric around the z-axis (when non-uniform spacing is used the center is still the z-axis). For the simplest case (uniform), the array factor for a cylindrical array consisting of M elements with N elements in each ring is found by

$$F(\theta, \phi) = \sum_{n=1}^{N} \sum_{m=1}^{M} e^{jk[r \sin\theta \cos(\phi - \phi_n) + z_n \cos\theta]} \tag{6.1}$$

where k is the wavenumber, r is the radius of the cylinder, and ϕ_n and z_n are the element azimuth and z location respectively. More generally for the non-uniform case, we can express the array factor for a cylindrical array consisting of N total elements as

$$F(\theta, \phi) = \sum_{n=1}^{N} e^{jk[r \sin\theta \cos(\phi - \phi_n) + z_n \cos\theta]} \tag{6.2}$$

The pattern response for a cylindrical array in nearly all applications will consist of non-isotropic elements with the main beam pointing in a radial direction, thus allowing for the capability of scanning with a range of 260°. In some applications, only a section of the elements are used at a particular time, such as any element with $\phi_n \in [0°, 90°]$ will be

considered "on" and used to transmit. This type of array topology is known as an active sector and will be discussed in more depth when we discuss the design of the EM-model.

Sampling points on a planar aperture was fairly straightforward, where a random or LDS was mapped to an x or y-coordinate so that an element can be generated at position (x_n, y_n) in the xy-plane.

6.3 Sparse Cylindrical Phased Array Antennas

In this section, we consider three separate cases with uniform sampling and two LDS sampling techniques (Halton ($b_1 = 2, b_2 = 7$) and Poisson disk sampling) to assess the performance of the LDS techniques at reducing the SLL of the sparse cylindrical arrays. The first case we consider is when we have a radius of $r = 14\lambda/2\pi$ and a height $h = 14\lambda$, which results in a squared area of $A = 196\lambda^2$. When the array is fully populated (rings spaced by $\lambda/2$ and elements within are spaced by $\lambda/2$), we have 28 rings with 28 elements in each ring, totaling up to 784 elements in total. We increase the element spacing to 1.4λ, which results in 10 rings with 10 elements each; resulting in a sparsity level of 12.74%.

For each case, we will examine the radiation pattern slices in all principal planes which consist of the xz, yz, xy-planes and the full 3D radiation pattern. The element distribution on the cylinder will also be provided, along with a bar plot of the minimum element spacings. Since we saw in Chapter 4 that when we are dealing with a high level of sparsity such as this, directivity will drastically drop from the fully populated case. So for our work with the cylindrical arrays, we will focus on measuring the SLL and the average minimum element spacing, where we measure the SLL in each principal plane of the radiation pattern.

When it comes to measuring the average minimum element spacing, we need to make several adjustments to our calculation for calculating the distance between the elements, since we are now dealing with cylindrical distance instead of euclidean distance. For two points $\boldsymbol{p}$ and $\boldsymbol{q}$ in a plane, we can can easily find the distance $d(\boldsymbol{p}, \boldsymbol{q})$ by

$$d(\boldsymbol{p}, \boldsymbol{q}) = \sqrt{(p_1 - q_1)^2 + (p_2 - q_2)^2} \tag{6.3}$$

which calculates the shortest path between $\boldsymbol{p}$ and $\boldsymbol{q}$. Geometrically, we can visualize this distance as the hypotenuse of a triangle, where the base of the triangle is $p_1 - q_1$ and the height is equal to $p_2 - q_2$. For calculating the cylindrical distance, it's the same concept but with a different geometry. When we try to find the distance between two points on a cylinder the points still make a triangular formulation, however, the base of the triangle and the hypotenuse are now curved which is a result of the curvature of the cylinder. When we go to solve for this curved hypotenuse, we see that we main we can still use the Pythagorean theorem but we must account for the radius and curvature of the base of the triangle, where the base b_T of the triangle is found by

$$b_T = r\alpha \tag{6.4}$$

where α is equal to

$$\alpha = \cos^{-1}\left(\frac{(p_1 q_1 + p_2 q_2)}{\sqrt{(p_1 - q_1)^2 + (p_2 - q_2)^2}}\right) \tag{6.5}$$

The height of the triangle h_T can then be found by

$$h_T = |p_3 - q_3| \tag{6.6}$$

which allows us to find find the cylindrical distance $d_C(\boldsymbol{p}, \boldsymbol{q})$ between the points $\boldsymbol{p}$ and $\boldsymbol{q}$

$$d_C(\boldsymbol{p}, \boldsymbol{q}) = \sqrt{(r\alpha)^2 + h^2} \tag{6.7}$$

Note that since the cylinder is wrapped, we will see a difference in the results for measuring the average minimum element spacing. Take for example the planar case where we are sampling on the unit square. A sample taken at $(0, 0)$ and second sample taken at $(0, 1)$ are separated by a large distance. However, since the cylinder is wrapped, we see that these points actually fall right on top of each other. Poisson disk sampling will succeed at avoiding this issue since it requires for each point to be some radial distance away from each other,

but since Halton sampling tries to equally disperse points in an aperture, we will see that we have a few samples relatively close to each other which will bring down the average minimum element spacing.

6.3.1 Case 1 - Cylindrical Platform with 14λ Length and 14λ Diameter

For the first case, the results for the Uniformly sampled aperture which consists of the principal plane slices, 3D radiation pattern, element distribution on the cylinder, and the bar plot of the minimum element spacings are displayed in Figure 6.1. Since the main beam is steered to $\theta = 90^\circ$ and $\phi = 0^\circ$, the main beam is located directly on the x-axis. With us using an element spacing of $d = 1.4\lambda$, we are reduced to 10 rings with 10 elements in each ring, which consists of 12.76% of the original elements in the fully populated array. In the 3D radiation pattern, we notice that despite that the grating lobes don't have a peak value of 0 dB, they are still heavily present within the radiation pattern. Each of the principal plane slices also depict the intensity of the grating lobes within the pattern, where the SLL in the xz, yz, and xy planes are -1.997, 0, and -1.997 dB respectively.

Our objective with the use of the two LDS techniques is to demonstrate that the non-uniform structure of the LDS techniques will remove the grating lobes and significantly improve the performance of the SLL. Since we saw in Chapter 4 that the two superior LDS methods were Halton ($b_1 = 2, b_2 = 7$) and Poisson disk sampling, so these two techniques will be used in the following cases. Chapter 4 demonstrated that when we reach high levels of sparsity, as we have here, the LDS methods are successful at removing the grating lobes and improving the SLL for the square planar aperture and even the rectangular, circular, and elliptical cases.

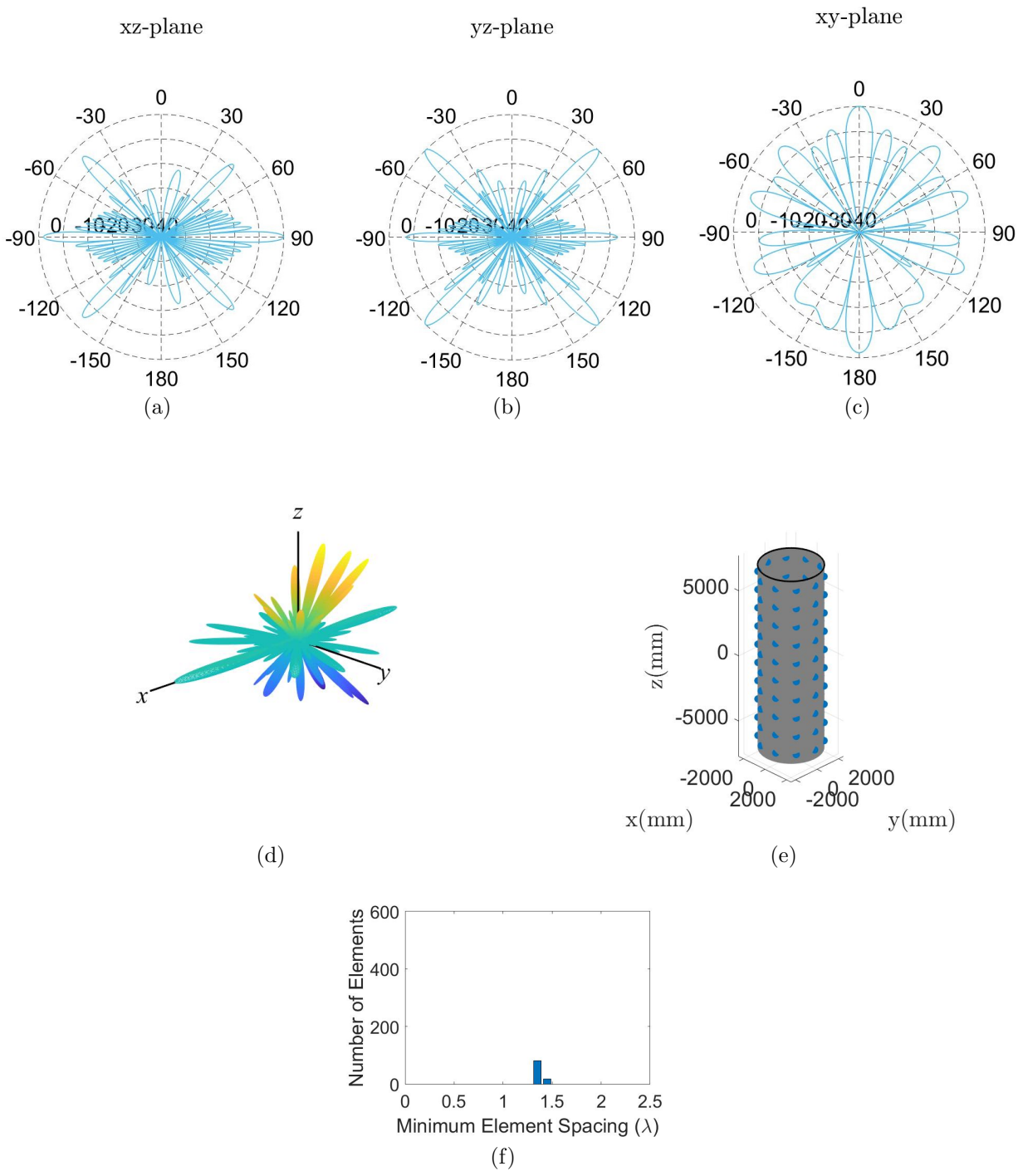

Figure 6.1 Radiation pattern slices in all principal planes, 3D radiation pattern, element distribution on the cylinder, and bar plot of the minimum element spacing for case 1 using uniform sampling: (a) Pattern slice in the xz-plane, (b) Pattern slice in the yz-plane, (c) Pattern slice in the xy-plane, (d) 3D radiation pattern, (e) Element distribution on the cylinder (f) Bar plot of the minimum element spacing

The results for the Halton ($b_1 = 2, b_2 = 7$) technique for case 1 are displayed in Figure 6.2. We are able to see in the 3D radiation pattern that the grating lobes and high SLL that we saw with uniform sampling are diminished and distributed throughout the rest of the pattern, which ultimately has resulted in a more concentrated radiation pattern. We are more easily able to see the improvements to the radiation pattern with the principal plane slice. In the xz-plane, the SLL was reduced from -1.997 dB to -12.863 dB with the use of Halton sampling. However, there was little to no improvement made in the yz-plane. Despite that the SLL remained at 0 dB in the yz-plane, we were able to reduce the intensity of the six large lobes that were appearing in this plane. The lobes were not able to be fully removed from the pattern but they are not as large or concentrated as we saw with uniform sampling. For the xy-plane, the SLL was able to be reduced from -1.997 dB to -8.083 dB. In this particular plane cut for uniform sampling, we see that for a majority of the sweep over ϕ that we have many areas where the sidelobes are > 10 dB and that we have a large lobe at $\phi = 180^\circ$ which almost has the same intensity as the main beam. With Halton sampling we were able to keep the sidelobes ≤ 10 dB for the majority of the sweep over ϕ and the large lobe that occurs at $\phi = 180^\circ$ is reduced down to -20 dB. It was mentioned previously that when we map the Halton points to the cylinder, we will encounter an issue that we didn't have with the planar aperture and that is the wrapping of the cylinder. Despite that Halton sampling outperforms both uniform and Poisson sampling for this case, Halton sampling has the lowest average minimum element spacing with the value of 0.854λ. With the cylinder being wrapped we can see that the elements come fairly close to each other at the wrapping point, where the minimum average spacing of an element falls to $\lambda/2$. Even though the minimum element spacing falls this low, we won't have to worry about mutual coupling or fabrication issues. It's when the element spacing falls $\leq \lambda/2$ that we must be concerned about mutual coupling or difficulties with fabrication.

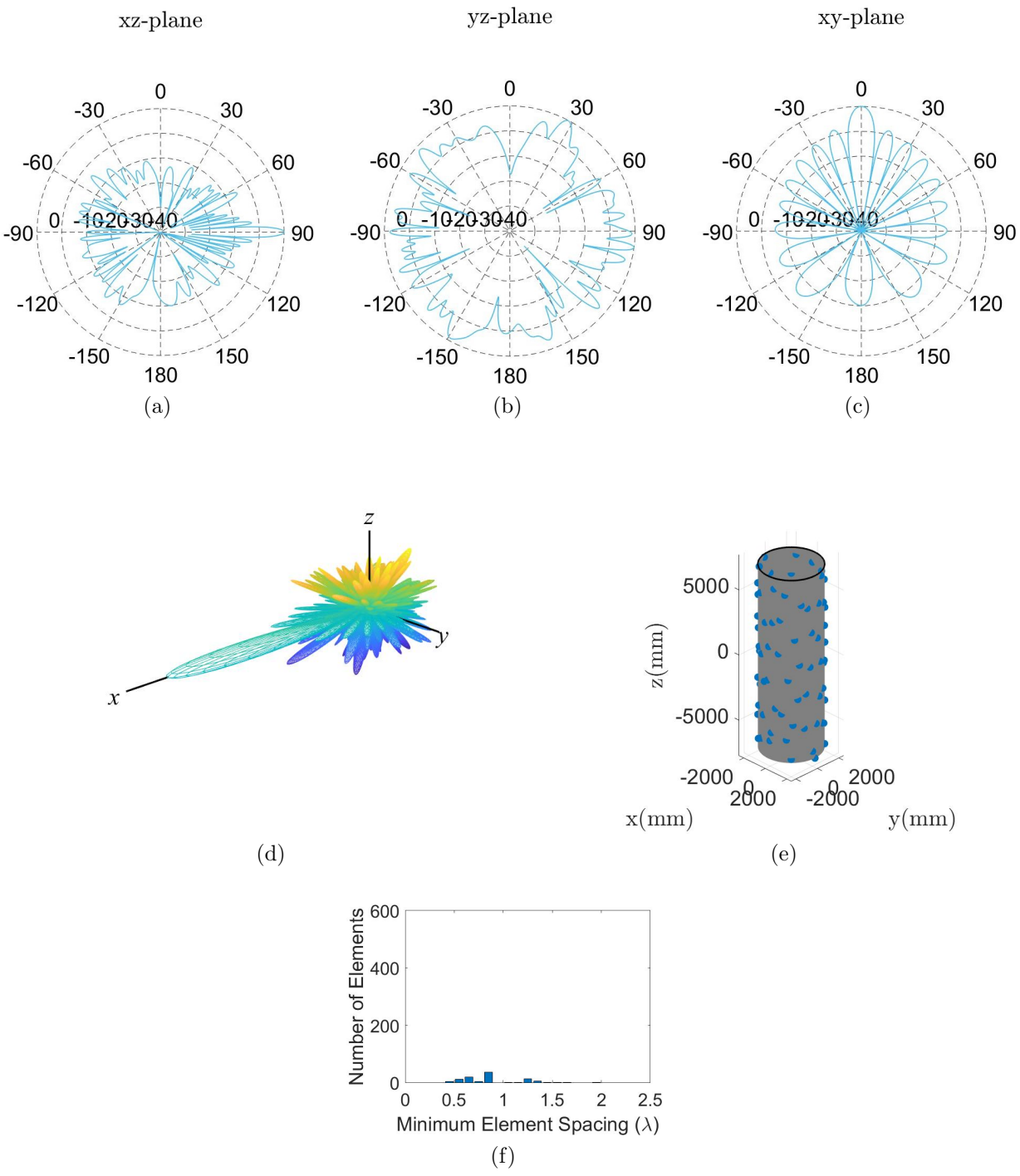

Figure 6.2 Radiation pattern slices in all principal planes, 3D radiation pattern, element distribution on the cylinder, and bar plot of the minimum element spacing for case 1 using Halton ($b_1 = 2, b_2 = 7$) sampling: (a) Pattern slice in the xz-plane, (b) Pattern slice in the yz-plane, (c) Pattern slice in the xy-plane, (d) 3D radiation pattern, (e) Element distribution on the cylinder (f) Bar plot of the minimum element spacing

The final technique we used for Case 1 was Poisson disk sampling, where the results for this technique are depicted in Figure 6.3. Similar the minimum element spacing calculations, we had to reform the Poisson disk algorithm so that it would calculate the cylindrical distance between elements instead of the euclidean distance, where the minimum spacing between any element was specified to be $R = \lambda$. Similar to Halton sampling, Poisson disk sampling was able to remove the grating lobes and many of the high sidelobes that we encountered with uniform sampling, as shown in the 3D radiation pattern. In the 3D pattern, we are clearly able to make out the main beam and see that most of the highest sidelobes occur in the xy-plane. In the xz-plane, the SLL was reduced to -12.023 dB which is a significant improvement compared to uniform sampling but is slightly higher than the SLL for Halton sampling in this plane. The yz-plane cut also shows that the six large sidelobes were able to be removed and spread throughout the rest of the pattern. Even though the SLL is still 0 dB in this plane, we no longer have six lobes each with a magnitude of 0 dB in the yz-plane. Poisson sampling was able to reduce the high SLL for uniform sampling down to -7.524 dB, which once again falls short to the performance of Halton sampling. However, the majority of the sidelobes were kept below -10 dB and the large beam appearing at $\phi = 180°$ in the pattern for uniform sampling was removed and the SLL in this direction was reduced below -20 dB, which was a significant improvement. Since Poisson disk sampling uses a minimum element spacing criterion R, the minimum element spacing depicts that we have no elements falling within λ of each other, where the average minimum element spacing for Poisson disk sampling is 1.13λ. The results indicate that the majority of elements have a minimum element spacing of λ, where there are few elements that have a minimum element spacing around 1.4λ.

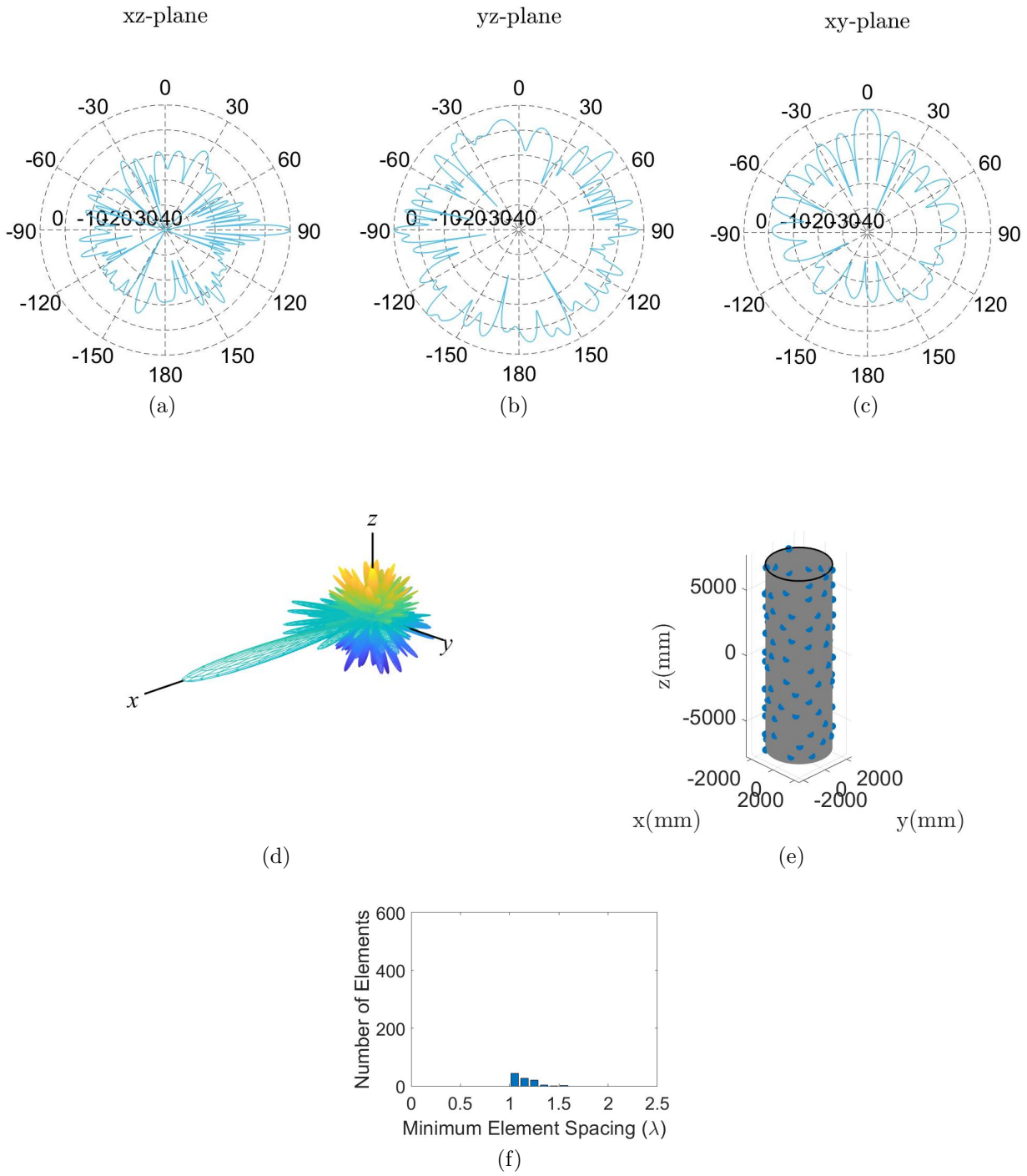

Figure 6.3 Radiation pattern slices in all principal planes, 3D radiation pattern, element distribution on the cylinder, and bar plot of the minimum element spacing for case 1 using Poisson disk sampling: (a) Pattern slice in the xz-plane, (b) Pattern slice in the yz-plane, (c) Pattern slice in the xy-plane, (d) 3D radiation pattern, (e) Element distribution on the cylinder (f) Bar plot of the minimum element spacing

For case 1, we are able to see that the LDS techniques are able to successfully remove the grating lobes and lower the SLL when the array has an element spacing $\geq \lambda$, particularly when we utilize 12.76% of the remaining elements to design the array. Uniform sampling results in many grating lobes and high sidelobes in each of the principal planes which makes it very difficult to distinguish the main beam from any of these other grating or sidelobes. With the use of the LDS techniques, the main beam becomes more visible in 3D space and the SLL in each of the principal planes except the yz-plane are reduced. This initial case also indicated that Halton sampling was superior than Poisson disk sampling sampling, where the SLL in the xz and xy-planes showed more improvements for Halton than Poisson disk sampling. However, we saw that in Chapter 5 that as we increase the aperture to larger sizes that Poisson disk sampling provided better results than Halton and Hammersley sampling. So as we increase the aperture size over the next two cases, we will see that Poisson disk sampling will outperform Halton sampling and that this trend holds for not only planar apertures but also cylindrical apertures. The performance metrics for each of the sampling techniques for case 1 are displayed in Table 6.1.

Table 6.1 Performance metrics for Uniform, Halton, and Poisson sampling for Case 1

Method	SLL xy-plane	SLL yz-plane	SLL xy-plane	Average Min. Spacing (λ)
Uniform	-1.997 dB	0 dB	-1.997 dB	1.4
Halton	-12.863 dB	0 dB	-8.083 dB	0.854
Poisson	-12.023 dB	0 dB	-7.524 dB	1.13

6.3.2 Case 2 - Cylindrical Platform with 28λ Length and 14λ Diameter

In case two, we increase the aperture size from $196\lambda^2$ to $392\lambda^2$ by doubling the height of the cylinder, so our new dimensions of the cylinder are $r = 14\lambda/2\pi$ and $h = 28\lambda$. For the fully populated scenario when the elements are separated by $\lambda/2$ spacing, the array will consist of 56 rings each with 28 elements, totaling up to 1668 elements. We then again increase the element spacing to $d = 1.4\lambda$, which then reduces the array down to 20 rings

with 10 elements in each ring, leaving the array with 11.99% of the original elements.

The results produced for case 2 using uniform sampling are displayed in Figure 6.4. The results produced using uniform sampling are similar to the uniform sampling results in case 1, where the 3D radiation pattern depicts many grating lobes and high sidelobes which makes it difficult to distinguish the main beam from the other lobes present within the pattern. The main difference which is expected from antenna array theory is that since we are populating a larger aperture for case 2, the main beam and the beams of the lobes are more narrow. When we examine the plane slice in the xz-plane, we notice that four large sidelobes are produced where each lobe has a magnitude of -10 dB. A grating lobe is also produced at $\theta = -90°$, where the magnitude of this lobe is -1.996 dB. The yz-plane also demonstrates a poor performance, where 4 grating lobes are present within the pattern which results in a SLL of 0 dB. Two other large sidelobes are also present within this plane cut at $\theta = 90°, -90°$, where these lobes have a magnitude -10 dB. In this xy-plane, the same trend once again follows, where the main beam is located at $\theta = 0°$ but a grating lobe is present at $\theta = 180°$ which results in a SLL of -1.995 dB. The rest of the sidelobes are once again relatively high, where the majority of them are > -10 dB.

In figure 6.5, the results for Halton sampling for case 2 are displayed. Overall, we see that Halton sampling is able to remove the grating lobes from the radiation pattern and keep the sidelobe level relatively low across all of the principal planes. The 3D radiation pattern depicts this statement, where the main beam is much more visible than in the results for uniform sampling. Despite that the grating lobes were removed and the SLL was reduced when compared with uniform sampling, the SLL increased for this larger aperture size when compared to Halton sampling for case 1 where we used a smaller aperture size. Such as in the xz-plane cut, the SLL increased from -12.863 to -10.926 dB. The increase in the SLL is the result of two large sidelobes that are located at $\phi = 40°, 140°$. We see this behavior also with the planar aperture case when Halton sampling is used, where the main beam is made more visible but usually one or two abnormally large sidelobes are present within the

pattern. Other than these two sidelobes, the performance in the xz-plane over ϕ is reasonably well, where the rest of the sidelobes are kept well below -10 dB. The performance in the yz-plane sees slight improvement, where the SLL was measured at -0.105 dB. This was the plane where we received the most grating lobes with uniform sampling and Halton is able to remove nearly all of them except for the two lobes at $\theta = 90°, -90°$. Like the xz-plane, the SLL in the xy-plane increased, particularly from -8.083 to -7.899 dB. This is caused by the two sidelobes on each side of the main beam. Despite the increase in SLL, we see that Halton sampling is consistent at reducing the rest of the sidelobes well below -10 dB. The grating lobe that appears at $\phi = 180°$ for uniform sampling is also removed with Halton sampling, proving that this LDS technique is still able to remove grating lobes and reduce the SLL for larger aperture sizes. However, by having a larger aperture size the elements were able to be distributed farther apart from each other, where the average minimum element spacing increased from 0.854λ for case 1 to 0.920λ for case 2. The bar plot depicts that the minimum element spacings started to converge more towards λ and away from $\lambda/2$, since there were very few elements that were remaining around $\lambda/2$ minimum element spacing.

The results for Poisson sampling confirmed that as the aperture size increases, the performance for Poisson disk sampling also improves, as suggested in Figure 6.6. The main beam is easily visible in the 3D radiation pattern and the grating lobes are once again removed from the pattern. The SLL is also significantly reduced where the pattern indicates that the largest sidelobes appear in the xy-plane cut. The xz-plane displays a tremendous performance from Poisson sampling, where the SLL is -12.398 which is due to the two lobes on both sides of the main beam. Everywhere else over θ, the rest of the sidelobes are kept close to or below -20 dB which is the best performance we've seen yet from any sampling method. Even though it's a slight decrease, the SLL decreased from 0 dB in case 1 to -1.806 dB for the yz-plane. This is the plane cut that is notoriously known for the 4 grating lobes produced by uniform sampling and when we examine this plane cut for Poisson sampling, we are able to see that the grating lobes are removed and the large sidelobe at $\theta = 90°$ is

starting to decrease in magnitude. Unlike Halton sampling, the SLL for the xy-plane cut for case 2 is reduced slightly, where the measured value for the SLL is -7.606 dB. The high SLL is caused by the two sidelobes on each side of the main beam. However, the rest of the lobes in the pattern for this plane cut are kept below -10 dB. The grating lobe that is encountered with uniform sampling at $\phi = 180^\circ$ is also removed, where the SLL at this particular angle is now reduced below -20 dB. The minimum element spacing distribution is relatively the same when compared to case 1, where the average minimum element spacing slightly increased to 1.16λ. From the bar plot, we are able to see that the majority of the elements have a minimum element spacing that is close to λ and very few elements have a minimum element spacing $\geq 1.4\lambda$.

For case 2, we double the height of the cylinder which increased the aperture size of the array. From antenna array theory, we know that a larger aperture size will result in a more narrow beam, which was depicted in each of the results. This larger aperture size didn't effect the LDS techniques ability to reduce the SLL of the array or remove the grating lobes from the radiation pattern. However, with a larger aperture size the continues on from Chapter 5, where we see that Poisson disk sampling becomes the dominant LDS technique when we have a larger aperture size. The performance of each array design is presented in Table 6.2 for case 2.

Table 6.2 Performance metrics for Uniform, Halton, and Poisson sampling for Case 2

Method	SLL xy-plane	SLL yz-plane	SLL xy-plane	Average Min. Spacing (λ)
Uniform	-1.996 dB	0 dB	-1.995 dB	1.4
Halton	-10.926 dB	-0.105 dB	-7.899 dB	0.920
Poisson	-12.398 dB	-1.806 dB	-7.606 dB	1.16

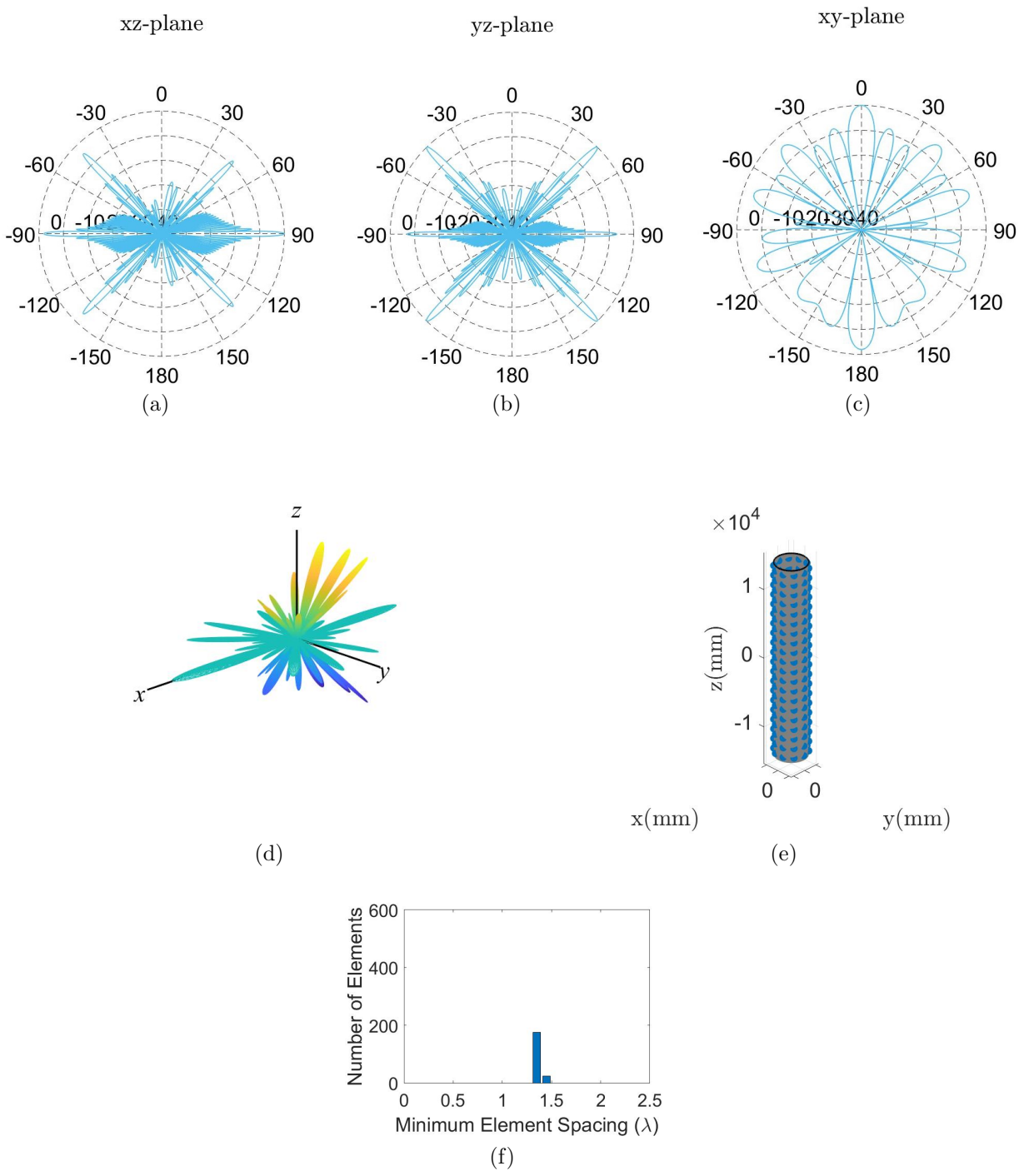

Figure 6.4 Radiation pattern slices in all principal planes, 3D radiation pattern, element distribution on the cylinder, and bar plot of the minimum element spacing for case 2 using uniform sampling: (a) Pattern slice in the xz-plane, (b) Pattern slice in the yz-plane, (c) Pattern slice in the xy-plane, (d) 3D radiation pattern, (e) Element distribution on the cylinder (f) Bar plot of the minimum element spacing

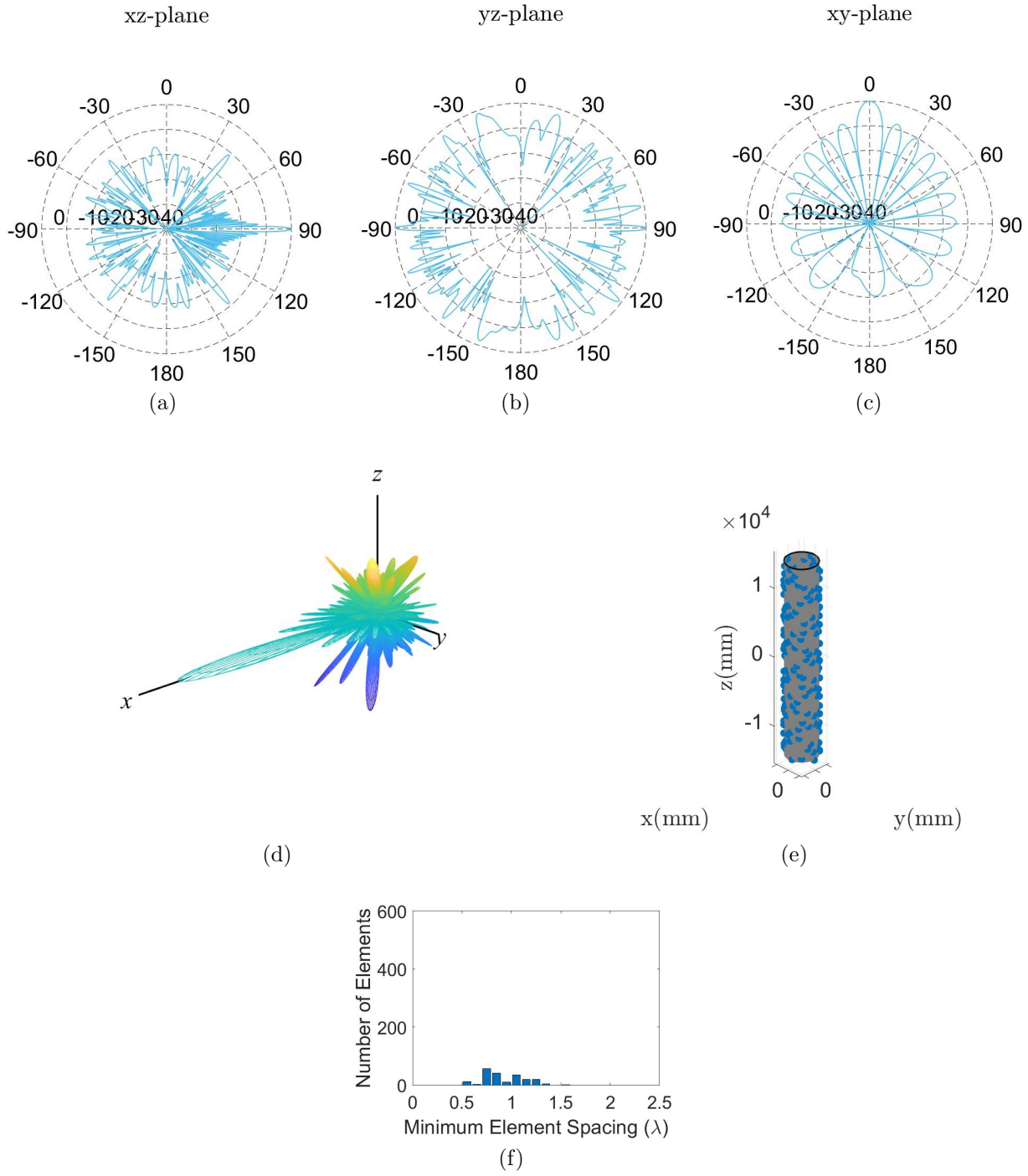

Figure 6.5 Radiation pattern slices in all principal planes, 3D radiation pattern, element distribution on the cylinder, and bar plot of the minimum element spacing for case 2 using Halton ($b_1 = 2, b_2 = 7$) sampling: (a) Pattern slice in the xz-plane, (b) Pattern slice in the yz-plane, (c) Pattern slice in the xy-plane, (d) 3D radiation pattern, (e) Element distribution on the cylinder (f) Bar plot of the minimum element spacing

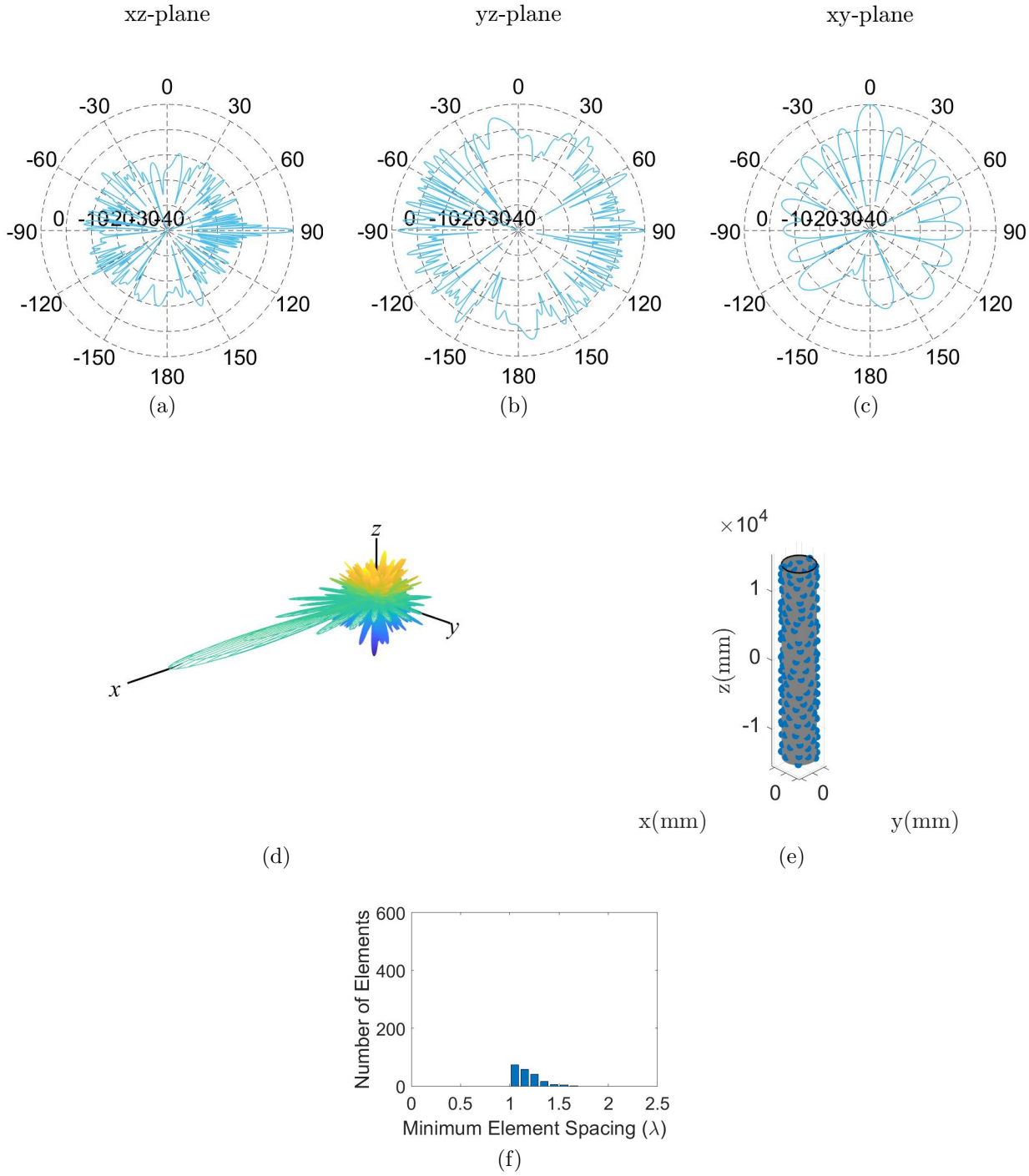

Figure 6.6 Radiation pattern slices in all principal planes, 3D radiation pattern, element distribution on the cylinder, and bar plot of the minimum element spacing for case 2 using Poisson disk sampling: (a) Pattern slice in the xz-plane, (b) Pattern slice in the yz-plane, (c) Pattern slice in the xy-plane, (d) 3D radiation pattern, (e) Element distribution on the cylinder (f) Bar plot of the minimum element spacing

6.3.3 Case 3 - Cylindrical Platform with 42λ Length and 8.4λ Diameter

For the final case, we increase the height of the cylinder again by 14λ and then decrease the radius which results in the following new dimensions $r = 8.4\lambda/2\pi$ and $h = 42\lambda$. The surface area of the cylinder that we can potentially populate has a larger area than case one but a smaller area than case two, where the area of the cylindrical aperture for case three is $336\lambda^2$. When the array is fully populated with elements spaced by $\lambda/2$, we can have up to 84 rings with 16 elements in each ring, totaling up to 1344 elements. After we increase the element spacing to 1.4λ to remove elements from the aperture, 30 rings of 6 elements are now able to fit on the cylindrical surface, resulting in a sparsity level of 12.76%.

The results produced for uniform sampling for case 3 are displayed in Figure 6.7. Like before, the aperture area is much larger than that of case 1, so the main beam that's produced is much more narrow. Likewise, the main beam is indistinguishable in the 3D radiation pattern, where the grating lobes are heavily present in both the yz and the xy-plane. By decreasing the size of the radius, the SLL in the xz-plane improves tremendously from the two previous cases, where the SLL decreases to -6.025 dB. This is caused by the grating lobe produced at $\theta = -90°$. Four other large sidelobes are also produced within the pattern, where two of them have a magnitude of -10 dB and the other two have a magnitude of -20 dB. The decrease in radius may have improved the xz-plane, but the energy from this plane was shifted to the two other planes. The yz-plane had a measured SLL at 0 dB, which is caused by the result of six grating lobes being present within this plane. The xy-plane also had a SLL of 0 dB, where two grating lobes are present in this plane and three large sidelobes are also present within the pattern at $\phi = -60°, 60°$, and 180°, where the SLL at these values of phi are > -10 dB.

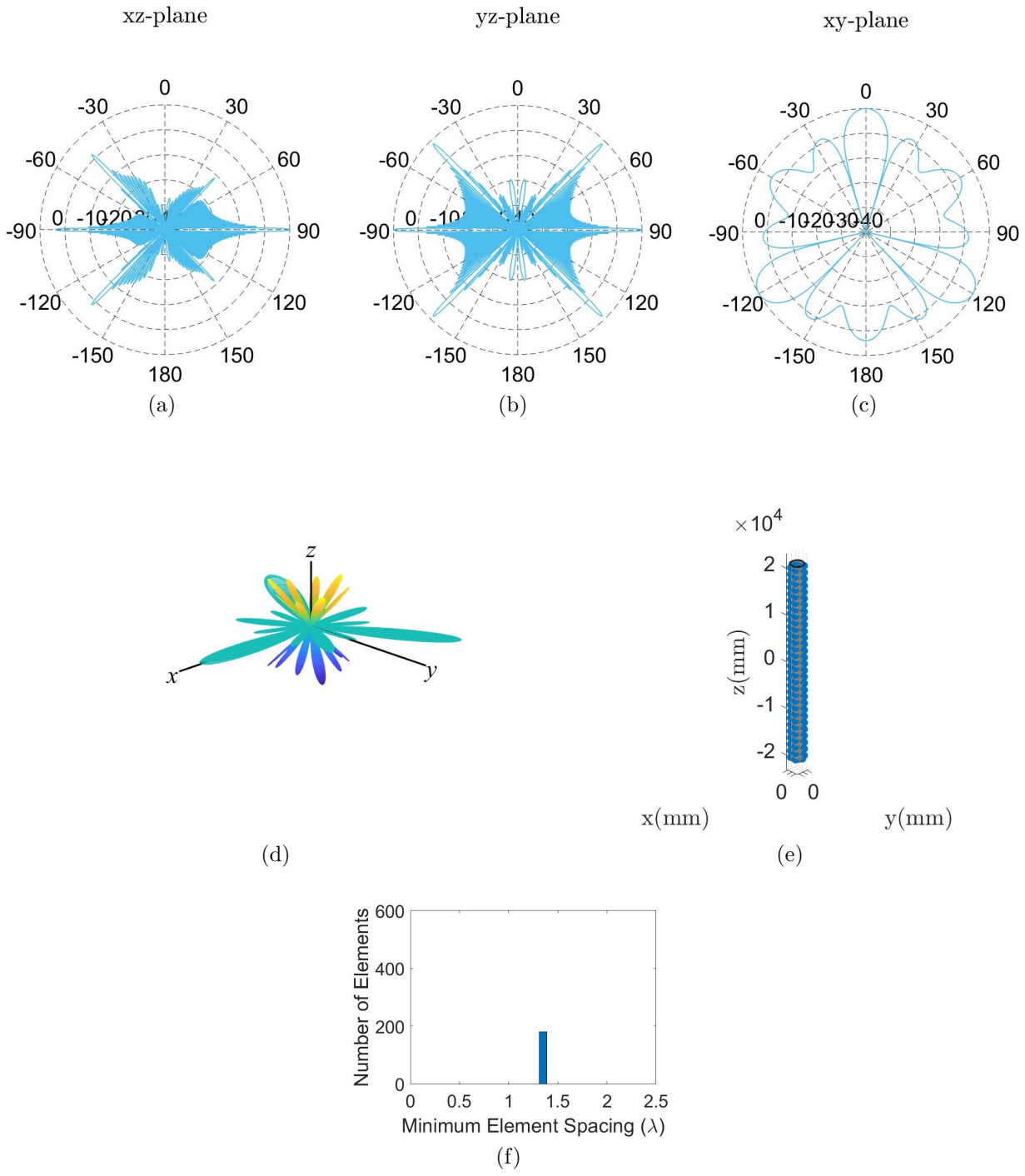

Figure 6.7 Radiation pattern slices in all principal planes, 3D radiation pattern, element distribution on the cylinder, and bar plot of the minimum element spacing for case 3 using uniform sampling: (a) Pattern slice in the xz-plane, (b) Pattern slice in the yz-plane, (c) Pattern slice in the xy-plane, (d) 3D radiation pattern, (e) Element distribution on the cylinder (f) Bar plot of the minimum element spacing

In Figure 6.8, the results produced by Halton sampling are displayed. Once more, Halton sampling proves its effectiveness by removing the grating lobes and reducing the SLL. The only noticeable difference between this case and the previous cases is that the beam is narrow in the xz-plane but broadens out in the xy-plane, which was also displayed in the results for uniform sampling for this case. In the xz-plane, the SLL is measured at -10.061, which was the worst performance out of all three cases but was only slightly worse than case two. Excluding the sidelobes close to the main beam, the rest of the sidelobes are kept below or around -20 dB. However, the yz-plane displays the best performance out of the two previous cases with a measured SLL at -1.010 dB. For case three, six grating lobes were produced with uniform sampling and Halton sampling was able to eradicate all six of the grating lobes as shown in the plane cut. As mentioned previously, the beamwidth increases with a smaller radius in the xy-plane as displayed in the radiation pattern. The SLL was measured at -7.899 dB and was once again caused by the two sidelobes on each side of the main beam. The two sidelobes that were produced with uniform sampling were also removed from the pattern. Uniform sampling previously produced three large sidelobes at $\phi = -60°, 60°$, and $180°$. With Halton sampling, the two sidelobes at $\phi = -60°, 60°$ were replaced with nulls and the sidelobe at $\phi = 180°$ was brought below -10 dB. The minimum element spacing shows another shift in the element distribution, where the average minimum element spacing was measured at 0.953λ. For the first time out of the previous two case, we see more elements fall $\geq \lambda$ and fewer elements having a minimum element spacing close to $\lambda/2$.

The final results produced by Poisson disk sampling for this final case can be found in Figure 6.9. Poisson disk sampling proved that it was able to remove all grating lobes and lower the SLL for each of the three cases, as shown in the 3D radiation pattern. Similar to Halton sampling, we see that the majority of the largest sidelobes appear within the xy-plane. In the xz-plane, the SLL is measured at -13.278 which was the lowest it has been over all three cases. Aside from the SLL produced by these two sidelobes, the rest of the sidelobe level is kept relatively low, where the majority of the sidelobes are kept below

-20 dB. Likewise, the yz-slice has a drop in the SLL from cases one and two, where the resulting SLL is -1.511 dB. Similar to Halton sampling, all six of the grating lobes were removed from the pattern slice, where these six grating lobes made it difficult to distinguish the main beam in the 3D radiation pattern. The xy-plane has a SLL at -7.808 dB, which again was the lowest value that this plane slice has reached over the previous two cases. The two grating lobes produced by uniform sampling are removed from the pattern with Poisson disk sampling and similar to Halton sampling, two nulls are placed at $\phi = -60°, 60°$ instead of two sidelobes with large magnitudes. The other sidelobe produced at $\phi = 180°$ was dropped to approximately -15 dB. For the minimum spacing between elements, we see that the majority of the elements have a minimum element spacing close to λ and very few $\geq 1.4\lambda$. This has caused for the average element spacing to drop back down to 1.13λ, which was the same for case one.

For this final case, we were able to see that once again, both Halton and Poisson disk sampling were able to remove the grating lobes produced by uniform sampling and reduce the SLL of the array. With this aperture size being the second largest next to case two; Poisson disk sampling was the more dominant LDS method, which was expected since the analysis of sparse planar arrays suggested that Poisson disk sampling is more successful at lowering the SLL when the aperture size is larger than any of the other LDS methods. By simultaneously decreasing the radius and increasing the aperture size, we see that the main beam becomes more narrow in the xz-plane but also widens in the xy-plane, becoming more like a fan beam which is produced by a single ring array, as shown in Appendix C. The measured SLL for each of the principal planes and the average minimum element spacings are displayed in Table 6.3.

Table 6.3 Performance metrics for Uniform, Halton, and Poisson sampling for Case 2

Method	SLL xy-plane	SLL yz-plane	SLL xy-plane	Average Min. Spacing (λ)
Uniform	-6.025 dB	0 dB	0 dB	1.4
Halton	-10.061 dB	-1.010 dB	-7.755 dB	0.953
Poisson	-13.278 dB	-1.511 dB	-7.808 dB	1.13

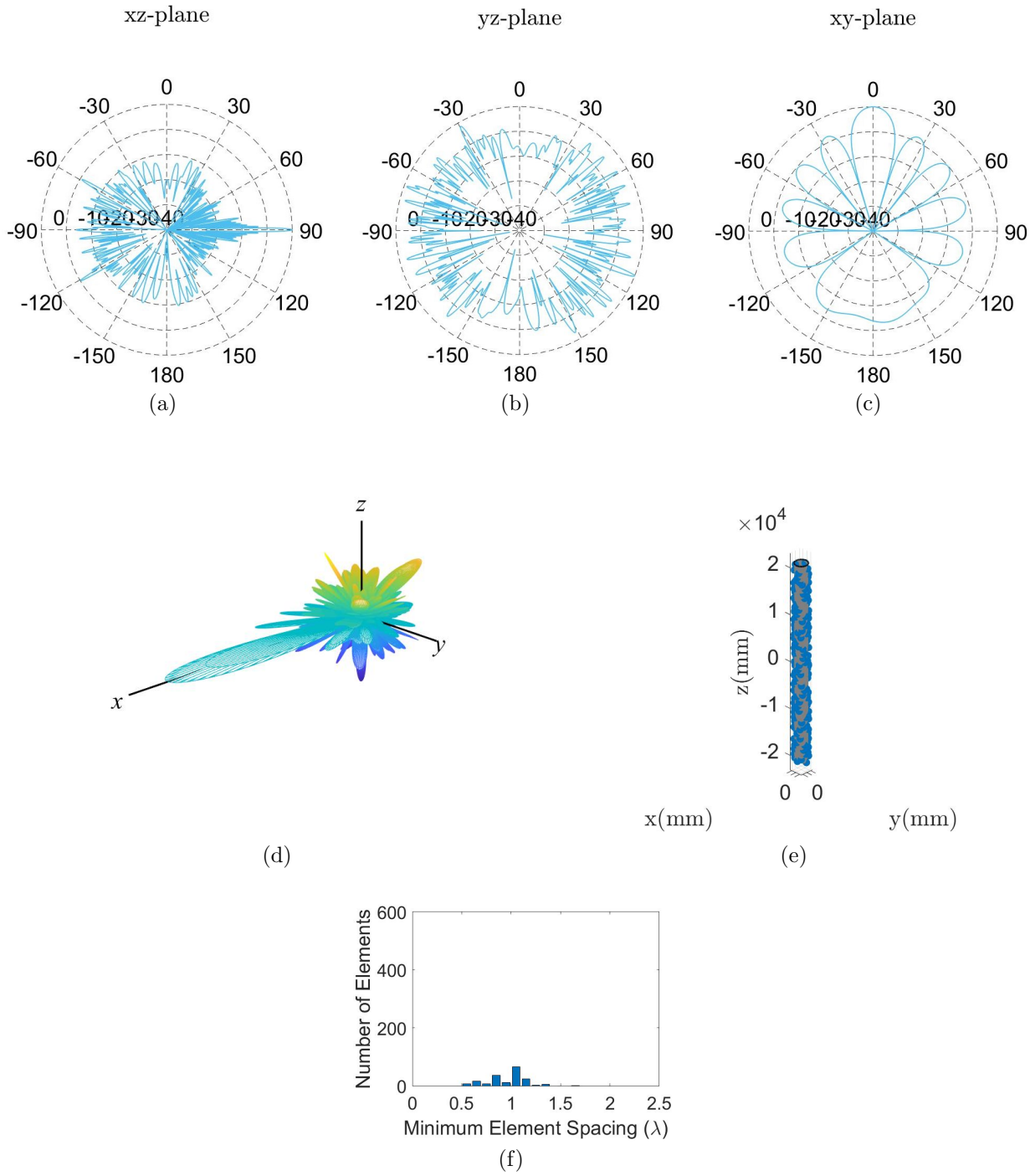

Figure 6.8 Radiation pattern slices in all principal planes, 3D radiation pattern, element distribution on the cylinder, and bar plot of the minimum element spacing for case 3 using Halton ($b_1 = 2, b_2 = 7$) sampling: (a) Pattern slice in the xz-plane, (b) Pattern slice in the yz-plane, (c) Pattern slice in the xy-plane, (d) 3D radiation pattern, (e) Element distribution on the cylinder (f) Bar plot of the minimum element spacing

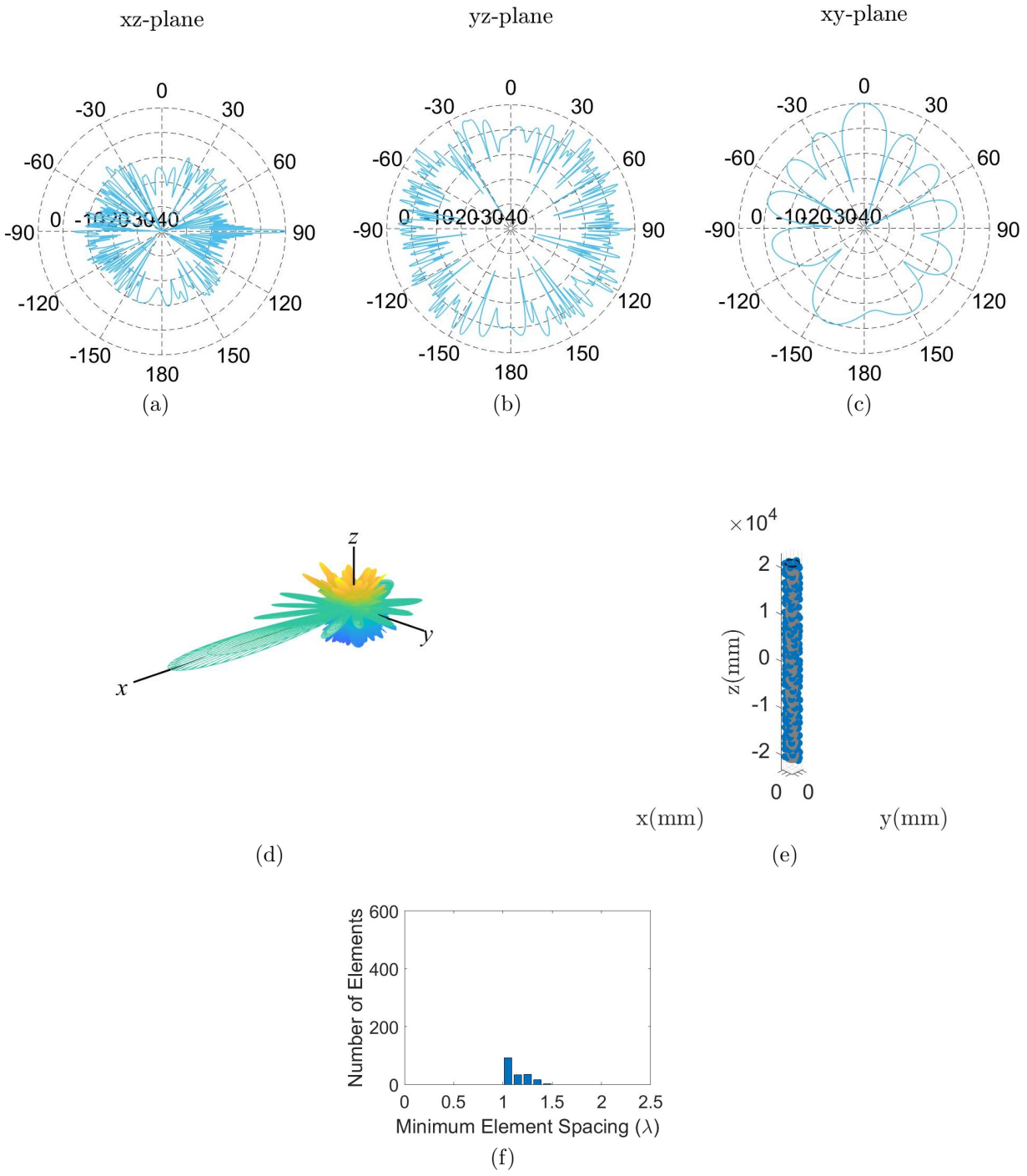

Figure 6.9 Radiation pattern slices in all principal planes, 3D radiation pattern, element distribution on the cylinder, and bar plot of the minimum element spacing for case 3 using Poisson disk sampling: (a) Pattern slice in the xz-plane, (b) Pattern slice in the yz-plane, (c) Pattern slice in the xy-plane, (d) 3D radiation pattern, (e) Element distribution on the cylinder (f) Bar plot of the minimum element spacing

6.4 Active Sector & EM-Model

In this section, the concept of an active sector for a cylindrical array is presented and a designed EM-model in HFSS for the uniform and Halton ($b_1 = 2, b_2 = 7$) arrays are presented. The purpose of this section is to demonstrate that the proposed LDS techniques not only work based off of array theory but can still successfully function when both array and EM-theory are considered.

The role of an active sector in a cylindrical array is to have a section of the the cylindrical array to transmit at once and have the rest of the elements turn "off". By doing so, we say that elements with an azimuthal angle that falls between $\phi_{\min} \leq \phi \leq \phi_{\max}$ are powered on and transmitting and the rest of the elements are powered down and not transmitting. There are several factors behind the use of an active sector. The first factor is that it's inefficient to have all the elements powered on for a particular application, where we may desire to only have elements on when they are within the line of sight of the receiver, since elements that aren't in the line of sight will have a long path to transmit to the receiver. Another motivation is that the application requires minimal interference and from the results in the first section, we see that a cylindrical array has full azimuthal coverage, meaning that we will be transmitting over the entire azimuthal range but with different gain levels.

6.4.1 MATLAB Model Active Sector

For our analysis of the active sector case, we base our MATLAB and HFSS model off of case 1 used for the cylindrical array. This case consisted of a cylinder that has a radius of $r = 14\lambda/2\pi$, height $h = 14\lambda$, and an aperture size of $196\lambda^2$. Particularly, we will be designing the array to operate at 10 GHz and have an inter element spacing of 1.4λ for when uniform sampling is used. For the active sector, we will specify the elements that fall between the azimuthal region $90° \leq \phi \leq 90°$ to be powered on. For the uniform sampled array, this will consist of five elements on each of the 10 rings to be powered on and transmitting. The results produced for both uniform and Halton sampling for the active sector case are

presented in Figures 6.10 and 6.11.

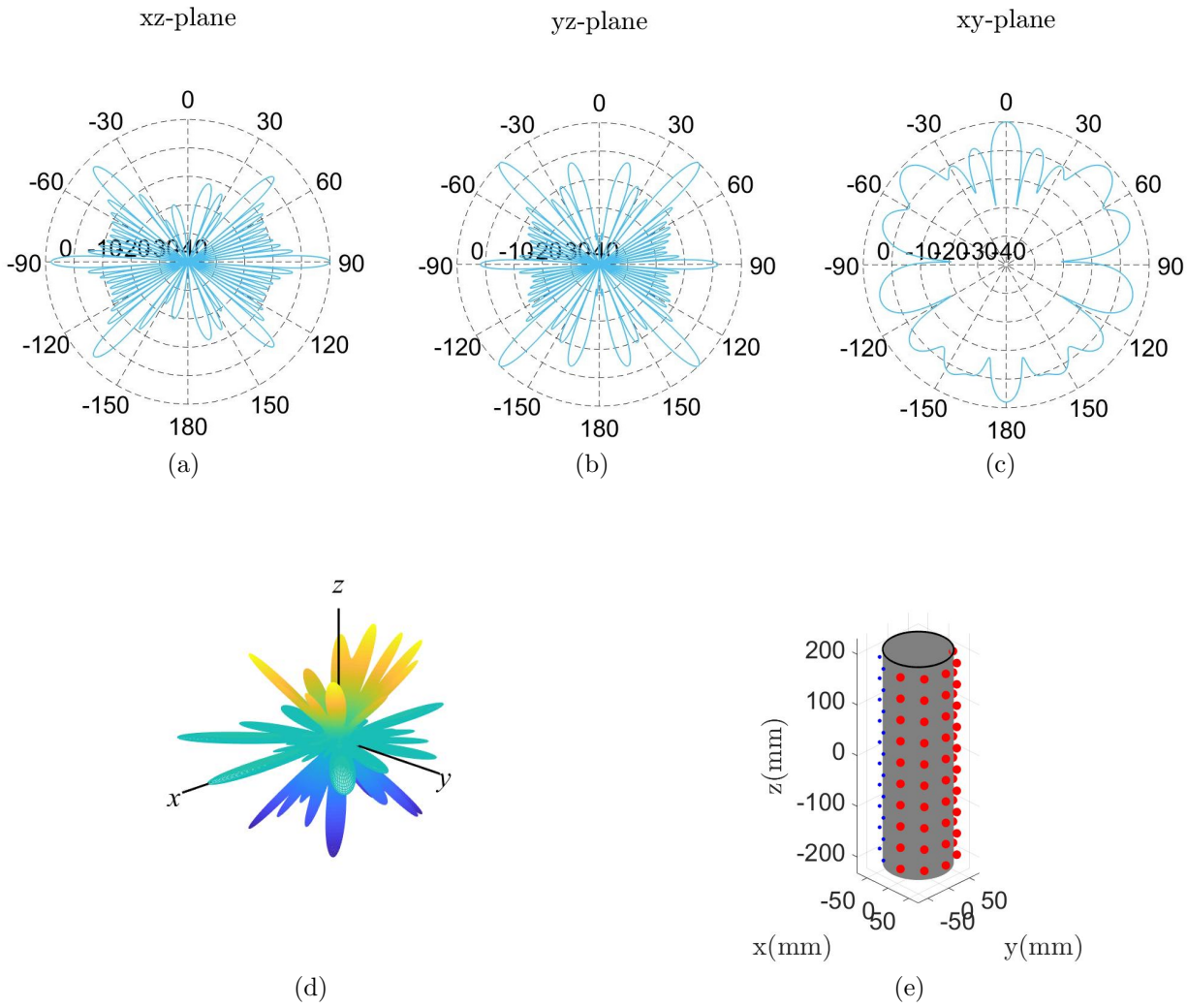

Figure 6.10 Radiation pattern slices in all principal planes, 3D radiation pattern, and element distribution on the cylinder for the active sector case with uniform sampling: (a) Pattern slice in the xz-plane, (b) Pattern slice in the yz-plane, (c) Pattern slice in the xy-plane, (d) 3D radiation pattern, (e) Element distribution on the cylinder where (red) signifies active elements and (blue) are the elements left off

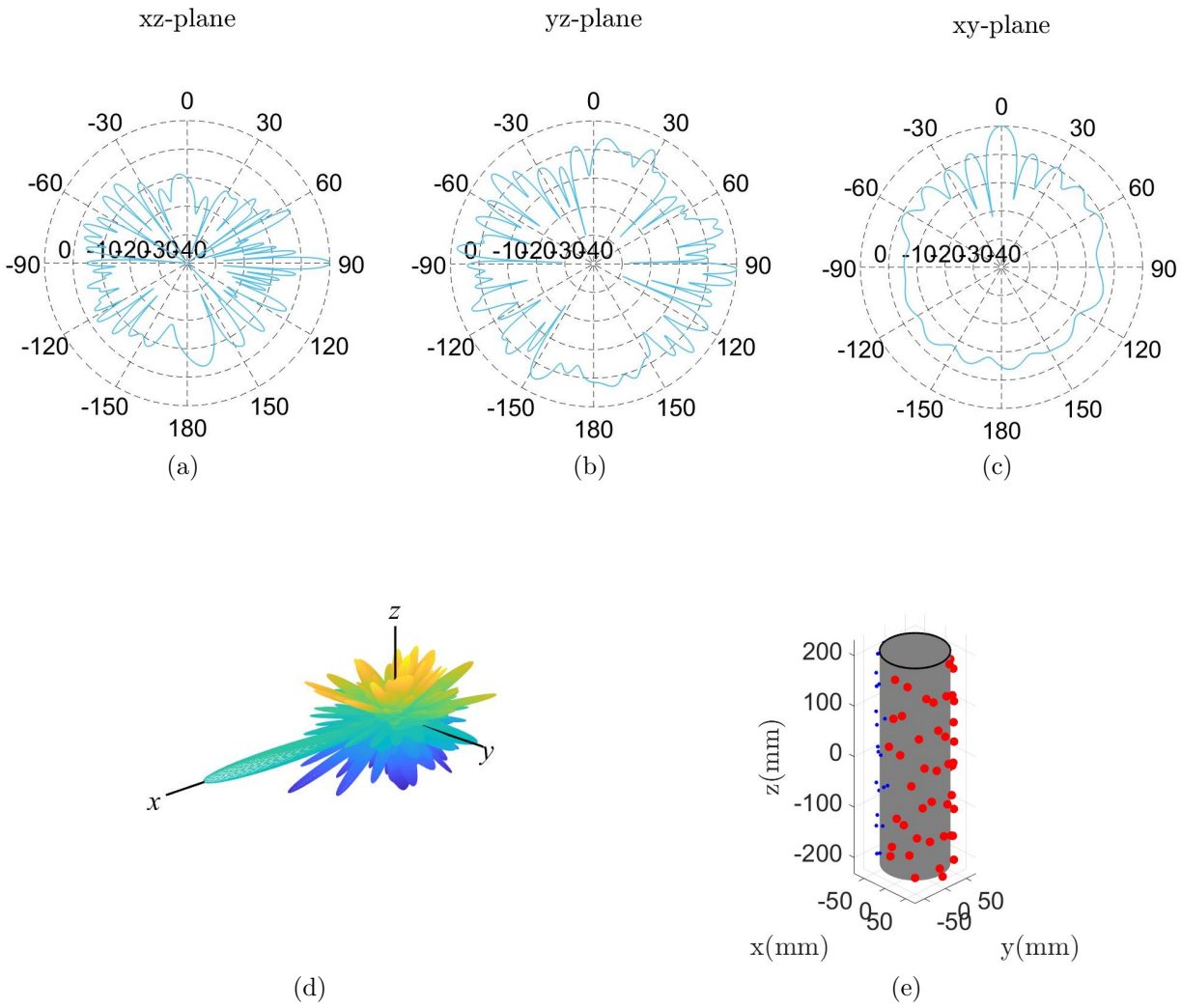

Figure 6.11 Radiation pattern slices in all principal planes, 3D radiation pattern, and element distribution on the cylinder for the active sector case with Halton sampling: (a) Pattern slice in the xz-plane, (b) Pattern slice in the yz-plane, (c) Pattern slice in the xy-plane, (d) 3D radiation pattern, (e) Element distribution on the cylinder where (red) signifies active elements and (blue) are the elements left off

The results produced for the active sector bear many similarities to that of the original cylindrical array cases that we studied for the previous sections. For uniform sampling, we see that with the active sector, there are many grating lobes and large sidelobes that make the main beam indistinguishable from all the other lobes that are produced in the 3D pattern. Meanwhile for Halton sampling, the grating lobes are removed from the pattern and

the large sidelobes are reduced to a low enough level to allow us to be able to distinguish which beam is the main beam in the pattern. Since we are only using a portion of the elements for the active case when compared to the original case 1 in the previous section, we have a lower degree of resolution which makes it difficult to greatly reduce the sidelobes, resulting in a higher SLL than for the instance of when we utilize all of the elements on the cylinder. As depicted in each of the pattern cuts, we have many grating lobes in the xz and yz-planes and very high SLL in the xy plane, where the majority of the sidelobes in this plane are over -10 dB. For the Halton sampled array, the grating lobes in the xz-plane are removed and we are only left with two large sidelobes with a magnitude of -10 dB. All of the grating lobes that were introduced into the yz-plane cut for uniform sampling are also removed with Halton sampling. We see that with the xy-plane cut, we do have two sidelobes over -10 dB but the majority of the rest of the sidelobes are kept below -10 dB, which is a major improvement to the array pattern when compared to uniform sampling.

6.4.2 HFSS Model Active Sector

For the HFSS model, we are able to see many of the phenomena and concepts that are either ignored or approximated in classical array theory. Such as for the array factor, the calculation is made off the assumption that the antenna elements are isotropic radiators. In the HFSS mode, we used a 10 GHz dipole antenna above a ground plane as our element of choice. From antenna theory, we know that an isotropic antenna has a spherical radiation pattern and a dipole antenna has a figure 8 shaped pattern, where radiation intensity is max in the directions normal to the dipole and nulls are present in the directions that are parallel to the antenna. The designed dipole and it's frequency response for S_{11} are displayed in Figure 6.12. In order to get the dipole to resonate at 10 GHz, we had to had to design the length of the dipole to be $\lambda/2$. For 10 GHz, the wavelength is approximately 29 mm and when we design and tune the dipole to perfectly resonate at 10 GHz, we resulting length of the dipole ended up being 13.1 mm. The corresponding radius for the dipole is 0.1 mm. The dipole receives the current excitation in the center, as indicated by the red rectangle in

Figure 6.12 (a), where the length of the excitation gap is 0.5 mm.

The dipole is place above a ground plane that has dimensions $2\lambda \times 2\lambda$, where we used the infinite ground plane function for the HFSS simulation. Since a dipole antenna radiates on each side of the copper wire, we use the ground plane to reflect the second half of the radiation pattern so that it meets in-phase with the front half of the pattern, effectively increasing the magnitude of the radiation pattern in only one normal direction. With our geometry setup, this corresponds to the direction $\theta = 0°$.

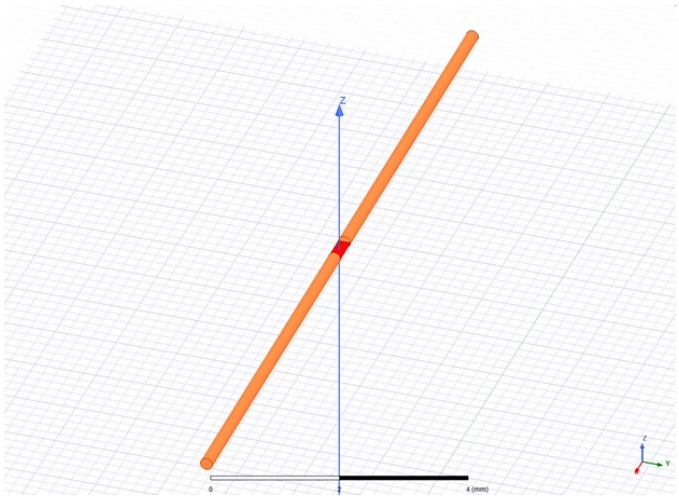

(a)

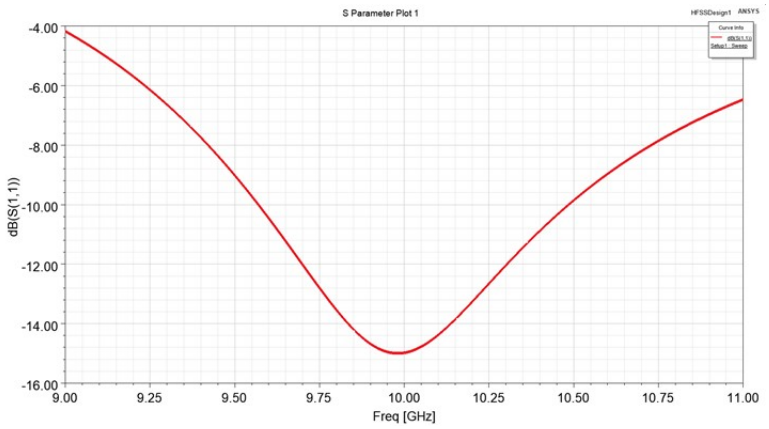

(b)

Figure 6.12 10 GHz dipole antenna designed in HFSS and its corresponding frequency response for S_{11}: (a) The dipole has a length of 13.1 mm and has a gap of 0.5 mm which is where the dipole is excited, (b) Frequency response of the dipole antenna from 9-11 GHz. We are able to see from the plot that the dipole has an operating frequency of $f_0 = 10$ GHz

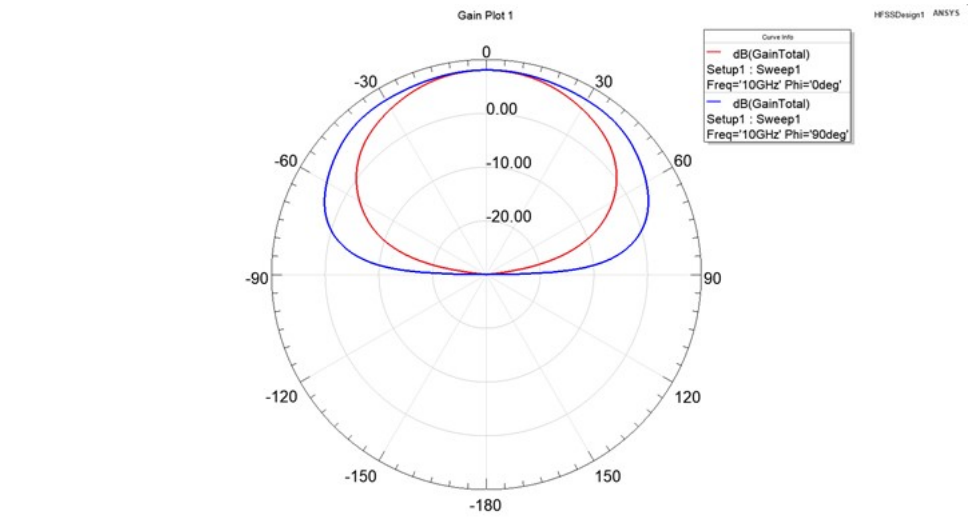

(a)

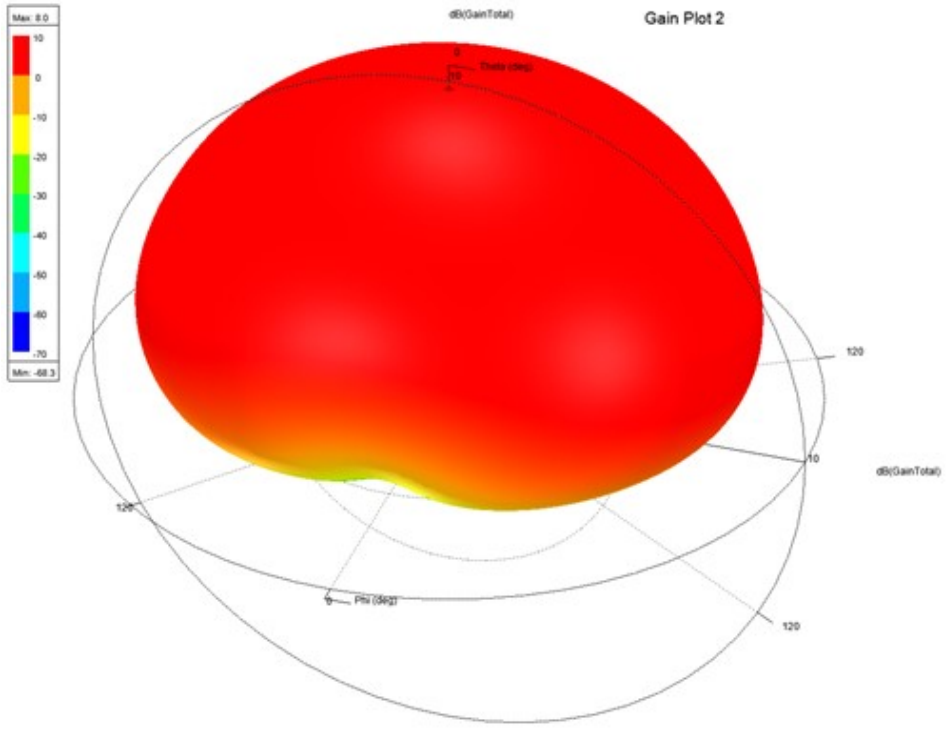

(b)

Figure 6.13 Radiation pattern slices for the E and H-field and 3D pattern of the 3D pattern of the designed dipole over the ground plane: (a) Pattern slices over θ for $\phi = 0°$ (red) and $\phi = 90°$ (blue). The red slice contained the E-field vector and the blue slice contains the H-field vector. We see that the H-field has a larger beamwidth than the E-field, (b) The full 3D radiation pattern of the 10 GHz dipole antenna over the ground plane. The reflected radiation from the ground plane adds constructively and the resulting gain of the antenna is 8 dB

Note that the dipole was placed 7.1 mm away from the ground plane and the radiation in the direction of the ground plane was reflected from the ground plane and added constructively in the direction of $\theta = 0°$. The plane slices containing the E and H-fields along with the 3D radiation pattern for the 10 GHz dipole antenna are shown in Figure 6.13. The pattern slices that contain the E and H-field vectors are when we scan over θ for slices at $\phi = 0°$ and $\phi = 90°$ respectively. We are able to verify with the 3D radiation pattern that we the radiation in the direction of the ground plane is reflected in the positive z-direction and adds constructively with the rest of the pattern, where the gain of a single dipole is 8 dB.

In order to verify the model, the position of the dipole is moved to an off-center location, as we see in Figure 6.14. Before we could move to the cylindrical case, we had to verify that the current distribution of the dipole would be symmetrical and centered around the position of the dipole and that these features wouldn't be affected when the dipole was moved off center of the ground plane. By moving the dipole off center, we see that there are no changes to the current distribution and we are able to move onto the cylindrical ground plane instance.

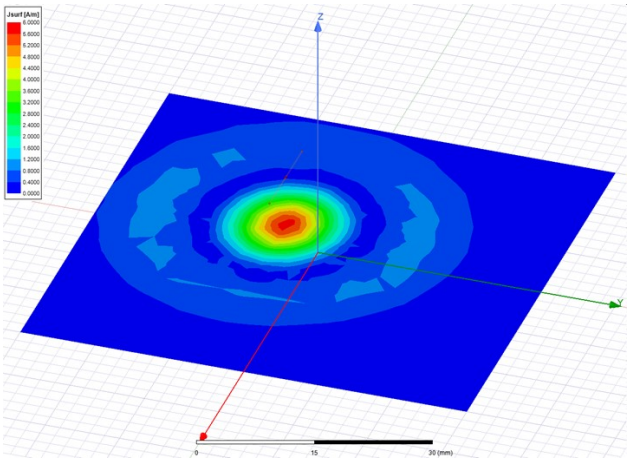

Figure 6.14 Current distribution of the dipole antenna over the ground plane when the dipole is placed to an off-center location

For the cylindrical ground plane instance, we model the dipoles placed on a cylindrical aperture. In our first step, the dipole was placed at the same distance away from the small cylinder. The cylinder has a height of 15λ and a circumference of 14λ. We are able to verify the current distribution on the cylindrical aperture, as shown in Figure 6.15 when the dipole was placed next to the large cylinder. This will serve as the platform for our array when we move to the active sector portion. Note that in order to minimize diffraction at the top and bottom edges, no element will be placed above $z = 7\lambda$ or below -7λ.

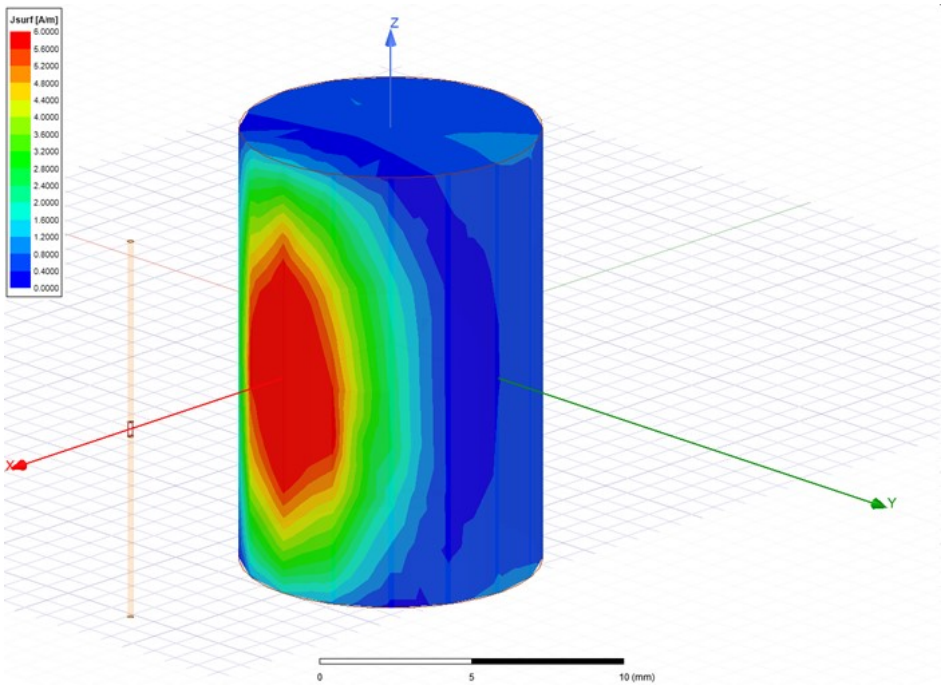

Figure 6.15 Current distribution of the dipole antenna over the cylindrical aperture

Once were were able to verify the current distribution for the cylinder, we were able to move on to designing the cylinder with the dimensions from case 1. At 10 GHz, the cylinder has a height of 450 mm and a radius of 66.85 mm. Note that the same dimensions of the dipole antenna were used. However for the cylindrical cases, our geometry in HFSS has changed, where the cylinder is oriented along the z-axis and the center of the cylinder placed in the xy-plane. For the single dipole test case, we oriented the dipole along the z-axis and placed it on the x-axis at a distance of 7.1 mm from the cylindrical surface.

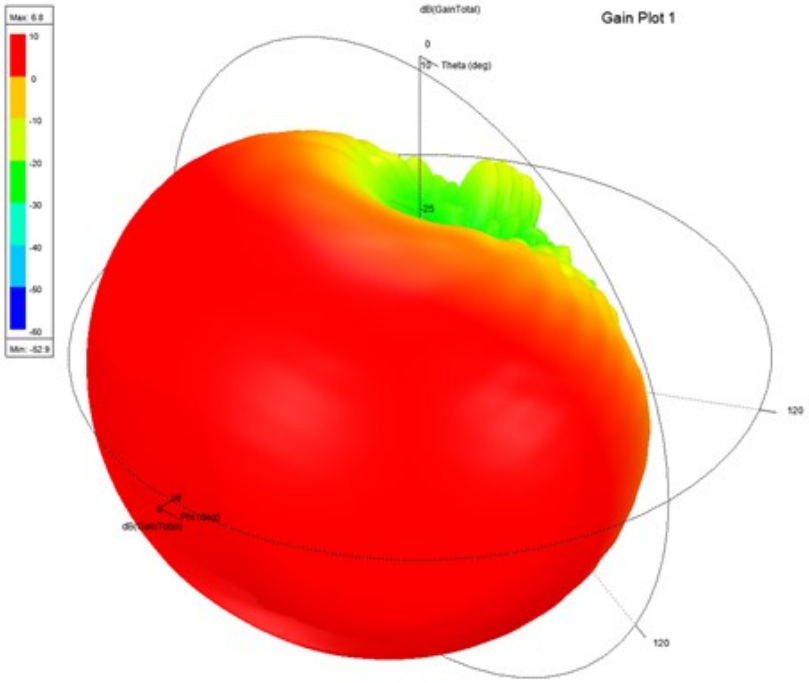

(a)

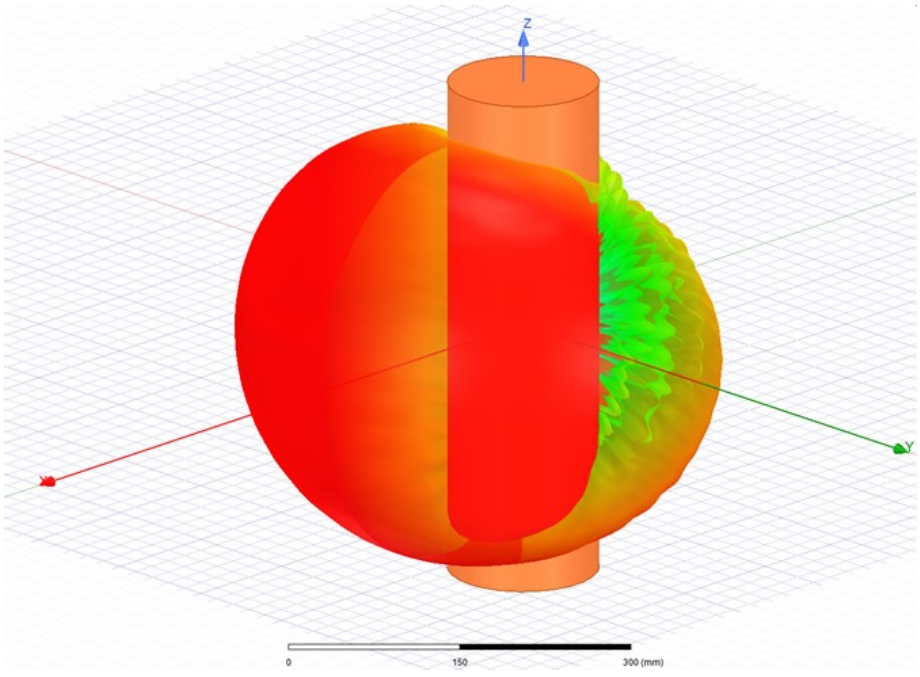

(b)

Figure 6.16 3D radiation pattern of the dipole antenna with a cylindrical ground plane: (a) 3D radiation pattern of the dipole antenna when the cylindrical ground plane is used. The dipole has a gain of 6.4 dBi, (b) The radiation pattern of the dipole displayed on the cylindrical aperture

The 3D radiation pattern of a single dipole with the cylindrical ground plane is shown in Figure 6.16. Note that along with the planar ground plane, the cylindrical ground plane is designed to be a perfect electrical conductor (PEC). In EM-theory, we know that a PEC can not sustain an electric field within the medium but only has charge present on the surface. It's because of this that we are able to have the E-field reflected away from the cylinder. Since the surface area behind the dipole decreases, we also see a decrease in gain of the antenna, where the resulting gain of the dipole is about 6.4 dBi.

For the uniform sparse array, we placed 50 dipole elements at a distance of 7.1 mm from the surface of the cylinder and uniformly distribute the elements along the z-direction. In the azimuth direction, the elements are placed in the range between $-90^\circ \leq \phi \leq 90^\circ$ which is identical to the MATLAB model where the active sector is half of the aperture of the cylinder.

When it came to the spare Halton array, we used the coordinates produced by Halton $(b_1 = 2, b_2 = 7)$ sampling to place the 50 elements that fall in the $-90^\circ \leq \phi \leq 90^\circ$ active sector 7.1 mm away from the cylinder. Since the dipole antennas are relatively small compared to the cylindrical aperture, Figure 6.17 displays the surface currents at 10 GHz of the uniform and Halton distribution on the cylindrical aperture.

In Figure 6.17, we are able to see that for the uniform case, the element spacing is so large that we can distinguish the current distribution for each individual dipole element. The distribution of the surface currents allows us to also visibly see the uniform element spacing between each of the elements and how none of the elements were allowed to fall 7λ from the top and bottom of the cylinder so that we can avoid diffraction. For the Halton sampled array, we are able to distinguish the non-uniform placements of the elements throughout the active sector in the cylindrical aperture. Since some of the antenna elements fall relatively close together with this particular sampling method, we are also able to see that in certain regions on the cylindrical aperture the surface currents of two individual elements is close to merging into a single surface current distribution. This signifies some of the effects that are

not considered in classical array theory.

Finally, Figure 6.18 to 6.20 display the results of the radiation patterns of the uniform and Halton sparse arrays. For the xy-plane cut, we know that the direction of maximal radiation should be at $\phi = 0°$. For the uniform sparse array, we see that this is not the case and that the grating lobes are much higher than the gain of the main beam, where the grating lobes have a gain of 20 dB and the main beam has a gain of 15 dB. We have two other sidelobes next to each of the grating lobes that match the performance of the main beam and a large back lobe as well. However, with the use of Halton sampling, we see that the grating lobes and sidelobes are removed from the pattern, where the direction of maximal radiation is in $\phi = 0°$. The large back lobe is also removed and we can see that Halton sampling has averaged out the pattern of all the dipole elements.

The xz-plane for the uniform array depicts the main beam at $\theta = 90°$ along with two grating lobes and three large back lobes within the pattern cut. Two of the back lobes have a relatively small gain but the back lobe at $\theta = -90°$ has a gain of 0 dB. Once more, we see that through the use of Halton sampling, the grating lobes are greatly reduced and the back lobes are now brought down well below 0 dBi. The plane cut shows that only the main beam has a gain above 10 dBi and the rest of the lobes are kept below this value.

From the results of the EM-model in HFSS, it can be concluded that the LDS technique is successfully able to remove the grating lobes from the radiation pattern and lower the sidelobes when we are handling extremely sparse arrays with element spacing $\geq \lambda$. In the pattern cuts and the 3D pattern, we are able to see the removal of the grating lobes and lowered sidelobe level with the use of the LDS technique. This proves that the use of LDS techniques branches beyond classical array theory and can be considered for the implementation and design of sparse antenna arrays as shown with the high frequency EM-model design in HFSS.

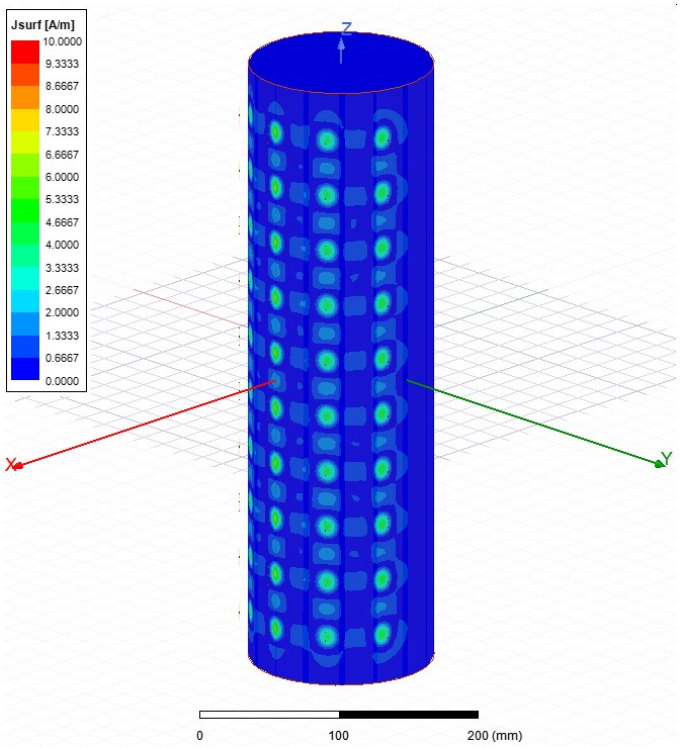

(a)

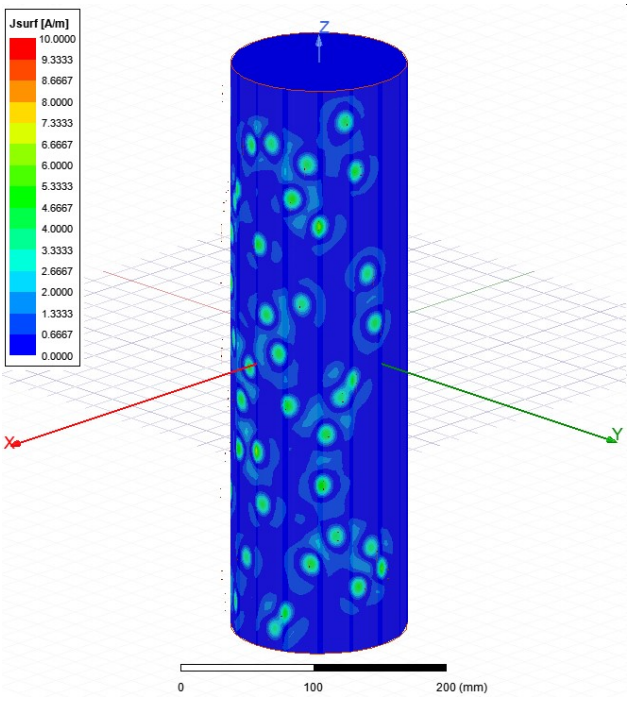

(b)

Figure 6.17 Surface currents for uniform and Halton distributions on the cylindrical aperture: (a) Surface currents for the uniform sparse array, (b) Surface currents for the Halton sparse array

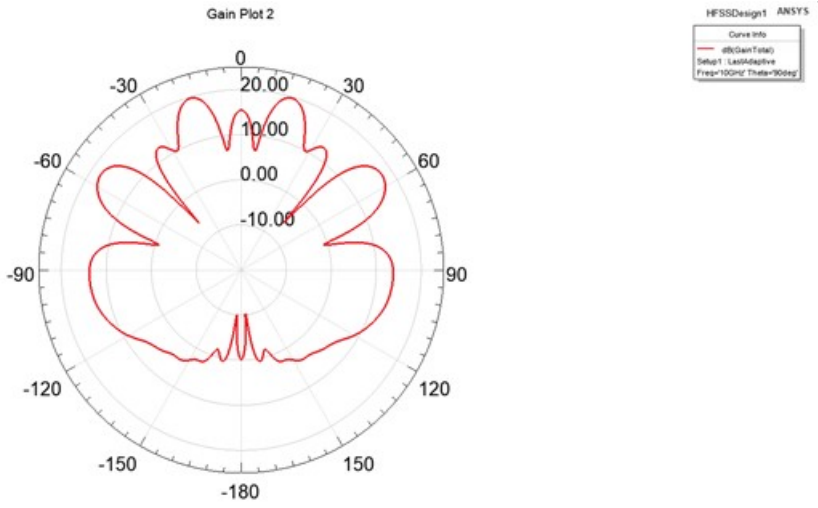

(a)

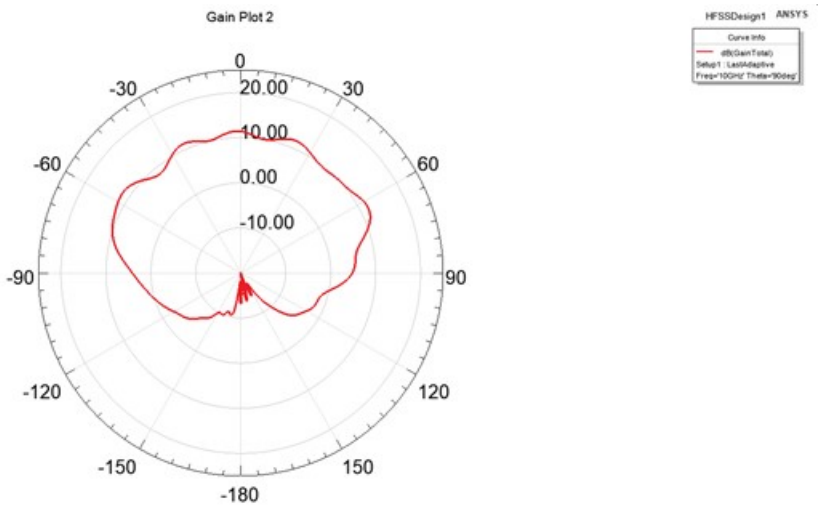

(b)

Figure 6.18 *xy*-plane cuts for the uniform and Halton sparse arrays: (a) Plane cut for the uniform array, (b) Plane cut for the Halton array

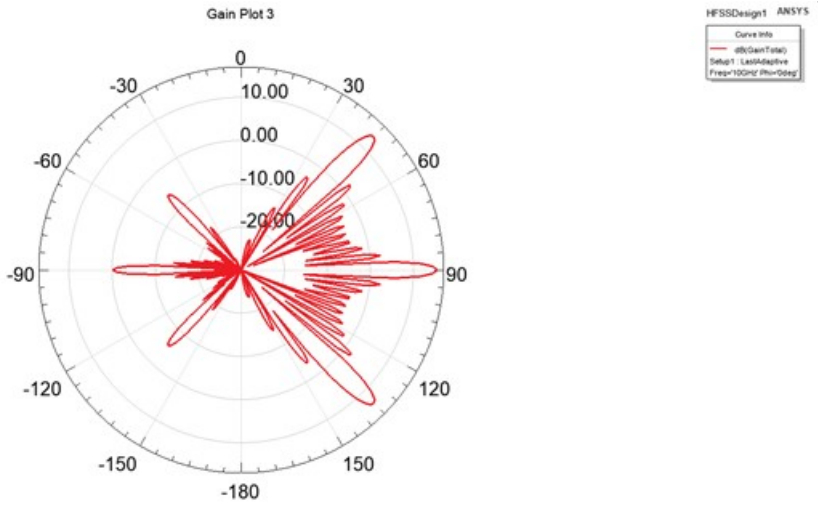

(a)

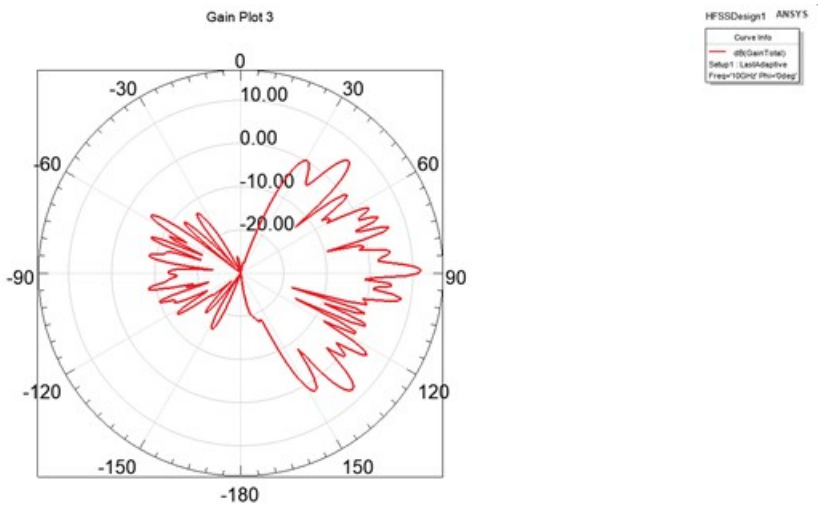

(b)

Figure 6.19 xz-plane cuts for the uniform and Halton sparse arrays: (a) Plane cut for the uniform array, (b) Plane cut for the Halton array

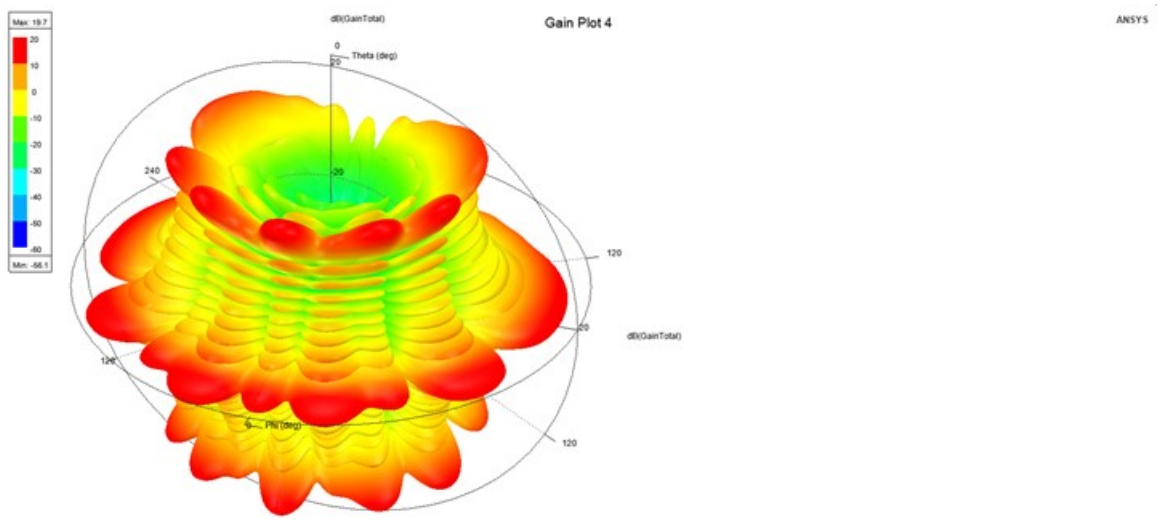

(a)

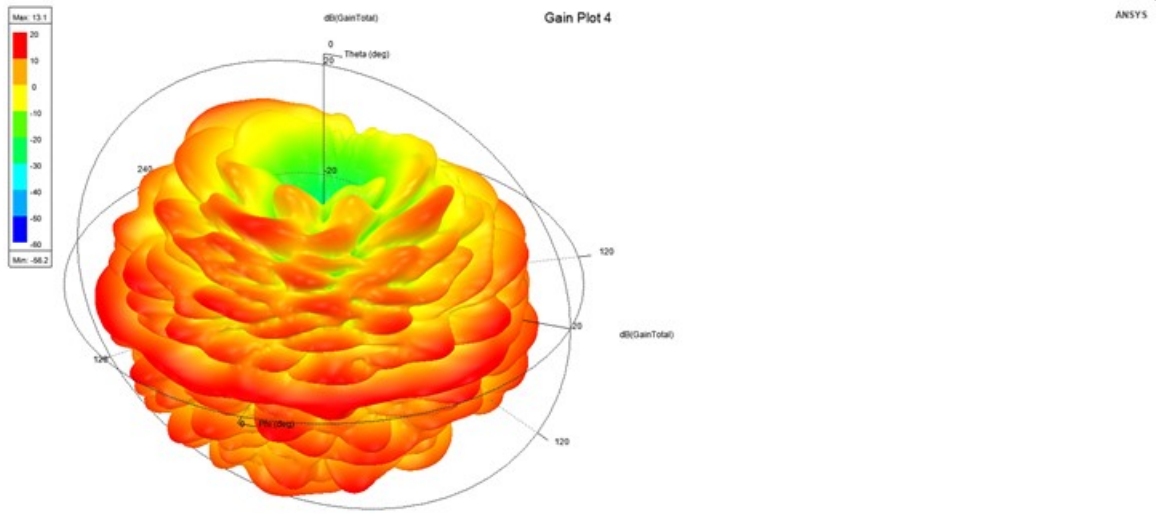

(b)

Figure 6.20 3D radiation patterns for the uniform and Halton sparse arrays: (a) Uniform array 3D pattern, (b) Halton array 3D pattern

CHAPTER 7
CONCLUSION AND FUTURE WORK

The research array of sparse antenna arrays is a growing field, where many in the defense and communications industry desire to design robust and efficient but affordable antenna arrays. A major problem however with sparse antenna arrays, is that when the element sampling for the array is uniform and exceeds one full wavelength, grating lobes are introduced into the radiation pattern, which are unwanted and reduce the amount of transmitted/received power in the direction of the main beam. However, by using LDS methods the elements can be distributed in a manner that provides a cost efficient array design and also removes the grating lobes from the radiation pattern. Random sampling of the array aperture removes the grating lobes from the patterns similar to LDS, however, they don't fully utilize the aperture and leave elements clustered together which results in an array configuration that isn't practical for fabrication. Other methods such as array thinning with GA and convex optimization can successfully design a sparse antenna array but they fall short to the LDS when we reach a high sparsity level or a larger aperture size with many elements. The LDS techniques proposed in this work have been proven to successfully design sparse planar and cylindrical surfaces with various aperture sizes, shapes, and enable beam steering capabilities.

7.1 Achievements & Summary

In Chapter 1, we highlight the desire and motivation for sparse antenna array design, along with current issues with practical design and implementation of them. Previous methods such as random sampling, array thinning, and convex optimization were briefly mentioned and discussed. The short comings of these methods then led us to the motivation for a newer technique that can capitalize on the shortcomings of the already existing methods and prove valuable for the direction that we believe that we see the field of sparse antenna array design heading in.

In Chapter 2, the basic concepts and theory of antenna functionality, EM-wave propagation, and radiation are given. Antenna parameters are also explained and presented for the reader. We then built off the operational theory of antenna radiation principles and gave an overview of the inset fed microstrip patch antenna and modeled it in HFSS for 2.45 GHz. The planar design of the inset fed patch antenna was then extended to the cylindrical case, where we demonstrated the effects of high amounts of curvature introduced to the antenna on the radiation pattern. The chapter then concluded with the fabricated results of planar and conformal microstrip inset fed patch antennas.

Chapter 3 then discussed the theory behind the low discrepancy sampling techniques that are used in this thesis for sparse antenna arrays, along with a more meaningful definition of sparsity in antenna arrays. The chapter also gave an overview of basic planar antenna array theory and the mapping of the low discrepancy sequences to a planar surface was also discussed.

Chapter 4 then introduces, sparse planar arrays based on LDS sampling techniques. Several case studies were conducted, and figures of merit were defined in order to quantify the performance of the LDS techniques, as well as to compare with traditional random approaches. These figures of merit looked at array layout, as well as array radiation patterns. Different aperture shapes, as well as beam-scanning was also studied, and the results showed that these LDS arrays can indeed remove the grating lobe issues associated with sparse planar arrays with any aperture shape and scan direction.

Chapter 6 built off of the planar case and provided the reader with an in depth overview of the most common sparse array design techniques that previously existed which include: array thinning using random element selection, array thinning and geometry optimization using GA, and convex optimization. The LDS techniques and the previous techniques were applied to various aperture sizes and sparsity levels, where we showed in this analysis that all of the previous methods fall short when we reach a sparsity level that is implemented by an element spacing that's $\geq \lambda$.

In Chapter 6, the LDS sampling methods were then applied to 3D arrays, particularly cylindrical arrays. From our discoveries in the work for the previous chapters, we only used two of the LDS techniques that demonstrated the best performance, particularly Halton and Poisson disk sampling. We performed sampling for three different cases which consisted of cylinders with various heights, radii, and aperture sizes. The results demonstrated that the proposed LDS methods were successful at removing the grating lobes and at reducing the high SLL that was encountered with uniform sampling.

7.2 Future Work

Previously in this dissertation, we emphasized on the hierarchical properties of LDS sampling methods. The benefit to having a hierarchical sampling method is that we can easily generate a new sample point without having to recalculate any of the previously generated points. Since the number of sample points can be increased as needed, in sensing or measurement applications, one can increase the number of sampling points to achieve a desired level of accuracy. Another advantage of the sampling methods we provide is the fast computation of the sample points, since they are based on mathematical sequences. Many applications in defense and first responder operations require real-time techniques for sparse array synthesis, and as such, the work here can serve as a time-efficient approach to this problem.

The importance of these two mentioned features is in the emerging field of dynamic sparse arrays. In dynamic sparse arrays, the array geometry has to be adjusted in real time by rapidly changing the positions of elements within the aperture or the volume. So with a technique being hierarchical and with a short computation time, a new configuration for the array can be rapidly adjusted or designed in a short amount of time. Heuristic optimization techniques, such as GA that were studied in this dissertation, take a significant amount of time, and cannot be used when real-time reconfiguration is needed. Also, since constrained optimization problems are often more difficult to solve than unconstrained problems, convex optimization would not be a practical solution for real-time reconfiguration. On the other

hand, with LDS methods that were presented in this work, new elements can be added or adjusted, and the array can be reconfigured with a very fast computation, which is why we believe that these proposed LDS techniques possess a lot of potential for future work in dynamic sparse arrays.

One other area of sparse arrays are digital arrays. While this dissertation focused on analog sparse arrays, the work presented serves as the basis to extend this approach to the digital domain. For interference cancellation or direction finding, typically the amplitude and phase of the elements are adjusted, which can be determined using fast digital beamforming algorithms such as MVDR and MUSIC. These approaches typically need to know the element locations. The LDS approach given in this dissertation, can be used to determine the element locations and combined with beamforming algorithms the elements amplitude and phase can be determined in a time-efficient manner.

REFERENCES

[1] Harry L Van Trees. *Optimum array processing: Part IV of detection, estimation, and modulation theory*. John Wiley & Sons, 2004.

[2] Fawwaz T Ulaby, Eric Michielssen, and Umberto Ravaioli. *Fundamentals of applied electromagnetics 6e*. Prentice Hall, 2001.

[3] IEEE Standards Association et al. 145-2013-ieee standard for definitions of terms for antennas. *IEEE, New York, NY*, 2013.

[4] Y Lo and S Lee. A study of space-tapered arrays. *IEEE Transactions on Antennas and Propagation*, 14(1):22–30, 1966.

[5] Brian P Flannery, William H Press, Saul A Teukolsky, and William Vetterling. Numerical recipes in c. *Press Syndicate of the University of Cambridge, New York*, 24 (78):36, 1992.

[6] Lawrence Davis. Genetic algorithms and simulated annealing. 1987.

[7] DE Goldberg. Genetic algorithms,(1989). *New York, AddisonWesley*.

[8] Randy L Haupt. Thinned arrays using genetic algorithms. *IEEE Transactions on Antennas and Propagation*, 42(7):993–999, 1994.

[9] Matthew B Hawes and Wei Liu. Robust sparse antenna array design via compressive sensing. In *2013 18th International Conference on Digital Signal Processing (DSP)*, pages 1–5. IEEE, 2013.

[10] Wenji Zhang, Lian Li, and Fang Li. Reducing the number of elements in linear and planar antenna arrays with sparseness constrained optimization. *IEEE Transactions on Antennas and Propagation*, 59(8):3106–3111, 2011.

[11] Jianyan Liu, Yanmei Zhang, Weijiang Wang, and Yilong Lu. Generalized design method for the difference co-array of the sum co-array. In *2016 IEEE International Conference on Digital Signal Processing (DSP)*, pages 385–387. IEEE, 2016.

[12] Xiaofei Zhang, Xin Lai, Wang Zheng, and Yunfei Wang. Sparse array design for doa estimation of non-circular signals: Reduced co-array redundancy and increased dof. *IEEE Sensors Journal*, 21(24):27928–27937, 2021.

[13] Shiwei Ren, Tao Zhu, and Jianyan Liu. Generalized design approach for fourth-order difference co-array. In *2018 International Conference on Radar (RADAR)*, pages 1–5. IEEE, 2018.

[14] Xiaomeng Wang, Xin Wang, and Xuehong Lin. Co-prime array processing with sum and difference co-array. In *2015 49th Asilomar Conference on Signals, Systems and Computers*, pages 380–384. IEEE, 2015.

[15] Mark W Maciejewski, Harry Z Qui, Iulian Rujan, Mehdi Mobli, and Jeffrey C Hoch. Nonuniform sampling and spectral aliasing. *Journal of Magnetic Resonance*, 199(1): 88–93, 2009.

[16] https://www.ansys.com/products/electronics/ansys-hfss.

[17] Warren L Stutzman and Gary A Thiele. *Antenna theory and design*. John Wiley & Sons, 2012.

[18] Travis Torres and Payam Nayeri. A circularly polarized u-slot array with high polarization purity and wide axial ratio beamwidth. In *2020 IEEE International Symposium on Antennas and Propagation and North American Radio Science Meeting*, pages 223–224. IEEE, 2020.

[19] Payam Nayeri, Kai-Fong Lee, Atef Z Elsherbeni, and Fan Yang. Dual-band circularly polarized antennas using stacked patches with asymmetric u-slots. *IEEE Antennas and Wireless Propagation Letters*, 10:492–495, 2011.

[20] Ami Desai and Payam Nayeri. A multi-linear polarization reconfigurable plus shaped dipole antenna for wireless energy harvesting applications. In *2018 International Applied Computational Electromagnetics Society Symposium (ACES)*, pages 1–2. IEEE, 2018.

[21] Ami Desai and Payam Nayeri. A wideband dual-polarized stacked microstrip patch antenna with a dumbbell shaped aperture. In *2019 United States National Committee of URSI National Radio Science Meeting (USNC-URSI NRSM)*, pages 1–2. IEEE, 2019.

[22] Kai Fong Lee, Kwai Man Luk, and Hau Wah Lai. *Microstrip patch antennas*. World Scientific, 2017.

[23] Constantine A Balanis. Antenna theory: A review. *Proceedings of the IEEE*, 80(1): 7–23, 1992.

[24] SW Schneider, C Bozada, R Dettmer, and J Tenbarge. Enabling technologies for future structurally integrated conformal apertures. In *IEEE Antennas and Propagation Society International Symposium. 2001 Digest. Held in conjunction with: USNC/URSI National Radio Science Meeting (Cat. No. 01CH37229)*, volume 2, pages 330–333. IEEE, 2001.

[25] DA Wingert and BM Howard. Potential impact of smart electromagnetic antennas on aircraft performance and design. In *Proc. NATO Workshop on Smart Electromagnetic Antenna Structures*, pages 1–10, 1996.

[26] EV Sohtell. Microstrip antennas on a cylindrical surface. *IEE electromagnetic waves series*, 2:1227–1256, 1989.

[27] Kwai-Man Luk, Kai-Fong Lee, and Jashwant S Dahele. Analysis of the cylindrical-rectangular patch antenna. *IEEE Transactions on Antennas and Propagation*, 37(2): 143–147, 1989.

[28] Randy L Haupt. *Timed arrays: wideband and time varying antenna arrays*. John Wiley & Sons, 2015.

[29] Randy L Haupt. *Antenna arrays: a computational approach*. John Wiley & Sons, 2010.

[30] Dhanesh G Kurup, Mohamed Himdi, and Anders Rydberg. Synthesis of uniform amplitude unequally spaced antenna arrays using the differential evolution algorithm. *IEEE Transactions on Antennas and Propagation*, 51(9):2210–2217, 2003.

[31] A Roederer, E Farr, LJ Foged, M Francis, R Hansen, R Haupt, and K Warnick. Ieee standard for definitions of terms for antennas. *IEEE Std*, pages 145–2013, 2014.

[32] URL https://xlinux.nist.gov/dads/HTML/sparsematrix.html.

[33] Emmanuel J Candès and Michael B Wakin. An introduction to compressive sampling. *IEEE signal processing magazine*, 25(2):21–30, 2008.

[34] Paolo Rocca, Giacomo Oliveri, Robert J Mailloux, and Andrea Massa. Unconventional phased array architectures and design methodologies—a review. *Proceedings of the IEEE*, 104(3):544–560, 2016.

[35] Giacomo Oliveri and Andrea Massa. Bayesian compressive sampling for pattern synthesis with maximally sparse non-uniform linear arrays. *IEEE Transactions on Antennas and Propagation*, 59(2):467–481, 2010.

[36] Giacomo Oliveri, Matteo Carlin, and Andrea Massa. Complex-weight sparse linear array synthesis by bayesian compressive sampling. *IEEE Transactions on Antennas and Propagation*, 60(5):2309–2326, 2012.

[37] Federico Viani, Giacomo Oliveri, and Andrea Massa. Compressive sensing pattern matching techniques for synthesizing planar sparse arrays. *IEEE Transactions on Antennas and Propagation*, 61(9):4577–4587, 2013.

[38] Kristopher Buchanan, John Rockway, Oren Sternberg, and Nam Nicholas Mai. Sum-difference beamforming for radar applications using circularly tapered random arrays. In *2016 IEEE Radar Conference (RadarConf)*, pages 1–5. IEEE, 2016.

[39] David G Leeper. Isophoric arrays-massively thinned phased arrays with well-controlled sidelobes. *IEEE Transactions on Antennas and Propagation*, 47(12):1825–1835, 1999.

[40] CG Christodoulou, M Ciaurriz, Y Tawk, J Costantine, and SE Barbin. Recent advances in randomly spaced antenna arrays. In *The 8th European Conference on Antennas and Propagation (EuCAP 2014)*, pages 732–736. IEEE, 2014.

[41] SW Ellingson, GB Taylor, J Craig, J Hartman, J Dowell, CN Wolfe, TE Clarke, BC Hicks, NE Kassim, PS Ray, et al. The lwa1 radio telescope. *IEEE Transactions on Antennas and Propagation*, 61(5):2540–2549, 2013.

[42] Michael P van Haarlem, Michael W Wise, AW Gunst, George Heald, John P McKean, Jason WT Hessels, A Ger de Bruyn, Ronald Nijboer, John Swinbank, Richard Fallows, et al. Lofar: The low-frequency array. *Astronomy & astrophysics*, 556:A2, 2013.

[43] Paola Di Ninni, Pietro Bolli, Fabio Paonessa, Giuseppe Pupillo, Giuseppe Virone, and Stefan J Wijnholds. Electromagnetic analysis and experimental validation of the lofar radiation patterns. *International Journal of Antennas and Propagation*, 2019, 2019.

[44] URL https://public.nrao.edu/telescopes/vlba/.

[45] URL https://public.nrao.edu/telescopes/alma/.

[46] URL https://public.nrao.edu/telescopes/vla/.

[47] Simon Scott and John Wawrzynek. Compressive sensing and sparse antenna arrays for indoor 3-d microwave imaging. In *2017 25th European Signal Processing Conference (EUSIPCO)*, pages 1314–1318. IEEE, 2017.

[48] N Amani, R Maaskant, and WA Van Cappellen. On the sparsity and aperiodicity of a base station antenna array in a downlink mu-mimo scenario. In *2018 International Symposium on Antennas and Propagation (ISAP)*, pages 1–2. IEEE, 2018.

[49] WA Van Cappellen, SJ Wijnholds, and JD Bregman. Sparse antenna array configurations in large aperture synthesis radio telescopes. In *2006 European Radar Conference*, pages 76–79. IEEE, 2006.

[50] Andy Shroyer and Eric Darnel. Self tapered array lattice for high efficiency transmit applications. In *2010 IEEE International Symposium on Phased Array Systems and Technology*, pages 410–416. IEEE, 2010.

[51] Kaushallya Adhikari and Benjamin Drozdenko. Design and statistical analysis of tapered coprime and nested arrays for the min processor. *IEEE Access*, 7:139601–139615, 2019.

[52] Archiman Lahiry, Amlan Datta, and Satyabrata Maiti. Improved self optimized variable antenna array amplitude tapering scheme to combat cell size breathing in umts and cdma networks. In *2015 2nd International Conference on Signal Processing and Integrated Networks (SPIN)*, pages 77–82. IEEE, 2015.

[53] Haider Ali and Karu P Esselle. Application of taylor tapering to a non-linear and irregular microstrip array with minimum power division ratios. In *2021 IEEE Region 10 Symposium (TENSYMP)*, pages 1–5. IEEE, 2021.

[54] Frank Papenfuss and Dirk Timmermann. Alias-free periodic signal analysis using efficient rate nonuniform sampling sets. In *2007 IEEE International Conference on Acoustics, Speech and Signal Processing-ICASSP'07*, volume 3, pages III–1497. IEEE, 2007.

[55] Ma Bota, Zhu Yilong, and Fan Hongqi. Tdc based radar signal reconstruction from periodic nonuniform samples. In *2007 8th International Conference on Electronic Measurement and Instruments*, pages 1–673. IEEE, 2007.

[56] Linjian Zhang, Yesheng Gao, Kaizhi Wang, and Xingzhao Liu. Azimuth signal reconstruction for hrws sar from recurrent nonuniform samples. In *2016 CIE International Conference on Radar (RADAR)*, pages 1–4. IEEE, 2016.

[57] Dongdong Qu, Baoshan Ma, and Jian Zhou. Optimal weighted periodic nonuniform sampling sequences for digital alias-free signal processing. In *IEEE 10th INTERNATIONAL CONFERENCE ON SIGNAL PROCESSING PROCEEDINGS*, pages 147–150. IEEE, 2010.

[58] URL https://www.probabilitycourse.com/chapter4/4_1_1_pdf.php.

[59] Felix J Herrmann and Gilles Hennenfent. Non-parametric seismic data recovery with curvelet frames. *Geophysical Journal International*, 173(1):233–248, 2008.

[60] Salvatore Torquato. Hyperuniform states of matter. *Physics Reports*, 745:1–95, 2018.

[61] Salvatore Torquato. Disordered hyperuniform heterogeneous materials. *Journal of Physics: Condensed Matter*, 28(41):414012, 2016.

[62] Zhenya Ding, Yu Zheng, Yaopengxiao Xu, Yang Jiao, and Wei Li. Hyperuniform flow fields resulting from hyperuniform configurations of circular disks. *Physical Review E*, 98(6):063101, 2018.

[63] Diego Di Battista, Daniele Ancora, Giannis Zacharakis, Giancarlo Ruocco, and Marco Leonetti. Hyperuniformity in amorphous speckle patterns. *Optics express*, 26(12): 15594–15608, 2018.

[64] Robert A DiStasio Jr, Ge Zhang, Frank H Stillinger, and Salvatore Torquato. Rational design of stealthy hyperuniform two-phase media with tunable order. *Physical Review E*, 97(2):023311, 2018.

[65] Hermann Weyl. Über die gleichverteilung von zahlen mod. eins. *Mathematische Annalen*, 77(3):313–352, 1916.

[66] John M Hammersley. Monte carlo methods for solving multivariable problems. *Annals of the New York Academy of Sciences*, 86(3):844–874, 1960.

[67] Il'ya Meerovich Sobol'. On the distribution of points in a cube and the approximate evaluation of integrals. *Zhurnal Vychislitel'noi Matematiki i Matematicheskoi Fiziki*, 7(4):784–802, 1967.

[68] Henri Faure. Discrépance de suites associées à un système de numération (en dimension s). *Acta arithmetica*, 41(4):337–351, 1982.

[69] Harald Niederreiter. Quasirandom sampling in computer graphics. *Image Processing in Medicine, Remote Sensing and Visualization of Information*, pages 29–34, 1992.

[70] William J Morokoff and Russel E Caflisch. Quasi-monte carlo integration. *Journal of computational physics*, 122(2):218–230, 1995.

[71] Spassimir Paskov and Joseph F Traub. Faster valuation of financial derivatives. 1996.

[72] Randy L Haupt. A sparse hammersley element distribution on a spherical antenna array for hemispherical radar coverage. In *2017 IEEE Radar Conference (RadarConf)*, pages 1383–1385. IEEE, 2017.

[73] Phuoc LT Bui, Paolo Rocca, and Randy L Haupt. Aperiodic planar array synthesis using pseudo-random sequences. In *2018 International Applied Computational Electromagnetics Society Symposium-China (ACES)*, pages 1–2. IEEE, 2018.

[74] Ladislav Kocis and William J Whiten. Computational investigations of low-discrepancy sequences. *ACM Transactions on Mathematical Software (TOMS)*, 23(2):266–294, 1997.

[75] Peter Jäckel. *Monte Carlo methods in finance*, volume 2. J. Wiley, 2002.

[76] Stephen Joe and Frances Y Kuo. Constructing sobol sequences with better two-dimensional projections. *SIAM Journal on Scientific Computing*, 30(5):2635–2654, 2008.

[77] URL https://www.mathworks.com/help/stats/sobolset.html.

[78] Scott A. Mitchell. Variable radii poisson-disk sampling. 24th Canadien Conference on Computational Geometry, 2012.

[79] JG van der Corput. Verteilungsfunktionen i. *Akad. Wetensch*, 38:813–821, 1935.

[80] Hee Sun Hong and Fred J Hickernell. Algorithm 823: Implementing scrambled digital sequences. *ACM Transactions on Mathematical Software (TOMS)*, 29(2):95–109, 2003.

[81] Travis Torres, Nicola Anselmi, Payam Nayeri, Paolo Rocca, and Randy Haupt. Low discrepancy sparse phased array antennas. *Sensors*, 21(23):7816, 2021.

[82] Hervé Lebret and Stephen Boyd. Antenna array pattern synthesis via convex optimization. *IEEE transactions on signal processing*, 45(3):526–532, 1997.

[83] Ling Cen, Wee Ser, Wei Cen, and Zhu Liang Yu. Linear sparse array synthesis via convex optimization. In *Proceedings of 2010 IEEE International Symposium on Circuits and Systems*, pages 4233–4236. IEEE, 2010.

[84] Giancarlo Prisco and Michele D'Urso. Maximally sparse arrays via sequential convex optimizations. *IEEE Antennas and Wireless Propagation Letters*, 11:192–195, 2012.

[85] Hui Chen, Qun Wan, An Min Huang, and Juan Wang. Array pattern synthesis via sparse weight vector finding and convex programming. In *2009 5th International Conference on Wireless Communications, Networking and Mobile Computing*, pages 1–4. IEEE, 2009.

[86] Xiangrong Wang, Moeness Amin, and Xianbin Cao. Analysis and design of optimum sparse array configurations for adaptive beamforming. *IEEE Transactions on Signal Processing*, 66(2):340–351, 2017.

[87] Peter Moschetti. *Increasing Drone Video Down Link Reliability Using Phased Array Technology*. Colorado School of Mines, 2020.

[88] Yi-Xuan Zhang, Yong-Chang Jiao, and Li Zhang. Antenna array directivity maximization with sidelobe level constraints using convex optimization. *IEEE Transactions on Antennas and Propagation*, 69(4):2041–2052, 2020.

[89] Yuen T Lo and SW Lee. *Antenna Handbook: antenna theory*, volume 2. Springer Science & Business Media, 1993.

[90] Daniels W. Hammerling D. Buchholz R. Duggal, M. Optimizing genetic algorithm parameters for atmospheric carbon monoxide modeling. *National Center for Atmospheric Research*, 2021.

[91] Lars Josefsson and Patrik Persson. *Conformal array antenna theory and design*, volume 29. John wiley & sons, 2006.

[92] Nguyen Dinh Tinh and Trinh Dang Khanh. An investigation on amplitude distribution for controlling side-lobe level of sparse cylindrical sonar arrays. In *2020 International Conference on Green and Human Information Technology (ICGHIT)*, pages 45–46. IEEE, 2020.

[93] Steele J.P.H. Developing real-time diagnostics for cutting heads on underground mining machines, 2001.

[94] RF Burchill. Development of sensitized pick coal interface detector system. final report. Technical report, Shaker Research Corp., Ballston Lake, NY (USA), 1982.

[95] GL Mowrey, SD Maksimovic, and MJ Pazuchanics. Staying in the seam: an overview of coal interface detection and steering. *Engineering and Mining Journal;(United States)*, 193(8), 1992.

[96] AL Craven and IR Muirhead. Horizon control technology for selective mining in underground coal mines. *CIM bulletin*, 93, 2000.

[97] K Nienhaus and AK Bayer. Innovative systems for horizon control of mining machines by means of laser induced fluorescence (lif). *Mine Planning and Equipment Selection, Kalgoorlie, WA*, pages 1–7, 2003.

[98] IY Bausov, GL Stolarczyk, LG Stolarczyk, and Sc DS Koppenjan. Look-ahead radar and horizon sensing for coal cutting drums. In *2007 4th International Workshop on, Advanced Ground Penetrating Radar*, pages 208–211. IEEE, 2007.

[99] Michael Kelly and David W Hainsworth. Outcomes of the landmark longwall automation project with reference to ground control issues. 2005.

[100] Nina B Fietz and Thomas Bartnitzki. Latest developments in libs for distinction of coal and waste rock in explosive areas. *Mining Rep.*, 152(5):1–9, 2016.

[101] James P Rider and Jay F Colinet. Benchmarking longwall dust control technology and practices. 2010.

[102] J Duncan and LG Stolarczyk. Mining complex geology, mitigation of float dust, and developing autonomous machine capability using horizon sensing technology for coal seam boundary detection. *Journal of the Southern African Institute of Mining and Metallurgy*, 115(11):1013–1020, 2015.

[103] https://mining.komatsu/en-in/product-details/joy-12cm12. Accessed: 2022-04-1.

[104] https://www.ettus.com/all-products/usrp-b200mini-i-2/. Accessed: 2022-04-7.

[105] Rob Miller. Fundamentals of radar signal processing (richards, ma; 2005)[book review]. *IEEE Signal Processing Magazine*, 26(3):100–101, 2009.

[106] https://www.digi.com/products/embedded-systems/digi-xbee/rf-modules/sub-1-ghz-rf-modules/xbee-pro-xsc. Accessed: 2022-04-8.

[107] Travis Torres, Payam Nayeri, Randy Haupt, and Paolo Rocca. Sparse cylindrical arrays with low discrepancy element spacing based on van der corput sequence. In *2021 IEEE International Symposium on Antennas and Propagation and USNC-URSI Radio Science Meeting (APS/URSI)*, pages 7–8. IEEE, 2021.

[108] Travis Torres, Payam Nayeri, and Randy Haupt. Sparse cylindrical arrays based on the low-discrepancy sobol sequence sampling.

[109] Robert J Mailloux. *Phased array antenna handbook*. Artech house, 2017.

[110] R Willey. Space tapaering of linear and planar arrays. *IRE Transactions on Antennas and Propagation*, 10(4):369–377, 1962.

[111] ML Skolnik, JIII Sherman, and F Ogg. Statistically designed density-tapered arrays. *IEEE Transactions on Antennas and Propagation*, 12(4):408–417, 1964.

[112] Paul Bratley and Bennett L Fox. Algorithm 659: Implementing sobol's quasirandom sequence generator. *ACM Transactions on Mathematical Software (TOMS)*, 14(1): 88–100, 1988.

[113] URL https://www.kennametal.com/us/en/home.html.

APPENDIX A

FUNDING AND MOTIVATION FOR RESEARCH

This research was accomplished from the support of National Institute for Occupational Safety and Health (NIOSH) through grant no. 75D30119C05413. We acknowledge that without the support of NIOSH, we would not have been able to conduct the research that we were able to over the past several years.

A.1 Smart Bit Concept

Two of the persisting health and safety issues in the US mining industry are ground control and dust. Automation of the equipment will allow for removal of the workers from the potentially harmful conditions in the mine. This research focuses on development of the "Smart Pick" concept which is a key component of automating the mechanical rock excavation units in various mining operations. The work involves development of the load sensing system to monitor the cutting forces on the pick, wireless communication of the data from the drum to the machine (focus of the dissertation), and pattern recognition algorithms to identify the rock being cut using machine learning (ML) and artificial intelligence (AI) systems. This enables the machines to operate without the need for the presence of personnel and their exposure to possible health and safety risks.

The proposed work involves full scale cutting of 7 types of rocks (including Coal, Shale, Sandstone, Limestone, Gypsum, Potash, Trona) with 2 type of picks at three levels of wear conditions (new, medium, and worn). Rock cuttings will be sampled and fines will be separated for dust studies. The dust study involves characterization of the fines and establishing a relationship between pick tip design, wear and dust generation. The results allow for developing solutions for reducing dust at generation point. The pattern recognition that allows the system to identify the rock types at the face also allows for monitoring the wear conditions of the picks and thus, resulting dust generation and issue a warning for tool change to

mitigate dust generation.

The focus of this work is on smart or instrumented bit/pick concept which is considered to be a key component of automation of rock excavation units used in soft/medium strength rock in different mining operations. This research topic was selected since a review of the available mining health and safety statistics show that despite the remarkable achievements in the past few decades, there are still some causes for injury and even fatalities that are persistent and needs to be addressed. This includes the roof fall and injuries related to powered haulage. Simultaneously, respiratory diseases have been on the rise since mid 1990's and there is a need for addressing this trend. One of the solutions that can address many of these issues is automation of mining activities and removing miners from the potentially unsafe and unhealthy work conditions. The automation of rock excavation units could be a first step in that direction.

Excavation of soft rock in mining applications is dominated by mechanical excavation units such as roadheaders, continuous miners (CM), long wall drum shearers or plough, borer miners, and surface miners, shown in Figure A.1. These machines serve various underground, and to lesser extent, surface mining operations in commodities including coal, gypsum, trona, salt, potash, and in gold mines in soft to medium strength rocks in Nevada. Nearly all the coal, potash, trona, and salt produced in underground operation are mined by these machines. The production rate of these machines are relatively high and they offer a safer working environment compared to drill and blast operations, which is the alternative means of rock excavation in mining operations. The cutting tools used on these machines are primarily drag type tools including conical/point attack picks and radial tools. The tools are the interface between the machine and the rock and pass through various formations at the face while working.

What we aim to do is to instrument the picks so that they are able to measure the cutting forces on real time basis and communicate that information with the machine. This information is the critical part of automation of the excavation units and can be used to

identify the various formations being cut, which allows for horizon control. The measured forces also allow the operators to identify the missing or broken tools, as well as picks that have lost their tip or are dull. Worn tools tend to generate more dust, which is a major issue in mining operations.

Figure A.1 Picture of a typical continuous mining machine

Development of smart, instrumented, or sensitized pick research is the key component of marking the rock-coal interface based on the forces observed at the pick tip during coal cutting in underground coal mines. The research on sensitized pick technology has originally started in British Coal (BC) in 1950s in order to keep the shearer drum in the seam, cutting coal but avoiding the over excavation of the coal seam into the surrounding rocks (roof/floor). Some studies on the instrumented pick systems were conducted in US and Poland [93]. These systems depended mainly on measuring the pick loads and vibrations in real-time by instrumenting a pick with a load cell based on strain-gauges (foil type). In addition, bit and head vibration is monitored using accelerometers to register signature vibrational characteristics of the cutting drum in various rock types. Sensor outputs can be transferred to the transmitter unit on the drum by wiring and then transferred to the machine control

unit using data telemetry. A phase indicator device (proximity sensor) has also been added to the system so that the position of the sensitized pick can be independently identifiable [94, 95].

The Smart Pick will fill the gap for the automation of the excavation units where the cutting tool that is in contact with the rock formation will be the sensor for identification of the rock type and cutting condition, without the need for additional optical or other sensory systems that can be blocked from sensing the working conditions at the face. This concept can be used on any rock excavation unit used in underground/surface mining. The surface machines are used in gypsum, coal, and in some operations in softer limestones. Highwall mining units can also benefit from autonomous machines with horizon controls.

Obviously, as the tools on these machines work, they often wear and become dull. As they wear, the cutting forces gradually increase and the level of forces in cutting the same rock under same operating conditions can be related to bit wear. Dull tools or the picks that had lost their tip require more energy of cutting which generate more dust in the process. In other words, ability to sense the load on the cutters allows the operators to monitor bit conditions and change them as needed to minimize dust generation at the source.

A.2 Research Background and Approach

Mining soft to medium strength rock has seen a drastic increase in productivity in the last few decades due to the use of mechanized excavation in related operations. This includes mining coal, salt, trona, potash, gypsum, and recently limestone. Mechanical excavation systems are primarily used in underground mines. The higher productivity per man shift, higher degree of mechanization that can lead to automation, lower number of miners at the face, better safety of the work environment, and better control on health of the miners are the benefits of the machines. Yet another step in improving the mine and safety is needed by removing the operators from the proximity of the machines and enabling them to operate autonomously. This requires some enabling technologies including a reliable positioning system and ability to distinguish various formations and rock types they are cutting. While

there are several companies working on underground positioning of the equipment in mining, the ability to sense the rock types being excavated is a complex problem that requires more work. This has been subject of some of the past work under the general theme of horizon control by various research groups but has not resulted in products that can be commissioned by the mining companies.

The main complexity of the horizon control is the identification of the various formation by different sensory systems. In the past different sensory systems have been proposed and tested with various degree of success. Lack of any operational units using these systems testifies to their limited capabilities and reliability for operational purposes. Craven and Muirhead [96] examined the possibility of implementing horizon control in longwall mining of coal by using methods rely on such characteristics as neutron gamma radiation, electromagnetic waves, vibration, infrared, optical, pick force, X-ray fluorescence, conductivity, gyroscopes and laser systems. They state: "The benefits obtained from existing horizon control systems include improvement in the quality of coal extracted, control of the mining horizon while limiting extraction height, more consistent roof and floor horizons leading to better roof control, reduced dust, improved safety and increased rates of production." [96] Their study concludes that technologies that are judged to be not applicable for at least ten years and that do not currently meet certain essential criteria include the Prompt Gamma Neutron Activation Analysis, Electron Spin Resonance, and Natural Gamma Ash/Sulphur Analysis methods. Technologies of medium-term interest were listed as electromagnetic spatial radar, machine heading and positioning, and acoustic and seismic vibrations.

Craven and Muirhead conclude that the technologies with immediate potential for application in longwall were machine position within the seam combining the Inertial Navigation System with the tomographic Radio Imaging Method (RIM), coal thickness measurement with the single frequency ground penetrating radar system, coal thickness measurement using EM radio waves, passive infrared measurements based on ply hardness variations, and machine energy level variations based on ply hardness variations. In examining these systems

the comment on the vibration system as follows: "The acoustical, seismic and mechanical vibrations that are produced by a mining machine have certain characteristics that are directly related to the geological material being cut, the type of mining machine being used, the condition of the cutter bits and the manner in which the machine is being used by the operator." [96]. This supports the hypothesis of the proposed Smart Bit concept.

Among the systems that have been tried for horizon control one can name the Laser Induced Fluorescence (LIF) (Nienhaus & Bayer 2003) [97]. The studies illustrated that the LIF could distinguish qualitatively between ore and waste rock in real time as optical, non-contact method. However, the researchers concluded that to guarantee a versatile utilization of LIF, a database including the fluorescent "fingerprints" of many different raw materials and deposit types has to be developed. Stolarczyk [98] worked on look-ahead radar (LAR), which must solve the radio geophysics problem of transmitting an electromagnetic (EM) wave through at least 20 feet (6.1 meters) of coal to an air or water filled void.

Kelly & Hainsworth [99] outlined the results of Landmark Longwall Automation Project with Reference to Ground Control Issues. They discussed various aspects of operating a longwall shearer and the importance of inertial positioning system for the drums in the larger context of horizon control and emphasized the side benefit of the system to be the improved ground control in the operation. Fietz [100] discuss the use of Laser-Induced Breakdown Spectroscopy (LIBS) for horizon control and operation of the longwall shearers. They conclude that While laser-induced breakdown spectroscopy is generally feasible for differentiating coal and waste rock from each other, but due to existence of the explosive conditions in underground hard coal mines, in-situ analyses with LIBS are not possible. Therefore the efforts was diverted to analysis of the generated dust to assess the cutting medium and environmental conditions by using this technology instead.

Another persisting health issue in mining is the respiratory problems of the mine workers and as stated in NIOSH website: From 2007 through 2016, CWP has been the underlying or contributing cause of death for 4,118 miners and a total of 75,178 miners from 1970 through

2016. Some of the recent advances in addressing this issue has been the development of Personal Dust Monitor (PDM) that allows measurement of the dust exposure of the mine workers and offers background data for development of potential solutions. Often time engineering solutions are used to reduce the exposure of the workers to the airborne dust. However, limited studies have been conducted on reducing the dust at generation point. Rider and Colinet [101] determined that approximately 40% of all dust particles smaller than 35μm originate from cutting. The rest of 60% can be assigned to all other areas in which dust can be formed.

Duncan and Stolarczyk [102] put the horizon control in the light of worker health as well as public health when they state: "reducing float dust exposure limits alone will not reverse the increasing incidence of coal mine dust lung disease seen in the current generation of miners. Trace and radioactive metals are concentrated in the thin boundary layers of the coal seam, and hence float dust includes silica and toxic trace metals." They continue their statement with emphasis on the use of instrumented picks as they note in their papers: "Because of constant changes in geology, seam thickness, and seam undulation, the horizon sensor must be located in the bit-block of the rotating cutter drum of the mining machine. Contaminants in ROM coal must be minimized at the source-that is, at the rock/coal crushing cone directly under the bit-tips of the cutting drum. Bit tip distances to the rock boundary layer must be automatically controlled in real time when mining in a complex and undulating coal bed. Horizon sensing (HS) technology enables the mining machine's cutting picks to stop at a specified distance from undulating horizons of the boundary rock. Preventing the metal picks from striking quartz-containing boundary rock also reduces the occurrence of methane ignitions. HS technology equipped with pick force vector sensing can allow optimization of the cutting pick lacing pattern for minimum coal and rock crushing, thereby reducing float dust." [102]

The above mentioned references seem to best capture the motivation and direction of our work for the development of smart/instrumentized picks and the monitoring of the dust

generation in full scale cutting tests.

A.3 Communication System Design Objectives

As mentioned above in the description of the Smart Bit concept, the focus of this dissertation is to develop the data transmission system that can communicate the data from the bit to the machine. The tasks that are involved in this area include:

- Design, fabrication, and testing of the data communication system to transfer data from the instrumented pick to the machine.

- System modeling of the communication system which involves examination of various communication tools, frequency channels, and protocols for high speed data transmission from the rotating drum to the stationary unit that is the machine. Different network communication topologies will also be explored to ensure system redundancy (maximize reliability) and minimize latency.

- Hardware design for the communication system which involves electromagnetic modeling, analysis, and optimization of antennas and radio-frequency sub-systems to ensure realization of a stable communication link. To ensure permissible1 operation of the communication system, a complete electromagnetic model of the system will also be created and used to determine the electric and magnetic fields for electromagnetic compatibility analysis and further refinement or modifications if required.

- Fabrication and test of the individual sub-systems, and integration and test of the complete communication system in lab setup.

APPENDIX B

DUMMY DRUM DESIGN

This appendix details the purpose and design of the mock mining drum (dummy drum) that was developed to perform testing and experimentation for the communication system. The particular machine we were targeting to design the Smart Bit for is a continuous mining machine, as shown in Figure B.1

Figure B.1 Picture of a continuous mining machine which will serve as the basis for our dummy drum design. Image from [103]

The drum usually consists of three separate heads (mini drums) that are all connected together. Each head possesses an arrangement of picks where each pick contains a bit. A 3D CAD model for the pick and bit is shown in Figure B.2. The concept we developed for the Smart Bit is to insert a capacitive sensor between the bit and the pick, which can take force measurements when the bit comes in contact with the rock. This will be explained more in depth in Appendix D, but the data that we will expect to measure will consist of a pulse train, where the pulses are generated from each slice through the rock. The interval

in between pulses will consist of zeros plus Gaussian noise, which is generated from sensor calibration and thermal heat within the vicinity of the sensor.

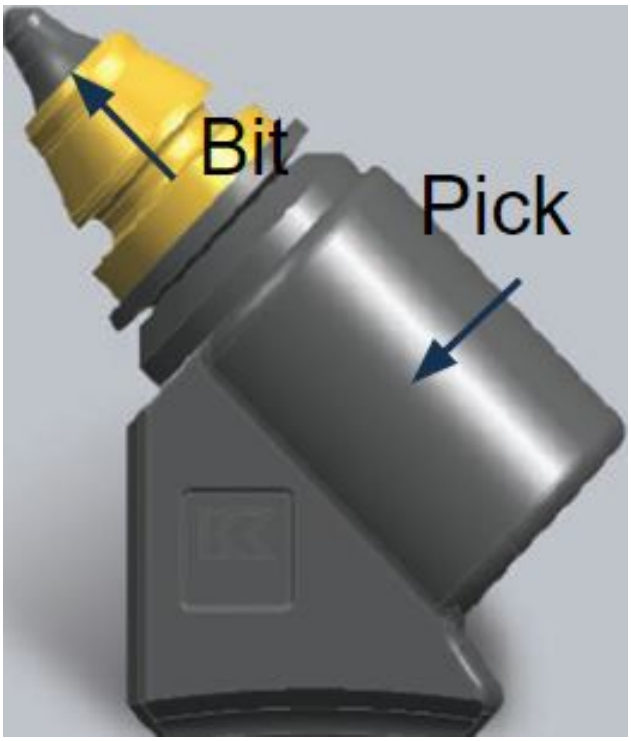

Figure B.2 3D CAD model of a bit and pick that go on the drum of the continuous mining machine

The purpose of designing a dummy drum is because it would be outside the scope of the budget for this contract to be able to test on an actual continuous mining machine. The continuous mining machine would also be too large to test our prototypes on as well, so we would need something that's on a much smaller scale. We design the drum based off of one of the heads, where the head has a diameter of 2 ft and a height of 2 ft. The first step we took was to design the drum in Solidworks, where the layout and 3D CAD model of the drum is shown in Figure B.3. In the environment we will be working in, we know that the transmitter will be placed in some location on the drum and the receiver will be placed anywhere from 12-24 inches away on the machine, so we will not have to worry about having to transmit long distances away from the drum. Our potential placements for the receiver are also depicted by the metallic posts, shown in Figure B.3. Since we want to also enable

dynamic capabilities for the dummy drum, we will need to build a frame and axle system, which would sustain the drum and allow for it to rotate as well.

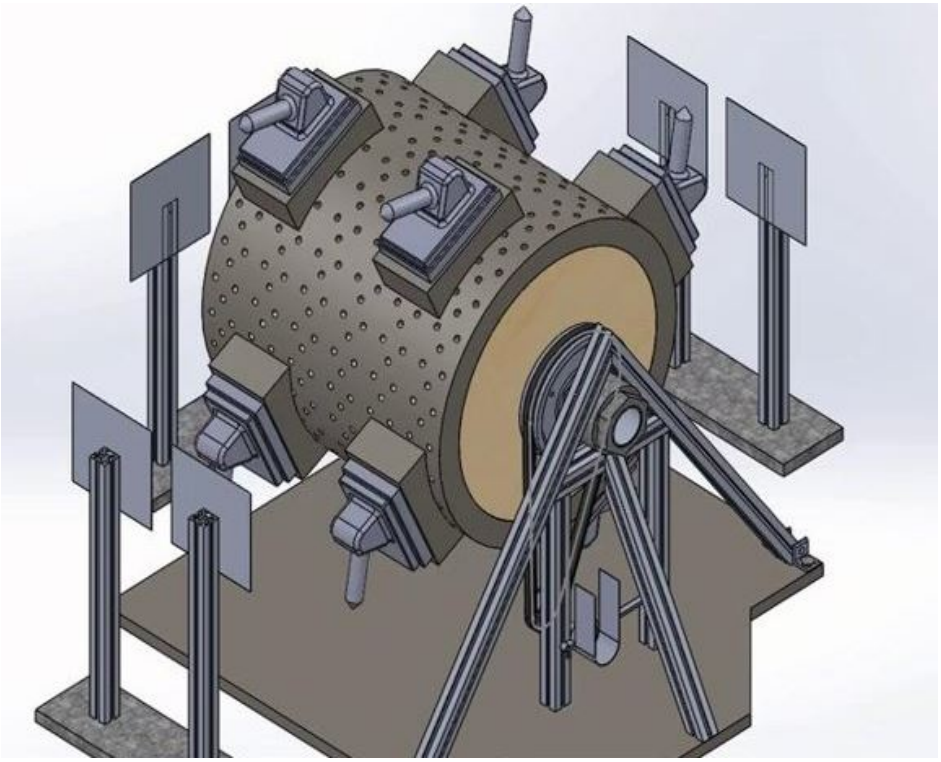

Figure B.3 3D CAD model of the dummy drum prototype

In order to design the drum so that it could move close to the speed of an actual continuous mining machine, we needed to design it so that it's physically lighter and could also mimic the same metallic properties of an actual drum. To do this, we carved out a cylindrical piece of styrofoam with a 2 ft diameter and 2 ft height. We then encased it within a sheet of aluminum foil, so that we can get as close to replicating the same environment we would see in a mine. The properties of the metallic drum would result in reflections from the transmitted signal, since antennas have side and back lobes which transmit signals in these directions as well. The signals being transmitted in those directions would reflect off of the drum and ultimately cause interference for our receiver. We would be receiving delayed-attenuated copies of our transmitted signal, a phenomena that is commonly known as multi-path fading. By placing the aluminum sheet of foil over the drum, we should be able to come close to replicating the

delayed-attenuated copies of our transmitted signal. The styrofoam cut out of the drum is depicted in Figure B.4.

Figure B.4 Cut out of the styrofoam drum

The last step for implementing the dummy drum involved designing a frame and axle so that they can be attach and hoist up the drum. Once this was completed, we would then design the pulleys, belt, and drill alignment piece for the axle. We then attached all mentioned pieces so that the drum can spin under power. The final design for the dummy drum is shown in Figure B.5.

The way the drum operates dynamically, is by plugging a power drill into the axle drill piece, which is contained in the yellow casing, shown by Figure B.5. After first initial tests for the dummy drum were conducted, we had to design a second piece to go onto the frame, since we experienced shaking and moving frames when the drill was applied to the axle. This is the orange piece that is attached to the bottom of the frame in Figure B.4. After re-conducting the tests with the drill again, we noticed that there were minimal movements

from the frame, so the drum design was complete and available for further testing.

Figure B.5 Final dummy drum design

APPENDIX C

RING AND PATCH ANTENNA ARRAY

This appendix details the design and implementation of the ring and patch antenna array for the dummy drum, which was described in Appendix B. Note that it was because of the cylinder shape of the drum, that inspired us to study the design of sparse antenna arrays for cylindrical surfaces.

C.1 Ring Arrays

Before we begin discussing cylindrical arrays, it's important to explain the theory behind ring antenna arrays because for the uniform cylindrical case, the array consists of M-concentric ring arrays around an axis. Ring arrays are a special case of planar arrays because a ring array resides in a plane, but the elements are concentric around a center point (usually an axis) and reside on a circle. The array geometry for a ring array consisting of $N = 20$ elements and radius $r = 10\lambda/2\pi$ is shown in Figure C.1.

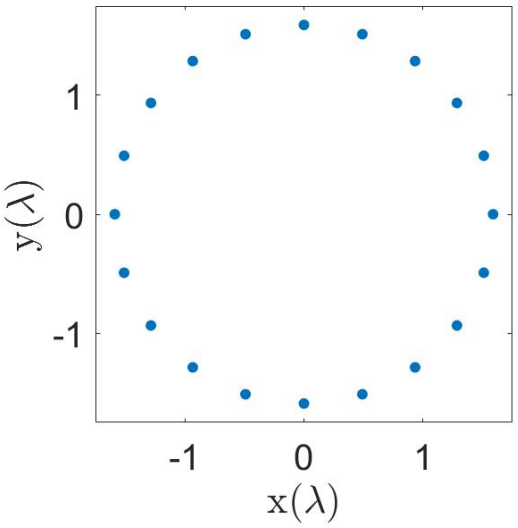

Figure C.1 Array geometry of a ring array where $r = 10\lambda/2\pi$ and $N = 20$

The beam pattern for a ring array with uniform weighting and isotropic elements can be expressed by the following

$$F(\theta,\phi)=\sum_{n=1}^{N}e^{jkr\sin\theta\cos(\phi-\phi_n)+j\beta_n} \tag{C.1}$$

where k is once again the wavenumber, ϕ_n is the azimuthal location of element n in the xy-plane, and β_n is the phase factor with respect to the origin so that we can orient the main beam in the direction (θ_0,ϕ_0). The proper expression for β_n is given by

$$\beta_n=-kr\sin\theta_0\cos(\phi_0-\phi_n) \tag{C.2}$$

We see by first glass, when looking at Equation C.1 that we can not properly express the radiation pattern in the uv-space, where $u=\sin\theta\cos\phi$ and $v=\sin\theta\sin\phi$. So what we need to do is define a new set of variables that we can substitute into Equation C.1 so that the radiation pattern can be expressed in the uv-coordinate system. We begin by defining a variable ρ, where

$$\rho=r[(\sin\theta\cos\phi-\sin\theta_0\cos\phi_0)^2+(\sin\theta\sin\phi-\sin\theta_0\sin\phi_0)^2]^{\frac{1}{2}} \tag{C.3}$$

and ξ, where we have

$$\cos\xi=\frac{\sin\theta\cos\phi-\sin\theta_0\cos\phi_0}{[(\sin\theta\cos\phi-\sin\theta_0\cos\phi_0)^2+(\sin\theta\sin\phi-\sin\theta_0\sin\phi_0)^2]^{\frac{1}{2}}} \tag{C.4}$$

From Equation C.4, we see that we can substitute u and v into their respective places, which allows us to now have a proper expression in the uv-space. We can now insert ρ and $\cos\xi$ into Equation C.1, which allows us to arrive at the following expression for the radiation pattern of a ring array, as seen in Equation C.5

$$F(\theta,\phi)=\sum_{n=1}^{N}e^{jk\rho\cos(\xi-\phi_n)} \tag{C.5}$$

For most planar arrays, we usually set the main beam to $\theta_0 = 0°$ and $\phi_0 = 0°$, but when we do this for ring arrays, we tend to get a high SLL and not fully utilize the benefits of their unique geometry. The radiation pattern slices in all principle planes, 3D pattern, and uv-space are shown in Figure C.2 for when then beam is scanned to $\theta = 0°$ and $\phi = 0°$.

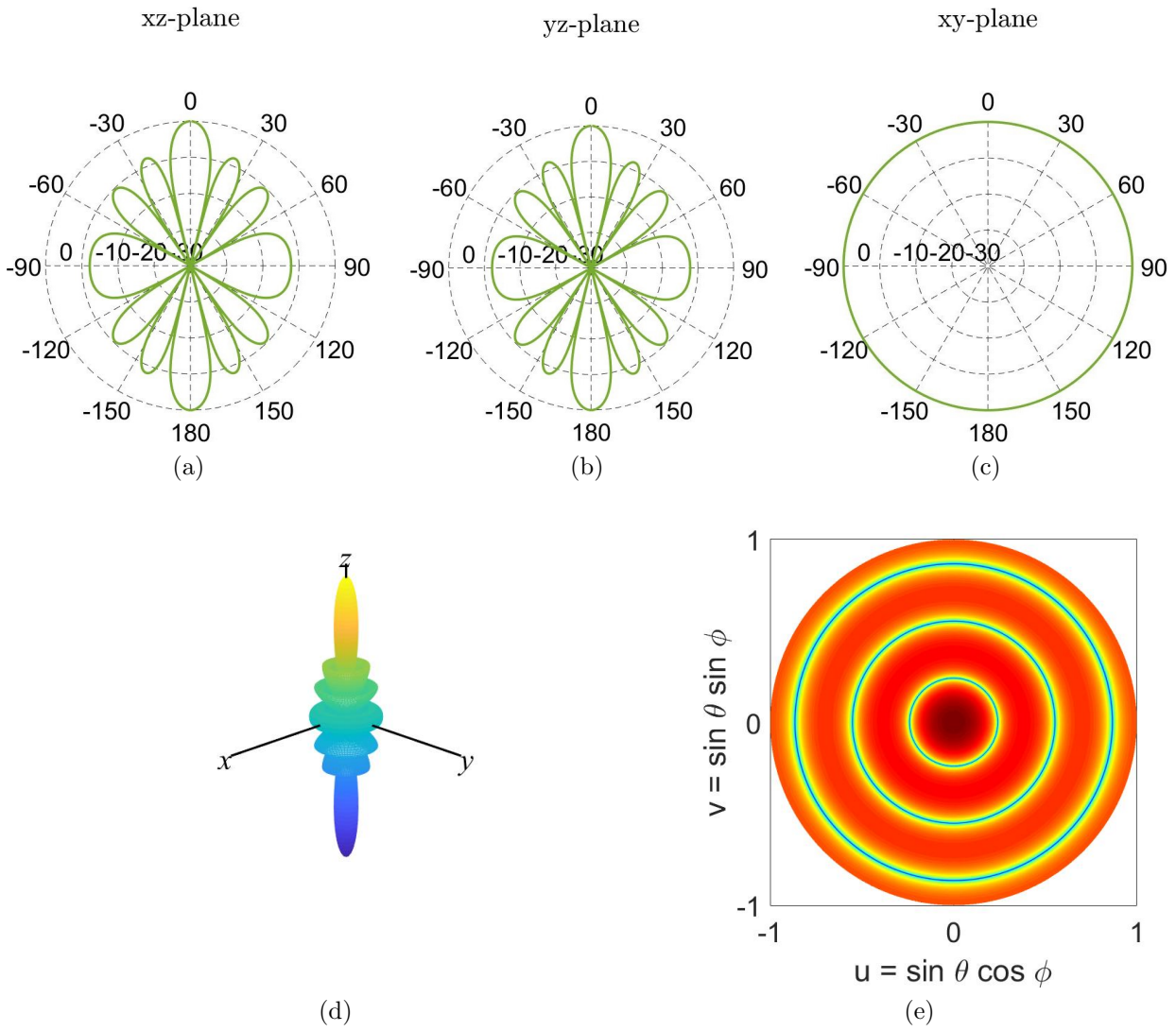

Figure C.2 Radiation pattern slices in all principle planes, uv-space, and 3D radiation pattern for the ring array: (a) Pattern slice in the xz-plane, (b) Pattern slice in the yz-plane, (c) Pattern slice in the xy-plane, (d) 3D radiation pattern, (e) Radiation pattern in the uv-space

The issue with this configuration when the beam is scanned to $\theta = 0^\circ$ and $\phi = 0^\circ$ is that the main beam is in the center of the array. For the majority of ring and cylindrical array applications, the elements reside on the surface of some medium, where the medium is within the center of the array. With the main beam transmitting in the center of the array, we would experience high lossy conditions. Realistically, the target we are transmitting to or receiving from is normal or orthogonal to the surface of the medium, so we steer the beam to $\theta = 90^\circ$ and $\phi = 0^\circ$. The pattern slices, 3D pattern, and pattern in the uv-space are shown in Figure C.3 for when we steer the beam to these exact coordinates.

What we see in Figure C.3 is that when we scan the beam to $\theta = 90^\circ$, we end up getting a fan beam for the main beam pattern. We see this by the main beam being very thin in the xy-plane and broad in the xz-plane. Note that with the circular radius and number of elements that we used, the elements will be spaced $\lambda/2$ from each of the neighboring elements.

C.2 Cylindrical Array Design

Since the radiation pattern for a cylindrical array is based off the summation of a series of separate ring arrays, we see that the radiation pattern for a cylindrical array with rings concentric around the z-axis and N total elements can be found by

$$F(\theta, \phi) = \sum_{n=1}^{N} e^{jk[r \sin\theta \cos(\phi - \phi_n) + z_n \cos\theta]} \tag{C.6}$$

where $r \sin\theta \cos(\phi - \phi_n)$ gives the azimuthal coordinates of each element and $z_n \cos\theta$ gives the location of the elements in the z-direction. Once more, we would steer the main beam to $\theta = 90^\circ$ so that the main beam isn't aligned along the z-axis. For this first initial case, we started out by populating the drum of the continuous mining machine when there were no picks mounted on it. This would give us an idea of the ideal pattern before rings and elements are removed to make way for the picks. Our design of the array is for WIFI frequency (2.45 GHz), which results in a wavelength of .1225 m. When we convert the dimensions of the

drum over from feet to meters, we get that $h = 2r = 609.6$ mm. With these dimensions, 10 rings and 32 elements per ring would result in approximately $\lambda/2$ spacing. The radiation pattern slices, element distribution, and 3D radiation pattern for the drum can be seen in Figure C.4.

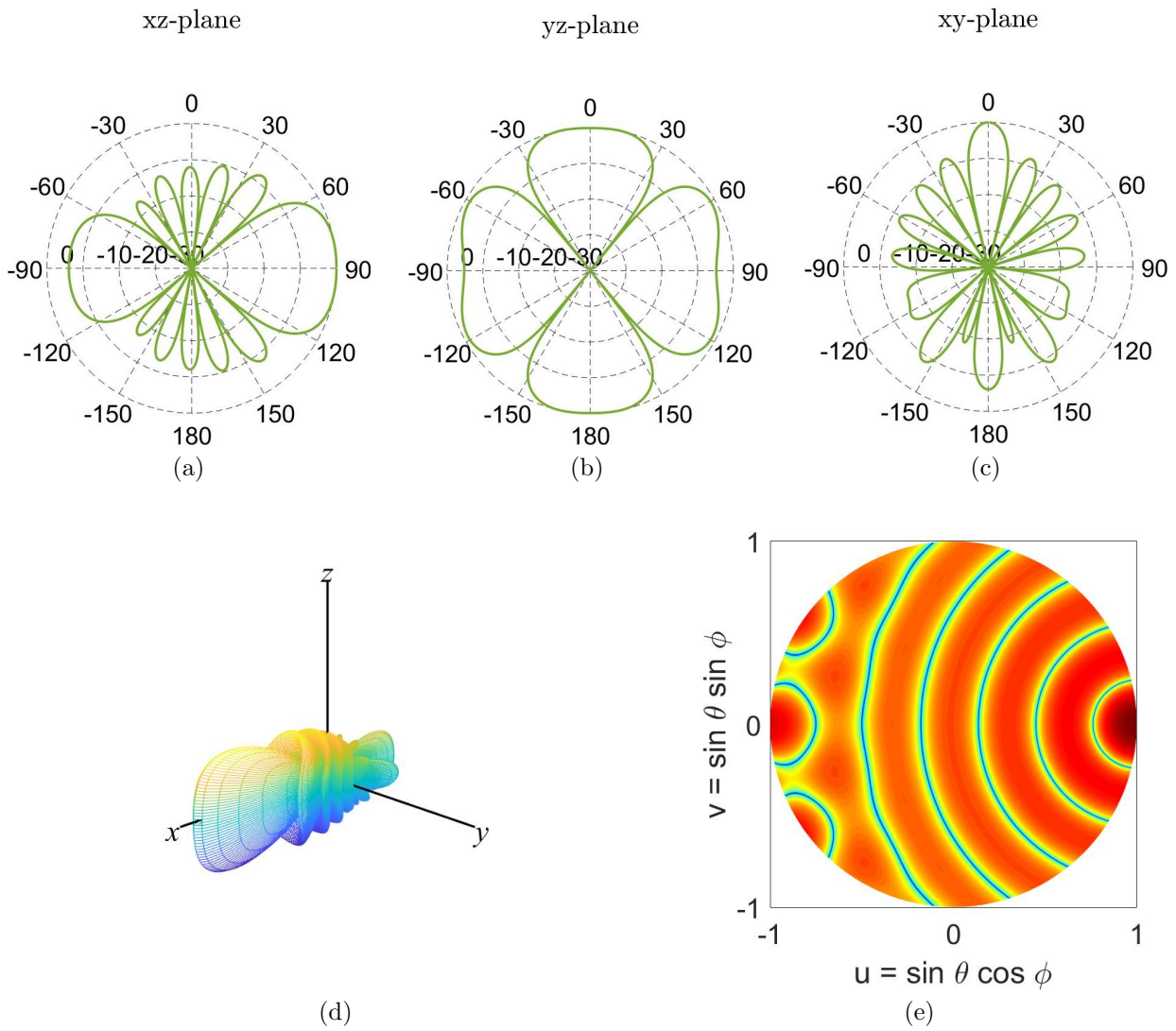

Figure C.3 Radiation pattern slices in all principle planes, uv-space, and 3D radiation pattern for the ring array when we steer the main beam to $\theta = 90°$ and $\phi = 0°$: (a) Pattern slice in the xz-plane, (b) Pattern slice in the yz-plane, (c) Pattern slice in the xy-plane, (d) 3D radiation pattern, (e) Radiation pattern in the uv-space

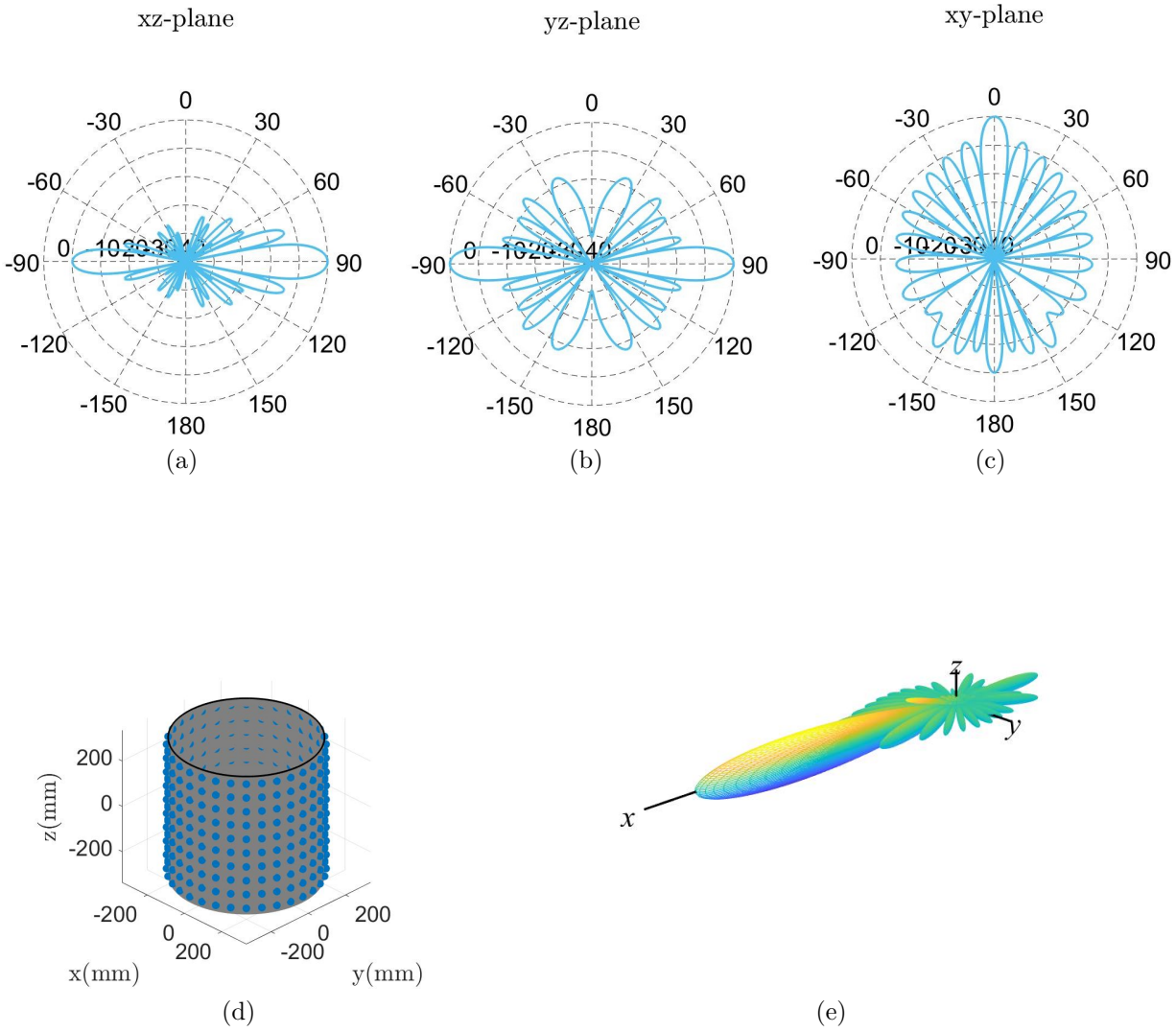

Figure C.4 Radiation pattern slices in all principle planes, element distribution, and 3D radiation pattern for the cylindrical array on the drum when we steer the main beam to $\theta = 90°$ and $\phi = 0°$: (a) Pattern slice in the xz-plane, (b) Pattern slice in the yz-plane, (c) Pattern slice in the xy-plane, (d) Element distribution on the drum of the continuous mining machine, (e) 3D radiation pattern

Altogether, there are 320 elements on the mining drum. Since we know that there will be picks placed on the drum, we will have to remove the amount of rings we have and elements per ring, which will implement sparsity within the array. From Figure C.5, we know that our transmission distance would be between 12 and 24 inches, so the amount of elements we need on the drum can be radically decreased.

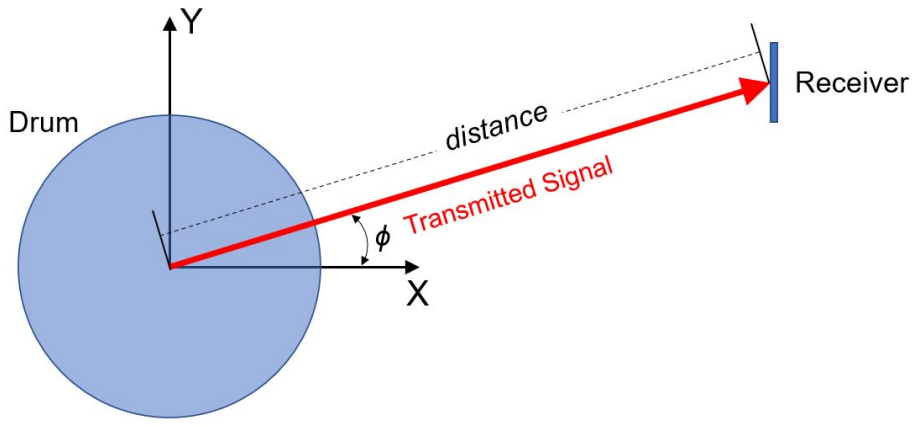

Figure C.5 Drum setup geometry for the transmitter and receiver on the continuous mining machine

However, the picks aren't the only problem that we need to consider when we are designing our array. We will likely experiencing falling debris and other destructive forces in this environment, which pose a threat to the well-being of the array on the drum. What we proposed/implemented, is to cut out a section of the surface going around the drum, so that the antenna elements and coax lines can be placed underneath the surface of the drum, which would shield them from any debris in the mine. The antenna elements would be attached to a circular ring that would wrap around the cut out section of the drum. The material for the ring would need to be non-metallic so that the current won't get shorted out, result in minimal reflections from the transmitted signals by the sidelobes and back lobe, and to also be flexible, so that the material can possibly wrap between picks and adjust to its surroundings. Our schematic for the ring design is shown in Figure C.6. The rings would be comprised of N elements, where the antenna that is used on the ring is the conformal inset

fed patch antenna that was presented at the end of Chapter 2. In Chapter 2, we saw that when we have a large cylindrical radius, the radiation pattern won't be heavily effected by the curvature of the cylinder. The reader is referred back to Chapter 2 for more information on the design and performance of the conformal inset fed microstrip patch antenna.

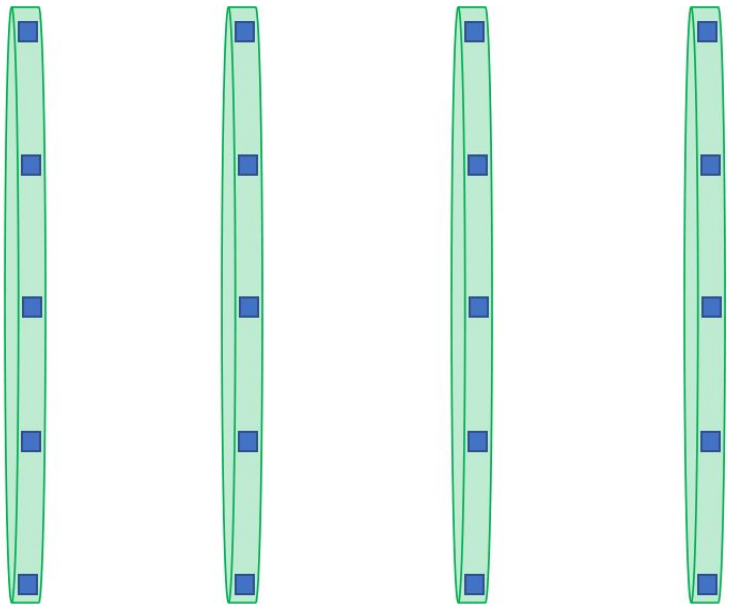

Figure C.6 Ring configuration for the drum. We would utilize M rings and N inset fed patch antennas per ring

After conducting several studies, we determined that there are two possible solutions, the first being that we have four rings with sixteen elements on each ring. This would correspond to having the rings being spaced by one wavelength from each other and for the elements within each of the rings to also be spaced one wavelength away from each of the neighboring elements. Note that depending on the desired gain of the array, we can significantly reduce the amount of elements within each ring which leads us to the second possible solution, otherwise known as the sparsest case. This is when we have four rings consisting of four elements, where the elements are placed at $\phi = 0°, 90°, 180°$, and $270°$ respectively. This will still give us full $360°$ coverage of the drum, where a region of picks will be associated with each transmitting sensor. Provided in Figure C.7 are the radiation pattern cuts, element

distribution, and 3D radiation pattern of the four ring cylindrical array when each ring has 16 elements on them. Due to our restraints with the picks, this is the densest and highest gain case, where the sparsest case to still have 360° range of coverage would be the four ring four element cylindrical array.

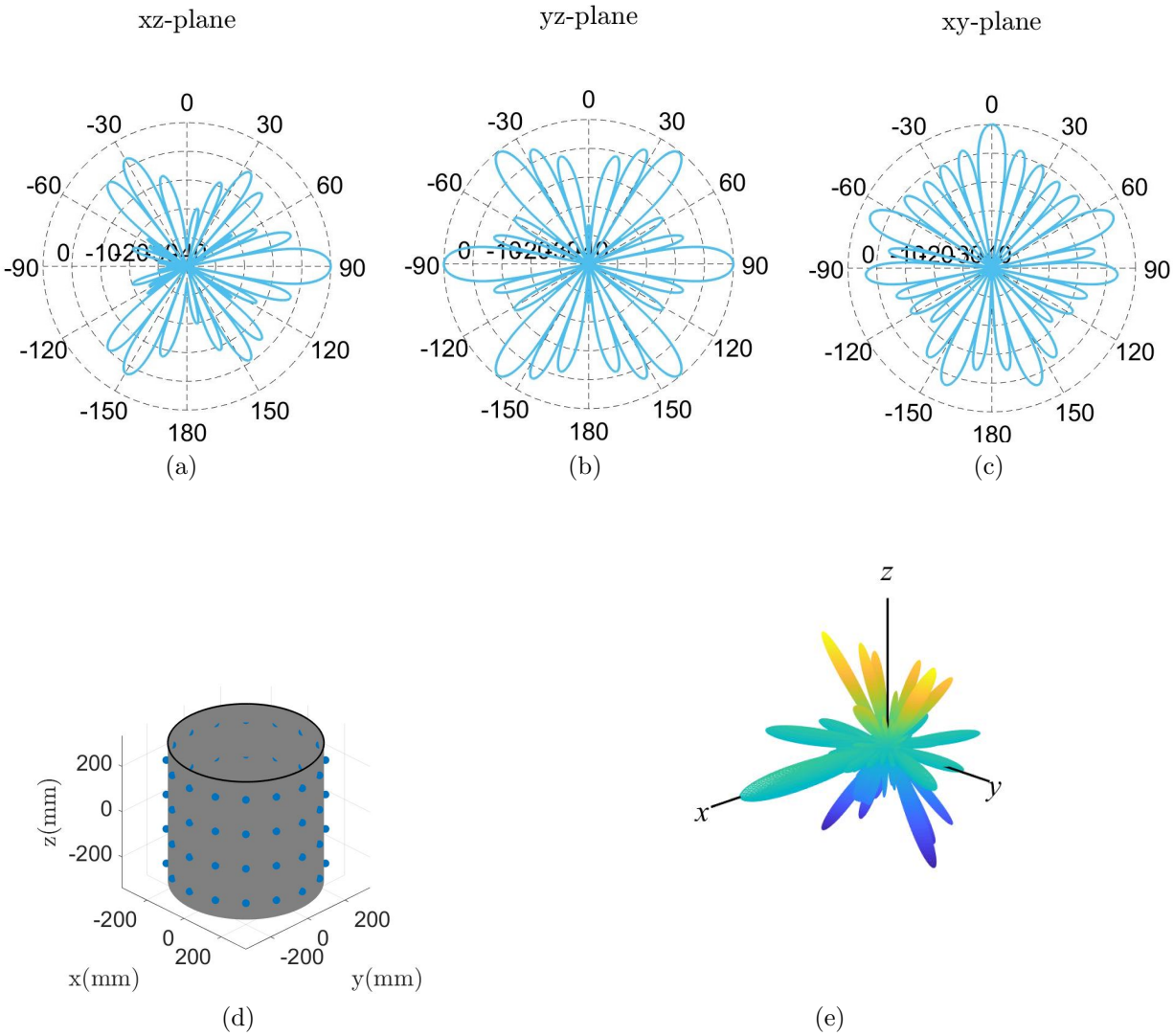

Figure C.7 Radiation pattern slices in all principle planes, element distribution, and 3D radiation pattern for the cylindrical array on the drum when we steer the main beam to $\theta = 90°$ and $\phi = 0°$ and when we increase the ring and element spacing to λ. This results in four rings with 16 elements each: (a) Pattern slice in the xz-plane, (b) Pattern slice in the yz-plane, (c) Pattern slice in the xy-plane, (d) Element distribution on the drum of the continuous mining machine, (e) 3D radiation pattern

From Figure C.7, we see that the SLL rises and that grating lobes are now present within the radiation pattern, where this is highly noticeable in all three plane cuts in the three principle planes.

C.3 Cylindrical Array (Active Sector)

In Chapter 6, we saw that an option we have is to implement an active sector for the cylindrical array. This section details the results for the three cases mentioned above which are when we have the elements spaced by a half wavelength, full wavelength, and have an element every 90° on each of the four rings. Unlike in Chapter 6, an EM-model will not be provided after presenting the MATLAB results. However, a fabricated prototype of one of the rings will be presented.

If the reader has not already gone through Chapter 6 explaining the active sector, the principles behind the active sector is that we first specify a range of ϕ, where the elements that fall within this region are the elements that are transmitting. In most active sector applications, once the active sector becomes aligned with the receiver, the sector will then transmit the collected data to the receiver and power down the elements and then repeat the process for when the next active sector becomes aligned with the receiver. Or the active sector can be synced to a clock to indicate when each sector transmits. The active sector can be more complex to implement but it's a convenient way to relay data without causing too much interference. For our particular application, the possibility of implementing a delay between transmission times with the active sector can ensure that we are being efficient with our data collection and channel use, in order to make sure that we are transmitting only the information that is of use.

To begin the active sector design, we first start off again with the maximum gain case, which consists of 10 rings with 32 elements on each ring. Note that for our active sector, the length of the active region is $\phi = 90°$. The results for the maximum gain case are shown in Figure C.8.

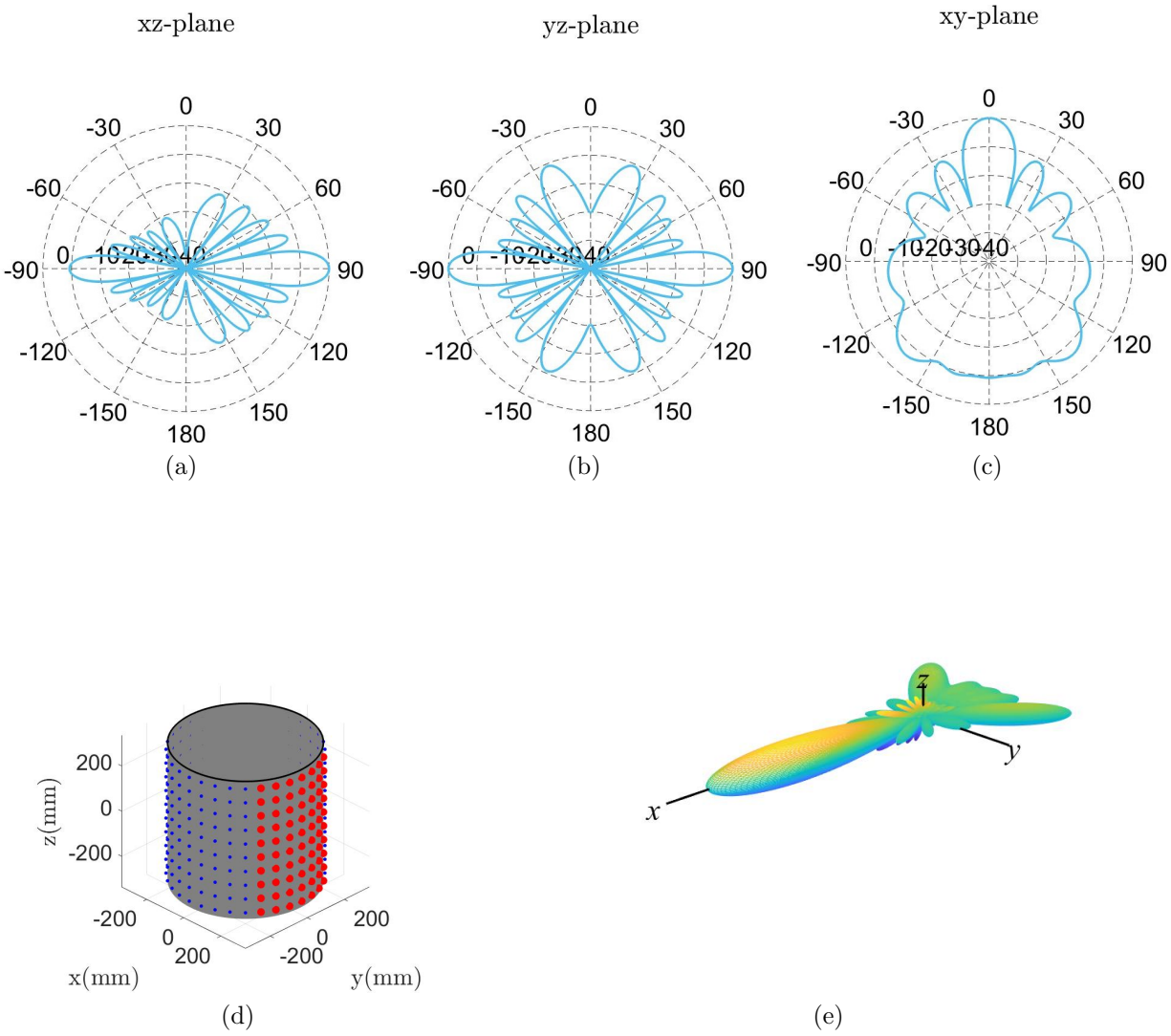

Figure C.8 Radiation pattern slices in all principle planes, element distribution, and 3D radiation pattern for the active sector on the drum when we steer the main beam to $\theta = 90°$ and $\phi = 0°$: (a) Pattern slice in the xz-plane, (b) Pattern slice in the yz-plane, (c) Pattern slice in the xy-plane, (d) Element distribution on the drum of the continuous mining machine, (e) 3D radiation pattern

Once more, we repeat the process of removing the amount of rings and elements per ring. The two cases we look at are the densest high gain case (4 rings 16 elements per ring) and the sparse case (4 rings 4 elements per ring). These results are displayed in Figures C.9 and C.10 respectively.

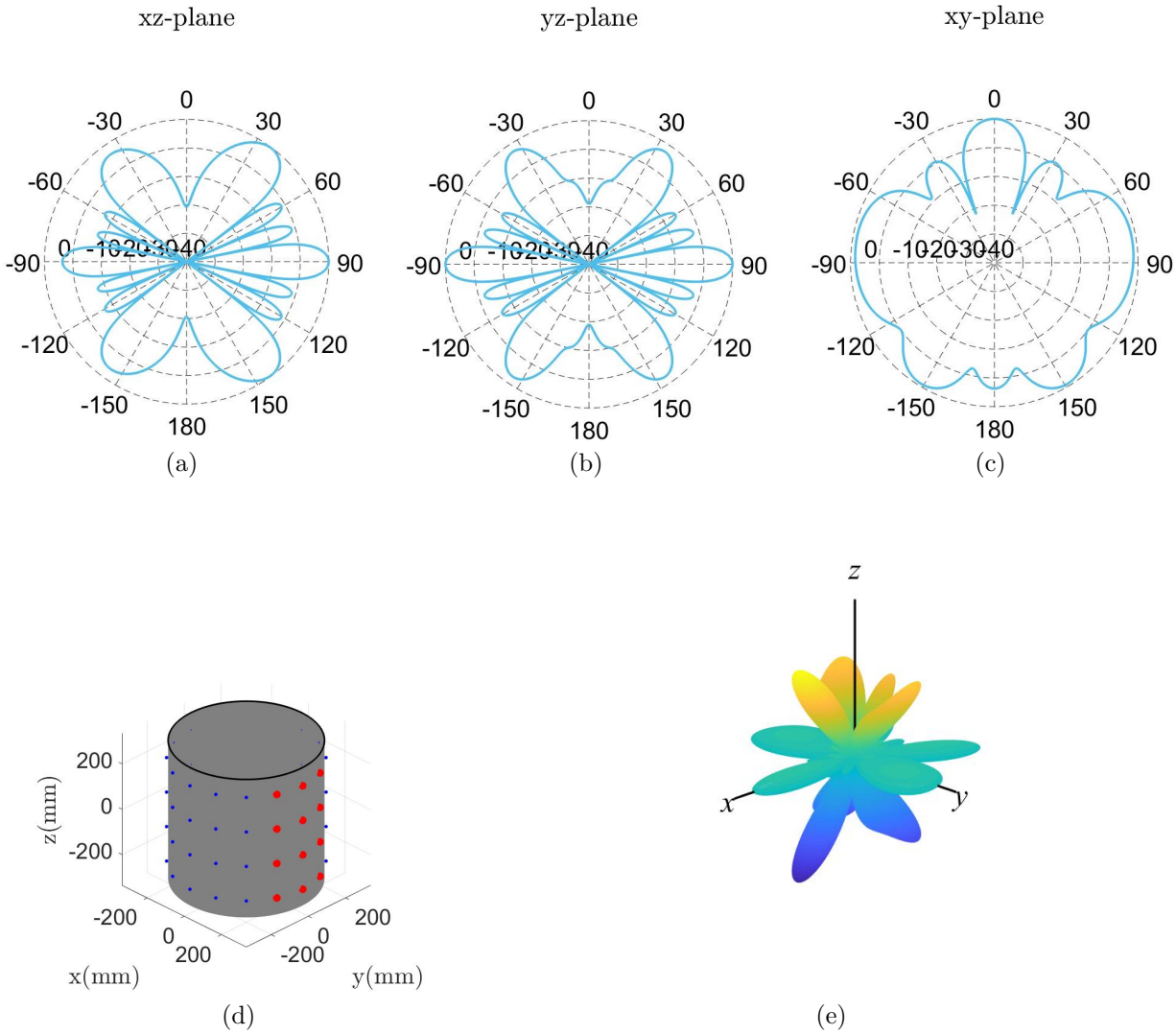

Figure C.9 Radiation pattern slices in all principle planes, element distribution, and 3D radiation pattern for the active sector (4 rings 16 elements per ring) on the drum when we steer the main beam to $\theta = 90°$ and $\phi = 0°$: (a) Pattern slice in the xz-plane, (b) Pattern slice in the yz-plane, (c) Pattern slice in the xy-plane, (d) Element distribution on the drum of the continuous mining machine, (e) 3D radiation pattern

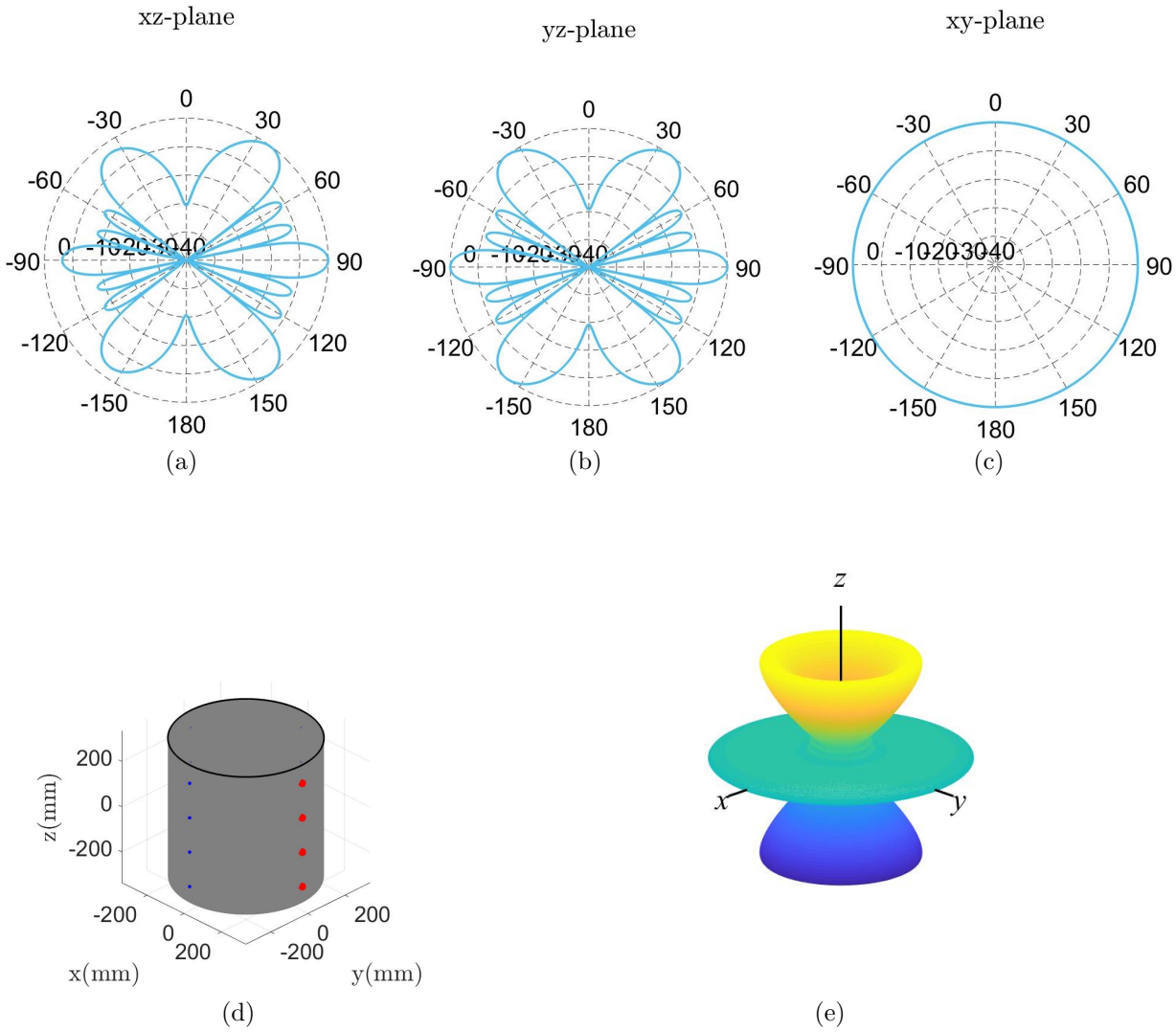

Figure C.10 Radiation pattern slices in all principle planes, element distribution, and 3D radiation pattern for the active sector (4 rings 4 elements per ring) on the drum when we steer the main beam to $\theta = 90°$ and $\phi = 0°$: (a) Pattern slice in the xz-plane, (b) Pattern slice in the yz-plane, (c) Pattern slice in the xy-plane, (d) Element distribution on the drum of the continuous mining machine, (e) 3D radiation pattern

We see that for the 4 ring 4 element case, that the active sector reduces down to a linear array where the elements are spaced by one full wavelength, thus explaining the reason for the results of the 3D radiation pattern and xy-plane cut.

C.4 Ring Fabrication

The ring concept from the previous section was fabricated, as shown in Figure C.11. The ring consists of a two foot diameter and is made out of a mold-able and flexible plastic, which allows it to wrap around the drum and generate minimal interference.

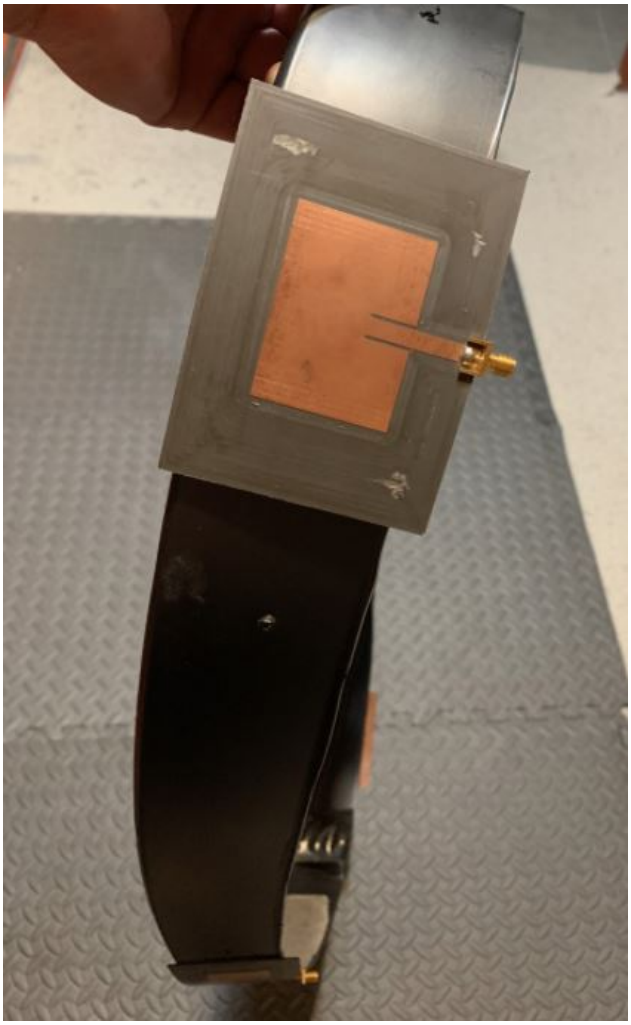

Figure C.11 Fabricated ring with four inset fed microstrip patch antennas

The ring, antennas and the coax lines would be placed under the surface of the drum so that they can be shielded from falling debris in the mine. If the ring was made of a more flexible material, the ring can bend and be conformed to fit between each of the picks, to ensure that we don't need to make anymore changes to the design of the drum. It's also suggested that a material with a low reflection coefficient is used to encase the antennas within the drum, so that we have minimal reflections when our signal is being transmitted through the medium. However, the material will also need to be durable so that it won't be prone to any damaging while the continuous mining machine is in operation.

APPENDIX D

COMMUNICATION SYSTEM

In this appendix, the functionality and testing of the communication system is discussed. In order to examine the performance and capabilities of the communication system, we used two separate means to do so. The first is with software defined radios, so we could physically analyze the received signal at the receiver. The second is with the XBEE pro wireless mesh kit which allowed us to examine the transmitted and received packets, where the packets were eventually decoded so that we could plot the received data. Note that the software defined radios and XBEE pros were used to model the data transmitted for a single pick. The sensor configuration on the pick is displayed in Figure D.1.

Figure D.1 Sensor configuration on the pick. The sensor we use has a total of four load cells

The sensor is placed in a sleeve between the pick and the bit (shown in the background of the image), where the bit is locked into the pick with a key. The sensor consists of an array of capacitive load cells that take force measurements at a rate of 400 Hz. The sensor consists of 4 or more load cells, where the sensor in Figure D.1 uses four. The data isn't lumped together but is instead treated as four separate channels, so for every second that goes by, we are collecting a total of 1600 samples.

Since the sensor is located within a sleeve, we can expect to see a DC offset in the collected data, where a large pulse will occasionally appear, which is when the pick makes contact with the surface of the wall. From these force measurements, we are able to determine which type of material we are drilling into and also determine what condition the bit is in, such as whether it is a newer pick in good condition or if the bit is approaching the end of its life span. This explains the importance of the reliability of the communication system. Since we can already expect for the data to be injected with a small amount of noise from the load cell sensor, we need to ensure that the collected data makes it to the receiver with the fewest amount of packets dropped as possible and with the fewest amount of bits flipped. These two concepts are measured by the bit error rate (BER) and packet loss. We can easily measure these two statistics by setting up the transmitter and receiver to be maximum 24 inches apart from another and transmitting load cell data to the receiver. By using a software defined radio (SDR), we can analyze the physical signal that we receive and use it to determine whether the signal is characterized by a "0" or a "1", which is typically accomplished by using a particular modulation scheme. This is done by using a matched filter, which is used to detect a known transmitted signal. Lastly, we will use the XBEE pro wireless mesh kit, which packetizes data off of a sensor and transmits it to another XBEE module, where a Python script can then be used to read in the packets, decode them, and plot the received data. Note that for the XBEE modules, they follow the Bluetooth protocol IEEE 802.15.4 and transmit at 2.45 GHz but for the SDRs, they transmit IQ-samples with a user specified carrier signal, where the carrier signal is then demodulated with another

carrier at the receiving end so that the data can then be received. Both the work for the SDRs and the XBEE pros will be described in more depth in the following two sections.

D.1 Software Defined Radios (SDRs)

For this work, we used the b200 mini software defined radios, which are provided by Ettus Research as shown in Figure D.2.

Figure D.2 Display of the b200 mini software defined radio. Image from [104]

The b200 mini consists of three channels which are a transmit channel (TRX), a receive channel (RX2), and a clock reference channel (REF). For our testing with the b200 minis, we did not use the REF channel and used another means so that we could avoid having to synchronize the transmitter and receiver to a reference clock (will be discussed later). This mini SDR is quite a powerful resource, where it can transmit and receive in a wide frequency range of 70 MHz to 6 GHz and has up to 56 MHz of instantaneous bandwidth. What makes the b200 SDRs convenient is that they are GNU Radio supported and maintained by Ettus Research through GR-UHD, which is an interface to the UHD distribution by GNU Radio. This means that any computer/laptop with the Linux OS and necessary libraries can communicate with the radios from the Linux command line and utilize Python scripts to generate, receive, and process the received data. Since the radios require a computer/laptop for operation, they are not the permanent solution to the communication system but are

instead a temporary one which will allow us to understand the modes of operation of our data transmission on the drum.

Without going into too much detail, the easiest way to describe the functionality of the SDRs is that they generate, transmit, and receive In-Phase and Quadrature (IQ) samples. IQ sampling is a slightly more complicated version of regular digital sampling, where we know from basic communication theory, a time dependent signal $x(t)$ is transmitted through a medium and is the sum of a $\cos(t)$ component and a $\sin(t)$ component as such

$$x(t) = I\cos(2\pi ft) + Q\sin(2\pi ft) \tag{D.1}$$

where f is the carrier frequency and I and Q are the magnitudes of the $\cos(t)$ and $\sin(t)$ components respectively. When we add these components together, we will receive another sine wave but with a different amplitude and phase.

When we talk about complex numbers, we can often think of them in a plane, where the x-axis represents the real component and the y-axis by the imaginary component. Take for example the imaginary number $0.7 + 0.5j$, we see that the imaginary number can be represented by a phasor with a magnitude of $\sqrt{a^2 + b^2} = 0.8602$ and a phase $\tan^{-1}(b/a) = 0.6202$ radians. This concept for imaginary numbers aligns directly with the concept of the IQ convention, where the real axis represents the In-Phase component and the imaginary axis is the Quadrature component. So when we translate this idea over, the sample $0.7+0.5j$ can be represented by

$$x(t) = 0.7\cos(2\pi ft) + 0.5\sin(2\pi ft) \tag{D.2}$$

When we use the trig identity $a\cos(x) + b\sin(x) = A\cos(x - \phi)$, where A is the magnitude and ϕ is the phase, we see that Equation D.2 is equal to

$$x(t) = 0.8602\cos(2\pi ft - 0.6202) \tag{D.3}$$

which is the signal that we are transmitting. It's important to notice that since there's no $\sin(t)$ component, the signal is purely real, is is convenient for transmitting because we can't actually transmit a complex signal with an electromagnetic wave. As mentioned, f is the carrier frequency, which is a usually a much higher frequency than the frequency content of our signal because from basic antenna theory, we know that the resonant frequency can be found by $\lambda = c/f$, where c is the speed of light and λ is the wavelength. Since antennas are designed and have dimensions based off of the wavelength, we would need a very large antenna to transmit a signal at lower frequencies, so the majority of carrier frequencies are in the upper MHz and mid to lower GHz range.

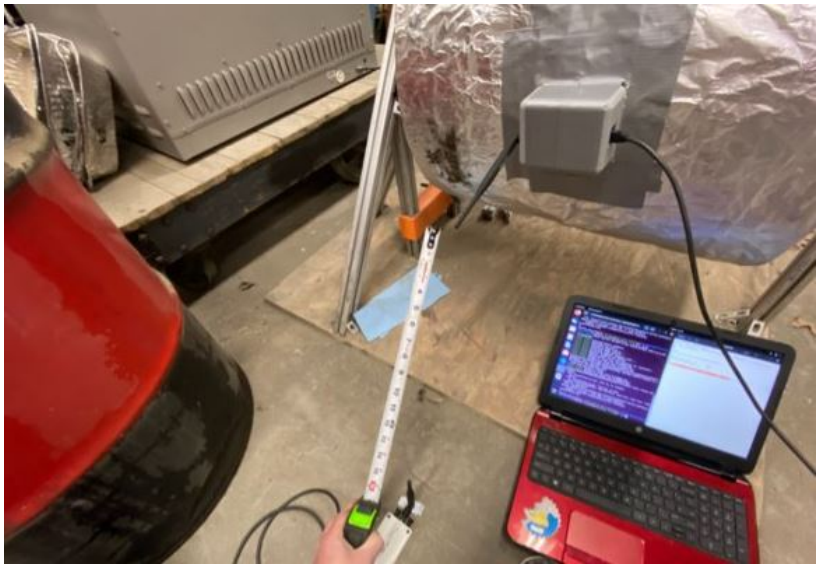

Figure D.3 Test setup with the SDRs on the dummy drum. The transmitter is placed on the drum and transmits to the receiver which is placed 24 inches away

At the receiving end, we sample the IQ components separately, where we would use two analog to digital converters (ADCs) to simultaneously measure the In-Phase and Quadrature components. After sampling the components, we would then combine the I and Q samples and store them as a complex number. So at each sample time, we take one I sample, one Q sample, and combine them into the form $I + Qj$, which is ultimately just a complex number. For our sampling notation, if we say that we are sampling at 10 MHz, then we are

taking ten million I and Q samples simultaneously, so then we would end up with ten million complex numbers per second. Thus explaining the concept of how imaginary numbers are transmitted, received, and stored with the SDRs.

For our test setup, we use two b200 mini SDRs, where one radio is serving as the transmitter on the drum and the second radio is 24 inches away serving as the receiver. Our testing setup on the drum is displayed in Figure D.3.

The antennas used are dipole antennas, since the inset fed microstrip patch antennas from Chapter 2 were shifted to higher frequency. The dipoles can operate at 2.45 GHz which is the desired operating frequency and the frequency that we transmit our signal at. The experiment that we performed is that we take a known signal and transmit the IQ samples from the drum and then use the receiver to take in the transmitted IQ samples. For simplicity, we transmit a pure tone at a frequency f_1, where the signal can be given by

$$s(t) = e^{j\omega t} \tag{D.4}$$

where $\omega = 2\pi f_1$ and $f_1 = 10$ kHz. The way that we are able to avoid using a reference clock is that we generate 1000 samples of $s(t)$ at a rate of 1 MHz and by using an infinite while loop, we only insert the transmit statement so that the SDR is constantly transmitting the pilot signal. So then at the receiver end, we then collect 1000 IQ samples at a rate of 1 MHz. Note that for the b200 mini, the sampler thresholds the received samples at 1, so that anything ≥ 1 is capped off at 1. The reason why we would rather collect a few amount of samples, is that when the data is transmitted, it is often encoded with a coding scheme. Such as we take the data measurements off of one of the channels of the load cell sensor, we take our data and turn it into bits (ones and zeros). For one of the more simpler modulation schemes, we use amplitude shift keying, where snippets of a sinusoid with a large amplitude would indicate a 1 and a smaller amplitude or no amplitude would indicate a zero. From here, we would use a matched filter to determine if we detect a zero or a one in the received samples. A matched filter is a detector that is used to detect when a known signal is present

within a sampled signal. This is very convenient for when we receive our known signal with noise and interference because the matched filter maximizes the signal to noise ratio (SNR) and can detect if and where the signal is present within the sampled signal.

The coefficients of the matched filter are found by desiring to maximise the SNR at a specific time T_M. Note that the spectrum of the receiver output $y(t)$ is given as $Y(\Omega) = H(\Omega)S(\Omega)$, where $H(\Omega)$ is the receiver frequency response and $S(\Omega)$ is the spectrum of our transmitted pilot signal. When we desire to maximize the SNR at a moment T_M, the power of the signal component at time T_M is given by

$$|y(T_M)|^2 = \Big|\frac{1}{2\pi}\int_{-\infty}^{\infty} S(\Omega)H(\Omega)e^{j\Omega T_M}d\Omega\Big|^2 \tag{D.5}$$

We then need to determine the output noise power, where we consider the case of where the interference is white noise and the power spectral density is given by σ_w^2 W/Hz. At the receiver, the receiver output is equal to $\sigma_w^2|H(\Omega)|^2$ W/Hz, where we get that the output noise power is

$$n_p = \frac{\sigma_w^2}{2\pi}\int_{-\infty}^{\infty}|H(\Omega)|^2 d\Omega \tag{D.6}$$

We can then express the SNR as

$$\chi = \frac{|y(T_M)|^2}{n_p} = \frac{\Big|(1/2\pi)\int_{-\infty}^{\infty} S(\Omega)H(\Omega)e^{j\Omega T_M}d\Omega\Big|^2}{(\sigma_w^2/2\pi)\int_{-\infty}^{\infty}|H(\Omega)|^2 d\Omega} \tag{D.7}$$

When we use the Cauchy Swarz inequality from Equation D.8, we see that we can achieve equality when $B(\Omega) = \alpha A^*(\Omega)$, where $\alpha \in \mathbb{R}$.

$$\Big|\int A(\Omega)B(\Omega)d\Omega\Big|^2 \leq \Big[\int |A(\Omega)|^2\Big]\Big[\int |B(\Omega)|^2\Big] \tag{D.8}$$

By using this concept, we can place an upper bound on Equation D.7 and the SNR is then bounded by

$$\chi = \frac{(1/2\pi)^2 \int_{-\infty}^{\infty} |S(\Omega)e^{j\Omega T_M}|^2 \int_{-\infty}^{\infty} |H(\Omega)|^2 d\Omega}{(\sigma_w^2/2\pi) \int_{-\infty}^{\infty} |H(\Omega)|^2 d\Omega} \tag{D.9}$$

and we see that the SNR is maximized when

$$H(\Omega) = \alpha S^*(\Omega) e^{-j\Omega T_M} \tag{D.10}$$

or equivalently

$$h(t) = \alpha s^*(T_M - t) \tag{D.11}$$

The optimal solution for maximizing the SNR of the receiver output is when the impulse response of the receiver is "matched" to the transmitted signal, particularly when the signal is time reversed and conjugated.

Before we discuss the matched filter results, we must briefly mention a common phenomena that is encountered with the use of SDRs known as carrier frequency offset. Carrier frequency offset (CFO) occurs because the RF oscillators in the transmitter and receiver are not perfectly in sync with each other, where they may be a couple kHz off the frequency that they're supposed to operate at. With that being so, when we remove the carrier and translate our signal back to baseband, the signal will not exactly be centered at baseband but instead will be offset by the difference between both the oscillator in the transmitter and in the receiver. CFO will also occur when either the transmitter or the receiver are in motion because a traveling wave will have a change in frequency whenever it is in motion relative to the wave source. This here is known as the doppler effect or doppler shift.

This offset from baseband is extremely problematic when we perform the matched filtering operation. As we match filter a signal with different frequency content than the template, we can expect the output of the matched filter to decrease as we stray further away from the frequency content of the template. If we were to plot the maximum output of the matched filter over change in the frequency, the output would take the shape of a sinc function, where

slight deviations in frequency result in a drastic decrease of the matched filter output as shown in [105].

The solution to this issue, is one that increases processing time but is able to accurately detect the desired signal even when CFO is present. We accomplish this by implementing a matched filter bank. The matched filter bank will be a filter bank containing copies of our template signal that are each shifted by different frequencies. We start off by estimating the range of frequencies that our signal can be offset by, where in our case we chose to have a range of ± 2 kHz, so the $f_{\max} = 12$ kHz and the $f_{\min} = 8$ kHz. This means that we are able to detect the signal if it's shifted anywhere between 8 kHz and 12 kHz. The next step in the filter bank design process is to determine the resolution of the filter bank. After sufficient testing in MATLAB, we found that with the amount of samples we collect, we can afford to have a filter bank with a resolution of 40, meaning that we have 40 matched filters in the filter bank where the shifted templates uniformly span the range of 8 kHz to 12 kHz. Once we receive the transmitted IQ-samples, we then match filter the received signal with each of the translated template signals and store the maximum output for each matched filter, where the maximum of the maximums represents the true output and the corresponding frequency bin that the received signal was shifted to. The matched filter can be viewed as a correlator, where we are correlating our signal with a known signal, and when we correlate two vectors that are pointing in relatively the same direction, we will have a high correlation value. In order to simplify our interpretation of the matched filter output, we normalize each of the template signals and the received signal by dividing each signal by the l_2-norm of itself. By using Cauchy Schwarz, we see that the maximum output of any matched filter will be 1.

For this experiment, we start by transmitting our pure tone with a carrier of 2.45 GHz and a gain of 70 dB. The signal is then received with a gain of 40 dB and put through the matched filter bank. For the first case, we test out the filter bank when we are not transmitting the sinusoid, so we are receiving only white noise $w[n]$, where n represents the sample number. So ultimately, the output of the receiver $y[n]$ is

$$y[n] = w[n] \tag{D.12}$$

The received signal and the output of the matched filter bank are shown in Figure D.4

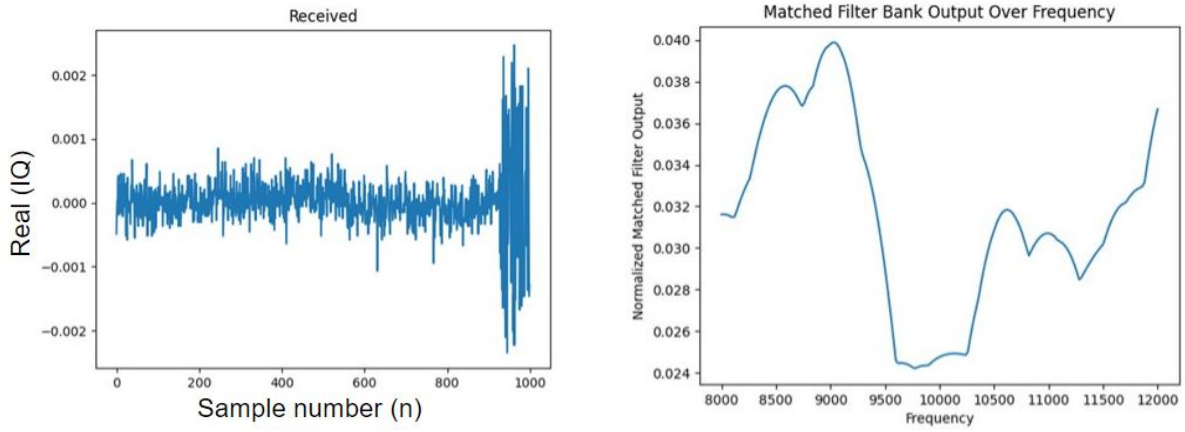

(a) (b)

Figure D.4 Received signal when we are not transmitting (white noise) and the output of the matched bank over frequency (a) Received noise when no signal is being transmitted (b) The maximum outputs of each matched filter over frequency. From the amplitude of the output, we can tell that there is no signal being transmitted.

From first glance at Figure D.4 (a), we can easily tell that there is no signal present within the received IQ-samples. When we examine the matched filter bank output, we see that despite there being a peak in the output, the amplitude of the peak is not indicating that a signal of interest is present, since the amplitude of the peak is $< .04$. For the next case, we set the transmitter so that it is transmitting our desired signal in an infinite loop. We see that the output of the receiver can be modeled as

$$y[n] = s[n] + w[n] \tag{D.13}$$

where we are receiving our signal with white noise added into it. The received signal and the matched filter bank are shown in Figure D.5.

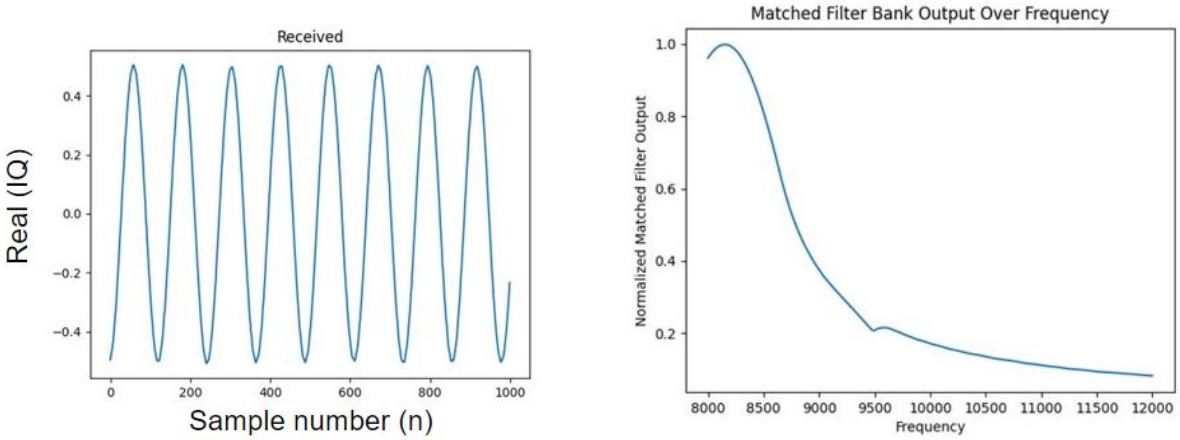

(a) (b)

Figure D.5 Received signal when we are transmitting the pure tone and the output of the matched bank over frequency (a) Received signal (b) The maximum outputs of each matched filter over frequency. From the amplitude of the output, we can conclude that the signal was received and shifted down to 8.25 kHz due to the peak of the output.

In the data for the IQ-samples, we are able to clearly see that we have received the pure tone from the transmitter on the drum. When we closely inspect the received signal, we are able to tell that the peaks have been slightly distorted, which can be due to quantization and noise. However, from the matched filter output, we are able to see that the frequency of the received signal is not the same as the one we transmitted, since we have a peak centered around 8.25 kHz. This amplitude of the peak is close to but not exactly 1, meaning that this is truly the signal that we were wanting to detect. We're able to see that if we were only to use the template for the matched filter at 10 kHz, the output of the matched filter would be 0.2. This is problematic because if we were to receive a signal that has similar frequency content to our transmitted signal, this can give rise to a false alarm, where we say that we detect a signal but it truly isn't the signal that we transmitted. Or in the opposite case, the noise power level is increased, in can reduce the matched filter output even more and we can have a missed detection, which is when we receive our desired signal but fail to detect it. So by using the matched filter bank, we can conclude that we are successfully able to receive a modulated signal when we are transmitting it from the drum and be able to distinguish

which bit that the modulated signal represents.

The final part in the work of using the SDRs is to determine which gains we should set the transmitter and receiver to. This is imperative because we want to be able to set the gain of the receiver as low as it can be so that we don't raise the noise floor and still be able to detect the transmitted signal. We also don't want to set the transmitter gain too high either so that we don't have to increase the amount of power required for the transmitting antenna elements. In order to determine this information, we would fix the gain of receiver, then transmit the signal at varied gains and capture the maximum output of the matched filter bank. We'd similarly repeat the process for the transmitter, where we would fix the gain and then vary the gain of the receiver. The results in Figure D.6 depict the matched filter output for when the gain of the transmitter is fixed at 50 dB and the receiver gain is varied and when the receiver gain is fixed at 30 dB and the gain of the transmitter is varied.

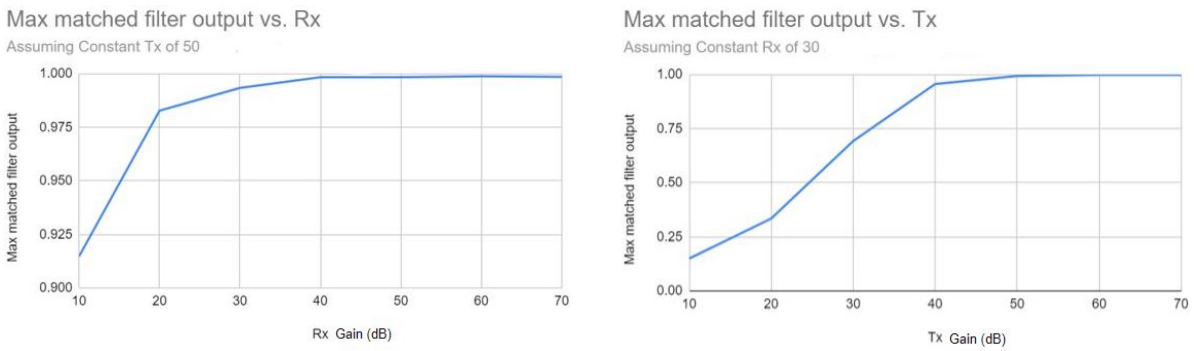

(a) (b)

Figure D.6 Matched filter bank output for when the gain is varied for either the transmitter or receiver (a) Matched filter bank output when the gain of the transmitter is fixed at 50 dB and the receiver gain is varied (b) The matched filter output when the gain of the receiver is fixed at 30 dB and the gain of the transmitter is varied.

The plots in Figure D.6 demonstrate the importance of having a high transmit gain. In Figure D.6 (a), we see that when we at least have a transmit gain of 50 dB, we can have the receiver gain as low as 10 dB and the matched filter bank still detect the signal with a max amplitude > 0.9. When we fix the receiver gain at 30 dB, the matched filter output detects

the transmitted signal but with a small amplitude, particularly when the transmit gain is ≤ 25 dB. It's not until we set the transmit gain to be ≥ 40 dB, where we are able to get the amplitude of the matched filter output to be ≥ 0.9. From the conclusion of this work, we see that it's optimal to have the transmit gain be at 50 dB and the receiver gain to be set to 20 dB, since it allows us to detect our transmitted signal at an amplitude ≥ 0.975, which would not give way to false alarms or any missed detections.

D.2 XBEE RF Modules

This final section details the work completed with the XBEE Pro wireless RF modules to transfer specific data from the load cell sensor. The XBEE Pro is a low power RF module used for wireless applications, where a single RF module draws less than 2.5 μA of current to function. XBEE pros can also function at lower frequency operations, particularly 900 MHz and can also transmit at 2.4 GHz, which makes it extremely flexible for operating at different frequencies in the frequency spectrum.

Figure D.7 Display of the XBEE Pro RF Module. Image from [106]

The Zigbee pros follow the Zigbee protocol IEEE 802.15.4. The reason why we chose to use a device that follows the Zigbee protocol for this particular application is because Zigbee is the optimal protocol for all short-duration/range wireless communication systems,

specifically ones that require low energy consumption for low-rate sensors. Particularly, the XBEE pro has a data rate of 250 kbps and can transmit up to 200 ft (60 m) in indoor/confined spaces. This particular module that we use, the Digi XBEE Pro S2C Zigbee requires 3.6 V to operate and has a transmit power of 3.1 mW (5 dBm). For the serial data interface, the UART protocol is used. A 10-bit ADC is also used on the chip. In terms of the antenna, a through-hole PCB antenna is used, where we do have the option to solder on an SMA connector but to keep things simple, we went with the stock antenna that it came with. Lastly, the XBEE Pro has a clock speed that goes up to 50.33 MHz, 32 kB Flash/2 kB RAM, and a 128-bit AES.

For the test with the XBEE pro RF modules, we separated the transmitting XBEE and the receiving XBEE 24 inches apart, where the receiving XBEE was connected to a laptop and a Python script was used to read in and decode the data. On the transmitting side, the load cell sensor was interfaced to the transmitting XBEE module with a microcontroller, where the particular microcontroller that was used was the Nucleo-L452RE model. The load cell sensor has four separate channels, where each load cell has a sampling rate of 400 Hz, totaling to 1200 total samples every second.

Since we were unable to connect the XBEE module and microcontroller to the load cell sensor while it was attached to a pick during a rock cutting sample, we had to generate our own force measurements. We did so by squeezing down on each of the load cells with our fingers so that we could get a response from the sensor. The collected data is then sent over to the microcontroller which then interfaces it to the XBEE pro.

When the data is received, its expressed in hexadecimal notation and some of the packets contain partial data or have part of the header missing, which completely disrupts the flow of the received data. In order to fix this issue, a Python script was written so that the data could properly be converted from hex to decimal. The script also goes through and makes sure that each packet contains all of the collected data. Since we know the length of each packet and are indicated in the header which packet we received, we can go through the entire

data stream and discard any partially received data, since each packet has measurements from each channel and we don't want to have one channel with more data than another. The received, decoded, and sorted data that we received from the load cell sensor is displayed in Figure D.8, where the plot depicts the raw encoded sensor measurement over time.

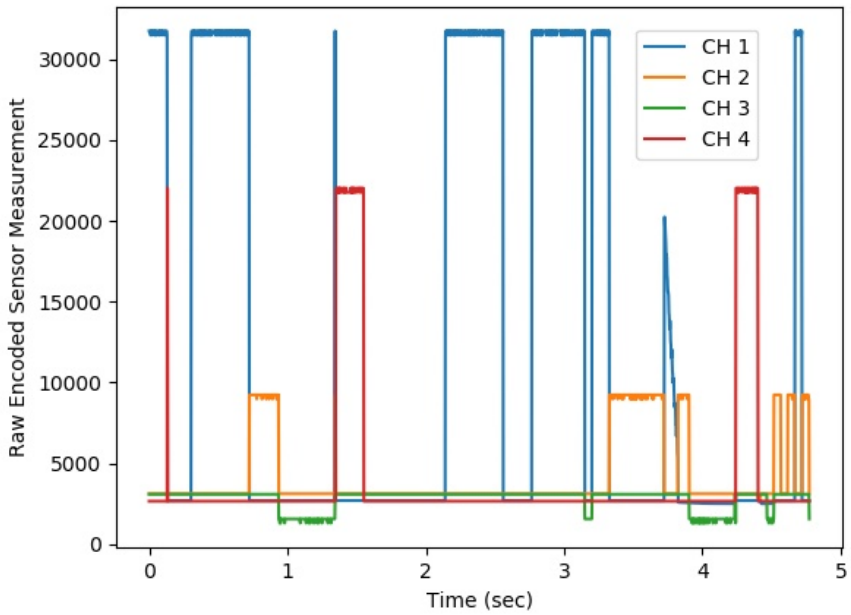

Figure D.8 Plot of the received data that was collected from the load cell sensor over all four channels. The measurements were generated by finger pressing down on each of the load cells. We see in the collected data the raw encoded sensor measurements and that all of the load cells had a force applied to it except channel 3

From the figure, we are able to see when we applied pressure to each of the load cells, where the load cell for channel one was the load cell that we applied the most pressure to. Originally, we collected more data but some packets were discarded because they didn't contain measurements for all four samples, where some of the measurements were lost in transmission. After sorting through and cleaning all of the packets, we had approximately five seconds worth of measured data. Altogether, we received a total of 2020 packets that were transmitted, where only 1970 packets were kept because they contained the data measurements for all four channels and didn't lose any in transmission. When we calculate the

losses, we had a packet loss percentage of 2.48%, where for our Smart Bit design, this is an acceptable packet loss rate. If we were to start losing more than 5% of our packets, then we would have a case to be concerned about the efficiency of our data communication system.

APPENDIX E

RF POWER BUDGET

In this appendix, we describe our calculated RF power budget for the antenna array system for a single ring that consists of 4 elements that are placed at $\phi = 0°, 90°, 180°$, and $270°$ respectively. With our four transmitters on the drum, we would then use a four way power divider to ensure that all transmitters would transmit the same signal to the receiver. Given the rotation speed of the drum, we then assume that at least the power associated with a single transmitter would be received by the receiver, since we know that the receiver would be between 12-24 inches away from the drum. For this power budget, we will assume that it's on the higher end, so we say that the receiver is 20 inches (0.5 meters) away. Finally, the operating frequency that we will be transmitting at will be 2.45 GHz. The schematic of our ring setup on the drum is depicted in Figure E.1.

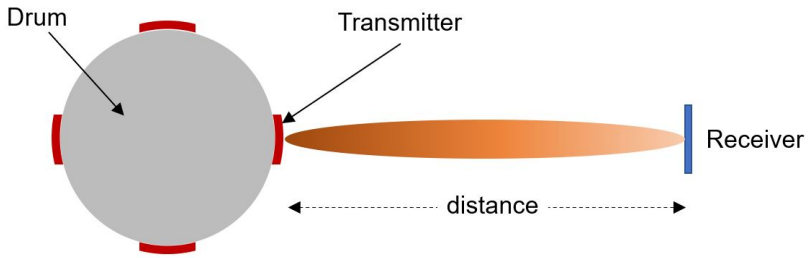

Figure E.1 Transmitter and receiver setup for the ring configuration

It was mentioned previously in Appendix C, that the antennas that we are using for the ring configuration are the conformal inset fed microstrip patch antennas from Chapter 2 in this dissertation. For a cylinder with a radius of 1 ft, we see that the curvature will reduce the gain of the microstrip patched down to 7 dBi. Note that for this power budget calculation, we assumed a noise floor of -30 dB. Since we have all of the necessary parameters, we could use the Friis power transfer formula to calculate what the received power would be, where the Friis power transfer formula is given by

$$P_r = \frac{P_t G_t G_r \lambda^2}{(4\pi R)^2} \tag{E.1}$$

where P_r represents the power received, P_t is the transmitted power, G_t is the gain of the receiver, G_r is the gain of the receiver, λ is the wavelength of the operating frequency, and R is the distance from the transmitter to the receiver.

By using this formula, we were able to run several cases so that we could determine what the receiver power would be for a particular transmit power. The receiver power for various transmit powers and the corresponding signal to noise ratio (SNR) is given in Table E.1.

Table E.1 Received power and SNR for corresponding power transmission levels

Tx Power (dBm)	Tx Power (mW)	Rx Power (dBm)	Rx Power (mW)	SNR (dB)
30.37	1089	10	10	60.37
20.37	108.9	0	1	50.37
10.37	10.98	-10	0.1	40.37
0.37	1.098	-20	0.01	30.37

For our desired application, we would want an SNR of 50 dB or higher so that we would get a low bit error rate (BER). This is important because in Appendix D where we discussed testing for the communication channel, we desire a system that would have a low packet loss and for the bits within the payload to not be flipped. Receiving data with flipped bits would add in more unnecessary noise to the sensor measurements which would in turn reduce the accuracy of the classification and detection algorithms for the data processing side of the Smart Bit system. Furthermore, we are willing to have a high transmit power so that we can have a high SNR, because increasing the gain on the receiving end would raise the noise floor and could possibly make it harder to determine if the bit is a "0" or a "1".

We can conclude from this power budget analysis that at a minimum, each transmitter would need to transmit the signal with an RF power of about 109 mW, so in total, a minimum of 0.5 Watts of RF power is needed. If we were to proceed and use the four ring configuration, then a total of 2 Watts would be needed per drum head to power the array.

Ultimately, this is a relatively low cost power system, however, the power source is suggested to also be placed underneath the surface of the drum so that it can be shielded from any falling debris in the vicinity.

APPENDIX F

SPARSE CYLINDRICAL ARRAYS BASED OFF THE VAN DER CORPUT SEQUENCE

In this appendix[2], we present the work completed for sparse cylindrical arrays for Hammersley sampling, lower bases of Halton sampling, and Sobol sampling. Note that Hammersley sampling and Halton sampling were used on a cylinder with different dimensions than for Sobol sampling.

F.1 Introduction

Array cost is proportional to the number of elements in the array; therefore, designers try to minimize the number of elements on the aperture [91, 109]. Large element spacing however results in grating lobes that degrade the array performance. For a dense array, thinning and aperiodic spacing are used to lower sidelobe levels [110, 111]. Sparse arrays however use thinning and aperiodic spacing to lower grating lobes, since low sidelobes are not an option for sparse arrays due to element spacings larger than one wavelength. While most work on sparse arrays focus on planar configurations, for many applications such as radar, sonar, etc., cylindrical arrays offer numerous advantages compared to planar arrays due to their azimuthal symmetry. Sparsity in these arrays result in the same problem of grating lobes. In this work, the use of nonuniform element spacing based on Van der Corput sequence and Sobol sequences is explored[73]. Specifically, the study consists of Hammersley, Halton, and Sobol samplings on the cylindrical array [74, 80, 112], and show that these element spacing distributions can eliminate the grating lobes with element spacing larger than one wavelength.

It was mentioned at the end of chapter 2 that the purpose of this work is to design an efficient sparse array that can be used to transmit the data collected on the drum from a continuous underground mining machine, and transmit the data from the drum to another

[2]The work is in collaboration with Randy Haupt [107, 108]

location in the mine, so that the data can be processed. For this instance, it will be assumed that there's no picks on the cylindrical drum, meaning that there are no regions that can not be sampled, so the entirety of the cylinder is able to be sampled.

F.2 Sampling Points on a Cylindrical Aperture

In the previous chapter, the array factor was given for a planar array, which was ultimately a sum of complex sinusoids, dependent on the elements position in the aperture. The array factor for a cylindrical array is more complex to compute, compared to the planar case. For the planar case, the element position was determined by its (x, y) coordinates in the xy-plane, however, for the cylindrical case, the sampled element coordinate is determined by its position relative to the angle ϕ, it's height z with respect to the z-axis, and the radius of the cylinder R. For an N-element array sampled on a cylindrical aperture, the array factor is given by

$$AF(\theta, \phi) = \sum_{n=1}^{N} e^{jk_0[R\sin\theta\cos\phi - \phi_n + z_n\cos\theta]} \tag{F.1}$$

where $k = 2\pi/\lambda$, λ is the wavelength, (ϕ_n, z_n) is the location of the element n, θ and ϕ are the elevation and azimuth angle respectively. Unlike the planar case, the cylindrical array can not be translated to the uv space, instead, the full 3D pattern is given and the radiation patterns in the three principle planes can also be used, (xy, xz, yz) planes.

F.3 Low Discrepancy Sparse Cylindrical Arrays

If elements of the array are placed on the regular cylindrical grid (ϕ, z), element spacings larger than one wavelength at the maximum scan angle will result in grating lobes. Random placement of the elements can potentially remove the grating lobes; however, it may require elements being placed too close together, as shown in chapter 4. While it is possible to avoid this by approaches such as random jitter [73], the use of more structured sequences that cover the aperture more uniformly are preferred. From chapter 4, it was shown that the

methods known as Hammersley and Halton sampling are comprised of the van der Corput sequence which is given by

$$\Psi_b(n) = \sum_{k=0}^{L-1} a_k b^{-k-1} \tag{F.2}$$

where, b is the prime base in which number n is represented and a_k is an integer in $[0, b-1]$. Since this sequence is only defined for the unit interval, the points can be generated and scaled to the correct aperture size, as seen in the planar case. The difference for the 3D case, particularly the cylindrical instance, is that the points need to be mapped to the cylindrical surface. Take for instance, the Hammersley case, where the n^{th} point for the x-coordinate is given by n/N and the y-coordinate is given as $\Psi_b(n)$. In order to generate a point on the cylindrical surface, the following mapping is needed

$$\left(\frac{n}{N}, \Psi_b(n)\right) \;\mapsto\; (\phi_p, z_p) \tag{F.3}$$

The first term is a linear scaling to an angle to the azimuthal plane and the second term is another linear scaling to the range of the height on the z-axis, where the generated point will then be in the cylindrical, $(\phi_p), z_p \in [0, 2\pi] \times [-h/2, h/2]$. The same idea follows for Halton sampling, where

$$\left(\Psi_{b_1}, \Psi_{b_2}\right) \;\mapsto\; (\phi_p, z_p) \tag{F.4}$$

In the study of Hammersley and Halton sampling on a cylindrical surface, the cylinder has a height of 12 wavelengths (λ) and a radius of $6\lambda/\pi$. 100 elements are placed on the cylindrical aperture. In the uniform case this corresponds to 10 circular arrays with 10 elements in each circular array, and an element spacing of 1.2λ. Hammersley and Halton distributions also consist of 100 elements, but with off-grid element locations determined by the low-discrepancy sequences. The element positions on the cylinder is given in Figure F.1.

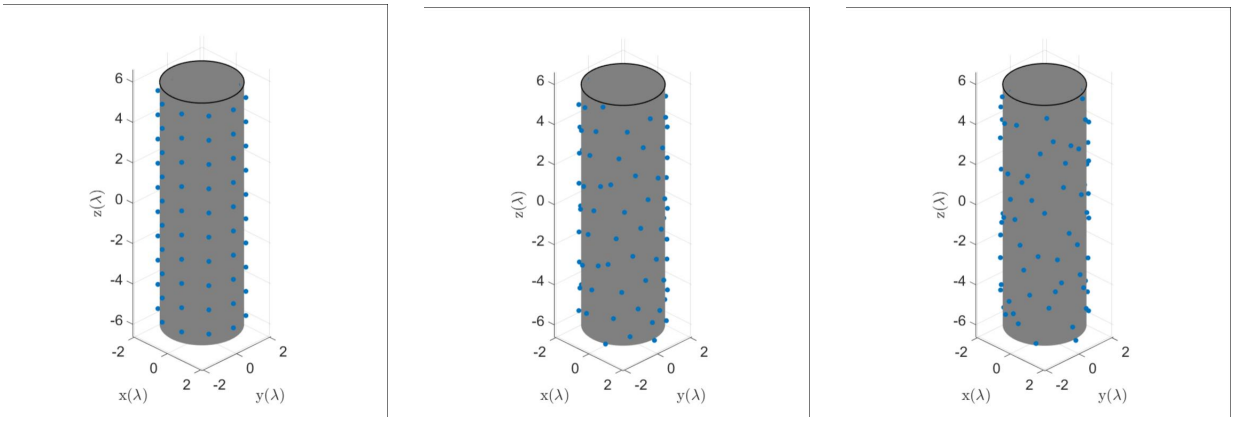

(a) (b) (c)

Figure F.1 Element positions on the cylindrical grid with different distributions: (a) Uniform, (b) Hammersley, (c) Halton

F.4 Sobol Sequences Sampling for Sparse Cylindrical Arrays

Recall that a Sobol sequence, is a base-2 digital sequence that can fill the space in a highly uniform manner [10]. The jth coordinate of the ith point, $p(i, j)$, in a Sobol sequence is given by a series of bitwise exclusive operations. Sobol sampling is hierarchical, since it does not depend on the total number of elements and adding additional elements doesn't require recalculation of element locations. For two-dimensional sampling with Sobol sequence, one option is to use the i points for one axis, and the j points for the orthogonal axis. Alternatively, one can use two Sobol sequences for the axes. In this chapter, the former is adopted. The concept for Sobol sampling on the cylindrical surface is the exact same for Hammersley and Halton sampling, specifically the latter. Two Sobol sets are generated and are then mapped to the cylindrical domain $[0, 2\pi] \times [-h/2, h/s]$ by using a linear scaling. The position of points on the unit square for a 100 element array with uniform and Sobol sequence sampling is given in Figure F.2. Note that this low discrepancy sequence breaks the periodicity of the element positions, while maintaining an equidistribution of sampling points.

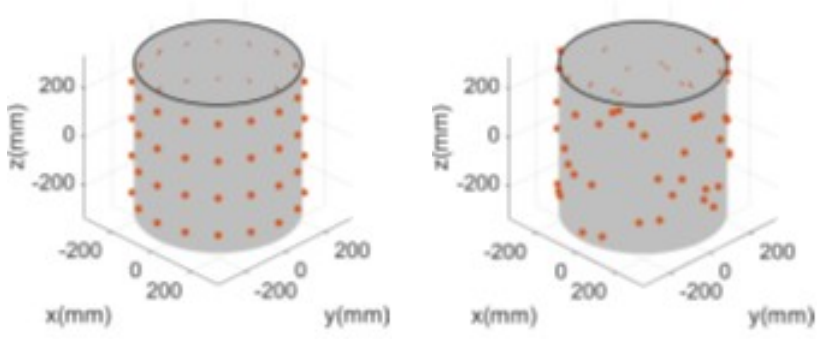

(a) (b)

Figure F.2 Position of points on the cylindrical array with different distributions: (a) Uniform, (b) Sobol Sequence

F.5 Radiation Patterns of Sparse Cylindrical Arrays

Using the element distributions in the previous section, the elements of the cylindrical array are phased to produce a beam in $(\theta = 90°, \phi = 0°)$ direction, and no amplitude taper is considered here. For a single circular array, this corresponds to endfire radiation [1, 109]. Note that while in the general case not all elements on a circular or cylindrical array are active at once, in the studies here it's assumed that the medium is free space and all elements are active.

The radiation pattern of the uniform sparse arrays are given in Figure F.3. The grating lobe problem associated with these arrays is clearly visible in these radiation pattern plots. The circular array has a fan beam as expected due to endfire radiation. The cylindrical array changes this pattern to a pencil-beam radiation; however, the grating lobe issue remains.

The radiation patterns of the cylindrical array with low-discrepancy element spacings are given in Figure F.4. Both Hammersley and Halton distributions result in a suppression of grating lobes, and significantly improve the radiation pattern compared to the uniform case, resulting in a more directive main beam. In the case studies conducted Halton sampling generally outperformed Hammersley. This is primarily due to the non-hierarchical sampling approach in Hammersley distribution. A comparison between the normalized radiation pat-

terns of the three different element distributions on the cylindrical array in the x-y plane is presented in Figure F.5. It can be seen that both low-discrepancy element spacing approaches reduce the grating lobes by about 9 dB. Similar results were observed in other plane cuts.

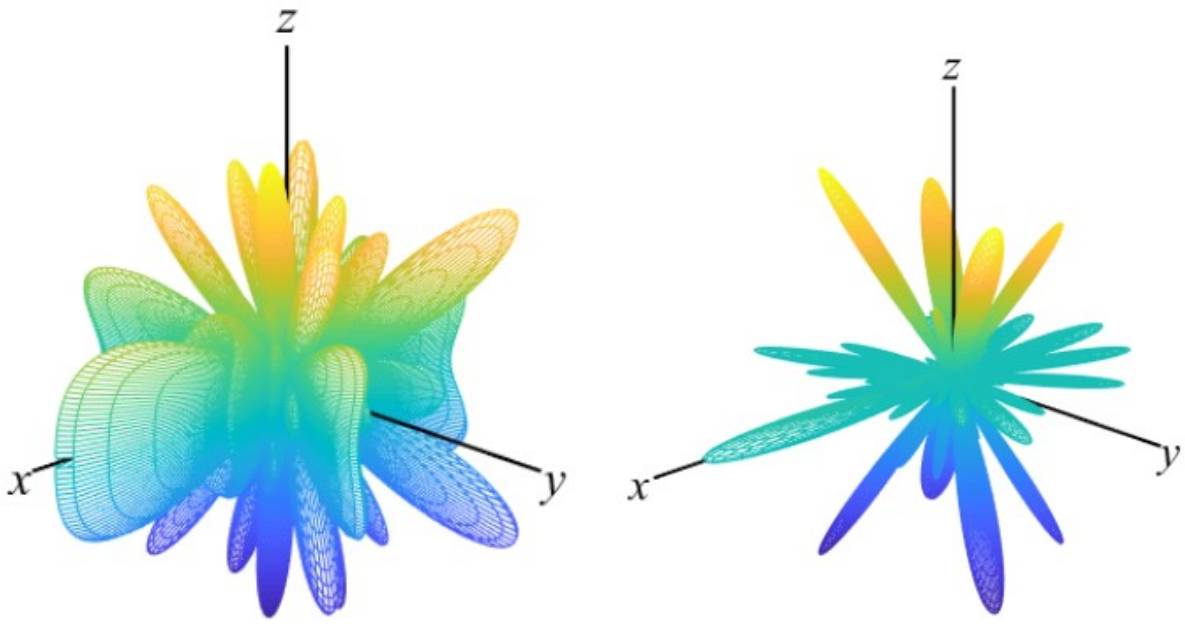

(a) (b)

Figure F.3 Radiation Pattern of the sparse arrays with uniform 1.2λ spacing: (a) 10-element circular array, (b) 100-element cylindrical array

For the Sobol instance, a cylindrical aperture with a diameter and length of approximately 24 inch which are the dimensions of an excavation drum used in mining operations [113] is considered. The array is designed for 2.45 GHz operation, which corresponds to a radius of 2.49 wavelengths (λ) and a height of 4.97λ at the center design frequency. 64 isotropic elements are placed on the cylindrical aperture. For the uniform case with the elements of the array placed on the regular cylindrical grid (ϕ, z), four ring arrays are used, each consisting of 16 equally spaced elements on the ring. This corresponds to element spacings of about 0.98λ and 1.24λ in ϕ and z, respectively. The Sobol sampled array also has 64 elements but with off-grid element locations, mapped to (ϕ_p, z_p), as outlined in the previous section.

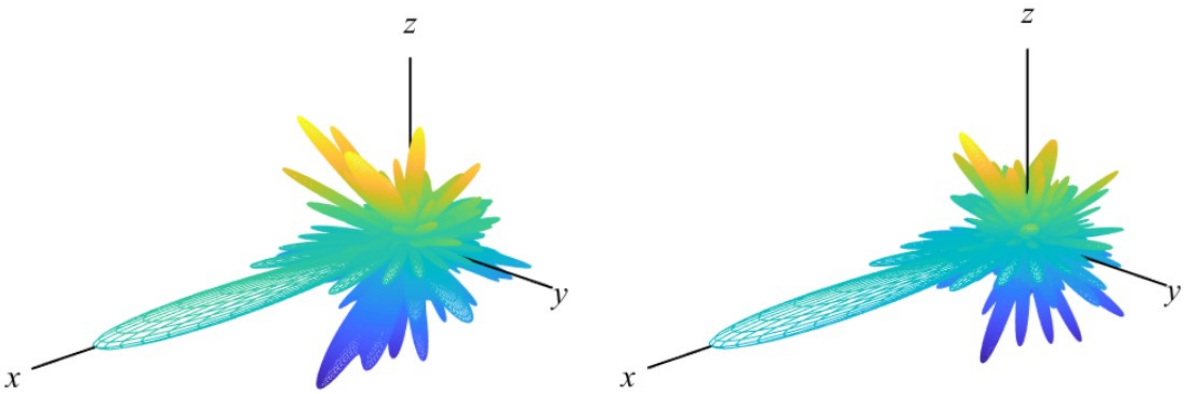

(a) (b)

Figure F.4 Radiation pattern of the cylindrical array with low discrepancy element spacings: (a) Hammersley, (b) Halton

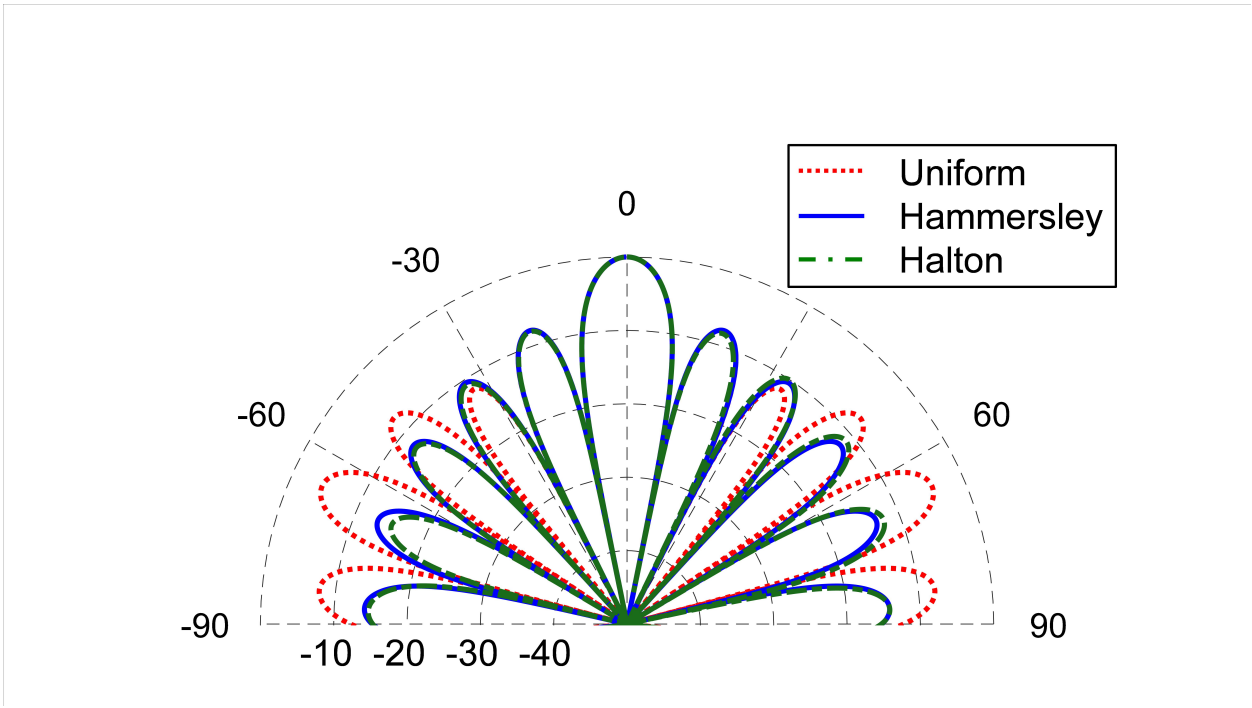

Figure F.5 A comparison of the radiation patterns of the cylindrical array in the x-y plane with uniform and low discrepancy element spacings

Using these distributions, the elements of the cylindrical array are phased to produce a beam in ($\theta = 90\circ, \phi = 0°$) direction, and no amplitude taper is considered here. Note that while in the general case not all elements on a circular or cylindrical array are active at once, in these studies it is assumed that the cylinder medium is free space and all elements are active. The radiation pattern of these sparse arrays are given in Figure F.6. The grating lobe problem associated with the uniform array is clearly visible in Figure F.6 (a). In comparison, the Sobol distribution in Figure F.6 (b) shows a notable suppression of the grating lobes and provides a significantly improved radiation pattern with a directive main beam.

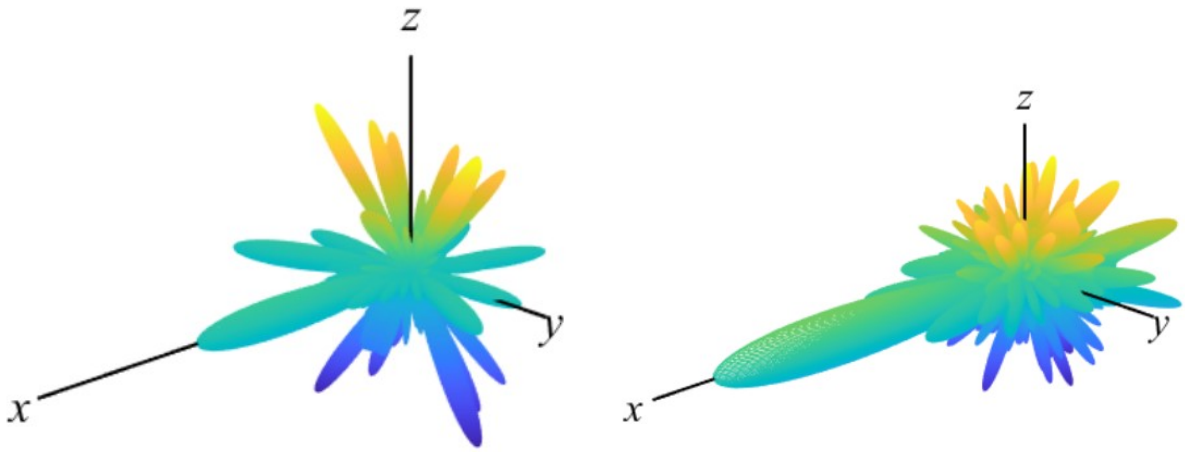

(a) (b)

Figure F.6 Radiation pattern of the cylindrical array with different distributions: (a) Uniform, (b) Sobol

To provide a better comparison, the xy-plane patterns of the sparse arrays are also given in Figure F.7, where it can be seen that the Sobol distribution has reduced the grating lobes by more than 10 dB. Similar results were observed in other plane cuts.

F.6 Conclusions and Future Work

Sparse cylindrical arrays have grating lobe problems associated with elements residing on the regular cylindrical grid. This chapter explores the use of nonuniform element spacing on a sparse cylindrical array using Hammersley, Halton, and Sobol samplings, which are

based on the low-discrepancy Van der Corput sequence and bitwise exclusive-or operations. Numerical studies are conducted, and the results indicate that these element distributions can significantly reduce the grating lobes for not only sparse planar arrays, but also for sparse cylindrical arrays with average element spacing larger than one wavelength. In comparison with the two techniques, Halton sampling has the best performance.

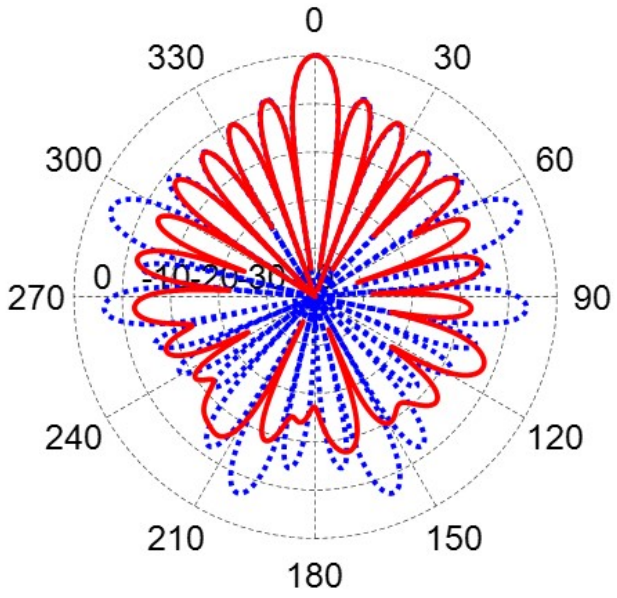

Figure F.7 Normalized radiation pattern of the sparse arrays in x-y plane with uniform (blue-dot)and Sobol (red-solid) distributions

For the study of sparse cylindrical arrays, additional work needs to be conducted. LDS distributions such as Hammersley and Halton with higher orders, as well as, Poisson sampling need to be studied. Furthermore, performance metrics on the element spacings, as well as far-field radiation pattern characteristics such as peak SLL, directivity, and aperture efficiency have to be conducted for all the case studies. Finally, for these conformal arrays it is important to study the impact of active region. For cylindrical arrays, typically a portion of elements are active (on) at any time, given by $\phi_{\min}$ and $\phi_{\max}$ in the azimuth plane and the rest are turned off. This is done so that the beam can be focused in a particular direction without having to use all of the elements, where this configuration can be thought of a curved planar array.

APPENDIX G

COPYRIGHT PERMISSION

Note that copyright permission (uploaded as a separate supplemental file) was provided by Dr. Randy Haupt for the use of: "Low Discrepancy Sparse Phased Array Antennas", "Sparse Cylindrical Arrays Based on the Low-Discrepancy Sobol Sequence Sampling", and "Sparse Cylindrical Arrays with Low Discrepancy Element Spacing Based on Van der Corput Sequence" in this dissertation.